1,3-*N*,*O*-Chelated Early-Transition-Metal Complexes for the Activation and Formation of C−E (E = H, C, N, O) Bonds

by

Samuel Elliot Griffin

B.Sc. (Hons.), The University of British Columbia Okanagan, 2016

A THESIS SUBMITTED IN PARTIAL FULFILLMENT OF

THE REQUIREMENTS FOR THE DEGREE OF

DOCTOR OF PHILOSOPHY

in

THE FACULTY OF GRADUATE AND POSTDOCTORAL STUDIES

(Chemistry)

THE UNIVERSITY OF BRITISH COLUMBIA

(Vancouver)

July 2021

The following individuals certify that they have read, and recommend to the Faculty of Graduate and Postdoctoral Studies for acceptance, the dissertation entitled:

1,3-*N*,*O*-Chelated Early-Transition-Metal Complexes for the Activation and Formation of C−E (E = H, C, N, O) Bonds

submitted by Samuel Elliot Griffin in partial fulfillment of the requirements for

the degree of Doctor of Philosophy

in Chemistry

Examining Committee:

Laurel L. Schafer, Professor, Chemistry, UBC
Supervisor

Parisa Mehrkhodavandi, Professor, Chemistry, UBC
Supervisory Committee Member

Michael O. Wolf, Professor, Chemistry, UBC
University Examiner

Gren N. Patey, Professor, Chemistry, UBC
University Examiner

Warren E. Piers, Professor, Chemistry, University of Calgary
External Examiner

Additional Supervisory Committee Members:

Harry Brumer, Professor, Chemistry and Michael Smith Laboratories, UBC
Supervisory Committee Member

Pierre Kennepohl, Professor, Chemistry, UBC
Supervisory Committee Member

Abstract

This thesis describes the exploration of 1,3-*N*,*O*-chelated early-transition metals and their applications in diverse catalytic reactions. While cyclopentadienyl-ligated metal complexes and their derivatives are highly robust and have found extensive catalytic applications in industry, their robustness limits their ability to act cooperatively with the metal centre to promote new and challenging transformations. In addition, the multi-step synthetic routes required to access modified cyclopentadienyl derivatives hinder tuning of the steric and electronic properties as needed. 1,3-*N*,*O*-chelating ligands are complementary to cyclopentadienyl ligands as a result of their highly modular syntheses and unsymmetrical donor properties, leading to flexible coordination modes, hemilability, and potential for metal-ligand cooperativity. However, 1,3-*N*,*O*-chelating ligands are comparatively underexplored despite promising recent advances in catalysis.

Chapter 2 describes the use of zirconium ureate complexes for the catalytic hydroamination of 2-vinylpyridine. Stoichiometric and mechanistic studies revealed that the reaction with 2-vinylpyridine proceeds through an aza-Michael mechanism, where the C−N bond forming step is reversible and can be directly observed by variable temperature ^{1}H NMR spectroscopy. In Chapter 3, these zirconium ureate complexes were investigated for their reactivity in hydroaminoalkylation. This led to the discovery of the first catalytic example of hydroaminoalkylation with alkyne substrates to directly access allylic amines. Stoichiometric and mechanistic studies suggest that the open coordination sphere of the zirconium catalyst aids in promoting the challenging reaction steps necessary for catalytic turnover.

Chapter 4 investigates the coordination chemistry and reactivity of vanadium pyridonate complexes, which were previously unexplored. These compounds can be made easily via protonolysis of amido or organometallic starting materials, as is the case for other early-transition

metal pyridonates. Vanadium(IV) pyridonates were found to undergo reduction to vanadium(III) in some cases, and mechanistic studies found that the released alkylamine during protonolysis was acting as the reductant. These compounds also showed hemilability, potential for metal-ligand cooperativity, and a tendency to aggregate. Chapter 5 then discusses the application of vanadium pyridonate complexes in the catalytic reductive coupling of alcohols. Mechanistic studies showed that bimetallic intermediates were involved, providing complementary experimental evidence for the mechanism proposed by DFT in a reported monometallic catalyst system.

Lay Summary

Chemical reactions that are promoted by metal-containing compounds have had an immense impact on society, with applications in various industries including pharmaceuticals, agriculture, plastics, electronics, and more. Modern society depends greatly on fossil fuel resources as they provide most of the energy and chemical building blocks needed for these important chemical transformations. However, due to their limited quantity and damaging effects on the environment, fossil fuels are not a sustainable source of energy and chemicals in the long term. Furthermore, many of the current methods used for making industrially relevant compounds rely on precious metals or generate harmful waste. Thus, this thesis describes the development of abundant, inexpensive metal compounds to make industrially relevant molecules efficiently, with a focus on the inner workings of these reactions. In addition, these abundant metals are used towards the conversion of biomass, a sustainable alternative to fossil fuels, into useful fuels and chemicals.

Preface

All of the research presented in this thesis, including the experimental work and analysis of the data, was designed and conducted by me in consultation with my supervisor, Prof. Laurel Schafer, with the exceptions described below. This document and the publications listed below were also written exclusively by me with helpful input from my supervisor, Prof. Laurel Schafer, except for the instances noted below.

Generally, X-ray crystallography data collection and refinement were performed by me with helpful input from Dr. Brian Patrick. However, Dr. Brian Patrick collected the X-ray data for compounds **4.10**, **4.14**, **4.15**, **4.16**, and **6.6**, and assisted directly with the refinement of the X-ray data for compound **3.5**. The experimental work presented in Chapter 3 was performed in collaboration with Mr. Erick Nuñez Bahena. Specifically, Mr. Erick Nuñez Bahena synthesized and characterized (except for X-ray crystallographic studies) compounds **3.2**-**3.7**, with me providing guidance in a mentorship role. The catalytic experiments and characterization of the compounds presented in Tables 3.1, 3.2, and 3.3 were performed collaboratively. Mr. Erick Nuñez Bahena also contributed to the writing of the corresponding publication that is referenced below. Finally, the experiments presented in Schemes 6.4 and 6.5 were inspired by initial results obtained by Ms. Amanda A. Fogh, an undergraduate student under my supervision.

A version of the data contained in Chapter 2 has been published by the American Chemical Society: **Griffin, S. E.**; Pacheco, J.; Schafer, L. L. Reversible C−N Bond Formation in the Zirconium-Catalyzed Intermolecular Hydroamination of 2-Vinylpyridine. *Organometallics* **2019**, *38*, 1011−1016. All of the research within this publication, including the experimental work and analysis of the data, was designed and conducted by me in consultation with my supervisor, Prof. Laurel Schafer. This publication was also written exclusively by me with helpful input from Prof.

Schafer. Preliminary results obtained by Mr. Pacheco inspired some of the experiments detailed in this publication.

A version of the data contained in Chapter 3 has been published by the American Chemical Society: Nuñez Bahena, E.[‡]; **Griffin, S. E.**[‡]; Schafer, L. L. Zirconium-Catalyzed Hydroaminoalkylation of Alkynes for the Synthesis of Allylic Amines. *J. Am. Chem. Soc.* **2020**, *142*, 20566−20571. [‡]These authors contributed equally. The research within this publication, including the experimental work and analysis of the data, was designed and conducted by me in collaboration with Mr. Nuñez Bahena as described above and in consultation with my supervisor, Prof. Laurel Schafer. This publication was also written by me in collaboration with Mr. Nuñez Bahena as described above with helpful input from Prof. Schafer.

A version of the data contained in Chapter 5 and some data contained in Chapter 4 has been published by the American Chemical Society: **Griffin, S. E.**; Schafer, L. L. Vanadium Pyridonate Catalysts: Isolation of Intermediates in the Reductive Coupling of Alcohols. *Inorg. Chem.* **2020**, *59*, 5256–5260. *ACS Editors' Choice.* All of the research within this publication, including the experimental work and analysis of the data, was designed and conducted by me in consultation with my supervisor, Prof. Laurel Schafer. This publication was also written exclusively by me with helpful input from Prof. Schafer.

Table of Contents

List of Tables

List of Figures

List of Schemes

List of Symbols and Abbreviations

anal	analysis
Å	angstrom, 10^{-10} m
aq.	aqueous
Ar	aryl
avg	average
br	broad (spectral)
Bu	butyl
calcd	calculated
cat.	catalyst
CI	chemical ionization
cm	centimetre
Cp	cyclopentadienyl
Cp*	pentamethylcyclopentadienyl
CV	cyclic voltammetry
d	doublet (spectral)
°	degrees
°C	degrees Celsius
δ	chemical shift
$\Delta G°$	standard Gibbs free energy change
$\Delta H°$	standard enthalpy change
$\Delta S°$	standard entropy change

DFT	Density Functional Theory
Dipp	2,6-diisopropylphenyl
DMAP	4-dimethylaminopyridine
e^-	electron
E	element or functional group
EA	elemental analysis
EBI	ethylenebis(indenyl)
EBTHI	ethylenebis(tetrahydroindenyl)
EE	electronic energy
ee	enantiomeric excess
EI	electron ionization
EMIM	1-ethyl-3-methylimidazolium
equiv.	equivalent(s)
ESI	electrospray ionization
Et	ethyl
η^n	eta, indicates hapticity of n atoms
FD	field desorption
Flu	fluorenyl
FMO	frontier molecular orbital
g	gram
GC-MS	gas chromatography-mass spectrometry
h	hour

HAT	hydrogen atom transfer
HMF	5-hydroxymethylfurfural
HRMS	high-resolution mass spectrometry
HSAB	hard/soft acid base
Hz	hertz
^{i}Pr	isopropyl
J	joule
J	coupling constant
K	kelvin
κ^{n}	kappa, indicates denticity of n atoms
kcal	kilocalorie
K_{eq}	equilibrium constant
kJ	kilojoule
L	supporting ligand
LIFDI	liquid injection field desorption ionization
L_n	ligand set
M	metal
m	multiplet (spectral)
m/z	mass per charge number
Me	methyl
MepyO	6-methyl-2-pyridonate
Mes	mesityl

MHz	megahertz
μL	microlitre
min	minute
mL	millilitre
mm	millimetre
mmol	millimole
mol	mole
molecular ion	$[M]^+$
MS	mass spectrometry
μ_B	Bohr magneton
μ_{eff}	effective magnetic moment
μ_n	mu, indicates bridging of ligand to n metal centres
$\mu_{(spin\text{-}only)}$	spin-only magnetic moment
N.D.	not detected
^{n}Bu	normal butyl
NMR	nuclear magnetic resonance
ORTEP	Oak Ridge thermal ellipsoid plot
PCET	proton-coupled electron transfer
Ph	phenyl
ppm	parts per million
psi	pounds per square inch
q	quartet (spectral)

QTOF	quadrupole time-of-flight
R	organic substituent
R	gas constant, 8.314 $J•K^{-1}•mol^{-1}$
r.t.	room temperature
s	singlet (spectral)
S	spin
sep	septet (spectral)
$\sum\theta_{N4}$	sum of bond angles about N4
t	time
T	temperature
t	triplet (spectral)
^{t}Bu	*tert*-butyl
TDMAV	tetrakis(dimethylamido)vanadium(IV)
Tf	triflyl, F_3CSO_2
THF	tetrahydrofuran
VMD	Visual Molecular Dynamics
VT	variable-temperature
wt.	weight
X	halide
XRD	X-ray diffraction
Z	generic functional group

List of Compounds

Chapter 2:

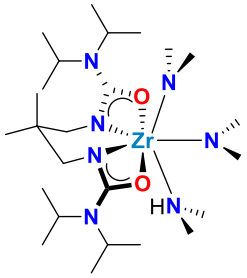

2.1

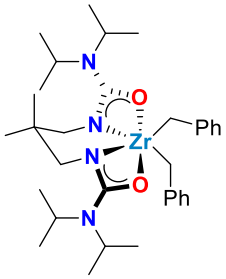

2.2

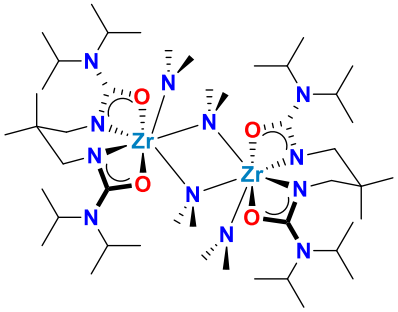

2.3

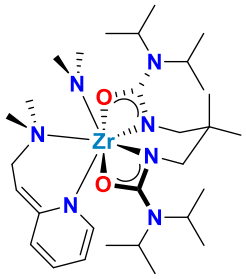

2.4

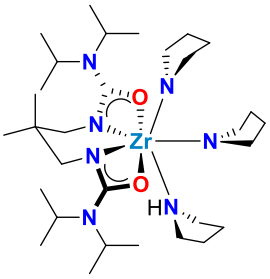

2.5

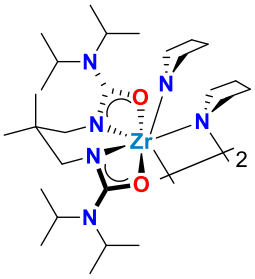

2.6

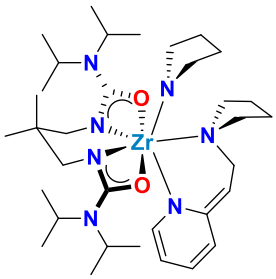

2.7

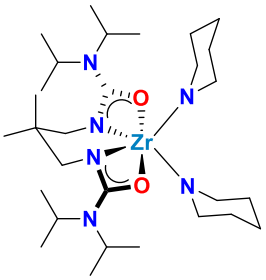

2.8

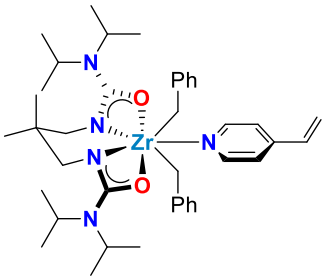

2.9

Chapter 3:

A

B

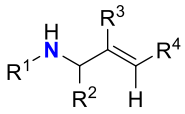

C

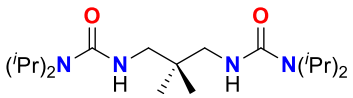

$H_2(N,O)_2$

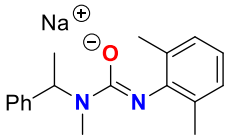

D

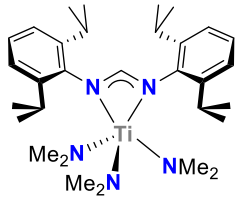

E

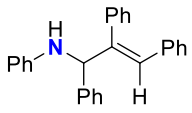

3.1

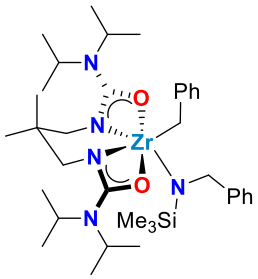

3.2

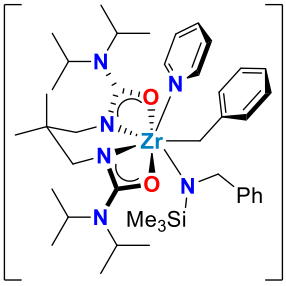

3.3

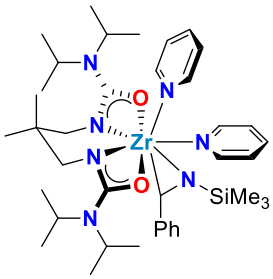

3.4

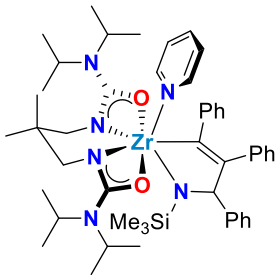

3.5

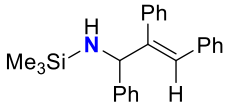

3.6

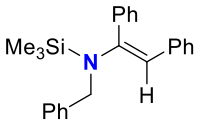

3.7

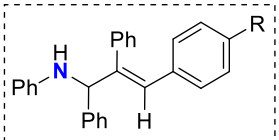

3.8a; R = Me
3.9a; R = OMe
3.10a; R = CF_3
3.11a; R = Cl

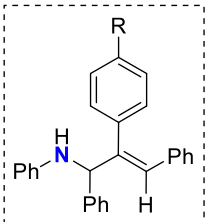

3.8b; R = Me
3.9b; R = OMe
3.10b; R = CF_3
3.11b; R = Cl

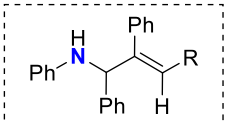

3.12a; R = 2-pyridyl
3.13a; R = Me
3.14a; R = C_6H_{11}
3.15a; R = $SiMe_3$

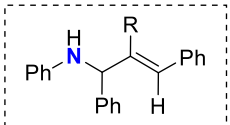

3.12b; R = 2-pyridyl
3.13b; R = Me
3.14b; R = C_6H_{11}
3.15b; R = $SiMe_3$

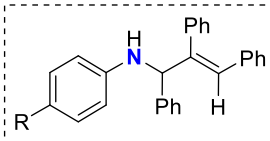

3.16; R = Me
3.17; R = Cl
3.18; R = F

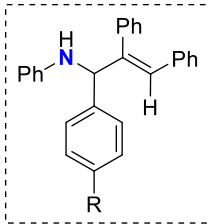

3.19; R = Me
3.20; R = Cl
3.21; R = F

Chapter 4:

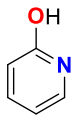

4.1

4.2

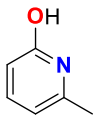

4.3

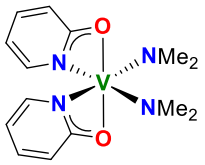

4.4

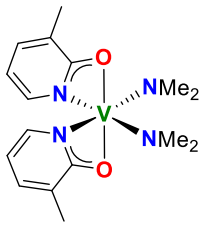

4.5

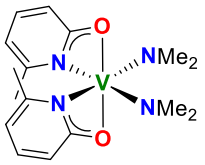

4.6

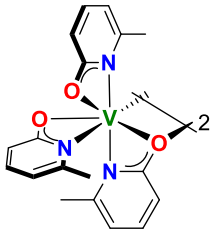

4.7

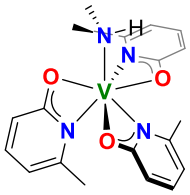

4.8

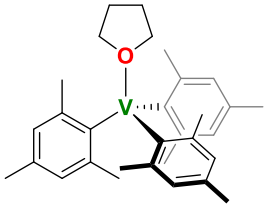

4.9

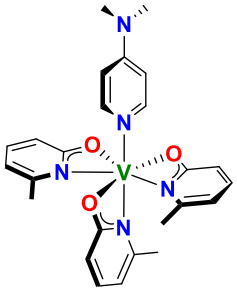

4.10

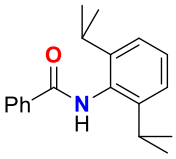

4.11

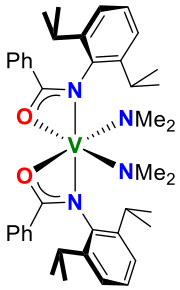

4.12

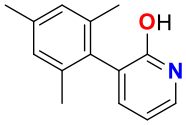

4.13

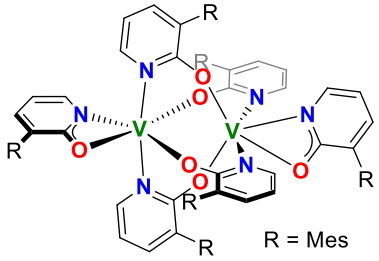

4.14

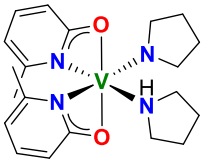

4.15

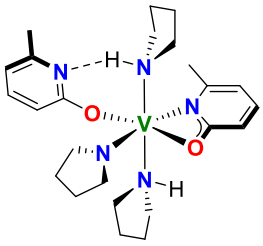

4.16

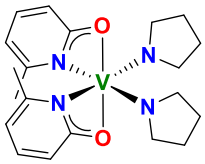

F

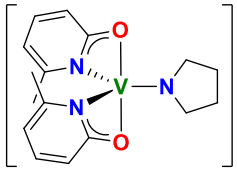

G

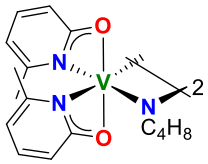

G'

Chapter 5:

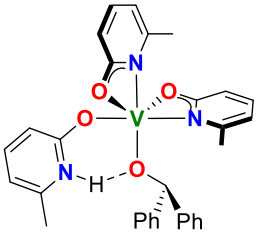

5.1

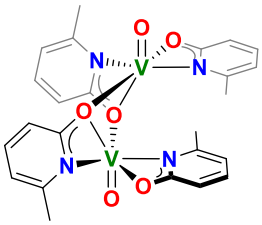

5.2

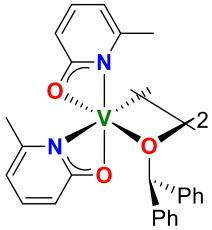

H

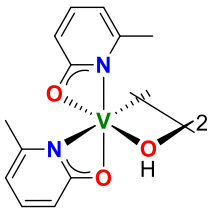

I

Chapter 6:

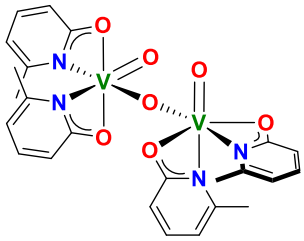

6.1

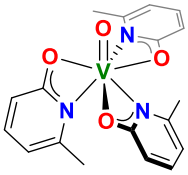

6.2

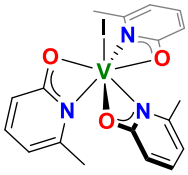

J

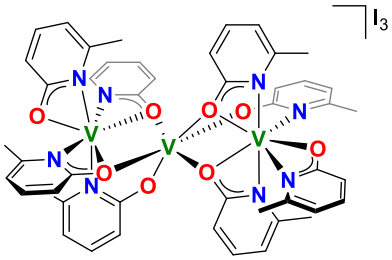

6.3

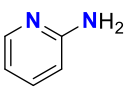

6.4

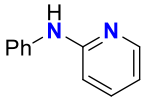

6.5

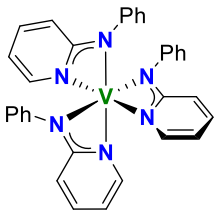

6.6

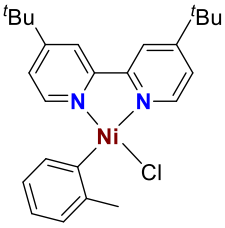

6.7

Acknowledgements

First, I would like to thank my supervisor, Prof. Laurel Schafer, for all her help and guidance over these past five years. Her patience and encouragement were critical in helping me build confidence in the early years of my degree. She also supported me in pursuing my own ideas and exercising independence. Laurel has given me many opportunities to develop my skills outside of experimental work, and I am very grateful for those enriching experiences. I also want to thank her for being a champion of diversity in chemistry and science and instilling those same values in those around her.

Next, I would like to thank my supervisory committee, Prof. Parisa Mehrkhodavandi, Prof. Harry Brumer, and Prof. Pierre Kennepohl for their valuable input and advice throughout my degree. I especially thank Prof. Mehrkhodavandi and Prof. Brumer for graciously offering to serve as readers for this thesis. Additionally, I would like to extend further thanks to Prof. Mehrkhodavandi for her teaching mentorship and support, which has played a significant role in my PhD and will have a lasting impact on my future career.

I am extremely grateful to NSERC (CGSM, PGSD) and UBC (4YF, Laird, Dr. F. J. Nicholson Scholarship) for funding me during my degree. I understand what a privilege it is to obtain an education and to have funding support. In addition, I am thankful to UBC Chemistry staff and facilities for enabling me to carry out this research. Special thanks go to Dr. Brian Patrick, who generously trained me as an amateur crystallographer and provided a substantial amount of help with the crystal structures found in this thesis. I thank Dr. Maria Ezhova for her NMR training and assistance with more sophisticated NMR experiments.

Several past and current Schafer group members have provided mentorship and meaningful conversations that have supported me in the completion of this thesis. In no particular order, thank

you to Drs. Marcus Drover, Joseph Clarkson, Jason Brandt, Erica Lui, Dawson Beattie, Sorin-Claudiu Rosça, and Damon Gilmour, among others, for answering all my questions and allowing me to bounce ideas off of them. Thank you to Nirmal Kuanr, as I cannot help but crack a smile when I hear him laugh in another room. Many thanks go to Erick Nuñez Bahena, Amanda Fogh, and Olivia Adamczyk for being fantastic researchers and people to mentor and work alongside. I especially thank Erick for his significant contributions to Chapter 3, which could not have been completed without his help. To all other past and current Schafer group members, thank you for welcoming me into the group and tolerating my unconventional music.

I want to thank my friends and extended family for all their support and encouragement over the years, who will be glad to know that I am finally finished "school". I also thank my former supervisors Prof. Wesley Zandberg and Prof. Kevin Smith for inspiring me to pursue graduate school in chemistry and supporting me along the way.

I want to thank my family for their unconditional love and support. I thank my mom, Connie, for always supporting me in my diverse interests growing up and going above and beyond as a mother to help me reach my goals. I thank my dad, Malcolm, for encouraging me to go outside of my comfort zone and for always believing in me. I also want to thank my brothers, Ethan and Zachary, for their support and for having lots of refreshingly non-chemistry related stories to share. Each of you has had an influence on who I am today, and I love you all.

Finally, I want to thank my partner, Leona Shum, for being the unsung hero behind this thesis and my degree. I have been so fortunate to have such a kind-hearted, supportive, strong, and compassionate person to be with me every step of my PhD and life for the past 5 years. I have learned more from her on how to be a good person than I could ever learn about chemistry. Truly, I could not have done this without her help and support.

Dedication

I dedicate this to my love,

Leona

Chapter 1: Introduction

1.1 General Introduction

Cyclopentadienyl ligands, which are introduced below, have been used extensively in catalytic applications with a wide range of metals. Chemists in the fields of organometallic chemistry and catalysis are thus very familiar with this class of auxiliary ligands. In contrast, 1,3-*N*,*O*-chelating monoanionic ligands are only being introduced to these communities, and their application in supporting catalytically active metal complexes is just beginning. As a result, the value of using 1,3-*N*,*O*-chelating ligands as alternatives to traditional cyclopentadienyl scaffolds is an active area of research. Notably, the 1,3-*N*,*O*-chelating ligand framework has shown particular promise in the development of electrophilic, early-transition-metal catalysts, and analogues of previously established cyclopentadienyl complexes have shown distinct reactivity trends. To date, a comparison of the properties of both ligand classes and their uses in transition metal catalysis is lacking.

This thesis investigates 1,3-*N*,*O*-chelating ligands, namely ureates and pyridonates, on group 4 and group 5 early-transition metals for their coordination chemistry and applications in catalysis. The principal motivation for this work is the discovery of new and active catalysts to address established shortcomings in catalytic transformations. This work has launched a new direction in the Schafer group focusing on vanadium catalysts relevant to biomass utilization, and otherwise informs the inorganic and organometallic community on design principles for earth-abundant early-transition-metal catalysts in organometallic chemistry.

1.2 Cyclopentadienyl Ligands

Transition-metal catalysis has greatly impacted the chemical community and society. Coupling reactions for C−C bond formation are ubiquitous in organic chemistry and have

important applications in natural product and materials synthesis as well as the fine chemical, pharmaceutical, and agrochemical industries.[1] Key to the advancement of transition-metal catalysis for C−C bond formation is the judicious choice of the ligands that bind the metal, as the reactivity of the metal centre can be carefully tuned by varying the steric and electronic properties of the ligands. In considering the array of transition-metal elements and types of ligands available, the number of possible combinations to be explored for tuning catalyst reactivity is virtually unlimited.

Cyclopentadienyl (Cp) ligands and their derivatives are some of the most ubiquitous classes of ligands in transition-metal catalysis (Scheme 1.1).[2,3] One cannot overstate the importance of Cp-ligated complexes in industrial processes, for example, olefin polymerization.[4,5] Consequently, numerous reviews have been assembled on the chemistry of Cp-ligated complexes.[2–4,6–11] Here, the following sections will introduce the structure and characteristics of Cp ligands and their complexes and explain the advantages of Cp complexes for catalysis more generally by highlighting specific examples. The limitations of Cp-based systems will also be considered, providing a rationale for exploring other ligand systems for transition-metal catalyzed reactions. The key attribute of Cp ligands that is both advantageous and disadvantageous is their robustness and insusceptibility to reactivity once installed on a metal centre. This will be elaborated in the following sections.

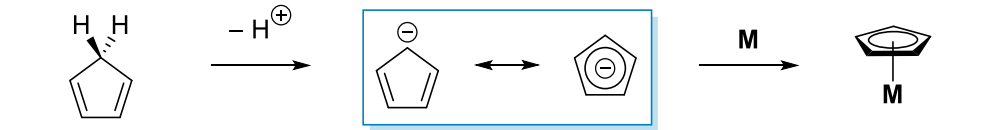

Scheme 1.1 Cyclopentadienyl as a ligand

1.2.1 Metal-Cp Bonding

The 6π-aromatic nature of the Cp anion gives rise to its stability, but the bonding interactions in Cp-M complexes are responsible for their remarkable stability and versatility in comparison to other organometallic species.[2] Specifically, the most common binding mode of Cp to a metal is η^5, where the Cp fragment occupies three facially oriented coordination sites at the metal centre (Figure 1.1). In this way, the η^5-Cp ligand is a formally L_2X-type ligand (two neutral, L-type olefin ligands and one anionic, X-type alkyl donor) and donates five electrons to the metal (using the Covalent Bond Classification method of electron counting).[2,12] Alternatively, one could account for the charged nature of the anionic Cp ligand and consider it as a six-electron donor to a cationic metal centre. Despite each of the five carbons being bound to the metal centre, free rotation of the η^5-Cp-M bond can still occur, as evidenced by a single ^{1}H NMR signal being observed for the Cp ring in complexes that lack rotational symmetry.[3] Orbital interactions involved in the bonding of η^5-CpM complexes invoke the π-orbitals of Cp, which are depicted on the right in Figure 1.1. Three of these frontier molecular orbitals (FMOs) are filled and can donate electron density to the metal, with one having σ-symmetry and two having π-symmetry. There are also two empty FMOs of δ-symmetry that can accept electron density from the metal. In combination with the electrostatic attraction of the anionic Cp and the cationic metal centre,[2] these multiple bonding interactions make η^5-CpM complexes exceptionally stable.

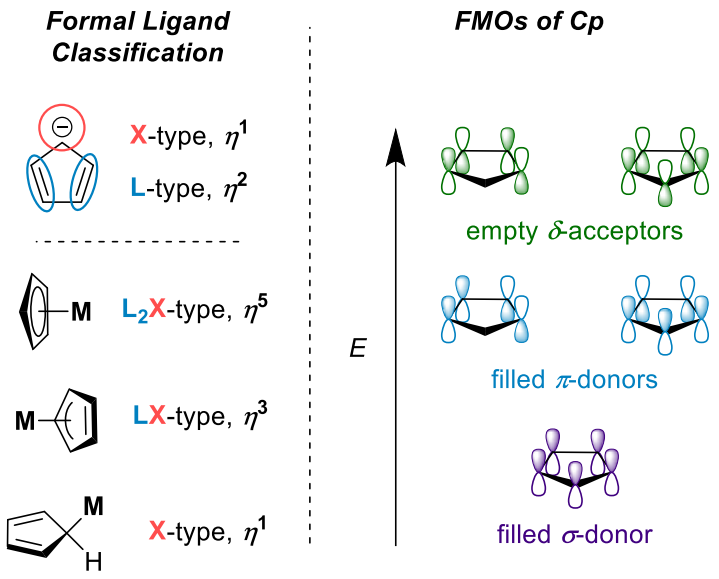

Figure 1.1 Binding modes and bonding orbitals of Cp

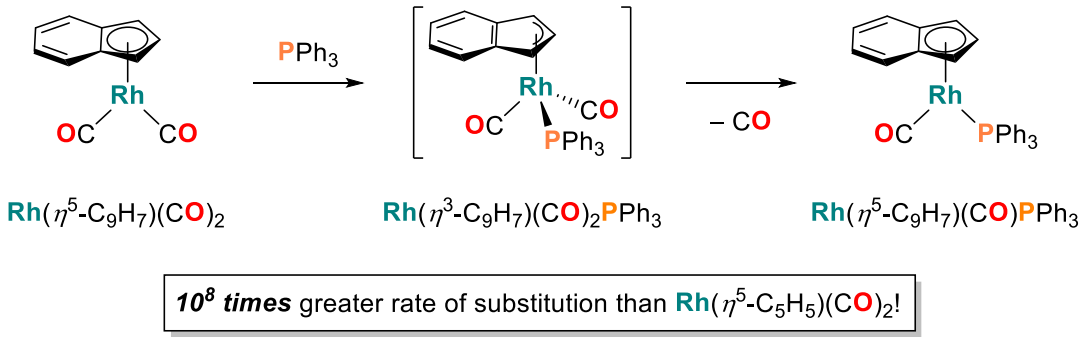

Scheme 1.2 Comparison of associative substitution rate in Rh indenyl/Cp complexes

While the η^5 binding mode is most common, Cp may also interact with a metal via the η^3 or η^1 binding modes, shown in Figure 1.1.[13] Using the same analysis of the binding characteristics, η^3-Cp and η^1-Cp can be classified as formally LX- and X-type ligands that donate three and one electron(s), respectively; η^3-Cp and η^1-Cp can similarly be considered to occupy two or one coordination site(s), respectively. The interconversion of the three possible binding modes has been termed "ring-slippage."[13] This can be particularly advantageous in catalysis as the Cp ligand can shift in hapticity, thus modifying the degree of electron donation and formal coordination

number, to accommodate changes at the metal centre and stabilize reactive intermediates. Indenyl (a derivative of Cp) complexes are known for their facile η^5/η^3 interconversion. This can result in increased rates of associative substitution to electronically saturated species compared to analogous Cp complexes (Scheme 1.2) and other modified reactivity.[14] This so-called "indenyl effect"[14–16] is a result of the weaker η^5-indenyl-metal bond compared to the η^5-Cp-metal bond combined with the stronger η^3-indenyl-metal bond compared to the η^3-Cp-metal bond, reducing the energy difference between the two binding modes compared to Cp.[15] The origin of this difference in bond strength is related to the aromaticity of the fused benzene ring in the indenyl ligand and has been investigated computationally.[15] As one of the π bonds is partially involved in the aromatic system rather than donating fully to the metal, the η^5-indenyl donates less than η^5-Cp and the resulting indenyl-metal bond is weaker. However, in electronically over-saturated intermediates or transition states, donation occurs to an antibonding orbital, thus the decreased donation of the indenyl produces a stronger bonding interaction relative to the Cp ligand. This phenomenon has been used to advantage in a number of catalytic processes including olefin polymerization,[17,18] alkyne cycloaddition,[19] and hydrofunctionalization reactions,[20,21] to name a few. In the case of indenyl complexes, a shift to an η^6 binding mode is also possible. In a recent example, Peters and co-workers demonstrated that oxidation of an indenyl Fe−H complex from Fe(II) to Fe(III) results in migration of the hydride ligand to the Cp fragment of the indenyl ligand, forming a Fe(I) arene complex (Scheme 1.3).[22] Clearly, the variable binding modes of Cp and its derivatives can be utilized to promote a variety of transformations.

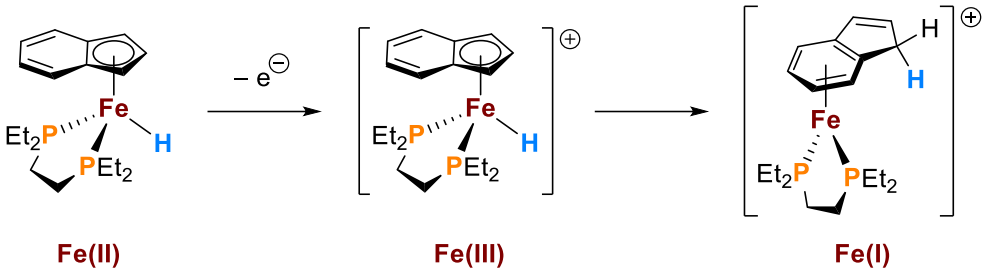

Scheme 1.3 Migration of a metal hydride to an indenyl ligand to give a η^6-arene complex

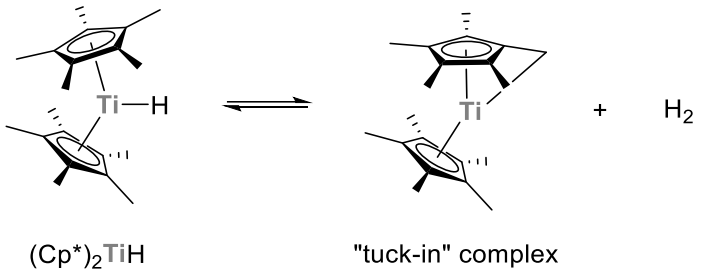

Scheme 1.4 Intramolecular C−H abstraction of a Cp* ligand to give a η^5:η^1 tuck-in complex

Substituted Cp derivatives can allow access to alternative binding modes to the typical η^5 coordination. Among the commonly used substituted Cp derivates, the fully-substituted Cp ligand C_5Me_5, or Cp* (Scheme 1.4),[2,23] is most broadly used.[8] Sterically-demanding Cp* has greater electron-donating properties and forms stronger bonds to metal ions compared to Cp.[23] Another advantage of Cp* is that it can form "tuck-in" complexes, where the Cp* binds in an η^5:η^1 binding mode as illustrated in Scheme 1.4.[24] This type of compound forms via deprotonation of a methyl C−H on the Cp* ligand to form a dianionic Cp* derivative. The example shown, with reversible formation of the tuck-in complex reported by Luinstra and Teuben, highlights the potential of these species for the activation of small molecules such as dihydrogen.[24] Similar to the indenyl case outlined above, Peters and co-workers have shown that hydride migration can occur to the C_5 unit of the Cp* ligand as well (Scheme 1.5).[25] The Cp*Fe(III)−H complex transfers the hydride from the metal centre to the Cp* ring upon coordination of carbon monoxide, producing a Fe(I) complex

with a neutral, η^4-pentamethylcyclopentadiene ligand. This short-lived species undergoes rapid proton-coupled electron transfer (PCET) to produce H_2 and a Cp*Fe(II) complex.[25] Overall, Cp and its derivatives demonstrate a variety of possible binding modes, supporting various electronic states and coordination environments of metal centres that promote diverse reactivity.

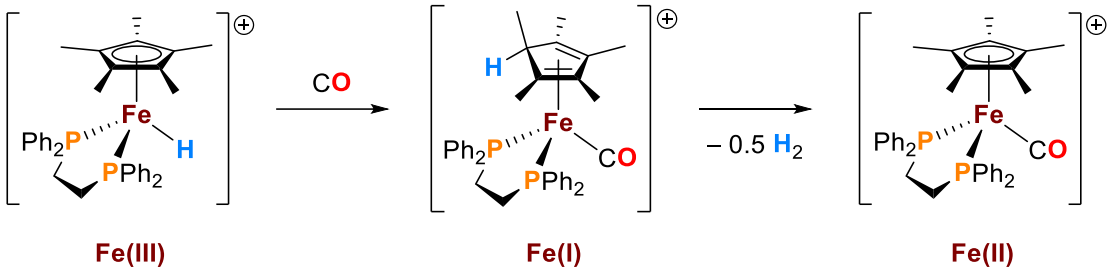

Scheme 1.5 Hydride migration to Cp* to give a neutral η^4-diene ligand followed by H_2 evolution

1.2.2 Metallocene Complexes

Metallocenes, with the formula Cp_2M, were the first type of Cp-bound metal complex to be discovered and are arguably the most important class of Cp compounds. Indeed, the first report of ferrocene (Cp_2Fe)[26] and the ensuing elucidation of its structure are considered by many to have initiated the field of modern organometallic chemistry.[2,27] These so-called "sandwich" compounds are formally six-coordinate, with a 180° angle along the Cp-M-Cp bond axis (Figure 1.2).[2] Ferrocene is particularly stable as it is an 18-electron species, which can be useful when considering related metallocene compounds. For example, cobaltocene (Cp_2Co) is a 19-electron species that can be used as a stoichiometric reductant, as the loss of an electron to form the cobaltocenium cation makes it isoelectronic with ferrocene (Figure 1.2).[28,29] The redox chemistry of ferrocene itself can also be utilized in catalysis. There have been many reports of using a ferrocene redox switch to modify catalyst reactivity, often turning-on or turning-off catalytic activity.[30–38] In one example, the ferrocene switch allowed for a polymerization catalyst to change its selectivity rather than its activity; Diaconescu and co-workers reported zirconium and titanium

catalysts containing a non-innocent ferrocene-derived ligand for copolymerization of cyclic esters and epoxides (Scheme 1.6).[37,38] While the parent catalyst with ferrocene [Fe(II)] in the backbone was selective for the polymerization of the cyclic ester monomers, oxidizing the ligand to a ferrocenium [Fe(III)] derivative modified the properties of the metal centre and switched the selectivity to polymerization of the epoxide monomers. The Fe(III) ligand could then be reduced back to Fe(II) to reverse the selectivity and precisely control the composition of the resulting copolymer. This principle has been applied in other polymerization reactions as well[39] and demonstrates the functionality of metallocene-based ligands in catalysis. However, due to their robustness even in the absence of additional supporting ligands, sandwich compounds find less application in catalysis than other Cp-derivatives.

It should be noted that another class of homoleptic Cp complex exists, namely tris(η^5-cyclopentadienyl) complexes or Cp_3M.[2] However, this type of structure is largely restricted to lanthanide and actinide metals and is therefore outside the scope of this introduction.[40]

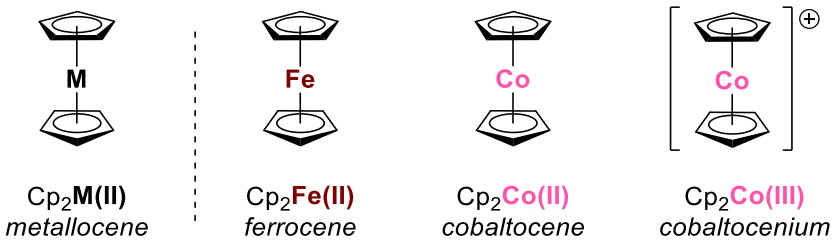

Figure 1.2 Structure of general metallocenes and ferrocene, cobaltocene, and cobaltocenium

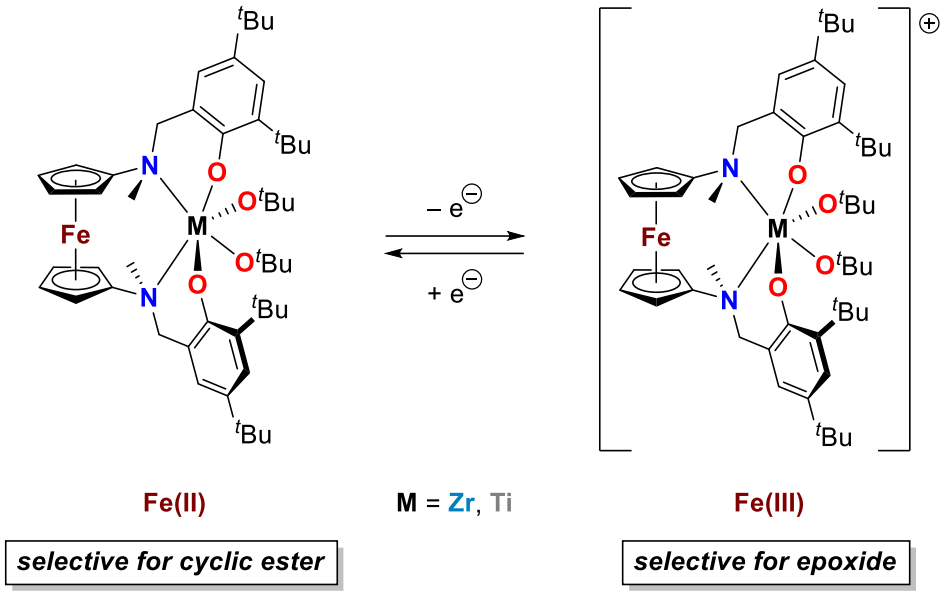

Scheme 1.6 Redox switching of polymerization catalyst selectivity for different monomers

1.2.3 Bent Metallocene Catalysts

Bent metallocenes, where the angle of the (η^5-Cp)-M-(η^5-Cp) axis is less than 180°, have been used extensively in catalysis and most famously for olefin polymerization, one of the most significant industrial reactions.[4,5] Specifically, group 4 complexes of this type and zirconium complexes in particular are highly active for ethylene and propylene polymerization.[5] Most bent metallocenes contain other neutral or anionic ligands to help stabilize the metal centre.[2] Zirconocene dichloride (Figure 1.3) is an example of this and is the base structure from which improved homogeneous group 4 olefin polymerization precatalysts were developed.[5]

Ansa-metallocenes contain a linker group connecting the two Cp ligands. This tethering strategy increases the stability of the Cp-M interactions due to the chelate effect and prevents free rotation of the Cp ring.[2] In addition to increased catalyst stability, this has important implications in the synthesis of stereoregular polymers. To clarify, the relative configuration of consecutive stereocentres along a polymer chain is its tacticity, which has consequences on the physical

properties of the polymer.[41] While atactic polymers have no order to these stereocentres, isotactic and syndiotactic polymers contain repeating stereocentres of the same configuration and with alternating opposite configurations along the polymer chain, respectively.[41] In this context, the C_2-symmetric ethylenebis(indenyl) (EBI) precatalyst shown in Figure 1.3 produces isotactic polypropylene[42,43] while the C_s-symmetric precatalyst containing a fluorenyl (Flu) ligand produces syndiotactic polypropylene.[44] This change in stereoselectivity is a result of the steric bulk of the Cp-based ligand influencing which face of the propylene monomer coordinates to the Zr centre during propagation.[5] Thus, for these polymerization reactions, the role of the Cp ligand is ancillary.

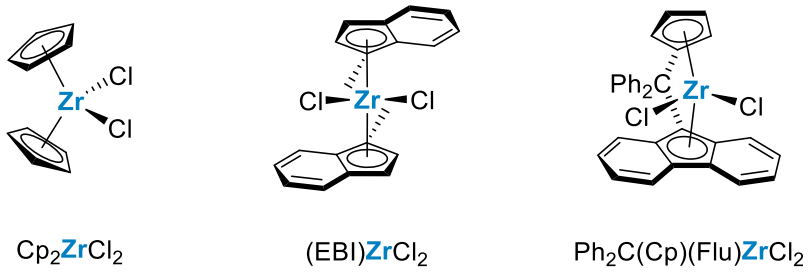

Figure 1.3 Some zirconium bent metallocene olefin polymerization precatalysts

Bent metallocene complexes are not limited to applications in olefin polymerization. For example, Buchwald and co-workers reported a chiral *ansa*-titanocene catalyst, supported by the ligand ethylenebis(tetrahydroindenyl) (EBTHI), for the enantioselective hydrogenation of sterically hindered alkenes,[45] imines,[46] and enamines[47] (Scheme 1.7). The catalyst was generated *in situ* and stabilized by excess phenylsilane, though dihydrogen was used as the reductant. Once again, the symmetry of the *ansa*-metallocene influences the stereochemistry of the product but does not directly participate in any steps of the catalytic cycle. This catalyst system could achieve enantioselectivities and yields up to >99% and 98%, respectively, depending on the type of substrate used. Overall, bent metallocenes, and especially those based on group 4 transition metals, have been used as highly active and selective catalysts for a wide range of transformations.

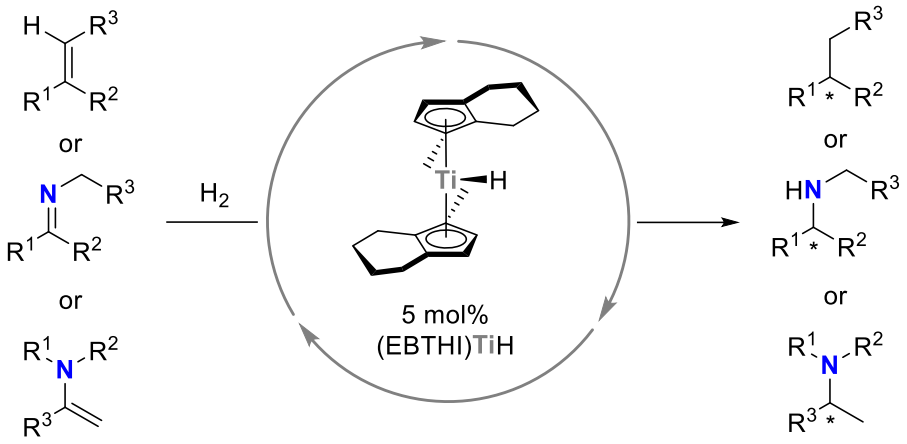

Scheme 1.7 Chiral *ansa*-titanocene hydride for catalytic asymmetric hydrogenation

Bent metallocenes have also been applied to small molecule activation reactions. For instance, Chirik and co-workers reported a sterically encumbered zirconocene complex that could mediate the hydrogenation of dinitrogen to ammonia (Scheme 1.8).[48] The dinitrogen-bound, dimeric zirconocene complex with tetramethylcyclopentadienyl ligands, prepared from the corresponding zirconocene dichloride under an N_2 atmosphere and reducing conditions,[48] reacts with 1 atmosphere of H_2 at room temperature to produce a diazenido complex. This species contains two new N−H bonds and two new Zr−H bonds while still retaining the bimetallic Zr_2N_2 core. From there, further reaction with H_2 upon heating releases free ammonia and the corresponding zirconocene dihydride complex, in addition to other zirconium-containing products.[48] Crucial to the observed reactivity is the substitution pattern of the Cp ligand, which influences the end-on versus side-on coordination of N_2 and, consequently, its potential to be functionalized to ammonia.[48] This further highlights the utility of substituted Cp derivatives in bond-breaking and -forming processes.

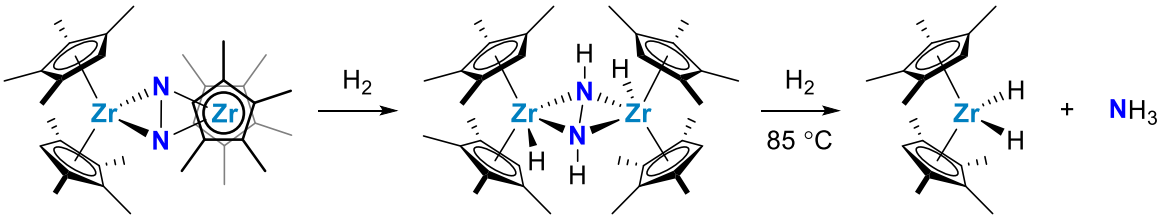

Scheme 1.8 Hydrogenation of dinitrogen to ammonia mediated by a zirconocene complex

Another class of tethered Cp complexes that has found success in catalytic reactions is "constrained geometry" complexes (Figure 1.4). These species contain only one Cp ligand bound to the metal, but the Cp ring is substituted with another chelating ligand.[2,5,49,50] The first example of this type of complex was reported by Bercaw and co-workers in 1990 (Figure 1.4).[49] This Sc complex contains a Cp*-derivative with a tethered amido ligand, increasing both the Lewis acidity and electron deficiency of the metal centre compared to the analogous scandocene species.[49] An example of a Cr constrained geometry complex reported by Theopold and co-workers is also shown.[51] As there is a linker between the Cp ligand and the other donor, these can be considered *ansa*-complexes,[2] but since there is only one Cp ligand they are technically not metallocenes. However, given their resemblance to *ansa*-metallocenes, one might surmise that the reactivity of constrained geometry complexes would be similar to that of *ansa*-metallocene complexes, and indeed this is the case; complexes such as those shown in Figure 1.4 are active for the polymerization of alpha-olefins.[5,49–51] Once again, using a tethered ligand provides enhanced reactivity and stability for catalysis. As is the case for bent metallocene catalysts, the role of the Cp ligand in these constrained geometry catalysts is ancillary.

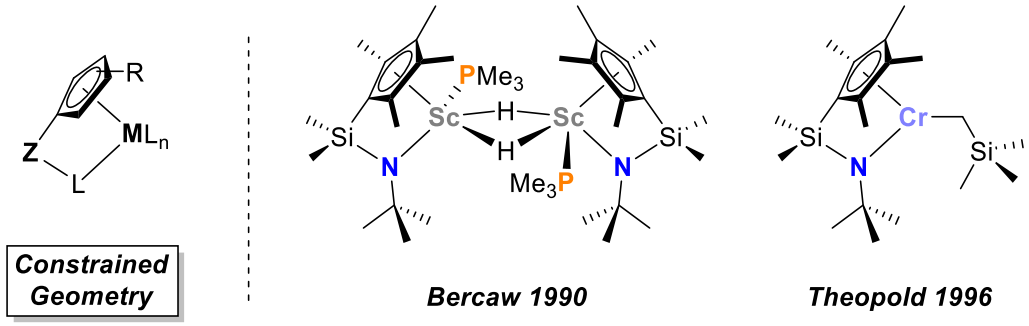

Figure 1.4 Constrained geometry catalyst structure and examples

1.2.4 Piano-Stool Catalysts

Although many Cp-based ligands are ancillary and do not participate in catalytic reactions, some Cp ligand frameworks demonstrate cooperative behaviour. Piano-stool complexes, also called "half-sandwich" complexes, contain just one Cp ligand and generally two to four other ligands.[2,52,53] Some examples of these types of compounds have already been highlighted in Schemes 1.2, 1.3, and 1.5 (*vide supra*). Most often, the steric bulk of the Cp ligand shields one face of the metal centre and reactivity occurs on the opposite side of the metal. However, there are cases where the Cp ligand can act in a cooperative fashion to promote catalytic reactions as opposed to acting in an ancillary role. For instance, the Shvo catalyst[54] (Scheme 1.9) is a Ru transfer hydrogenation catalyst that contains a Cp ligand with a hydroxyl substituent. This catalyst has also inspired a similar, more earth-abundant Fe catalyst (Scheme 1.9) for the hydrogenation of ketones[55] and amination of alcohols through a borrowing-hydrogen reaction pathway.[56,57] In both systems, the hydroxyl substituent is critical to the operative reaction pathway. Focusing on the Fe system, when the catalyst is in its oxidized form [although it is formally Fe(0)], it has an η^4-cyclopentadienone ligand (Scheme 1.9). In its reduced form [with a formally Fe(II) centre] as a result of H_2 transfer (as either the free molecule or from an alcohol substrate) to the Fe complex, it has an η^5-CpOH ligand. Part of the driving force for oxidation of the alcohol is the aromatization

and formation of the strong Fe-(η^5-Cp) bond. This intermediate, like the Shvo catalyst, has both an acidic and a hydridic hydrogen for transfer to an unsaturated species.[55] This is an example of metal-ligand cooperativity,[58] as both metal and ligand are involved in the bond activation processes necessary for catalytic turnover. Additionally, the Shvo catalyst demonstrates how a Cp ligand framework can support bimetallic species, although monomeric Cp complexes are more common than their aggregated counterparts.[2]

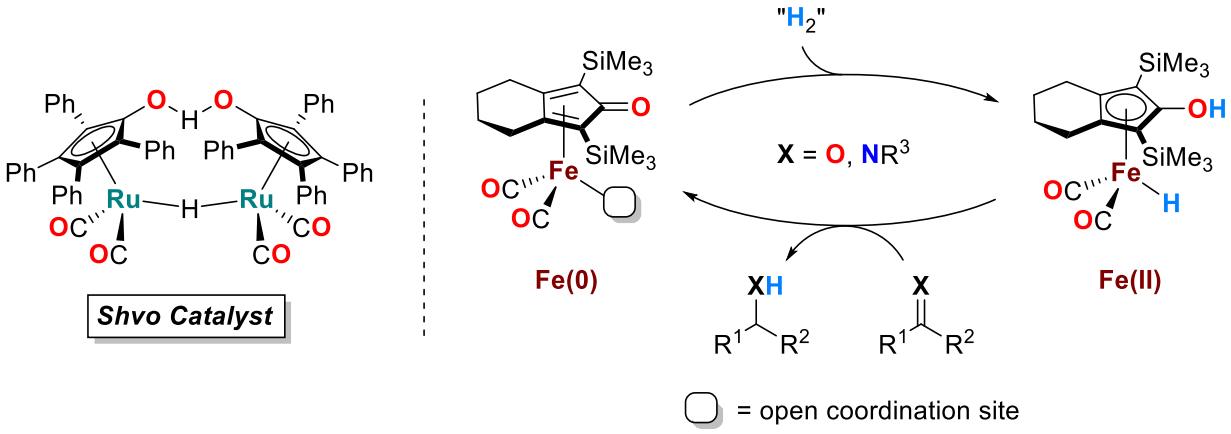

Scheme 1.9 The Shvo transfer hydrogenation catalyst and the mode of action of an Fe analogue

1.2.5 Limitations of Cp-Based Catalysts

Considering the sections above, metallocenes and other Cp-containing compounds have had a substantial impact in the field of catalysis and have facilitated landmark achievements in chemistry. However, Cp-based catalysts do have some disadvantages and there has been considerable attention since the later half of the 1990s, particularly in the field of early-transition-metal-catalyzed olefin polymerization, towards the exploration of alternative ligand systems.[59–65] One disadvantage of Cp ligands is what makes them effective ligands in the first place: Cp ligands are sterically large in three-dimensional space and are strongly bound to the metal centre, blocking a large portion of the metal coordination sphere and limiting the use of large substrates.[5,65] This is

especially true for *ansa*-metallocenes and constrained geometry catalysts, where the chelate effect limits dissociation from the metal centre during the reaction.[5] This is disadvantageous for transformations that require varying amounts of space at the metal centre during the different steps of the reaction. Additionally, the use of Cp ligands limits the degree to which a unique stereochemical environment can be generated at the metal centre, which may be necessary for certain transformations or desired stereochemical outcomes.[63] Expanding the level of control over product formation or the reactivity that is possible beyond what can be achieved with Cp-based systems requires expansion of the types of ligands used.

Furthermore, the methods for the preparation of Cp ligands and their introduction onto metal complexes have some drawbacks. The most common method of installing Cp onto a metal centre is through salt metathesis (Scheme 1.10),[2,5] which requires pre-metalation of cyclopentadiene to make the Cp anion. Often, both the reagent used for metalation and the resulting Cp anion are air-sensitive and/or pyrophoric (for example, ^{n}BuLi is used to make LiCp, Scheme 1.10).[5] Additionally, the subsequent salt metathesis reactions to make the desired transition metal Cp complexes can suffer from poor yields; NaCp can act as a reducing agent and reduce a metal halide MX rather than undergo metathesis to release NaX as intended,[66] and the formation of "ate" complexes in these reactions is also a common problem.[5]

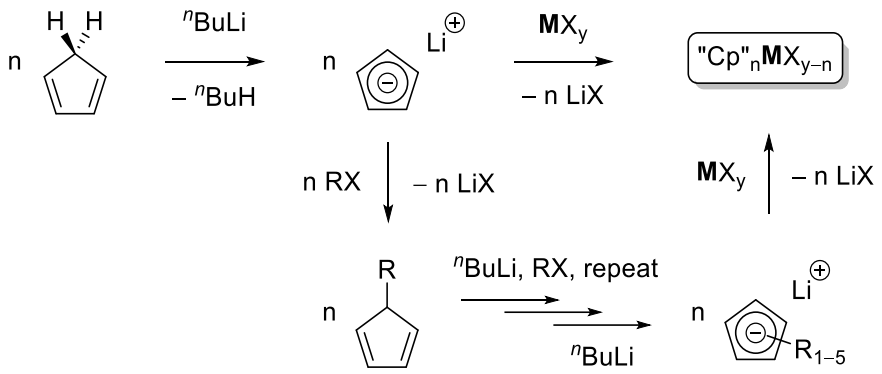

Scheme 1.10 Typical salt metathesis procedure for the synthesis of Cp ligands and complexes

Further underscoring these challenges is the synthetic process for preparing substituted Cp derivatives, in which multiple metalation-salt metathesis iterations with alkyl halides or other halide-substituted groups are required to generate the desired proligand (Scheme 1.10).[5,8] Thus, elaborate modification of the steric and electronic properties of Cp ligands can be synthetically challenging. As a result, catalyst development for Cp-based systems has required substantial effort. Overall, while it can be relatively straightforward to install one substituent on a Cp ligand, it is more difficult to synthesize numerous variants of the ligand for a given purpose.

Most importantly, although several of the examples discussed in the previous sections highlighted cooperative behaviour between the metal and the Cp ligand, Cp ligands most often play an ancillary role in catalytic reactions.[5] Whether a ligand is directly involved in bond activation processes or significantly changes its binding mode or denticity during a reaction to vary the coordination number of the metal, metal-ligand cooperation can facilitate challenging new catalytic transformations.[58] For all of the reasons outlined above, the Schafer group has a longstanding interest in using 1,3-*N*,*O*-chelating ligands for catalysis, as these ligands can be prepared easily and in a modular fashion, have contrasting electronic properties to Cp ligands, and

commonly exhibit hemilability and metal-ligand cooperativity. These aspects will be elaborated in the following sections.

1.3 1,3-*N*,*O*-Chelating Ligands

In contrast to Cp ligands and their derivatives, monoanionic 1,3-*N*,*O*-chelating ligands (Figure 1.5) are highly tunable with respect to both their steric and electronic properties.[67] This tunability arises from the ease with which the *N*-substituent or central atom *Z*-substituent can be exchanged for various functional groups when assembled.[68] Several classes of monoanionic 1,3-*N*,*O*-chelating ligands are illustrated in Figure 1.5, including amidates, ureates, pyridonates, phosphoramidates, and sulfonamidates.[68] Each of these ligand classes has distinct characteristics from one another, providing a variety of steric and electronic options to optimize for a desired application. Another contrasting feature of 1,3-*N*,*O*-chelating ligands in comparison to Cp ligands is that they are widespread in nature and can be found in a variety of metalloenzymes.[69] While 1,3-*O*,*O*-chelates[70–74] and 1,3-*N*,*N*-chelates[75–81] are similar in structure in that they form a four-membered metallacycle when bound to a metal in bidentate fashion, the distinctive advantage of the 1,3-*N*,*O*-chelating framework is the unsymmetrical nature of its donor atoms, leading to increased potential for ligand hemilability and opportunities for ligand cooperativity.[68,82,83] Hemilability is a term used to describe the tendency of a chelating ligand to dissociate one of its donor atoms in order to open a coordination site at the metal centre, which can be particularly useful in catalytic reactions (Scheme 1.11).[83,84] Thus, 1,3-*N*,*O*-chelated transition metals have found application as catalysts for various organic transformations.[67,68,82,85,86] The following sections discuss the bonding and synthesis of 1,3-*N*,*O*-chelating ligands and their metal complexes along with examples of their catalytic applications.

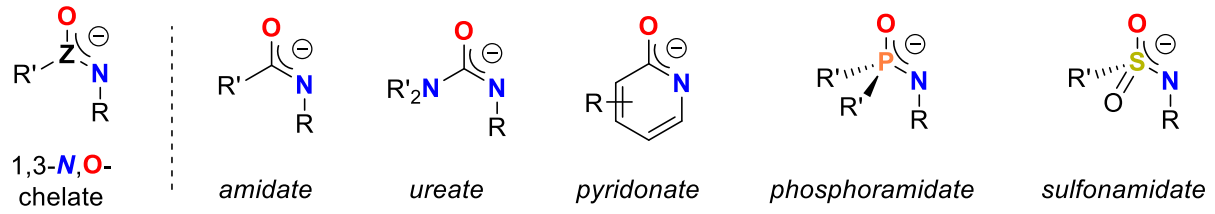

Figure 1.5 General structure and examples of 1,3-*N*,*O*-chelating ligands

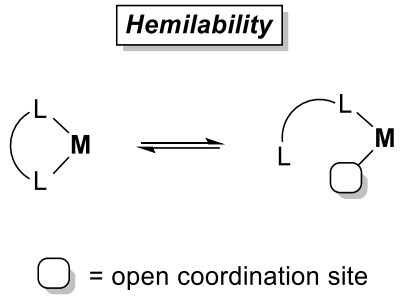

Scheme 1.11 General depiction of ligand hemilability

1.3.1 Metal-(1,3-*N*,*O*) Bonding

In terms of Pearson hard/soft acid base (HSAB) theory,[87] 1,3-*N*,*O*-chelating ligands are comparably "harder" than Cp ligands and exhibit more ionic bonding character with transition metals. For this reason, 1,3-*N*,*O*-chelated complexes of early-transition metals are most common,[67] however there are many examples of such complexes with late-transition metals.[68] Although binding modes may vary depending on the nature of the metal centre, there are several possible coordination modes for 1,3-*N*,*O*-chelating ligands, as illustrated in Figure 1.6 using an amidate ligand as an example. The κ^2-*N*,*O* (LX-type) binding mode is commonly observed for early-transition metals, while the κ^1-*N* (X-type) binding mode is typically observed for late-transition metals. The κ^1-*O* (X-type) coordination mode is also possible for monometallic systems, particularly when the central *C*- and *N*-substituents are sterically bulky. For systems involving multiple metal centres, 1,3-*N*,*O*-chelates can also bridge two metals via the μ_2-*N*,*O*, μ_2-*O*, or μ_2-*N* coordination modes or some combination of the three, demonstrating the potential for

hemilability.[83] 1,3-*N*,*O*-chelating ligands provide a flexible coordination environment that can support various levels of coordinative (un)saturation for both monometallic and multimetallic complexes alike.

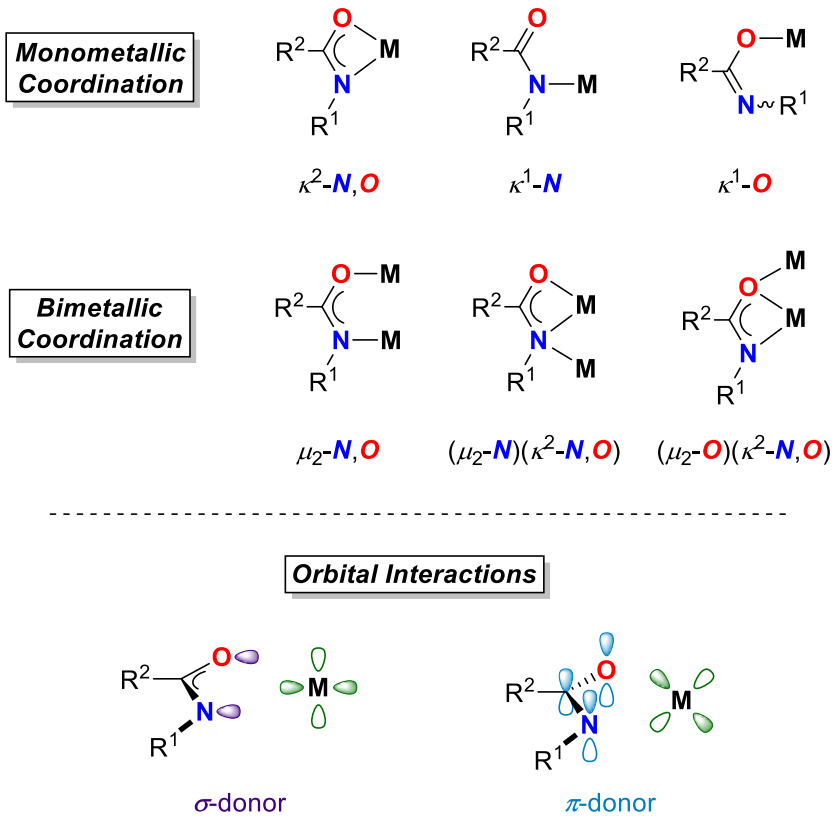

Figure 1.6 Various coordination modes and bonding interactions of 1,3-*N*,*O*-chelating ligands

Figure 1.6 also shows the FMOs of the 1,3-*N*,*O*-chelate that can interact with orbitals on a metal centre, using the κ^2-*N*,*O* coordination mode of the amidate as an illustrative example. In addition to the σ-donating capabilities of both the *N*- and *O*-donors, the N-C-O π system can also act as a π-donor (via the *N*- and *O*-donors) to the metal centre. As such, 1,3-*N*,*O*-chelating ligands are monoanionic with orbitals suitable for σ- and π-bonding interactions, similar to Cp, although the nature of this bonding is fundamentally different. The bonding between the electronegative *N*- and *O*-donors and the metal centre is much more polar than the Cp-M bond, especially for early-

transition-metal complexes. This polarity can be advantageous, as complexes containing polarized metal-ligand bonds may consequently have increased electrophilicity and be more reactive in catalytic applications. For example, a 1,3-*N*,*O*-chelated early-transition-metal complex may mimic the reactivity of a cationic metallocene catalyst while retaining the stability of a neutral species.[88,89] Furthermore, as the M-N-C-O metallacycle is planar, the steric profile of the 1,3-*N*,*O*-chelate is dependent on the size of the *C*- and *N*-substituents, which can be varied easily during synthesis of the ligand (*vide infra*). Overall, in comparison to Cp-based complexes, 1,3-*N*,*O*-chelating ligands allow for the generation of reactive metal centres with easily tuneable steric properties.

With common hydrogen-bond (H-bond) accepting N and O atoms incorporated directly into the ligand, 1,3-*N*,*O*-chelated transition metal complexes also have the potential for H-bonding in the second coordination sphere. A rather elegant example of this was reported by Moore and Szymczak, synthesizing a Cu(II) fluoride complex with a tetradentate ligand incorporating three neutral κ^1-*N* pyridone donors (Scheme 1.12, top).[90] The pendant hydroxide groups of the pyridones each act as a H-bond donor to the Cu-bound fluoride anion. Remarkably, reduction of the Cu(II) centre is not accompanied by dissociation of the fluoride, rather the H-bonding interactions with the pyridone groups capture the fluoride in the secondary coordination sphere and prevent its dissociation from the complex. Conversely, pyridonates may also act as H-bond acceptors; Clarkson and Schafer reported a H-bonded W(VI) pyridonate complex that forms reversibly upon protonation of an imido group by an incoming pyridone proteoligand (Scheme 1.12, bottom).[83] In this case, the κ^1-*O* pyridonate acts as a H-bond acceptor via the uncoordinated N atom. The application of this H-bonding behaviour of 1,3-*N*,*O*-chelating ligands for metal-ligand cooperativity, specifically for element-hydrogen activation processes for catalytic reactions, will

be discussed further in later sections. Overall, 1,3-*N*,*O*-chelating ligands offer a variety of binding motifs that may be used to advantage in catalysis.

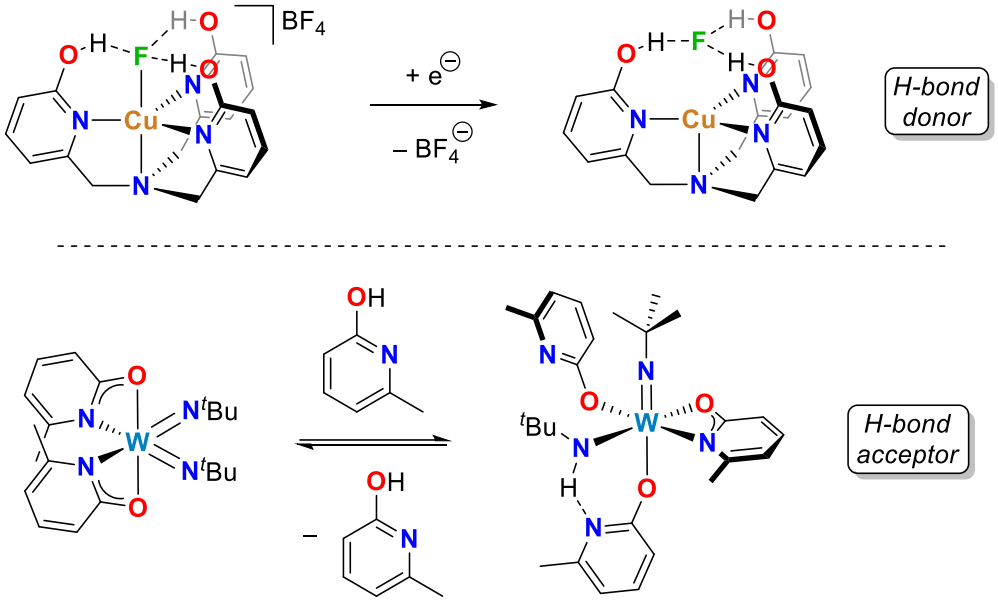

Scheme 1.12 Examples of 1,3-*N*,*O*-chelates as H-bond donors and acceptors

1.3.2 Synthesis of 1,3-*N*,*O*-Chelating Ligands and their Complexes

One of the benefits of 1,3-*N*,*O*-chelating ligands is their simple and highly modular syntheses. Amide and urea proligands can be synthesized in one or two steps from commercially available starting materials (Scheme 1.13). Amides are usually formed through the addition of a primary amine to an acyl chloride in the presence of base.[91] Judicious choice of the two reacting partners allows for customization of the steric and electronic properties of both the *C*- and *N*-substituents. Ureas can be synthesized through a similar procedure in which a primary amine is first added to triphosgene or a chloroformate, followed by addition of a secondary amine.[92] The amide or urea proligand can then either be used directly in the synthesis of the corresponding metal complex or deprotonated with base prior to installation on the metal centre, depending on the metal starting material (*vide infra*). In contrast to amides and ureas, pyridone proligands are assembled

in a modular fashion using transition-metal-catalyzed cross-coupling chemistry (Scheme 1.13). Bromide substituted 2-hydroxypyridine is commercially available and may undergo Suzuki-type cross-coupling reactions with arylboronic acids to generate aryl substituted pyridones.[93] Additionally, several alkyl substituted pyridones are commercially available.[83,93] As they are not the focus of this thesis, the syntheses of phosphoramide and sulfonamide proligands are excluded here. However, it should be noted that the syntheses of these ligands are also straightforward and modular in nature.[94,95]

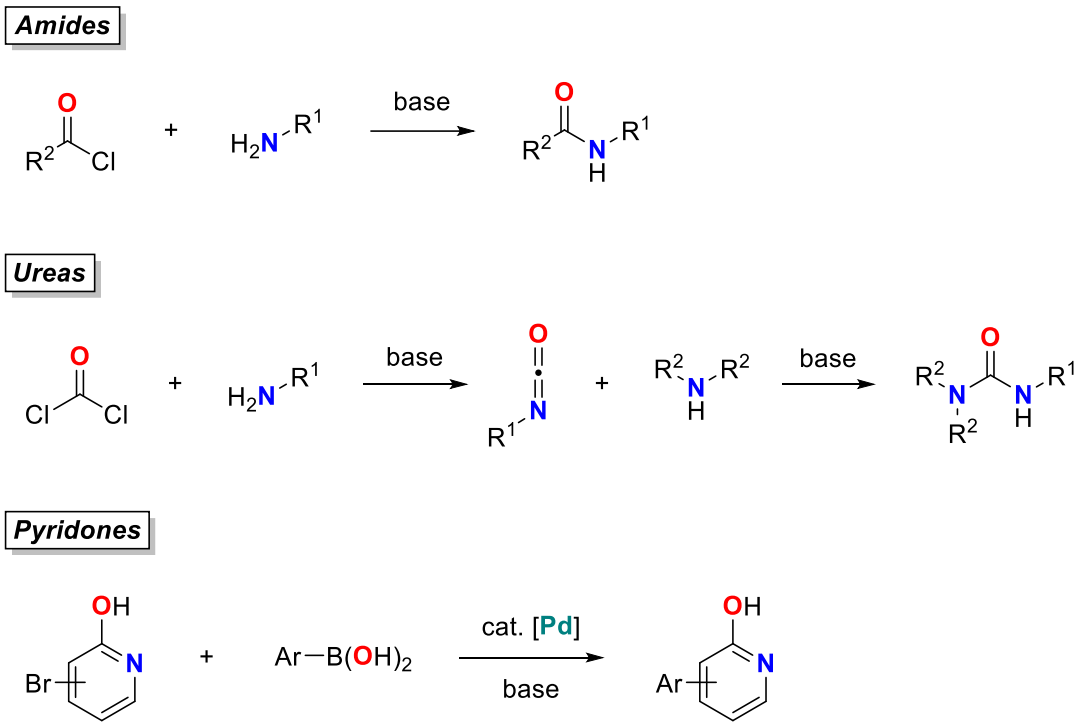

Scheme 1.13 Synthetic strategies for the modular preparation of amides, ureas, and pyridones

After simple preparation of the proligand, the synthesis of the corresponding 1,3-*N*,*O*-chelated transition-metal complex is also straightforward and can be similar to the procedure for installing Cp proligands onto metal centres (*vide supra*). Specifically, salt metathesis and protonolysis are the most common methods for making 1,3-*N*,*O*-chelated transition-metal

complexes (Scheme 1.14).[68,82] The salt metathesis procedure requires that the 1,3-*N*,*O*-proteoligand (*e.g.,* amide) be deprotonated with a base (*e.g.,* sodium hexamethyldisilazide) prior to reacting with a M−X precursor, though this may be done *in situ* without isolating the deprotonated intermediate. In contrast, protonolysis allows for direct reaction of the proteoligand with the M−X precursor to give the desired product and release HX as a byproduct.[82] Other methods of synthesizing 1,3-*N*,*O*-chelated transition-metal complexes include, but are not limited to: isocyanate insertion into an M−X bond for the synthesis of amidate (X = R) and ureate (X = NR_2) complexes;[96,97] N−H oxidative addition of the proteoligand to a reduced metal to generate the 1,3-*N*,*O*-chelate and a hydride ligand simultaneously;[98] and nitrile insertion into an M−OH bond followed by tautomerization for the synthesis of amidate complexes (Scheme 1.14).[99] Altogether, 1,3-*N*,*O*-chelated transition-metal complexes can be easily prepared using a variety of synthetic strategies for both early- and late-transition metals.

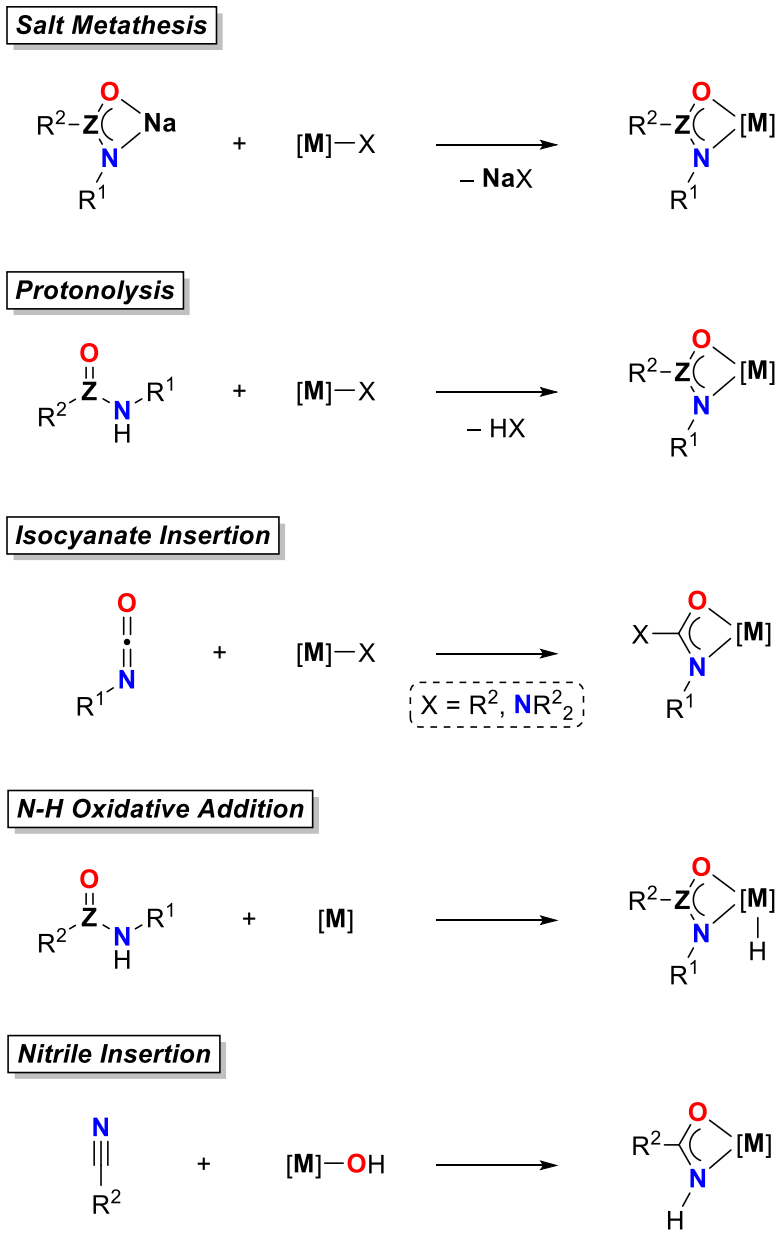

Scheme 1.14 Various methods of preparation of 1,3-*N*,*O*-chelated transition-metal complexes

1.3.3 1,3-*N*,*O*-Chelated Transition Metal Catalysts

Both early- and late-transition-metal complexes of 1,3-*N*,*O*-chelating ligands have found extensive use in catalysis, taking advantage of the cooperative behaviour of these ligands to promote various transformations. In the Schafer group, a bis(amidate) titanium complex (Figure 1.7, left) has been the focus of much investigation as a hydroamination catalyst and has been used

for amine and *N*-heterocycle synthesis.[100–109] The hydroamination reaction itself will be discussed in detail in Chapter 2, but the method by which this catalyst operates highlights the utility of 1,3-*N*,*O*-chelating ligands in catalysis. Recently, Hao and Schafer disclosed a computational analysis of the mechanism of action of the titanium catalyst by DFT in order to understand the origins of its exquisite regioselectivity for the *anti*-Markovnikov hydroamination product.[110] In both the preceding intermediate and transition state of the turnover-limiting step, one of the amidate ligands adopts a κ^1-*O* binding mode in order to open a coordination site for the incoming amine substrate (Figure 1.7, right). Additionally, the uncoordinated N atom forms a hydrogen bond with the N−H bond of the coordinated amine to stabilize the intermediate. Thus, hemilability and metal-ligand cooperativity of the amidate ligand are crucial to the efficiency of the catalyst, while the simultaneous bulky steric profile of the amidate ligands is responsible for the observed regioselectivity.

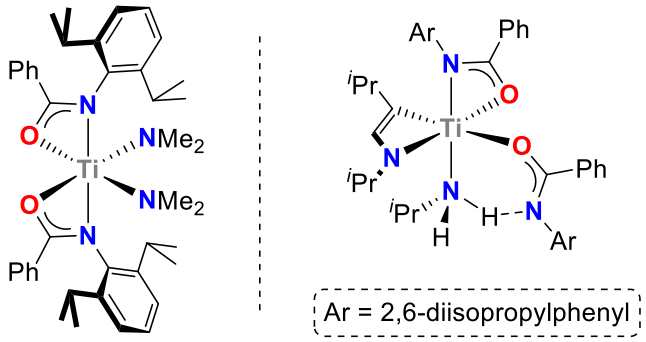

Figure 1.7 Titanium hydroamination catalyst (left) and computed catalytic intermediate (right)

Late-transition-metal amidate complexes can also be useful catalysts. For example, Berry and co-workers reported a dirhodium paddle-wheel complex constructed from two tethered bis(amidate) ligands for nitrene transfer catalysis (Figure 1.8).[111] Not only does the 1,3-*N*,*O*-chelating framework allow for the formation of a bimetallic species needed for catalysis via the μ_2-*N*,*O* bridging mode, the *N*-donor helps stabilize the compound; the corresponding 1,3-*O*,*O*

ligand binds less strongly to the two Rh centres, resulting in catalyst decomposition under catalytic conditions.[111] This further demonstrates the utility of amidates as stabilizing ligands for catalytic applications and the ability of 1,3-*N*,*O*-chelating ligands to support bimetallic catalysts.

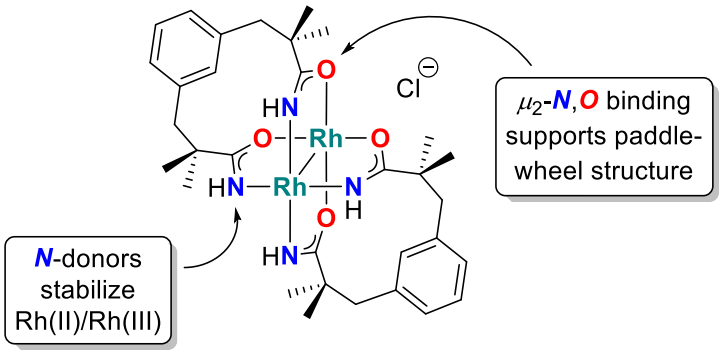

Figure 1.8 Dirhodium paddle-wheel amidate complex for nitrene transfer catalysis

Tethered 1,3-*N*,*O*-chelating ligands can also influence reactivity in similar fashion to their *ansa*-metallocene and constrained geometry analogues. For instance, the Schafer group previously reported a chiral, tethered bis(amidate) zirconium catalyst for the enantioselective cyclohydroamination of primary aminoalkenes (Scheme 1.15).[89] The chirality of the catalyst originates from the axially chiral biaryl backbone of the tethered ligand, which in turn influences the relative spatial orientation of the mesityl groups on the amidate moieties. The spatial orientation of these bulky groups ultimately imposes the metal-bound substrate into a particular conformer, producing enantioselectivities as high as 93% *ee*.[89] This stereochemical influence from the tethered ligand is reminiscent of the *ansa*-metallocene catalysts that allow for control over the tacticity of the growing poly(propylene) chain (*vide supra*). Thus, this example shows how 1,3-*N*,*O*-chelating ligands can provide stereochemical control akin to metallocene catalysts while enhancing the electrophilicity of the metal centre for catalytic applications.

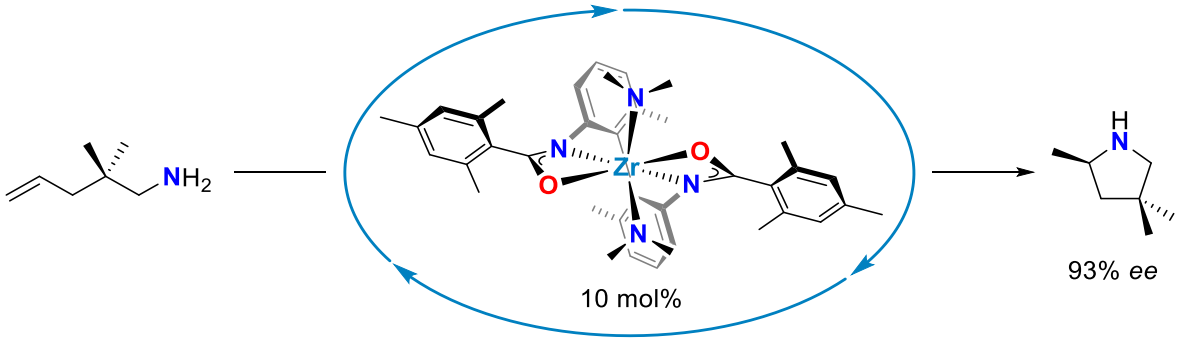

Scheme 1.15 Chiral tethered bis(amidate) zirconium catalyst for enantioselective hydroamination

Interestingly, (κ^2-1,3-*N*,*O*)$_2$M complexes without any additional supporting ligands, tethered or untethered, have not been reported. These species would be analogous to sandwich complexes (Cp_2M) and would likely be very reactive due to the coordinative unsaturation and steric availability imparted on the metal centre. If such complexes could be accessed even transiently, they could potentially be highly active catalysts, in contrast to sandwich complexes (*e.g.*, ferrocene) that are generally unreactive.

Pyridonate-ligated complexes of both early- and late-transition metals have been widely used for catalytic applications.[68,85,86] One change with the pyridonate compared to the amidate is the reduced steric profile as a result of its planarity while maintaining similar electronic properties to amidate ligands. For instance, the Schafer group reported a tantalum pyridonate catalyst for hydroaminoalkylation (a reaction discussed in detail in Chapter 3) capable of promoting reactivity with sterically-demanding internal alkenes (Scheme 1.16).[112] Previous state-of-the-art catalysts utilizing sterically-bulky amidate and phosphoramidate ligands were unable to achieve reactivity with such substrates and were limited to the use of terminal alkenes in the reaction. The less imposing pyridonate complex mimics the electrophilicity of the previous catalysts but allows for the binding of sterically demanding internal alkenes. This illustrates the utility that the variable steric environment of 1,3-*N*,*O*-chelating ligands has in promoting challenging catalytic

transformations. Notably, more recent investigation of early-transition-metal ureate hydroaminoalkylation catalysts as alternatives to amidate and pyridonate catalysts has led to important advances in this area.[113–116] This improved reactivity demonstrates the opportunity accessible with subtly changed steric and electronic parameters of 1,3-*N*,*O*-chelating ligands.

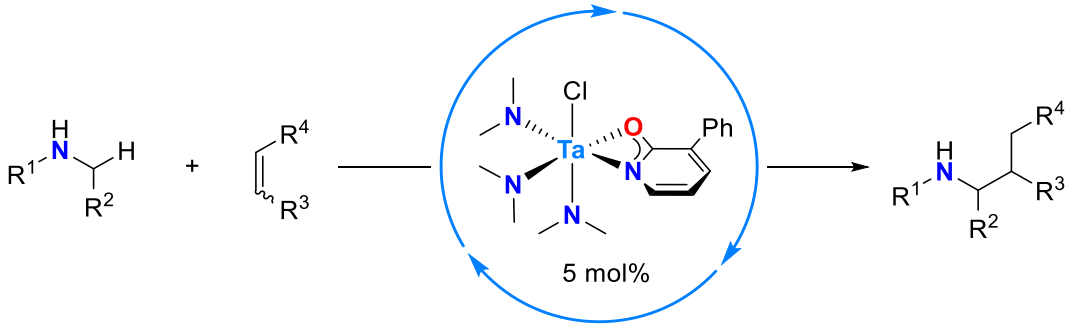

Scheme 1.16 Tantalum pyridonate catalyst for the hydroaminoalkylation of internal alkenes

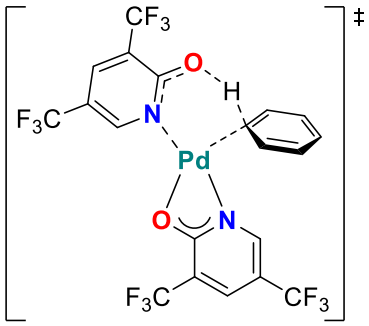

Figure 1.9 Computed transition state for arene C−H activation with a Pd pyridonate catalyst

Pyridonates are also well-known for their cooperative behaviour in catalysis.[68] For example, Yu and co-workers reported a Pd pyridonate catalyst system for the C−H functionalization of unactivated arenes.[117] Figure 1.9 illustrates the computed transition state for the key C−H activation step in this reaction. While one of the two pyridonate ligands is bound κ^2-*N*,*O* in order to help stabilize the Pd centre, the role of the other pyridonate is two-fold: 1) the hemilabile pyridonate binds via the κ^1-*N* coordination mode, opening a coordination site and allowing the arene substrate to approach; and 2) the uncoordinated O atom directly participates in

activation of the C−H bond to ultimately produce the requisite M−C bond for subsequent cross-coupling. The Yu group has been very active in using the cooperative behaviour of pyridonate ligands to advantage in catalytic C−H activation reactions.[118–126] This cooperative reactivity is an excellent example of the general utility of pyridonate ligands in catalysis.

Finally, 1,3-*N*,*O*-chelated complexes have been useful for catalytic reactions involving PCET. For example, a κ^1-*N* amidate complex of Mn[127] and a dicopper complex containing four κ^1-*N* ureate ligands[128] were found to promote catalytic oxidation reactions via PCET. To gain insight into the behaviour of the amidate ligands in these reactions, McDonald and co-workers studied a model Ni(III) complex containing a bis(κ^1-*N*-amidate) ligand and a supporting terpyridine ligand (Scheme 1.17).[129] In the presence of substituted phenols, the amidate ligand acts as a proton-acceptor through the anionic *N*-donor, forming a new N−H bond, producing a phenoxyl radical, and reducing the Ni(III) centre by one electron to Ni(II). Notably, the binding mode of the amidate ligand switches from κ^1-*N* to κ^1-*O* to accommodate the change to the more weakly-donating N−H group. This illustrates the advantage of the flexible binding modes of 1,3-*N*,*O*-chelating ligands in supporting redox processes such as PCET. This type of reactivity is also complementary to the Cp*-ligated Fe complex discussed above (Scheme 1.5) that produces dihydrogen through a PCET mechanism.

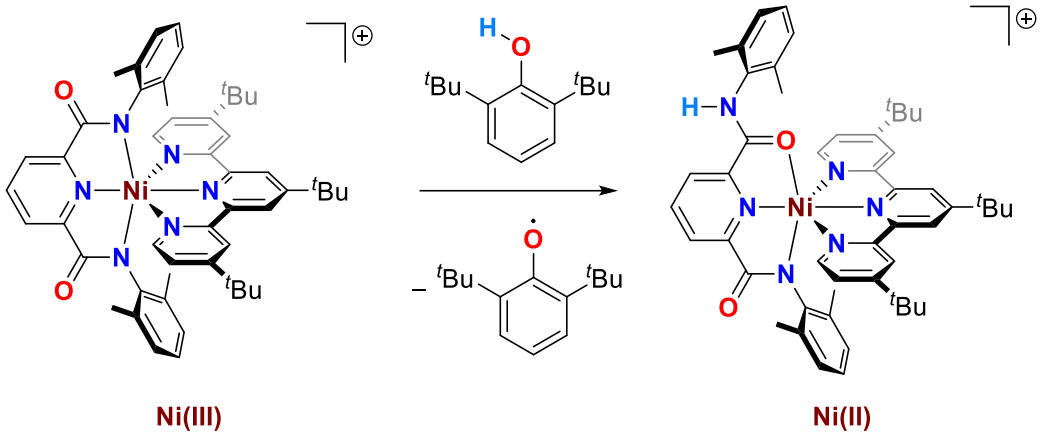

Scheme 1.17 Oxidation of a phenol with a Ni amidate complex via PCET

Overall, 1,3-*N*,*O*-chelating ligands can be exploited for their tuneability, hemilability, and metal-ligand cooperativity in various early- and late-transition-metal-catalyzed reactions. Although many advances have already been made, the breadth of chemistry that has been explored using 1,3-*N*,*O*-chelating ligands in catalysis is limited in comparison to the amount of research that has been explored with Cp-based systems. Thus, further study of this class of ligands, the fundamental coordination chemistry of the resultant complexes, and their applications in transition metal catalysis is expected to lead to important discoveries and reactivity that cannot be achieved with more traditional ligand sets.

1.4 Goals and Scope of this Thesis

This thesis aims to investigate the coordination chemistry and catalytic activity of 1,3-*N*,*O*-chelated transition-metal complexes, with the development of mechanistic insights being the focus of these investigations. As outlined above, the properties of these ligands are well-suited for catalytic applications and there is much room for further exploration of their chemistry with transition metals. Here, the focus is on early-transition metals as a sustainable and complementary alternative to late-transition metals due to their natural abundance, low cost, and different reaction

mechanisms. Specifically, ureate and pyridonate ligands are investigated in this work as they have been less-studied than amidate complexes of early-transition metals. It is hypothesized that by investigating non-conventional 1,3-*N*,*O*-chelated early-transition-metal complexes for their structure and reactivity, improved catalysts for existing transformations or catalysts for new transformations will be discovered. Additionally, mechanistic insights gained from these studies can support development of improved catalysts. Recurring themes in this thesis include the coordinative flexibility and hemilability of 1,3-*N*,*O*-chelating ligands and the metal-ligand cooperativity of 1,3-*N*,*O*-chelated metal complexes. The areas of investigation in each chapter are outlined below.

Chapter 2 explores tethered bis(ureate) zirconium complexes for the catalytic, intermolecular hydroamination of alkenes. The discovery of a system in which reversible C−N bond formation can be directly observed and its context in intermolecular hydroamination is the primary focus of this chapter.

Chapter 3 discusses the same tethered bis(ureate) zirconium complexes for the catalytic, intermolecular hydroaminoalkylation of alkynes. In addition to expanding the substrate scope of this reaction to include alkynes, model catalytic intermediates are isolated to provide insight into the reaction mechanism.

Chapter 4 investigates vanadium pyridonate complexes, which are very rare in the literature, to gain insight into their fundamental coordination chemistry. Specifically, their synthetic routes, structural features, hemilability, metal-ligand cooperativity, and tendency to undergo one-electron redox processes are highlighted.

Chapter 5 demonstrates the applicability of vanadium pyridonate complexes as catalysts for the reductive coupling of alcohols, a reaction relevant to biomass conversion. Isolation of

catalytic intermediates provides experimental evidence for the proposed mechanism that was previously informed solely by computational studies.

Finally, Chapter 6 summarizes the conclusions of the work completed and proposes future directions for these projects and more broadly, the fields of research discussed. Preliminary results are included that serve as starting points for future researchers in the Schafer group.

Chapter 2: Zirconium Ureates for Catalytic C−N Bond Formation

2.1 Introduction

Hydroamination, the 100% atom-economic addition of an N−H bond across a C−C unsaturation, is an efficient, catalytic method of synthesizing amines (Scheme 2.1).[130] While this transformation has been extensively investigated,[130–137] the intermolecular variant with alkenes remains a challenge in catalysis.[138] This is primarily due to the reaction's nearly ergoneutral nature[139] and high kinetic barrier.[130] Nevertheless, numerous strategies have been developed to circumvent the lack of driving force in intermolecular alkene hydroamination. One powerful strategy is to activate the amine using photocatalysis to provide a substantial thermodynamic driving force for addition to alkenes.[140] Other methods include using directing groups to overcome kinetic barriers and unfavourable reaction entropies[141,142] or employing activated amine derivatives in formal hydroamination reactions.[134,143–150] Experimental insights into C−N bond formation in direct hydroamination inform the synthetic community in devising new catalysts for this transformation.

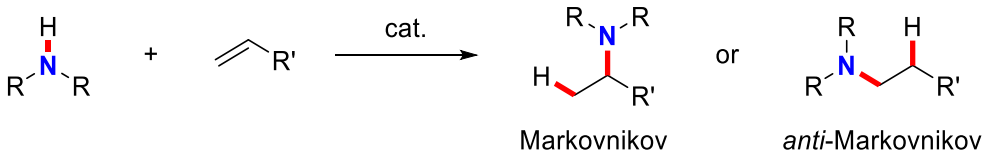

Scheme 2.1 General hydroamination reaction with an alkene substrate

Direct evidence for insertion of an alkene into an M−N bond is rare,[151–159] making it difficult to study the bond forming processes relevant to alkene hydroamination in detail. Previously, the Schafer group reported bis(ureate) zirconium precatalysts **2.1** and **2.2** for the intermolecular hydroamination of alkynes and intramolecular hydroamination of alkenes with primary and secondary amines (Figure 2.1).[160,161] Insertion of an alkyne into the Zr−N bond of **2.1**

was observed, providing direct evidence for a σ-insertive mechanism for alkyne substrates.[162] Contrarily, kinetic and DFT investigations have shown **2.1** to catalyze intramolecular hydroamination of alkenes via a proton-assisted mechanism.[160,163] It should be noted that precatalysts **2.1** and **2.2** generate the same catalytically active bis(amido) species upon reaction with amine substrate. The solid-state molecular structure obtained for complex **2.2** (Figure 2.2) highlights the planarity of the tethered 1,3-*N*,*O*-chelating ligand, allowing ample space around the rest of the metal centre for reactivity to occur.

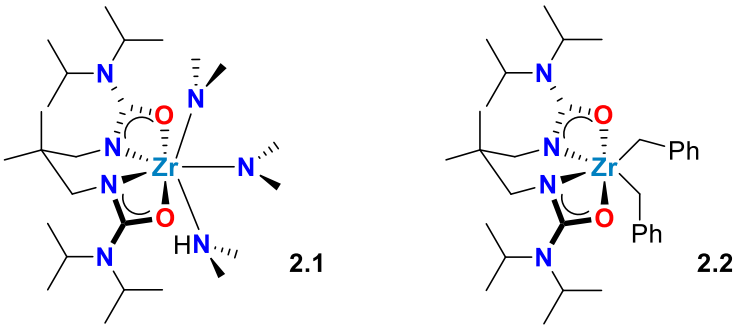

Figure 2.1 Schafer group precatalysts for the hydroamination of aminoalkenes and alkynes

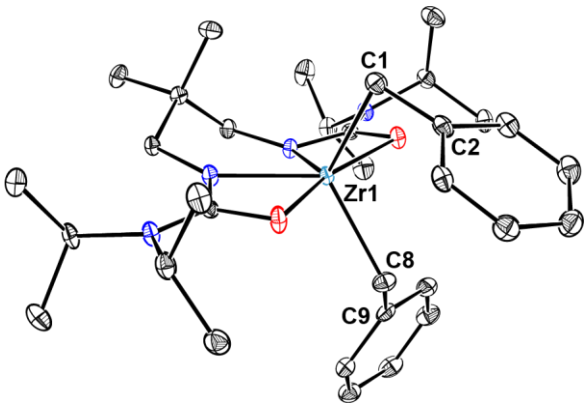

Figure 2.2 ORTEP representation of complex **2.2** with ellipsoids shown at 50% probability and hydrogen atoms omitted for clarity. Selected bond lengths: Zr1−C1, 2.3073(16) Å; Zr1−C8, 2.3017(16) Å; C1−C2, 1.482(2) Å; C9−C8, 1.484(2) Å. Selected bond angles: C2−C1−Zr1,

95.27(9)°; C9−C8−Zr1, 118.62(10)°; C8−Zr1−C1, 118.44(6)°. Selected atom distances: Zr1−C2, 2.8545(14) Å

Considering the mechanistic diversity of precatalysts **2.1** and **2.2** and precedent for observing efficient catalytic C−N bond formation using either primary or secondary amines with both alkynes and aminoalkenes, we aimed to gain insight into C−N bond forming processes toward intermolecular alkene hydroamination. Herein we report the first example of stoichiometric and catalytic *anti*-Markovnikov intermolecular hydroamination using a group 4 catalyst. Mechanistic investigations revealed an aza-Michael type reaction and reversible C−N bond formation has been directly observed in an isolated catalytic intermediate.

2.2 Catalytic Activity of 2.1 for 2-Vinylpyridine Hydroamination

Previously, Schulz and coworkers disclosed the *anti*-Markovnikov hydroamination of styrenes with secondary amines using an yttrium binaphthylamido catalyst generated *in situ* from an organometallic precatalyst (Scheme 2.2).[164] Therein, 2-vinylpyridine was found to be a very active substrate, achieving full conversion at room temperature in 5 minutes in the reaction with pyrrolidine. This high activity was attributed to coordination of the pyridyl nitrogen.[164] With zirconium system **2.1**, it is proposed that the highly ionic nature of the ureate ligand generates a very electropositive metal centre, thereby promoting increased reactivity akin to that of rare-earth metals.[91,161,165–167] It was thus hypothesized that **2.1** and **2.2** would also promote intermolecular hydroamination of the reactive 2-vinylpyridine substrate.

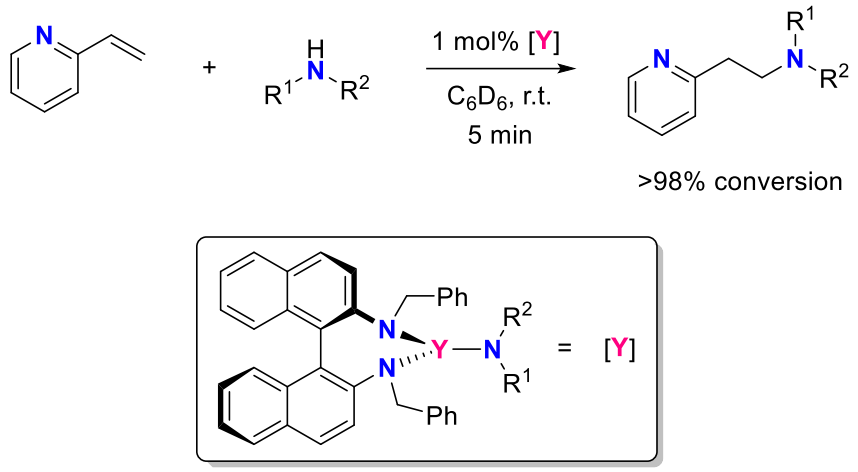

Scheme 2.2 *anti*-Markovnikov hydroamination of 2-vinylpyridine using an yttrium catalyst

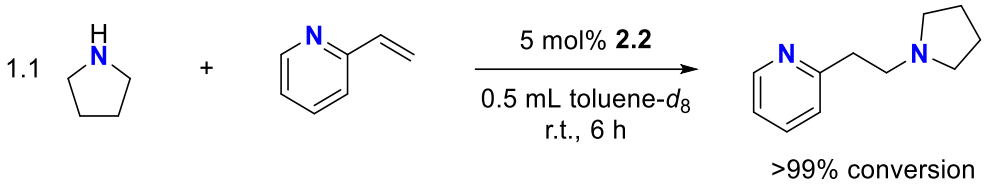

Scheme 2.3 Catalytic *anti*-Markovnikov hydroamination of 2-vinylpyridine using catalyst **2.2**

First, the catalytic activity of the tethered bis(ureate) zirconium complex was established (Scheme 2.3). Pyrrolidine was chosen as the amine substrate.[164] Dibenzyl precatalyst **2.2** was used to avoid the potential formation of hydroamination products resulting from both dimethylamine and pyrrolidine, which could occur with the use of **2.1**. Gratifyingly, the reaction between 2-vinylpyridine and pyrrolidine with 5 mol% **2.2** proceeds to completion at room temperature within 6 h (Scheme 2.3). This reaction can be monitored by ^{1}H NMR spectroscopy (Figure D.5, see Appendix D), in which the olefinic resonances disappear and two new multiplets at 2.97 and 2.84 ppm, corresponding to the new methylene protons of the product, are observed. Having shown zirconium to be proficient in catalyzing this transformation, stoichiometric experiments were conducted to gain mechanistic information.

2.3 Stoichiometric Studies

Numerous mechanisms have been proposed for alkene hydroamination by metal-based catalysts and they vary greatly depending on the nature of the metal.[130] For example, σ-insertive[168,169] or proton-assisted[160,170] pathways are often proposed for early transition, rare-earth, alkaline earth, and alkali metal catalysts (Figure 2.3). DFT studies support the σ-insertive mechanism in several systems, invoking reversible C−N bond formation for the insertion step.[171–176] Despite these predictions, evidence for reversible C−N bond formation has scarcely been reported[152,177–182] and reversible C−N bond formation has not been observed directly. With 2-vinylpyridine as the alkene substrate, an aza-Michael-addition mechanism is another viable pathway (Scheme 2.4). Indeed, the addition of amines to 2-vinylpyridine via an aza-Michael-addition has been achieved by various Lewis acid catalysts.[183–185] Given the number of pathways possible for this transformation, we sought to gain mechanistic insight into this group 4 catalyzed hydroamination reaction.

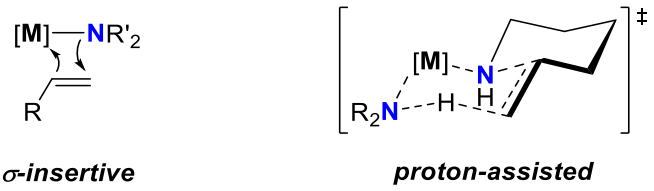

Figure 2.3 Example σ-insertive and proton-assisted mechanisms for alkene hydroamination

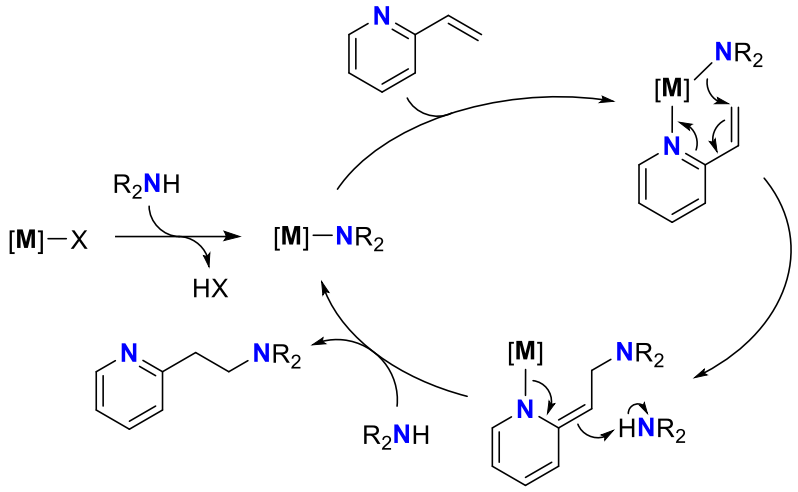

Scheme 2.4 Plausible mechanism for aza-Michael-addition of amines to 2-vinylpyridine

Expecting the stoichiometric reaction of **2.1** and 2-vinylpyridine to cleanly afford the dimethylamine-containing hydroamination product, **2.1** was dissolved in toluene-d_8 and 2-vinylpyridine was added to the solution, causing a colour change from colourless to orange not observed in the catalytic reaction (Scheme 2.5). The ^{1}H NMR spectrum showed diagnostic methylene signals at 2.90 and 2.65 ppm for the expected product (Figure D.6). However, a multitude of other new ligand-based resonances were present, consistent with new metal-containing species being formed in solution.

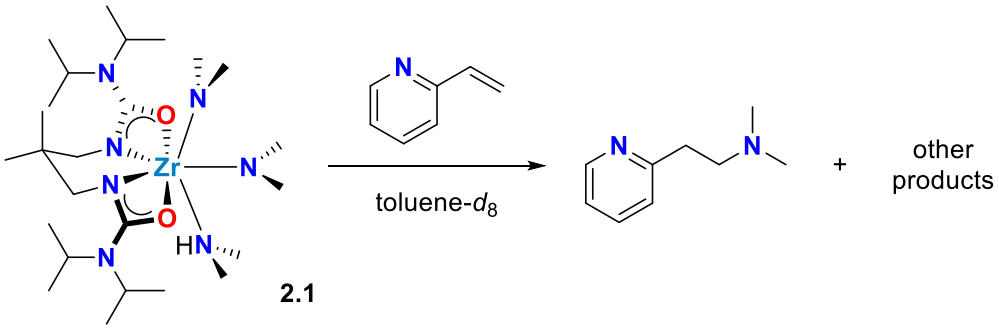

Scheme 2.5 Stoichiometric reaction of **2.1** with 2-vinylpyridine

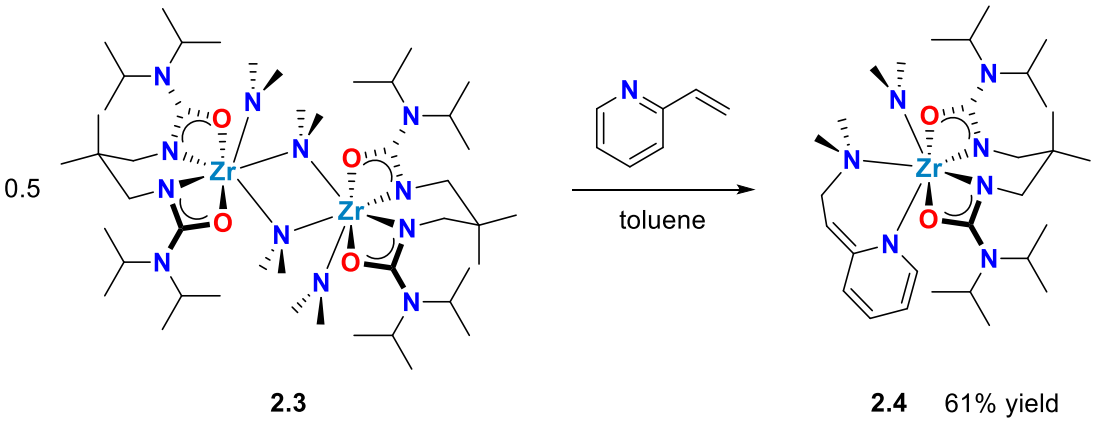

Scheme 2.6 Reaction of dimer **2.3** with 2-vinylpyridine to give aza-Michael complex **2.4**

To prevent catalytic turnover, the previously reported dimeric complex **2.3**, which does not contain neutral dimethylamine, was synthesized (Scheme 2.6).[160] Addition of 2-vinylpyridine to a toluene solution of **2.3** resulted in a colour change to orange once again. Cooling for several days afforded orange crystals of complex **2.4** suitable for X-ray diffraction. The solid-state molecular structure of **2.4** (Figure 2.4) shows a seven-coordinate complex with C_s symmetry and distorted pentagonal bipyramidal geometry. This structure results from nucleophilic attack of the equatorial amido ligand on coordinated 2-vinylpyridine to realize C−N bond formation in an aza-Michael-addition reaction (Scheme 2.4). While a proton-assisted mechanism cannot be excluded under catalytic conditions, it also cannot be the only mechanistic route as we show that C−N bond formation occurs in the absence of a proton trigger.

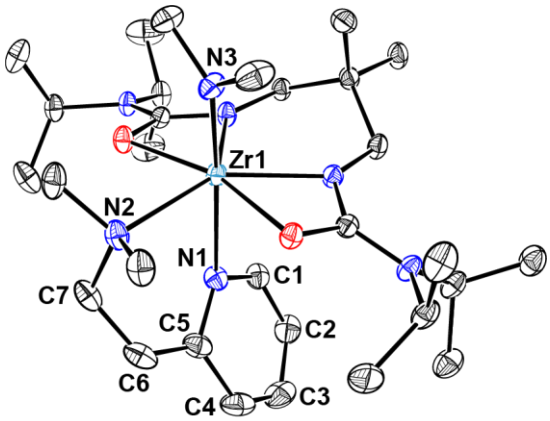

Figure 2.4 ORTEP representation of complex **2.4** with ellipsoids shown at 50% probability and hydrogen atoms omitted for clarity. Selected bond lengths: C1−C2, 1.370(2) Å; C2−C3, 1.431(3) Å; C3−C4, 1.360(3) Å; C4−C5, 1.461(2) Å; C5−C6, 1.368(2) Å; C6−C7, 1.497(2) Å; Zr1−N1, 2.3558(12) Å; Zr1−N2, 2.4401(12) Å; N2−C7, 1.513(2) Å; N1−C5, 1.413(2) Å; N1−C1, 1.3691(19) Å; Zr1−N3, 2.0962(12) Å. Selected bond angle: N1−Zr1−N3, 169.62(5)°

Notably, the pyridine ring has been dearomatized and a six-membered zirconacycle has formed. The alternating C1−C2, C2−C3, C3−C4, and C4−C5 bond lengths (1.370(2), 1.431(3), 1.360(3), and 1.461(2) Å, respectively) show limited delocalization within the ring. These alternating short and long bond lengths are consistent with a study by Rosenthal and co-workers, in which a five-membered zirconacycle involving a dearomatized pyridine ring was synthesized from 2-vinylpyridine and $Cp_2Zr(THF)(\eta^2\text{-}Me_3SiC_2SiMe_3)$.[186] Additionally, the depiction of C5−C6 as a double bond and C6−C7 as a single bond is further supported by bond metrics (1.368(2) and 1.497(2) Å, respectively).[187] Considering that the Zr1−N1 bond length in **2.4** (2.3558(12) Å) is much shorter than that of the corresponding bis(dimethylamido) pyridine complex (2.508(3) Å)[160] supports its assignment as an amido ligand. Furthermore, the Zr1−N2 bond distance is consistent with that of a neutral amine donor (2.4401(12) Å). While there are many examples of metal complexes with a dearomatized pyridine ligand,[188–192] they are most often

generated via pre-coordination of the neutral pyridine followed by deprotonation with a strong base. In this case, C−N bond formation triggers the dearomatization of the pyridine ring.

2.4 Direct Observation of Reversible C−N Bond Formation

Solution phase characterization of isolated **2.4** by NMR spectroscopy revealed a complex chemical environment. Firstly, the tethered ureate ligand has reduced symmetry; the geminal methyl groups produce two separate resonances in the ^{1}H NMR spectrum (1.22, 0.90 ppm), as do the methylene protons (3.44, 3.25 ppm) and isopropyl methyl protons (1.25, 1.17 ppm). This is consistent with reduced flexibility in the ureate ligand.[162] The ^{13}C{^{1}H} NMR resonance for the carbonyl carbon (167.3 ppm) is also shifted slightly upfield relative to that of bis(amido) complex **2.3** (170.8 ppm). For the *N*,*N*-chelate resulting from C−N bond formation and dearomatization of the pyridyl ring, the resonances in the ^{1}H NMR spectrum appear upfield compared to 2-vinylpyridine; for example, the C−H proton next to the pyridyl nitrogen appears at 8.48 ppm in 2-vinylpyridine and 7.06 ppm in **2.4**. Additionally, an upfield-shift of the methyl protons in the *N*,*N*-chelate (2.61 ppm) relative to the amido protons in **2.3** (3.39 ppm) is consistent with conversion of the equatorial amido ligand in **2.3** to a more weakly donating amino ligand in **2.4**.

Interestingly, signals for 2-vinylpyridine and unreacted **2.3** are also observed in the ^{1}H NMR spectrum of dissolved crystalline **2.4**. Hypothesizing that these species were in equilibrium, variable-temperature NMR spectroscopy was used to probe the solution phase dynamics (Scheme 2.7, Figure 2.5). The doublet-of-doublet signals due to the olefin protons of 2-vinylpyridine at 6.33 ppm and 5.27 ppm (H_a and H_b, respectively) decrease in intensity as temperature is lowered, until they disappear at −30 °C. Concomitant with this phenomenon is the increase in intensity of the signals at 6.12 ppm and 5.10 ppm, which correspond to H_d, H_e and H_c of **2.4**, respectively. At −9 °C, the doublet-of-doublet signal originating at 6.12 ppm begins to split into multiple signals as

H_d and H_e become distinguishable; these signals are similarly resolved in the room temperature spectrum in C_6D_6. Both the isopropyl methine and methyl signals for **2.3** also decrease in intensity at lower temperature. Thus, complex **2.4** forms preferentially at low temperature while 2-vinylpyridine and **2.3** are favoured at higher temperature. Altogether, reversible C–N bond formation is observed directly in this variable-temperature experiment.

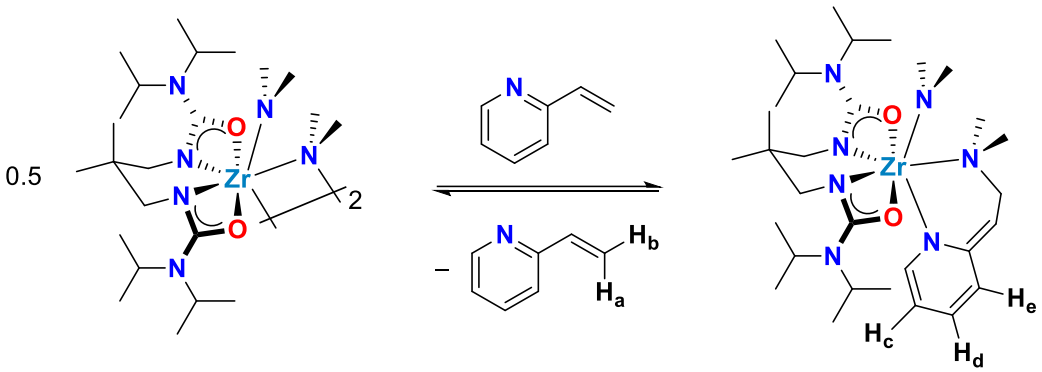

Scheme 2.7 Equilibrium of dimer **2.3** and 2-vinylpyridine with complex **2.4** in solution

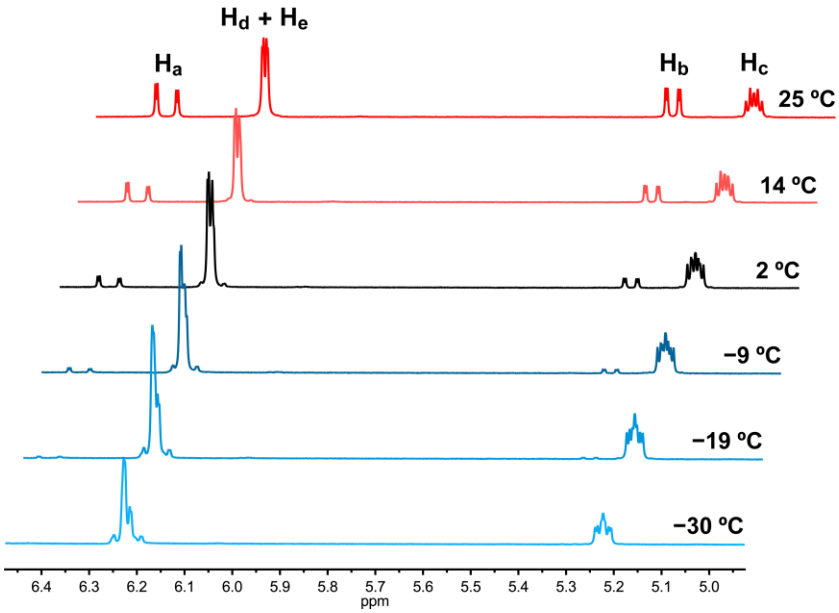

Figure 2.5 Variable-temperature ^{1}H NMR spectra of **2.4**, focusing on the olefinic region (400 MHz in toluene-d_8)

2.5 Comparison of 2.4 to Bulkier Analogues

To observe this phenomenon using other amido precursors, analogous experiments were conducted using pyrrolidine. The stoichiometric reaction of 2-vinylpyridine with seven-coordinate complex **2.5** afforded the hydroamination product; the corresponding bis(amido) dimer **2.6** is also clearly observed as the only byproduct (Scheme 2.8). This contrasts with the analogous reaction with **2.1** (*vide supra*), in which incomplete product formation and multiple metal-containing species are observed. Next, **2.6** was synthesized independently (Scheme 2.9, Figure 2.6) and reacted with 2-vinylpyridine, affording aza-Michael intermediate **2.7** (Scheme 2.10). The solid-state molecular structure is analogous to that of **2.4**, with only minor differences in the bond lengths and angles (Figure 2.7).

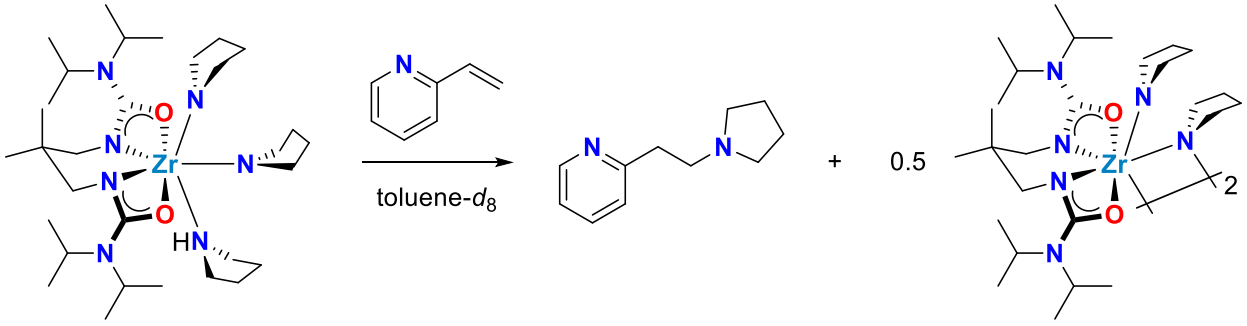

2.5 **2.6**

Scheme 2.8 Stoichiometric reaction of **2.5** with 2-vinylpyridine

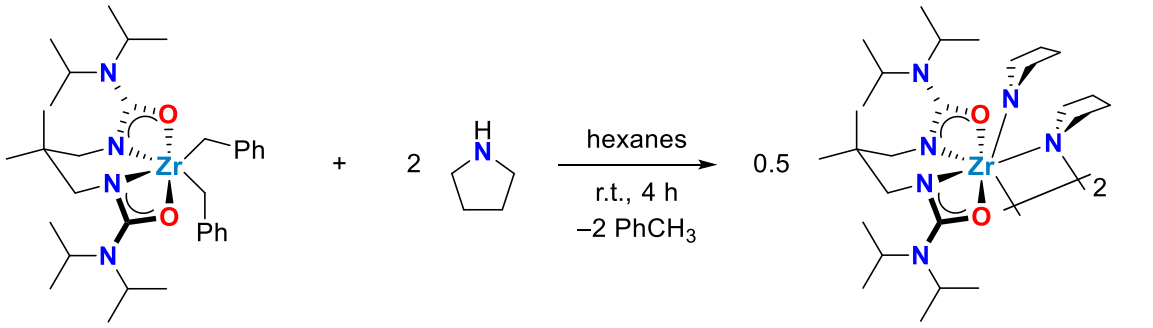

Scheme 2.9 Synthesis of bis(pyrrolidido) dimer **2.6**

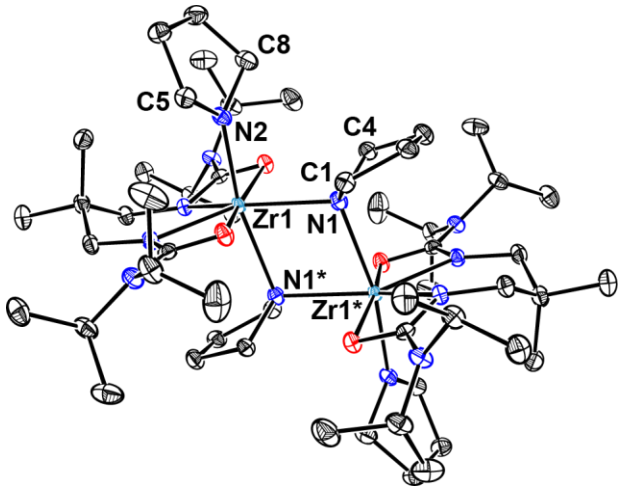

Figure 2.6 ORTEP representation of complex **2.6** with ellipsoids shown at 50% probability and hydrogen atoms and co-crystallized toluene omitted for clarity. Selected bond lengths: Zr1−N2, 2.1182(18) Å; Zr1−N1, 2.3398(17) Å; Zr1−N1*, 2.3644(18) Å. Selected bond angles: Zr1−N1−Zr1*, 104.05(6)°; N1*−Zr1−N2, 168.55(6)°; N1−Zr1−N2, 92.73(6)°. Selected sum of angles: N1, 321°; N2, 359°

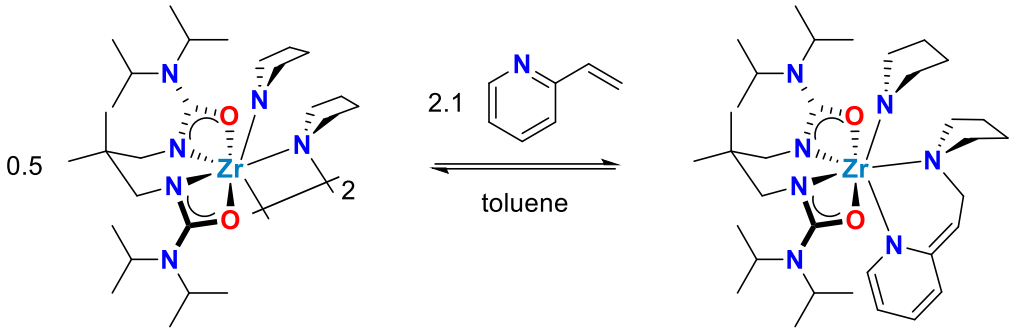

Scheme 2.10 Reaction of dimer **2.6** with 2-vinylpyridine to give aza-Michael complex **2.7**

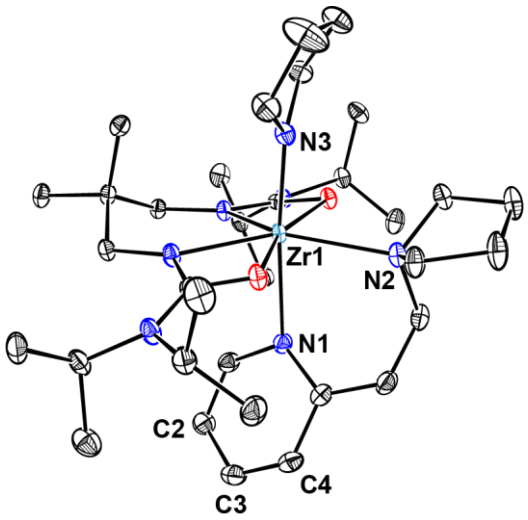

Figure 2.7 ORTEP representation of complex **2.7** with ellipsoids shown at 50% probability and hydrogen atoms omitted for clarity. Selected bond lengths: C1−C2, 1.363(2) Å; C2−C3, 1.430(2) Å; C3−C4, 1.360(2) Å; C4−C5, 1.460(2) Å; C5−C6, 1.369(2) Å; C6−C7, 1.494(2) Å; Zr1−N1, 2.3703(13) Å; Zr1−N2, 2.4250(12) Å; N2−C7, 1.5218(19) Å; N1−C5, 1.4149(19) Å; Zr1−N3, 2.0916(12) Å; N1−C1, 1.3757(19) Å; Selected bond angle: N1−Zr1−N3, 173.82(5)°

Surprisingly, the solution phase behaviour of **2.7** is strikingly different from that of **2.4**. When **2.7** is dissolved in solution, insoluble material suspected to be poly(vinylpyridine) immediately begins precipitating out. Electrophilic metal complexes are known to polymerize 2-

vinylpyridine under similar conditions.[164,193–197] From the ^{1}H NMR spectrum, **2.7** decomposes readily to give **2.6** and various unidentified species. Forming **2.7** *in situ* gives resonances analogous to those of **2.4** and the same unidentified impurities. Characterization of *in situ*-generated **2.7** by variable-temperature NMR spectroscopy reveals the same reversible C−N bond formation observed in **2.4** (Scheme 2.11, Figure 2.8). Thus, as free 2-vinylpyridine forms from C−N bond cleavage in **2.7**, it may irreversibly polymerize. This process is much slower when **2.7** is formed *in situ*, likely due to the dilute conditions. Thermal parameters for these equilibria, determined using van't Hoff plots (Figures A.1 and A.2), change slightly between complexes ($\Delta H°$ = −113 ± 5 kJ/mol, $\Delta S°$ = −380 ± 20 J/mol•K for **2.4**; $\Delta H°$ = −127 ± 7 kJ/mol, $\Delta S°$ = −460 ± 30 J/mol•K for **2.7**). The thermodynamics of reversible C−N bond formation in this system is subtly affected when switching from dimethylamido to pyrrolidido as the nucleophile. The free energies can also be calculated at 298 K and converted to kcal/mol ($\Delta G°$ = −0.36 ± 0.03 kcal/mol for **2.4**; $\Delta G°$ = 2.5 ± 0.3 kcal/mol for **2.7**) to compare to the computed free energy for a reversible C−N bond forming step in Mg-catalyzed hydroamination ($\Delta G°$ = 9.2 kcal/mol).[171] These free energies show that C−N bond formation in **2.4** is slightly exergonic at 298 K, while that in **2.7** is slightly endergonic. However, both reactions are more favourable than C−N bond formation in the Mg-catalyzed reaction, likely due to the aza-Michael mechanism forming a new Zr-amido bond with the pyridyl nitrogen versus the Mg system which operates via a σ-insertive mechanism involving no such favourable interaction.

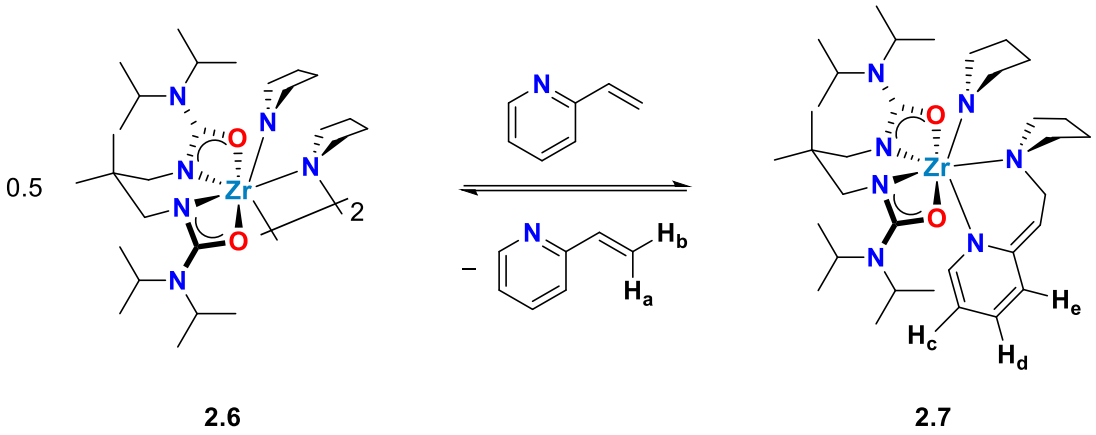

Scheme 2.11 Equilibrium of dimer **2.6** and 2-vinylpyridine with complex **2.7** in solution

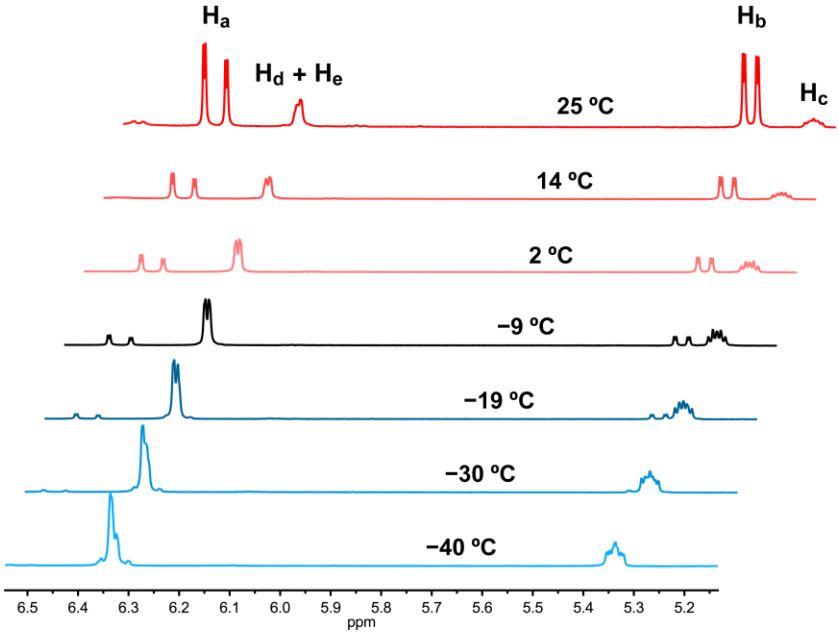

Figure 2.8 Variable-temperature ^{1}H NMR spectra of **2.7**, focusing on the olefinic region (400 MHz in toluene-d_8)

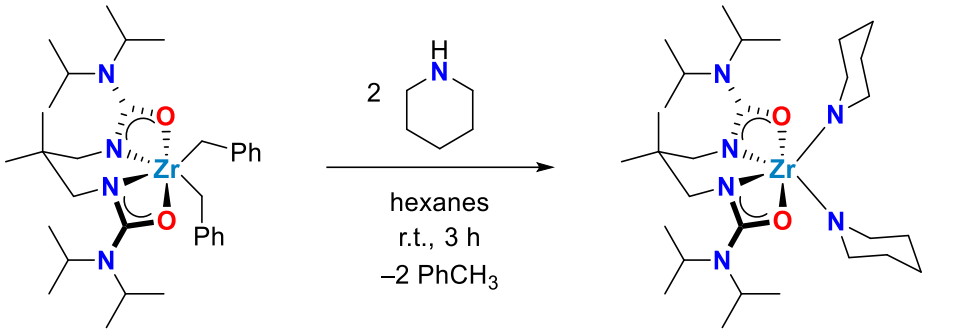

Scheme 2.12 Synthesis of bis(piperidido) complex **2.8** from dibenzyl complex **2.2**

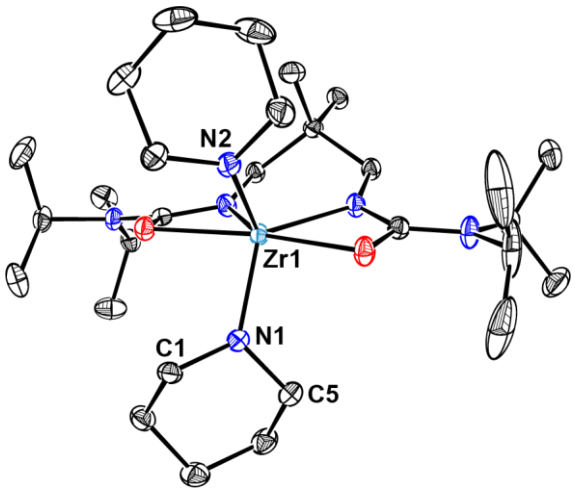

Figure 2.9 ORTEP representation of complex **2.8** with ellipsoids shown at 50% probability and hydrogen atoms omitted for clarity. Selected bond lengths: Zr1−N2, 2.0775(15) Å; Zr1−N1, 2.0676(14) Å. Selected bond angles: N1−Zr1−N2, 117.67(6)°; C1−N1−Zr1, 126.04(10)°; C5−N1−Zr1, 122.74(11)°; C1−N1−C5, 111.22(13)°. Selected sum of angles: N1, 360°

Without a clear electronic rationale for the disparity in solution phase behavior between **2.4** and **2.7**, the propensity for solutions of **2.7** to undergo C−N bond cleavage and further react to form what is likely poly(vinylpyridine) over time was hypothesized to be due to the different steric effects imposed by the dimethylamido versus pyrrolidido ligands. To test this hypothesis, the even larger bis(piperidido) complex **2.8** was synthesized (Scheme 2.12). Similar to the other bis(amido)

complexes, this compound is easily prepared via protonolysis by adding 2 equiv. of piperidine to dibenzyl complex **2.2**. Interestingly, **2.8**, unlike **2.3** and **2.6**, is monomeric in both solution and solid state (Figure 2.9). Reacting **2.8** with 2-vinylpyridine results in no coordination or C−N bond formation, as observed by ^{1}H NMR spectroscopy (Figure D.8). Furthermore, after a few days at room temperature, all the 2-vinylpyridine polymerizes. These results demonstrate extreme sensitivity to steric effects in C−N bond formation with this system. In contrast, the catalytic reaction with piperidine proceeds smoothly (Scheme 2.13), giving full conversion to the *anti*-Markovnikov hydroamination product under the same conditions as the reaction with pyrrolidine (Scheme 2.3). This may suggest that an alternative mechanism is operative under catalytic conditions. For instance, the C−N bond forming step may also occur outside the coordination sphere of the catalyst. Nevertheless, specific steric requirements must be met for reversible C−N bond formation to be directly observable in this system.

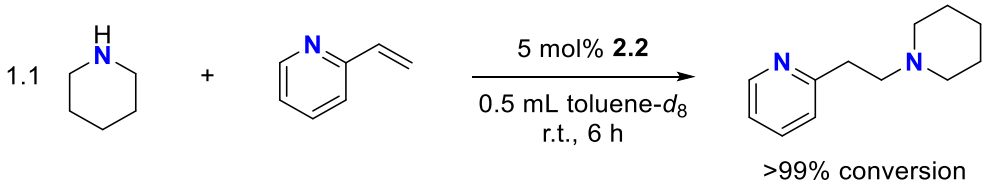

Scheme 2.13 Catalytic hydroamination of 2-vinylpyridine with pyrrolidine using catalyst **2.2**

2.6 Attempts with Other Alkene Substrates

As this hydroamination reaction with 2-vinylpyridine proceeds through an aza-Michael-addition/Lewis acid-catalyzed mechanism, we considered whether related electron-deficient alkenes would demonstrate similar reactivity. Like 2-vinylpyridine, 4-vinylpyridine is known to undergo hydroamination via a Lewis acid-catalyzed mechanism.[183–185] Thus, it was hypothesized that this system would catalyze the *anti*-Markovnikov hydroamination of 4-vinylpyridine as well. Indeed, the reaction between 4-vinylpyridine and pyrrolidine with 5 mol% **2.2** proceeds to

completion at room temperature (Scheme 2.14), as is the case with 2-vinylpyridine (*vide supra*). This result suggests that the mechanism for the reaction with 4-vinylpyridine is similar to the mechanism of hydroamination of 2-vinylpyridine using catalyst **2.2**. Accordingly, we turned our attention to analogous stoichiometric studies with 4-vinylpyridine to those carried out with 2-vinylpyridine.

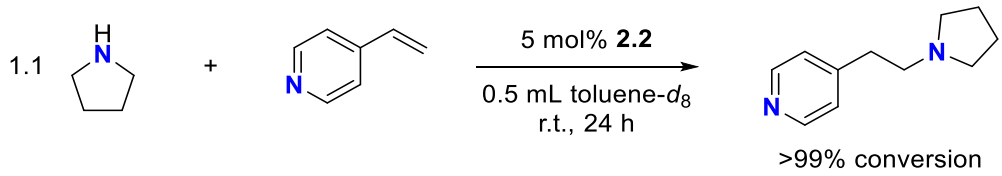

Scheme 2.14 Catalytic *anti*-Markovnikov hydroamination of 4-vinylpyridine using catalyst **2.2**

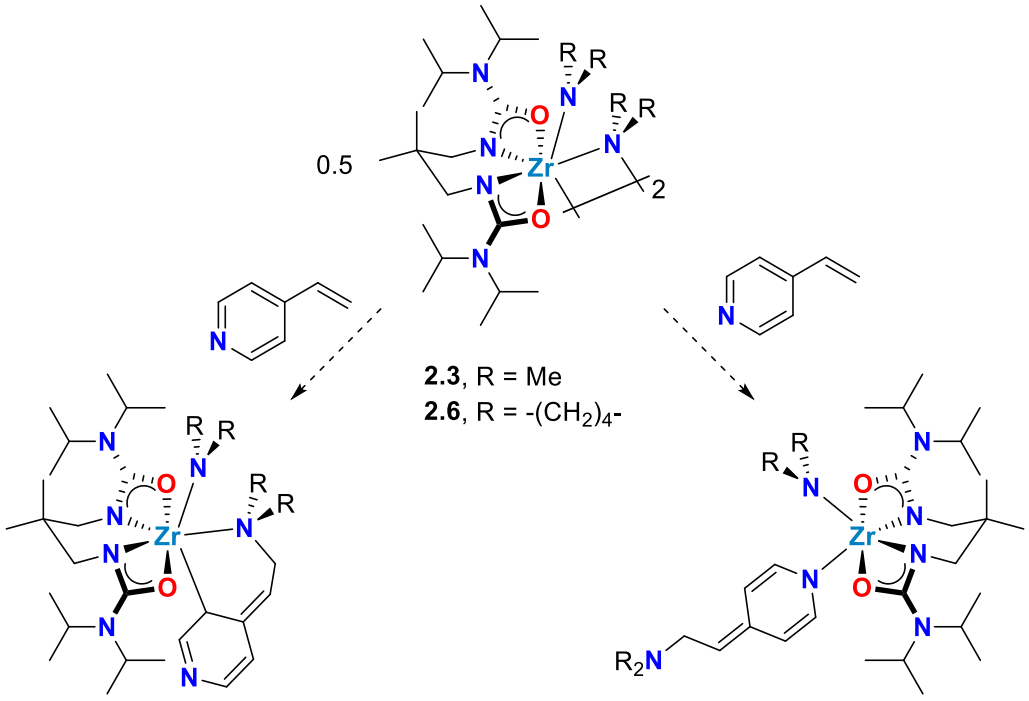

Scheme 2.15 Theoretical aza-Michael-addition intermediates with 4-vinylpyridine

Theoretically, an aza-Michael-addition intermediate with 4-vinylpyridine could result in a new Zr–C bond or a new Zr–N bond upon dearomatization, with the former producing a chelating ligand analogous to **2.4** or **2.7** (Scheme 2.15). Addition of excess 4-vinylpyridine to a concentrated

toluene solution of **2.3** or **2.6** resulted in an immediate colour change to dark orange-red, though all attempts to isolate crystals or even crude solid were futile. In both cases, the corresponding bis(amido) complex crystallized without 4-vinylpyridine present and only crude oils were achieved upon removal of volatiles. As such, though the catalytic reaction with 4-vinylpyridine proceeds smoothly, the absence of well-defined intermediates for the stoichiometric hydroamination of 4-vinylpyridine precluded any investigation into the reversibility of the C–N bond-forming step with this substrate.

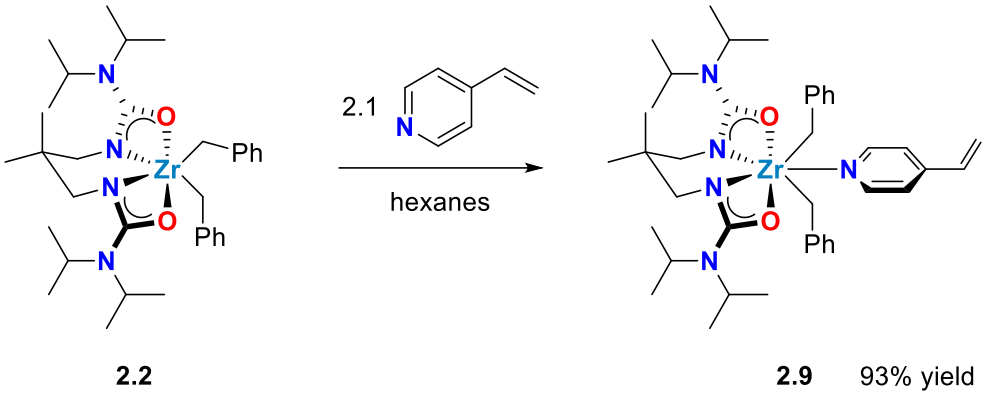

2.2 **2.9** 93% yield

Scheme 2.16 Coordination of 4-vinylpyridine to dibenzyl complex **2.2**

Similarly, efforts to evaluate the difference in nucleophilicity towards 2-vinylpyridine between the alkyl ligands of **2.2** and the amido ligands of **2.3** or **2.6** were ineffective. All attempts at forming a 2-vinylpyridine adduct of **2.2** were unsuccessful, giving only crystallized **2.2** or a crude yellow oil. Addition of excess 2-vinylpyridine to **2.2** in C_6D_6 resulted in no noticeable colour change and no apparent coordination of 2-vinylpyridine by ^{1}H NMR spectroscopy, which contrasts the immediate change to bright orange when pyridine is added.[198] The inability of 2-vinylpyridine to coordinate to the metal centre may be due to steric clashing of the *ortho*-vinyl group and the isopropyl groups of the ureate ligand. Consistent with this hypothesis, addition of excess 4-vinylpyridine to a concentrated solution of **2.2** instead caused an immediate colour change to dark

red, with red crystals of adduct **2.9** precipitating out of solution within one minute (Scheme 2.16). These crystals were suitable for X-ray diffraction studies, and the solid-state molecular structure is shown in Figure 2.10. The structure of **2.9** is analogous to that of the corresponding pyridine complex,[198] with only slight differences in the bond and angle metrics between the two structures. As expected, given the distance between the anionic carbons of the benzyl ligands and the electrophilic *para*-vinyl moiety, no C−C bond formation was observed for this adduct.

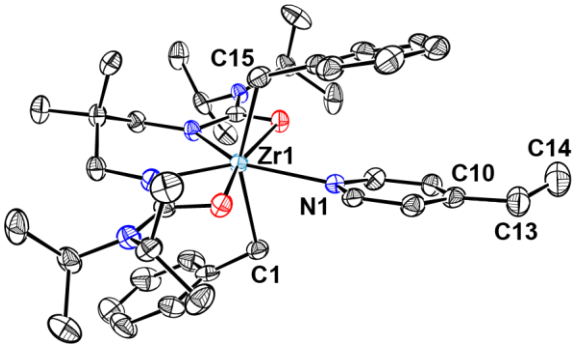

Figure 2.10 ORTEP representation of complex **2.9** with ellipsoids shown at 50% probability and hydrogen atoms and co-crystallized toluene omitted for clarity. Selected bond lengths: Zr1–C1, 2.364(3) Å; Zr1–C15, 2.388(3) Å; Zr1–N1, 2.399(2) Å; C10–C13, 1.485(5) Å; C13–C14, 1.295(5) Å

In addition to 4-vinylpyridine, other activated alkenes were also tested for the stoichiometric hydroamination with pyrrolidine via reaction with complex **2.5**. Specifically, various olefins containing an electron-donating group to enhance coordination to the metal centre or an electron-withdrawing group to activate the alkene were attempted, but none were active for hydroamination with pyrrolidine (Figure 2.11). The reaction of *in situ*-generated **2.5** with 2-vinylfuran and acrylonitrile resulted only in substrate polymerization, while the same reaction with 2-bromostyrene, allyl ether, and *trans*-1-phenyl-1,3-butadiene showed no reactivity even at

elevated temperatures for days. Accordingly, future efforts may focus on modification of the catalyst to improve the alkene scope for this intermolecular hydroamination reaction.

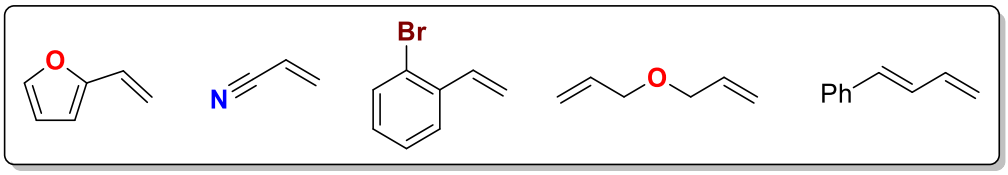

Figure 2.11 Unsuccessful substrates for stoichiometric hydroamination with complex **2.5**

2.7 Conclusions

In summary, we have shown that zirconium, a group 4 metal, can mediate intermolecular hydroamination of 2-vinylpyridine with pyrrolidine. Stoichiometric experiments resulted in isolation of reactive intermediates consistent with C−N bond formation occurring by an aza-Michael addition reaction resulting in dearomatization of the pyridine ring. Furthermore, we have discovered a system in which reversible C−N bond formation can be directly observed by variable-temperature NMR spectroscopy. Consequently, thermodynamic parameters for C−N bond formation could be experimentally determined in two related systems. Here we show that minor changes in the steric profile of the substrate play an important role in the reversibility and degradation of these intermediates in solution. Since stoichiometric C−N bond formation was least favourable with bulkier amido ligands, we speculate that the additional steric bulk may impede the approach of the amido nucleophile to the coordinated 2-vinylpyridine or the initial coordination of 2-vinylpyridine substrate to the metal centre. These results are consistent with challenges associated with developing a general catalyst for intermolecular hydroamination of simple alkenes and amines. As the catalytic reactivity could be extended to 4-vinylpyridine but stoichiometric studies concerning reversible C−N bond formation were unsuccessful with this alternative substrate, future directions will focus on investigation of analogous reactivity with other Michael-

acceptors and amines towards gaining further mechanistic understanding and developing new catalysts.

Chapter 3: Zirconium Ureates for Catalytic C−H Functionalization

3.1 Introduction

Allylic amines (Figure 3.1) are prevalent structural motifs in natural products, agrochemicals, and pharmaceuticals.[199,200] Accordingly, much research has been directed toward the development of efficient methods for their construction. Transition metal-catalyzed C−N bond formation represents a powerful tool for the synthesis of allylic amines and other nitrogen-containing compounds.[130,131,204–210,132,134–137,201–203] Late-transition-metal-catalyzed hydroamination of dienes[211–213] and allenes[214] enables the direct and atom-economic synthesis of allylic amines from simple starting materials by regioselective C−N bond formation (Scheme 3.1). Alkynes are also viable substrates for this transformation via isomerization of the alkyne to an allene *in situ*.[215–220] Notably, this approach limits the substrate scope to the use of alkyl-substituted alkynes. An alternative catalytic hydroaminoalkylation strategy would feature C−C bond formation between a simple alkyne and the α-carbon of amine starting materials (*vide infra*). While stoichiometric variants of this transformation are well established,[221–225] the catalytic variant has thus far been unknown, albeit with one caveat; a combined rhodium/photoredox system can catalyze the hydroaminoalkylation of 1-phenyl-1-propyne with tertiary and secondary amines.[226] However, as this reaction proceeds through formation of π-allyl intermediates, homoallylic amines are formed rather than allylic amines (Figure 3.1, Scheme 3.1).

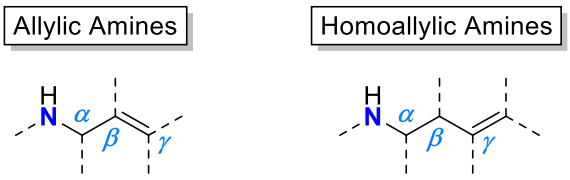

Figure 3.1 General structure of allylic and homoallylic amines with *a*, *β*, and *γ* positions labelled

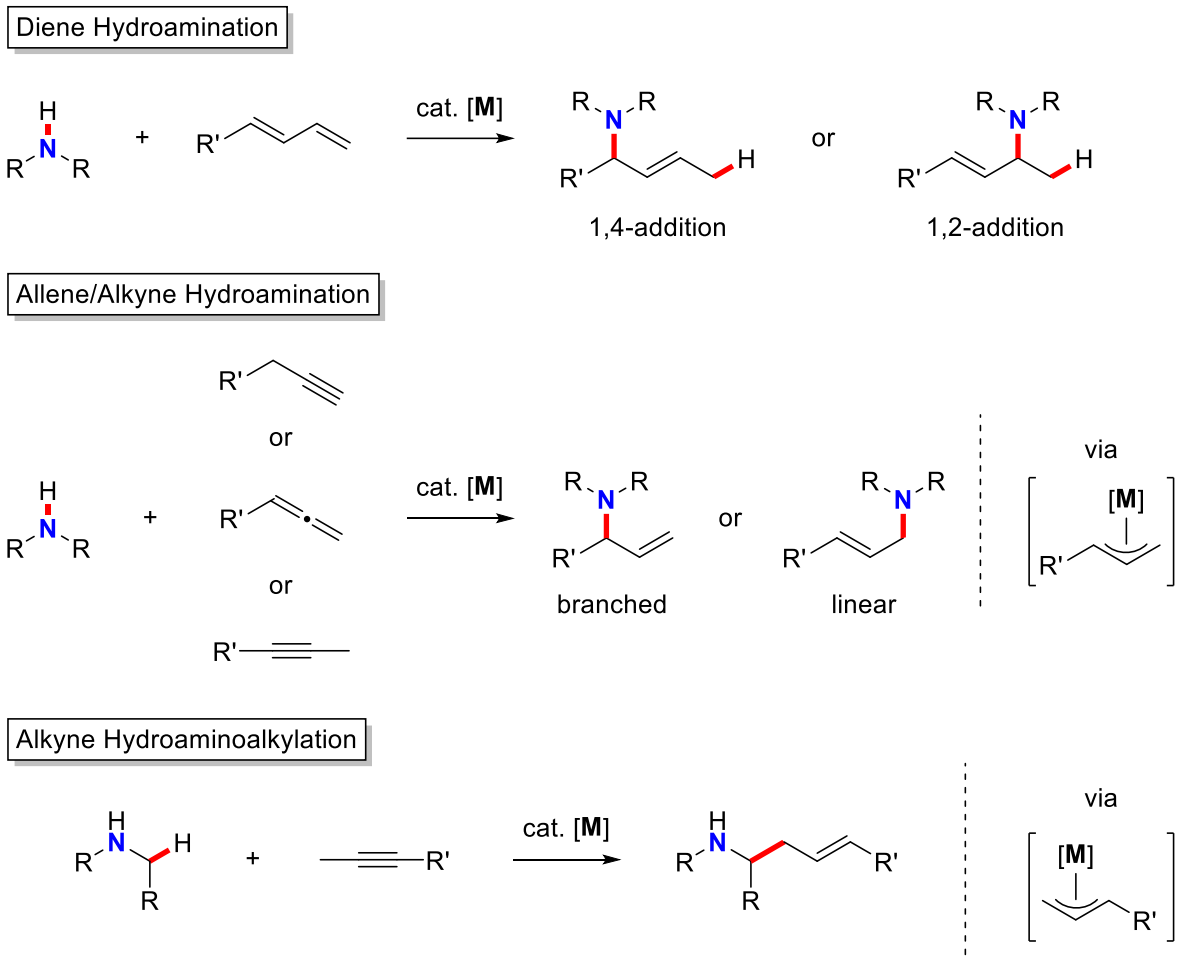

Scheme 3.1 Hydroamination of dienes, allenes, and alkynes to give allylic amines and hydroaminoalkylation of alkynes to give homoallylic amines

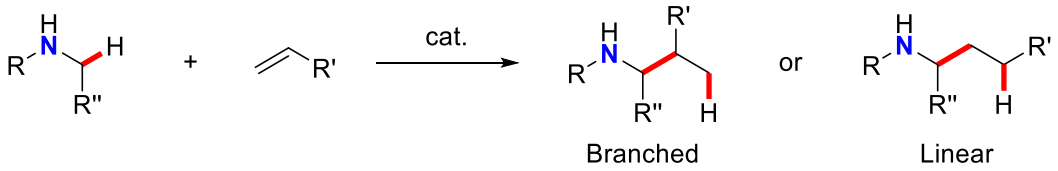

Scheme 3.2 General hydroaminoalkylation reaction with an alkene substrate

Hydroaminoalkylation, in which the α-C−H bond of an amine is added across an alkene (Scheme 3.2), can be catalyzed by late-transition-metals,[227–229] early-transition-metals,[82,85,86,116,230–232] and photocatalysts.[233–237] Early transition metals are often overlooked but

are attractive due to their abundance and low cost. While catalytic hydroaminoalkylation of alkynes was previously unknown, the stoichiometric reaction was pioneered by Buchwald and co-workers and further developed by Norton and others (Scheme 3.3).[221–225] Insertion of a variety of alkyl and aryl substituted alkynes into the Zr–C bond of zirconaaziridines (**A**) resulted in the formation of an observable five-membered metallacycle (**B**). Aqueous workup of the insertion product afforded the *α,β,γ*-allylic amine product **C**, along with stoichiometric amounts of zirconium oxide byproducts. To the best of our knowledge, this was previously the only method to synthesize *a,β,γ*-allylic anilines where each substituent is an aryl group. Notably, these stoichiometric studies showed that the insertion of alkynes into group 4 metallaaziridines could be achieved at room temperature,[221,222,224,238,239] but catalytic turnover could not be realized under any conditions.

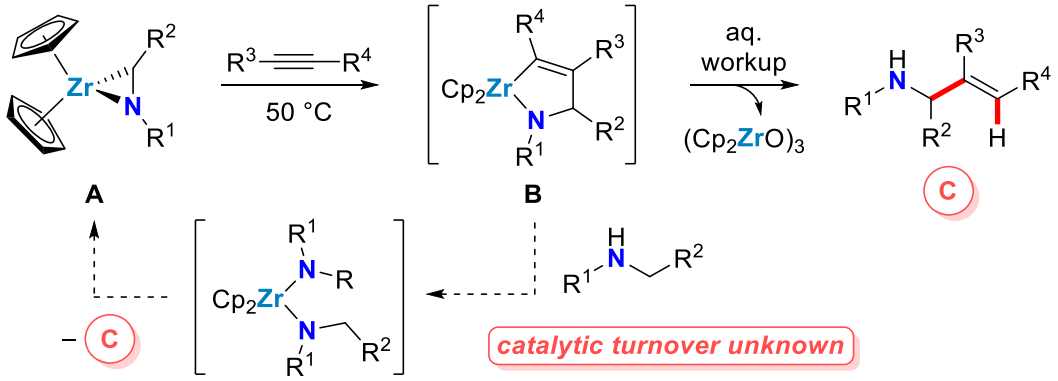

Scheme 3.3 Previous stoichiometric hydroaminoalkylation of alkynes using zirconium

Although our group and others have realized advances in alkene hydroaminoalkylation catalysis with *N,E*-chelated early-transition-metal complexes,[114,115,240] none of these systems show reactivity with alkyne substrates (*vide infra*). To address this challenge, we considered mechanistic insights gained from studies on alkene hydroaminoalkylation catalysts developed by the Schafer group,[241–245] in which DFT calculations revealed a turnover-limiting protonolysis of the five-

membered metallacyclic intermediate analogous to **B** (Scheme 3.4). This high energy transition state demands amine coordination to a coordinatively saturated metal centre.[245] We hypothesized that using a catalyst in which amine coordination would not exceed the preferred coordination number would lower the barrier for protonolysis and allow catalytic turnover for reactions with challenging alkyne substrates.

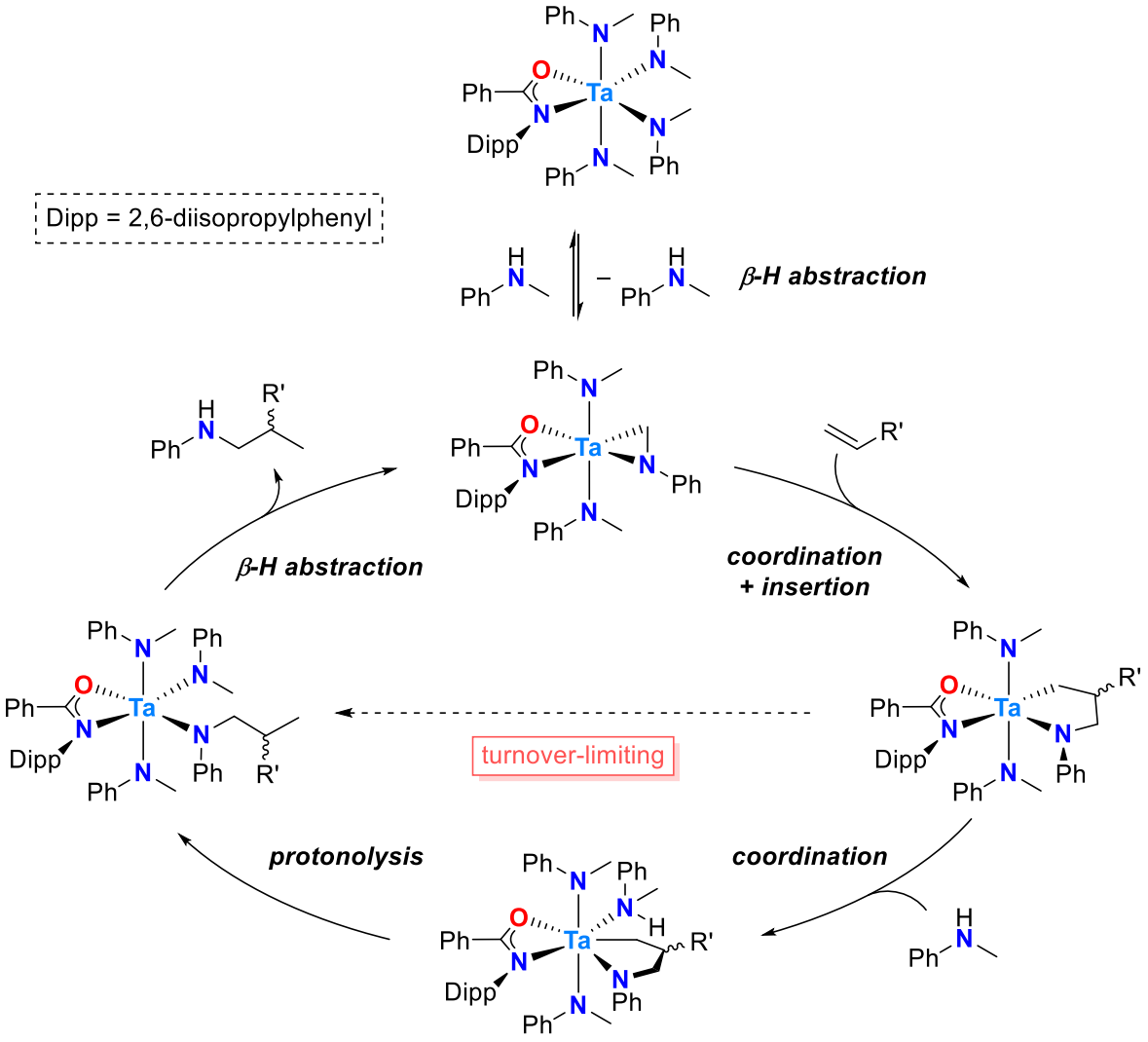

Scheme 3.4 Mechanism of alkene hydroaminoalkylation by a tantalum amidate catalyst based on computational studies

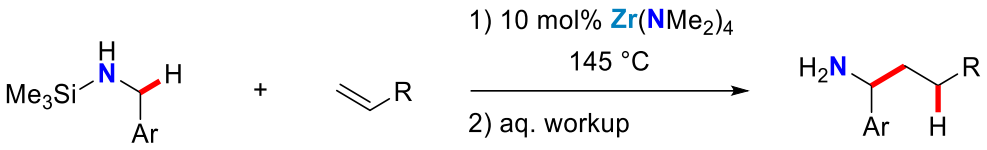

Scheme 3.5 Zirconium-catalyzed hydroaminoalkylation of alkenes with silyl amines

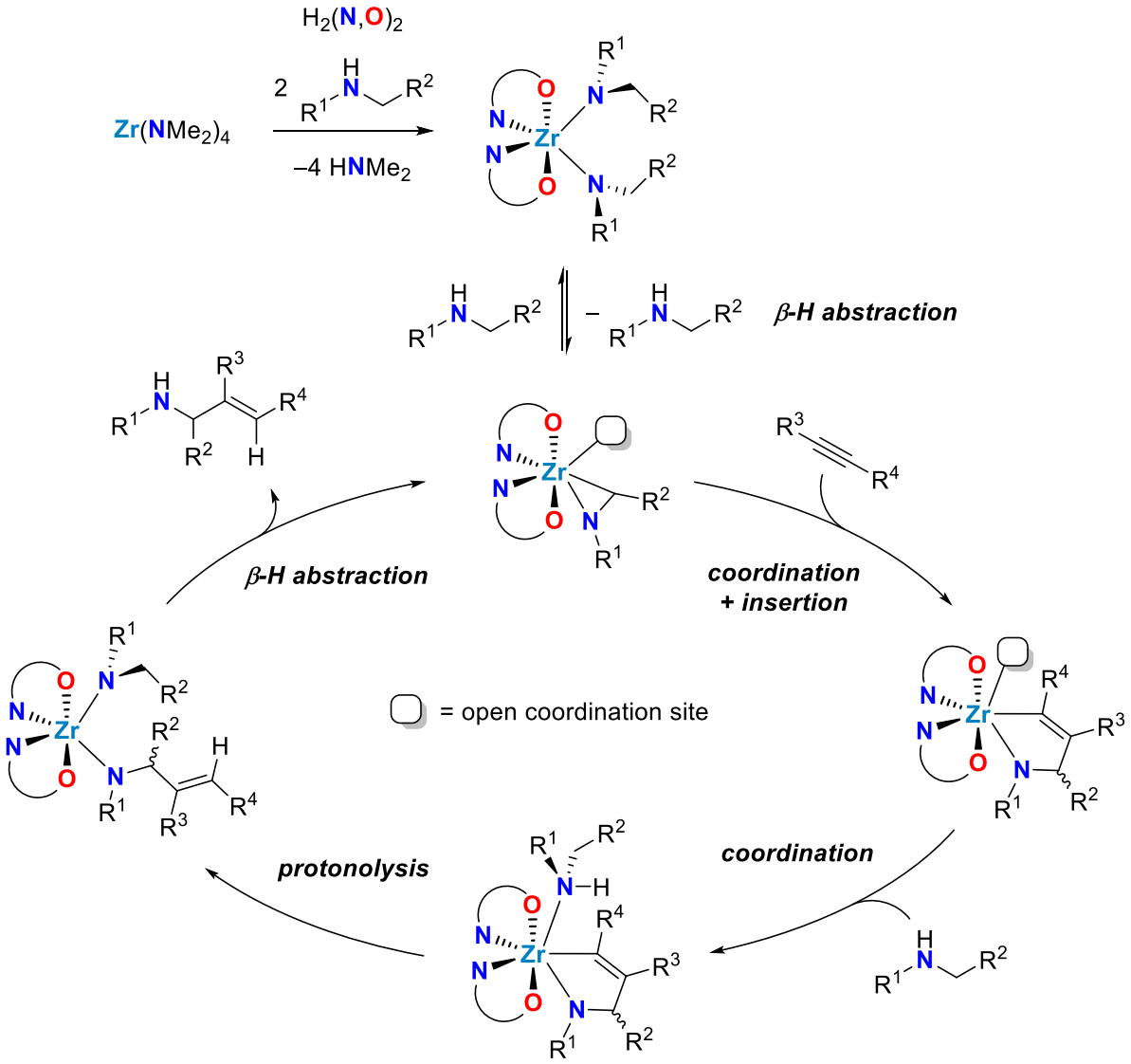

Scheme 3.6 Proposed mechanism of alkyne hydroaminoalkylation by a tethered bis(ureate) zirconium catalyst

More recently, the Schafer group reported the hydroaminoalkylation of alkenes with sterically demanding *N*-(trimethylsilyl)amines using $Zr(NMe_2)_4$ as a catalyst (Scheme 3.5).[114] In hydroamination catalysis, the Schafer group showed that zirconium complexes bearing a tethered bis(ureate) ligand readily form seven-coordinate complexes (see Chapter 2), which could be used to advantage in the coordination of neutral amines for the desired associative catalytic turnover step.[160–163,246,247] We therefore envisioned that in the proposed catalytic cycle for alkyne hydroaminoalkylation (Scheme 3.6), the tethered bis(ureate) zirconium complexes discussed in Chapter 2 would make ideal catalysts for this challenging transformation. Here we show that complex **2.1** (Figure 2.1), generated *in situ*, catalyzes the hydroaminoalkylation of alkynes to make allylic amines (Scheme 3.7), likely in part by enabling the amine coordination for the protonolysis step. These mechanistic insights are supported by characterization and reactivity studies of model catalytic intermediates, and preliminary substrate scope investigations are presented.

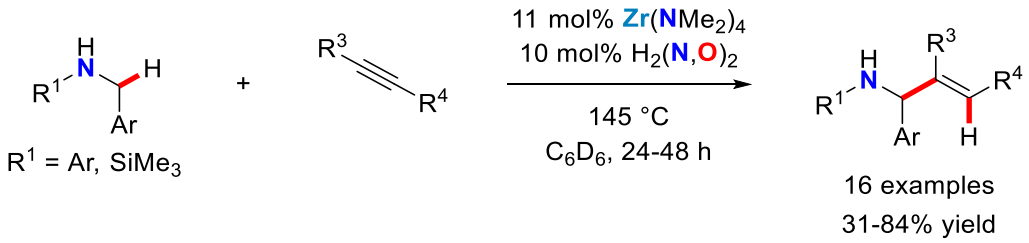

Scheme 3.7 General zirconium-catalyzed alkyne hydroaminoalkylation reaction discussed herein

3.2 Evaluation of Alkene Hydroaminoalkylation Catalysts

Prior to our investigations with the tethered bis(ureate)-ligated zirconium catalysts, we first sought confirmation that current hydroaminoalkylation catalysts were not effective for catalyzing the hydroaminoalkylation of alkynes. This work was performed collaboratively with Mr. Erick Nuñez Bahena. Specifically, three state-of-the-art catalysts for alkene hydroaminoalkylation (Figure 3.2)[114,115,240,248] were tested for the hydroaminoalkylation of *N*-benzylaniline with

diphenylacetylene to form allylic amine product **3.1** (Table 3.1). *N*-benzylaniline was chosen as the amine substrate for these test reactions as it was successfully applied to the catalytic hydroaminoalkylation of allenes as recently reported by Doye and co-workers.[249] Firstly, 11 mol% $Zr(NMe_2)_4$ was attempted as a catalyst, giving only 15% conversion to amine **3.1** after 24 h at 145 °C in C_6D_6. Though the conversion to product was poor, this result was promising in that Zr could catalyze the hydroaminoalkylation of an alkyne to some extent. This reaction also serves as a control for generating tethered bis(ureate) catalyst **2.1** *in situ* (*vide infra*), showing that poor conversion is achieved in the absence of the 1,3-*N*,*O*-chelating ligand. In contrast, the *in situ* tantalum ureate system comprised of 10 mol% ureate **D** and $Ta(CH_2SiMe_3)_3Cl_2$ (Figure 3.2), reported by the Schafer group as a highly active hydroaminoalkylation catalyst for unactivated alkenes,[115] gave no conversion at all under the same conditions. Notably, the titanium formamidinate catalyst **E** reported by Bielefeld and Doye (Figure 3.2)[240] provided a modest increase to 25% conversion to amine **3.1**. This result provided further confirmation that group 4 metals could catalyze the hydroaminoalkylation of alkynes (albeit in low conversions) and showed that improved reaction performance could be achieved using a sterically demanding 1,3-*N*,*E*-chelating ligand. Therefore, this gave us added encouragement to test our hypothesis that tethered bis(ureate) complex **2.1** would be an active catalyst for this transformation.

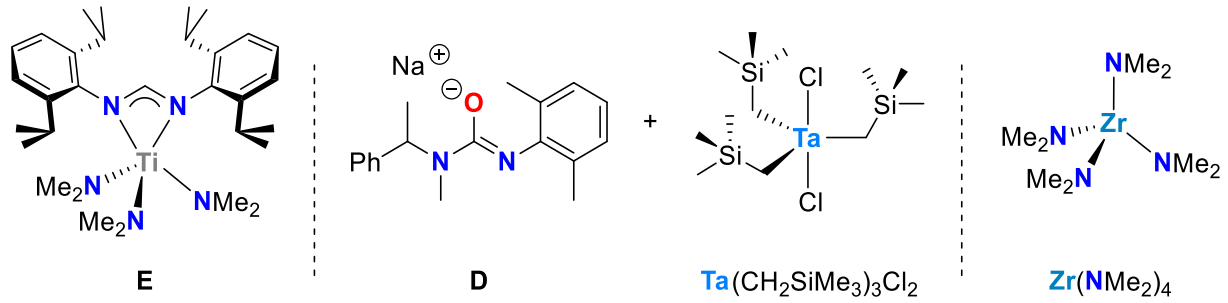

Figure 3.2 State-of-the-art alkene hydroaminoalkylation catalysts

Table 3.1 Screening of known hydroaminoalkylation catalysts for the reaction with diphenylacetylene

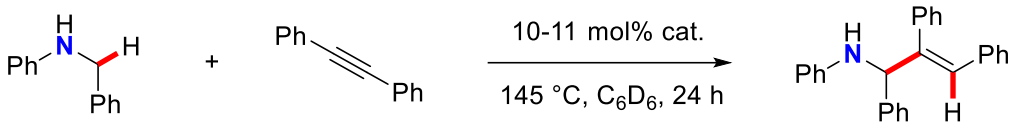

3.1

cat.	mol% (%)	conversion (%)
$Zr(NMe_2)_4$	11	15
D + $Ta(CH_2SiMe_3)_3Cl_2$	10	0
E	10	25

Conversions determined by ^{1}H NMR spectroscopy.

3.3 Stoichiometric Studies

Initial investigations with the bis(ureate) zirconium system began by synthesizing model complexes to study the stoichiometric transformations involved in alkyne hydroaminoalkylation. The experimental work described in this section was carried out by Mr. Erick Nuñez Bahena, except for the X-ray diffraction studies discussed below. Therefore, the discussion here is largely limited to the overall synthetic schemes and the ensuing structural characterization in the solid state. Mixed alkyl amido complexes are known precursors to metallaaziridines.[250] Thus, complex **3.2** was prepared via protonolysis of the corresponding dibenzyl complex **2.2**[198,246] with 1 equiv. of *N*-(trimethylsilyl)benzylamine (Scheme 3.8). This same amine substrate was previously utilized in similar stoichiometric studies by Buchwald and co-workers.[221] Six-coordinate **3.2** was isolated as a colourless crystalline solid in 71% yield and was fully characterized, including by X-ray crystallography; the solid-state molecular structure of complex **3.2** is shown in Figure 3.3. Six-coordinate complex **3.2** has a distorted pentagonal pyramidal geometry with pseudo-C_s symmetry and resembles the overall structure of other six-coordinate zirconium complexes bearing this

tethered bis(ureate) ligand. For example, the N1–Zr1–C1 bond angle (116.41(17)°) is just slightly contracted compared to the C–Zr–C bond angle of the benzyl ligands in **2.2** (118.44(6)°, Figure 2.2) and the N–Zr–N bond angle of the amido ligands in **2.8** (117.67(6)°, Figure 2.9). Most importantly, the benzylic protons on C8 are in close proximity to the anionic C1 carbon of the benzyl ligand, facilitating *β*-H abstraction to produce the key zirconaaziridine intermediate in hydroaminoalkylation catalysis.

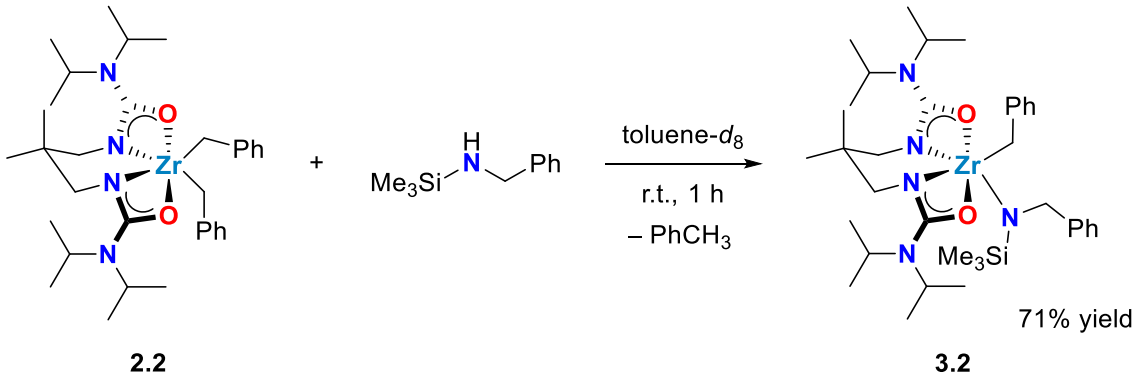

Scheme 3.8 Synthesis of mixed alkyl amido complex **3.2**

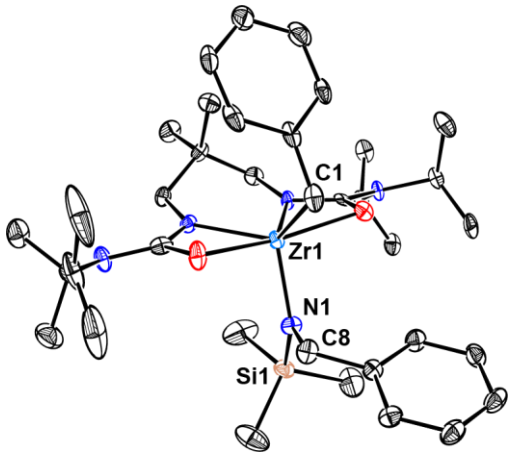

Figure 3.3 ORTEP representation of complex **3.2** with ellipsoids shown at 50% probability and hydrogen atoms omitted for clarity. Selected bond lengths (Å) and angles (°): Zr1–N1, 2.034(4); Zr1–C1, 2.322(5); N1–C8, 1.476(6); Si1–N1, 1.731(4); N1–Zr1–C1, 116.41(17); Si1–N1-Zr1, 135.1(2); N1–Zr1–C8, 30.65(15)

Elimination of toluene via *β*-H abstraction was induced via the postulated formation of seven-coordinate species **3.3** upon adding pyridine to complex **3.2** (Scheme 3.9). Heating this pyridine adduct resulted in the formation of **3.4** and 1 equiv. of toluene. Crystals grown from cold hexanes suitable for X-ray diffraction confirmed the molecular structure of **3.4** (Figure 3.4). Seven-coordinate zirconaaziridine **3.4** has a distorted pentagonal bipyramidal geometry with pseudo-C_s symmetry and the aziridine moiety in the axial position. The bond lengths, bond angles, and geometric conformation of the aziridine in **3.4** are in agreement with reported zirconaziridines.[221,225,251] While the aziridine is best described as a dianionic bidentate ligand, therefore making **3.4** a formally-eight-coordinate complex, here the aziridine is considered to occupy one coordination site to simplify discussion between complexes. With a model zirconaaziridine intermediate in hand, the alkyne insertion step of hydroaminoalkylation was investigated.

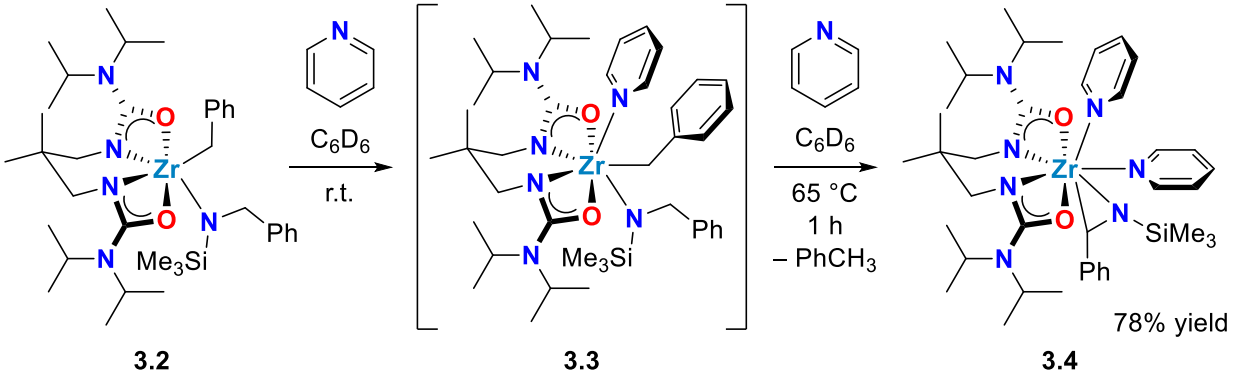

Scheme 3.9 Synthesis of zirconaaziridine **3.4** via *β*-H abstraction

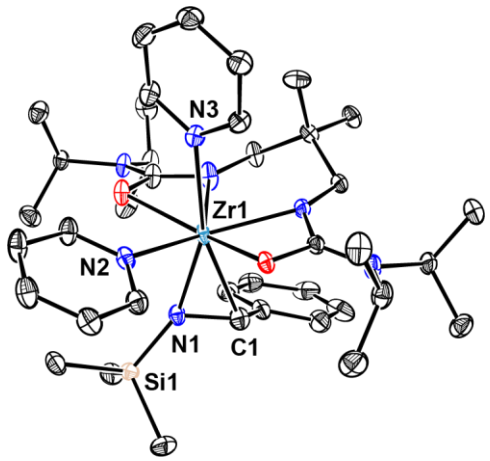

Figure 3.4 ORTEP representation of complex **3.4** with ellipsoids shown at 50% probability and hydrogen atoms omitted for clarity. Selected bond lengths (Å) and angles (°): Zr1–N1, 2.0600(17); Zr1–C1, 2.322(2); N1–C1, 1.434(3); Zr1–N2, 2.4230(17); Zr1–N3, 2.5488(17); N1–Zr1–C1, 37.60(7); N1–Zr1–N2, 84.16(6); C1–Zr1–N2, 112.95(7); N2–Zr1–N3, 73.78(6), N1–Zr1–N3, 156.77(6); C1–Zr1–N3, 162.32(7)

Insertion of diphenylacetylene into the Zr–C bond of **3.4** resulted in the formation of five-membered metallacycle **3.5** (Scheme 3.10), with the coordinated pyridine ensuring that a seven-coordinate complex is retained. The structure of **3.5** was confirmed by X-ray crystallography (Figure 3.5), using crystals grown from cold hexanes. Complex **3.5** has distorted pentagonal bipyramidal geometry and pseudo-C_s symmetry, with the alkene substrate resulting in an equatorial Zr1−C3 bond. Notably, this bond is significantly longer than the corresponding Zr−C bond of an analogous constrained geometry complex reported by Norton and co-workers[224] that contains the same zirconacycle fragment (2.314(9) and 2.263(3) Å, respectively). This difference is likely due to competitive donation to Zr in the equatorial plane by the two 1,3-*N*,*O* ligands in **3.5**, weakening the Zr−C bond. In contrast, the bond distance for the Zr-amido bond in **3.5** (Zr1–N1, 2.088(7) Å) is in good agreement with that of the constrained geometry analogue (2.097(2)

Å).[224] As the neutral pyridine donor is coordinated next to the Zr−C bond, **3.5** is primed for protonolysis in the presence of coordinating secondary amine.

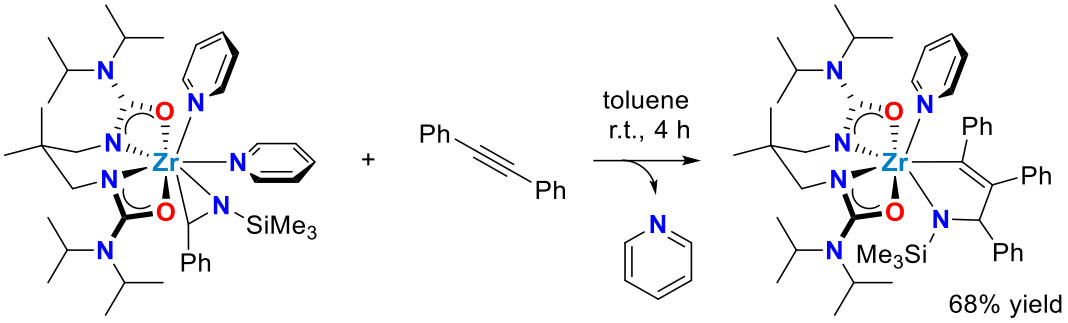

3.4 **3.5**

Scheme 3.10 Synthesis of metallacycle **3.5** via insertion of diphenylacetylene

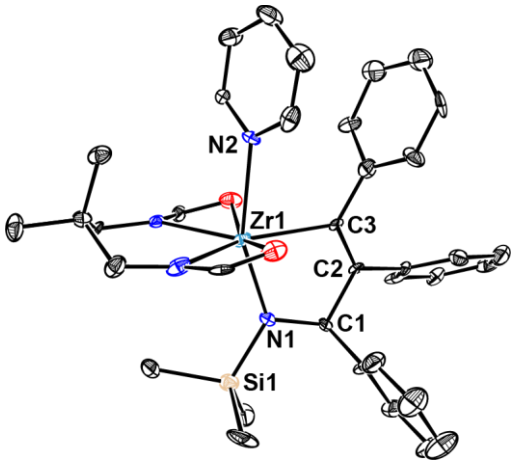

Figure 3.5 ORTEP representation of complex **3.5** with ellipsoids shown at 50% probability and hydrogen atoms and N(^{i}Pr)$_2$ omitted for clarity. Selected bond lengths (Å) and angles (°): Zr1–N1, 2.088(7); Zr1–C3, 2.314(9); Zr1–N2, 2.429(7); N1–C1, 1.49(1); C3–C2, 1.36(1); C1–C2, 1.53(1); N1–Zr1–C3, 76.9(3)

To explore the protonolysis step, **3.5** was reacted with an excess of pyrrolidine (Scheme 3.11). After 5 min at room temperature, **3.5** was fully converted to **2.5** (Chapter 2),[246] pyridine, and allylic amine **3.6**. These results show that facile product release can be realized with simple amine substrates, rather than protic stoichiometric workups. We propose that the sterically open

coordination sphere stabilized by the tethered bis(ureate) ligand promotes this reactivity. Most importantly, the stoichiometric reactions described provided a framework for catalytic alkyne hydroaminoalkylation (*vide infra*).

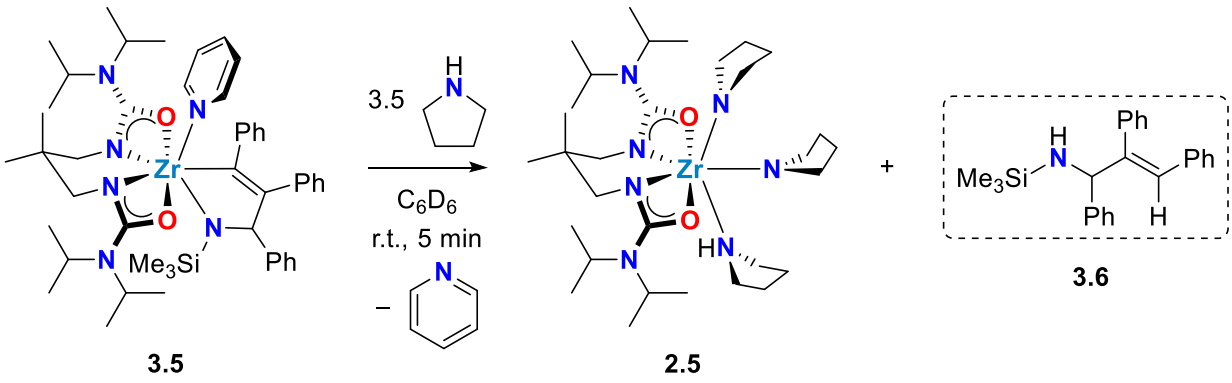

Scheme 3.11 Model protonolysis reaction of metallacycle **3.5** with excess pyrrolidine

3.4 Catalytic Alkyne Hydroaminoalkylation

The following experiment was carried out and analyzed by Mr. Erick Nuñez Bahena. Combining 11 mol% $Zr(NMe_2)_4$ and 10 mol% bis(urea) proligand in C_6D_6 to generate catalyst **2.1** *in situ*, the reaction of *N*-(trimethylsilyl)benzylamine with diphenylacetylene at 145 °C for 24 h produced the desired allylic amine **3.6** in 60% yield, as determined by ^{1}H NMR spectroscopy (Scheme 3.12). The catalytic contribution of the excess $Zr(NMe_2)_4$ is negligible based on control experiments (Table 3.1). Also, hydroamination was observed as a side-reaction,[161,162] producing the corresponding enamine **3.7** in 14% yield. Several other unidentified minor products were also formed.

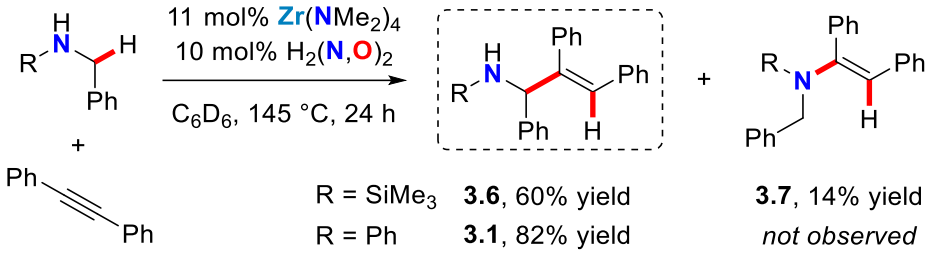

Scheme 3.12 Initial results using catalyst **2.1** for catalytic alkyne hydroaminoalkylation

The remainder of the experimental work described in this chapter was performed collaboratively with Mr. Erick Nuñez Bahena. Previous work using tethered bis(ureate) zirconium catalyst **2.1** for the hydroamination of alkynes with secondary amines showed that arylamines are not reactive in hydroamination.[161,162] Thus, by using *N*-benzylaniline as the hydroaminoalkylation substrate, the hydroamination product could be avoided and the desired allylic amine was produced as the exclusive organic product in 82% yield after 24 h (Scheme 3.12). This result is consistent with the test reactions described above (Table 3.1) that show productive catalysis with this arylamine substrate.

Table 3.2 Alkyne scope for hydroaminoalkylation

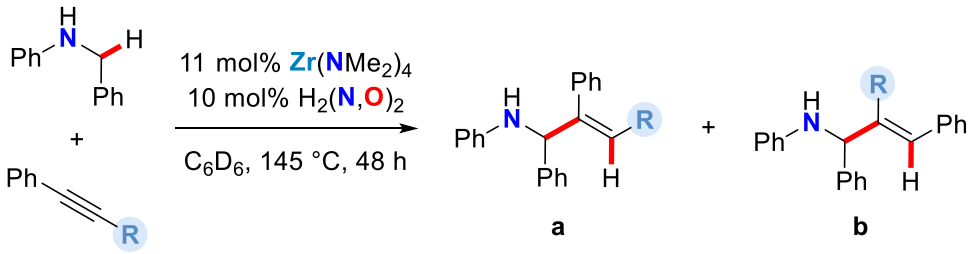

product	R	combined yield (%)	a:b
3.8	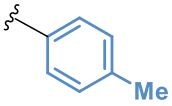	75	1.1:1
3.9	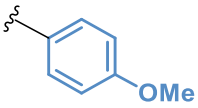	76	1.4:1
3.10	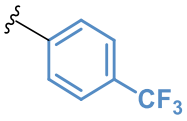	63	1:1
3.11	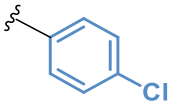	74	1:1.2
3.12	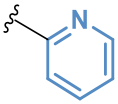	49	a only
3.13		40	1:4.7
3.14	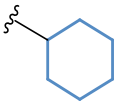	76	1:1.2
3.15		31	a only

$H_2(N,O)_2$ (0.01 mmol) and $Zr(NMe_2)_4$ (0.01 mmol) were allowed to mix prior to addition of amine (0.10 mmol) and alkyne (0.10 mmol). Combined yields and a:b ratios were determined by ^1H NMR spectroscopy using 1,3,5-trimethoxybenzene as a standard.

The substrate scope for the catalytic hydroaminoalkylation of alkynes was evaluated (Table 3.2). Using *N*-benzylaniline as the benchmark amine substrate and the same conditions as those in Scheme 3.12, several diarylacetylenes were investigated. Substituting the 4-position of one of the phenyl groups with electron-donating or electron-withdrawing groups (**3.8**-**3.11**) reduced the yield

somewhat, though there was a more noticeable reduction in yield for the CF_3-substituted alkyne (63%). In each case, the regioselectivity is negligible. This is rationalized based on the polarization of the alkyne in the transition state for insertion, where π-donation can stabilize positive charge build-up or destabilize negative charge-build up at the benzylic position. Conversely, replacing the phenyl substituent with 2-pyridyl (**3.12**) resulted in the exclusive formation of one regioisomer, attributed to the directing ability of the pyridyl nitrogen.[252] However, a substantial decrease in yield was observed, partially due to competitive hydroamination with the dimethylamine that evolves upon activation of the $Zr(NMe_2)_4$ precatalyst. The more polarized 1-phenyl-1-propyne also gave improved regioselectivity with a moderate yield (**3.13**) while the cyclohexyl-substituted variant (**3.14**) provided an increase in yield, although no significant regioselectivity was observed. A comparison of the regioisomeric distribution in **3.13** and **3.14** suggests that steric effects may influence the regioselectivity more than the electronic properties of the alkyne. Indeed, using 1-phenyl-2-trimethylsilylacetylene, which is both electronically and sterically biased, gave exclusive formation of one regioisomer (**3.15**).[253]

Table 3.3 Amine scope for hydroaminoalkylation

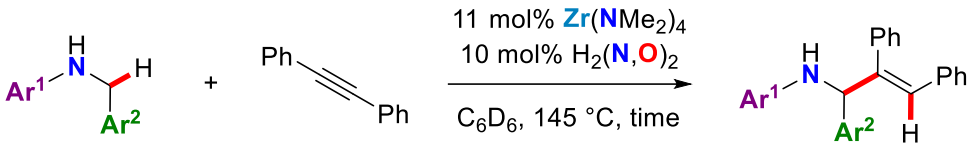

product	Ar^1	Ar^2	time (h)	yield (%)
3.16	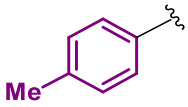	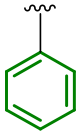	24	84
3.17	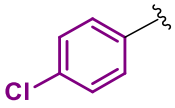	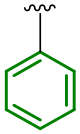	48	42
3.18	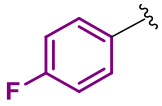	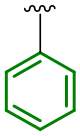	48	78
3.19	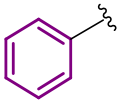	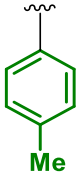	48	72
3.20	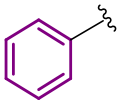	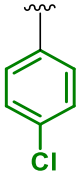	24	79
3.21	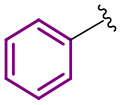	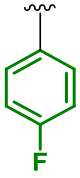	24	80

$H_2(N,O)_2$ (0.01 mmol) and $Zr(NMe_2)_4$ (0.01 mmol) were allowed to mix prior to addition of amine (0.10 mmol) and alkyne (0.10 mmol). Yields were determined by ^1H NMR spectroscopy using 1,3,5-trimethoxybenzene as a standard.

Several variations of the amine substrate were also investigated using diphenylacetylene as the alkyne (Table 3.3). Substituting the 4-position of the aniline moiety with methyl gave similar results to unsubstituted *N*-benzylaniline (84% yield, **3.16**). With longer reaction times, the

corresponding chloro substitution decreased the yield considerably (**3.17**), while the fluoro-substituted arene decreased the yield only slightly (**3.18**). In contrast, substituting the 4-position of the benzyl fragment with methyl (**3.19**) required a 48-h reaction time to achieve a yield of 72%, while the chloro (**3.20**) and fluoro (**3.21**) substitutions gave comparable yields to **3.16** in only 24 h. This effect may be due to the decreased bond dissociation energy of the benzylic C−H bond for more electron-poor benzyl groups. The solid-state molecular structure of **3.20** was also obtained using crystals grown from a saturated methanol solution of **3.20** at room temperature (Figure 3.6). The tetrahedral geometry about C7 and the C7–C14 and C20–C14 bond lengths (1.5316(18) and 1.3450(18) Å, respectively) clearly indicate that no isomerization of the alkene has occurred, and the geometry of **3.20** confirms its assignment as the *E* isomer. Overall, both electron-donating and electron-withdrawing substituents are tolerated on the amine and alkyne substrates in this preliminary substrate scope scan for C−H alkenylation.

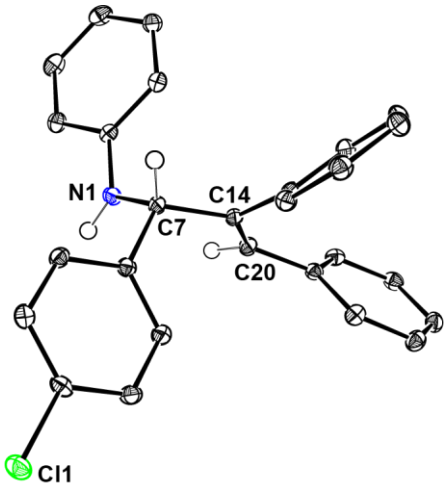

Figure 3.6 ORTEP representation of product **3.20** with ellipsoids shown at 50% probability and aryl hydrogen atoms omitted for clarity. Selected bond lengths (Å) and angles (°): N1–C7, 1.4635(16); C7–C14, 1.5316(18); C20–C14, 1.3450(18); C20–C14–C7, 120.70(11)

3.5 Conclusions

In summary, the catalytic hydroaminoalkylation of alkynes to give allylic amine products can be achieved. Zirconium complexes bearing a tethered bis(ureate) ligand that favours the formation of seven-coordinate complexes were found to promote the stoichiometric transformations required for the catalytic reaction. The isolation and characterization of model intermediates suggest that the steric availability at the zirconium centre plays a role in facilitating insertion reactions and challenging protonolysis reactions required for catalytic turnover. This system could also catalyze alkyne hydroaminoalkylation. The yield of α,β,γ-allylic amine obtained could be improved by using more electron-deficient arylamines as amine substrates to suppress the hydroamination side-reaction. Several electron-donating and electron-withdrawing groups were tolerated on both the amine and alkyne substrates to give the desired products. Future directions currently being carried out by Mr. Erick Nuñez Bahena focus on a detailed investigation of the mechanism of the reaction, including the specific role that the tethered bis(ureate) ligand plays in promoting catalytic turnover. These mechanistic insights will be used to modify ligand design to enhance activity, regioselectivity, and stereoselectivity for this hydroaminoalkylation reaction that offers a new disconnection for making allylic amines.

Chapter 4: Vanadium Pyridonate Complexes: Aggregation, Redox Behaviour, and Metal-Ligand Cooperativity

4.1 Introduction

As discussed in Chapter 1, pyridones, or 2-hydroxypyridines, are a broadly useful class of ligands for transition-metal-catalyzed reactions.[68,82,254] Anionic pyridonate ligands have been applied successfully to a variety of catalytic processes, including C−H activation,[85,86,93,112,117−126,243,255−258] dehydrogenation,[259−269] and hydrogenation[259–261,267,268,270–272] reactions. Key to the utility of these ligands is their tendency to engage in metal-ligand cooperativity and hemilability, owing to the unsymmetrical nature of the *N*,*O* donors (Scheme 4.1).[68] In addition to the activation of C−H bonds as highlighted in Figure 1.9, metal-ligand cooperativity in pyridonate complexes has enabled the activation of a variety of E−H bonds to promote catalytic turnover, such as O−H,[262,264,266,267,269] N−H,[259–261] and H−H bonds.[271,272] While proton shuttling is the most common manifestation of this reactivity, the pyridonate may act cooperatively as a Lewis base to other elements like boron.[273] The hemilabile character of these ligands can also promote catalysis by changing the binding mode to stabilize coordinatively-unsaturated intermediates or create an empty coordination site for incoming substrates.[68,83] Pyridonate catalysts of both early- and late-transition-metals are known and the specific role of the ligand differs depending on the system, demonstrating the versatility of these 1,3-*N*,*O*-chelating ligands.

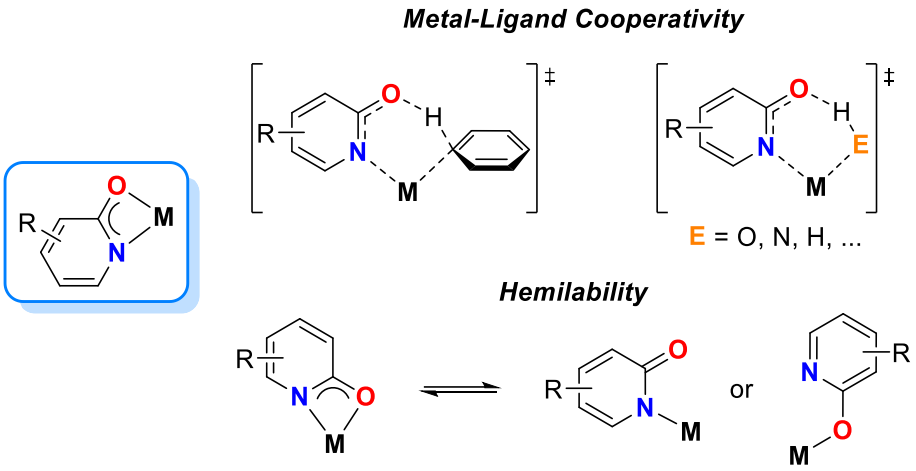

Scheme 4.1 Versatile functionality of pyridonate ligands

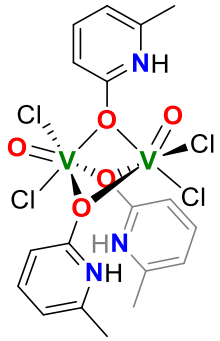

Figure 4.1 The only reported vanadium pyridone or pyridonate complex

Despite the breadth of pyridonate-ligated complexes and catalysts that have been reported, vanadium pyridonate complexes are rare and the fundamental coordination chemistry of this class of compounds is unexplored. In fact, only one pyridone or pyridonate complex of vanadium has been reported; Cotton and co-workers synthesized a dinuclear vanadium(IV) complex containing three neutral μ_2-O pyridone ligands (Figure 4.1).[274] As a result, the factors that influence the aggregation, redox chemistry, and metal-ligand cooperativity of vanadium pyridonate complexes specifically are not well-understood. Gaining a better understanding of these factors could lead to the development of improved catalysts utilizing earth-abundant vanadium for various transformations, including (but not limited to) hydroamination and hydroaminoalkylation (Figure

4.2).[275,276] Thus, we set out to synthesize heteroleptic vanadium(IV) and vanadium(III) pyridonate complexes in order to gain insight into their structure and reactivity. We hypothesized that the interaction of such complexes with amines would provide insight into the coordination chemistry and reactivity of vanadium pyridonates with respect to aggregation, redox behaviour, and metal-ligand cooperativity.

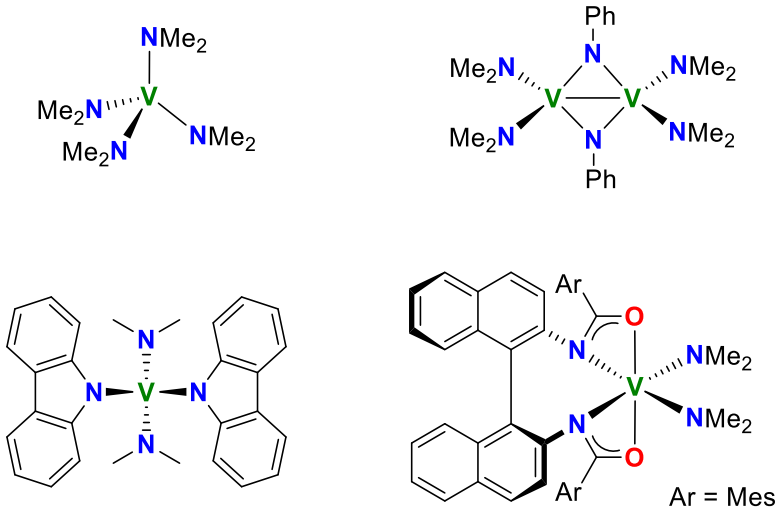

Figure 4.2 Known hydroamination and hydroaminoalkylation vanadium catalysts

4.2 Synthesis of Bis(pyridonate)vanadium(IV) Complexes

Several bis(pyridonate) complexes of vanadium were synthesized (Scheme 4.2). Previously, it has been shown that bis(amidate)bis(amido) complexes of vanadium(IV) can be readily synthesized from $V(NMe_2)_4$ and 2 equiv. of amide.[276] Moreover, the analogous protonolysis reaction with $Ti(NMe_2)_4$ and pyridones has been shown by the Schafer group to be an efficient route to bis(pyridonate)bis(amido)titanium(IV) complexes.[93] Pyridones **4.1-4.3** were chosen as they are commercially available. Then, $V(NMe_2)_4$ was reacted with 2 equiv. of pyridone in toluene to afford compounds **4.4-4.6** in moderate to good yields as red crystals after crystallization from a concentrated hexanes solution at −35 °C (Scheme 4.2). Alternatively, these

compounds can be isolated in quantitative yields as red powders. The structures of the resultant complexes were confirmed by X-ray crystallography (Figure 4.3). Each solid-state molecular structure has a distorted octahedral geometry with C_2 symmetry, *trans*-O donors, and *cis*-amido ligands as observed in analogous titanium complexes.[93] Alternatively, the tight bite angle pyridonate ligand can be considered to occupy one coordination site, giving the complex a pseudo-tetrahedral geometry; however, here the pyridonates will be considered to occupy two coordination sites as described above. The actual geometry is likely something in between, as evidenced by the N–V–N_{avg} angle of the amido ligands (96.23(7)°). The O-V-O angle in **4.6** (150.79(9)°) is slightly larger than that in **4.4** and **4.5** (145.26(4)° and 145.82(4)°, respectively), likely to accommodate the sterically-imposing 6-methyl substituent. Only minor differences in bond lengths are observed between the three complexes, and distances for the V−N_{avg} (2.231(2) Å) and V−O_{avg} (2.010(1) Å) bonds to the *N*,*O*-chelated ligands are longer and shorter, respectively, compared to those of a related V(IV) bis(amidate) complex (V−N, 1.978(2); V−O, 2.149(2) Å).[276] This is indicative of more anionic character on the oxygen versus the nitrogen for the pyridonate ligand, and this trend is seen with Ti(IV) as well.[93,100] This result is not unexpected, as it allows for the aromatic character of the pyridyl ring to be maintained.

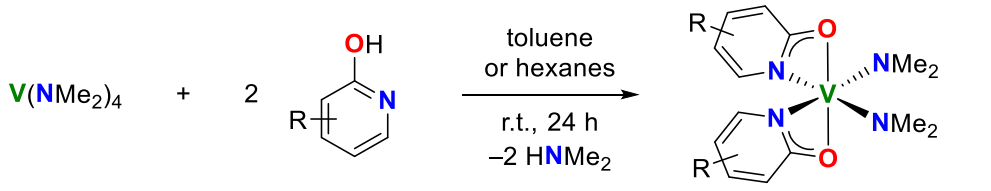

4.1: R = H
4.2: R = 3-Me
4.3: R = 6-Me

4.4: 70% yield; μ_{eff} = 2.04 μ_B
4.5: 55% yield; μ_{eff} = 1.97 μ_B
4.6: 66% yield; μ_{eff} = 2.07 μ_B

Scheme 4.2 Synthesis of bis(dimethylamido)bis(pyridonate)vanadium(IV) complexes

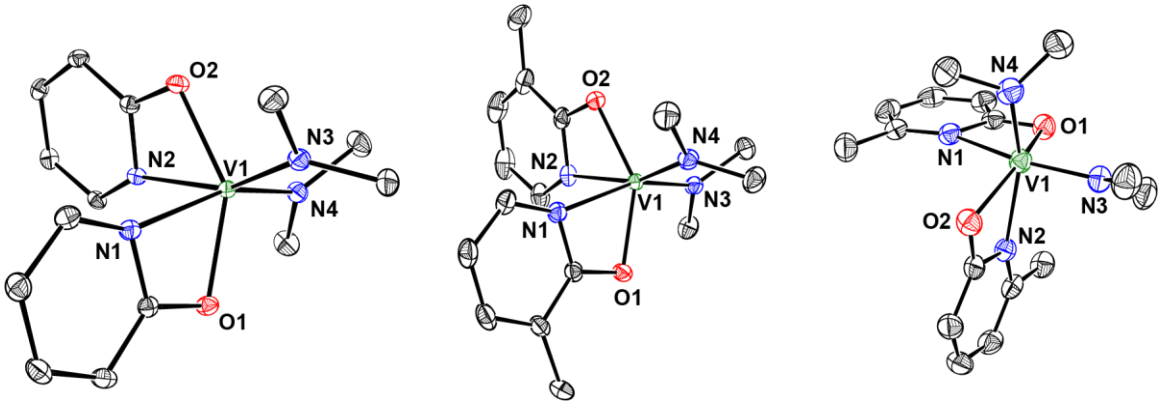

Figure 4.3 ORTEP representations of complexes **4.4** (left), **4.5** (middle), and **4.6** (right) with ellipsoids shown at 50% probability and hydrogen atoms omitted for clarity. Selected bond lengths (Å) and angles (°) for **4.4**: V1–N1, 2.2118(12); V1–O1, 2.0125(9); O2–V1–O1, 145.26(4); N4–V1–N3, 97.01(5); N4–V1–N3, 97.01(5). Selected bond lengths (Å) and angles (°) for **4.5**: V1–N1, 2.2169(10); V1–O1, 2.0063(9); O1–V1–O2, 145.82(4); N4–V1–N3, 96.26(5). Selected bond lengths (Å) and angles (°) for **4.6**: V1–N1, 2.253(3); V1–O1, 2.005(2); O1–V1–O2, 150.79(9); N3–V1–N4, 95.42(12)

In terms of the electronic properties of the vanadium centre, the range of μ_{eff} values obtained for these paramagnetic complexes (1.97-2.07 μ_B, C_6D_6 solution, 25 °C) is consistent with a V(IV) centre with one unpaired *d*-electron ($\mu_{(spin\text{-}only)}$ = 1.73 μ_B). Additionally, Density-Functional Theory (DFT) calculations on each complex (B3LYP/6-311++G(d,p)') show that the unpaired spin density is localized entirely on the metal centre (Figure 4.4), consistent with previous studies by the Schafer group on a related Ti(III) pyridonate complex.[277] Taking further inspiration from these studies, in which tris(pyridonate)titanium(IV) complexes could be reduced with a simple amine (Scheme 4.3),[277] we looked to explore the redox chemistry of these vanadium(IV) complexes through reactivity with pyridones and amines.

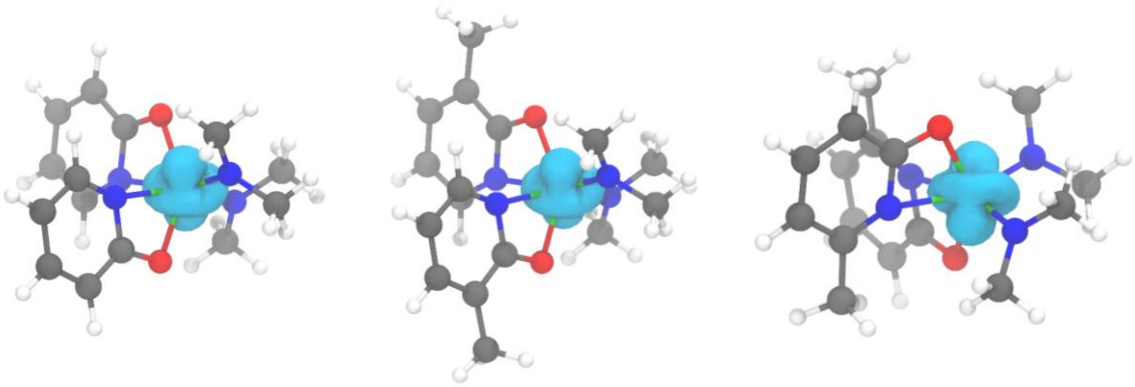

Figure 4.4 Spin density plots of complexes **4.4** (left), **4.5** (middle), and **4.6** (right) obtained from their optimized structures (B3LYP/6-311++G(d,p)', spin density = cyan, isovalue = 0.01)

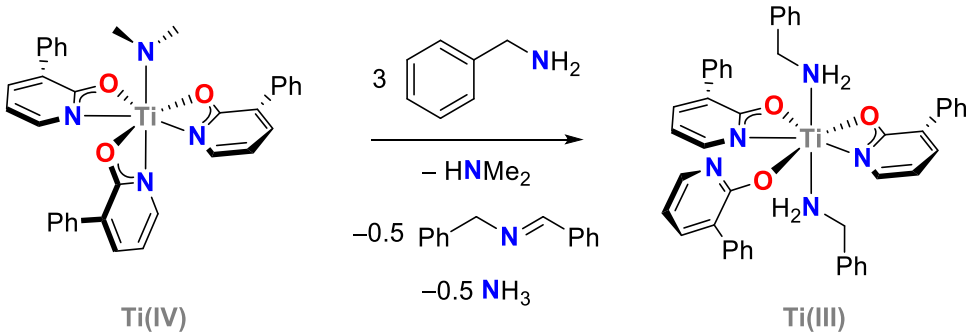

Scheme 4.3 Reduction of a Ti(IV) pyridonate using benzylamine by the Schafer group

4.3 Synthesis of Tris(pyridonate)vanadium(III) Complexes

Next, we attempted the synthesis of dimethylamidotris(pyridonate)vanadium(IV) complexes.[277] When $V(NMe_2)_4$ was reacted with 3 equiv. of pyridone **4.3** (Scheme 4.4), the red solution turned dark green over the course of hours. However, during workup this green solution gradually changed to gold-orange with concomitant precipitation of an insoluble pink powder that was initially difficult to characterize but was later identified as tris(pyridonate)vanadium(III) dimer **4.7** (*vide infra*) rather than the expected V(IV) complex. Additionally, orange crystals of monomeric dimethylamine-coordinated complex **4.8** suitable for X-ray diffraction studies could

be obtained from the same reaction mixture in trace quantities, and the solid-state molecular structure is shown (Figure 4.5).

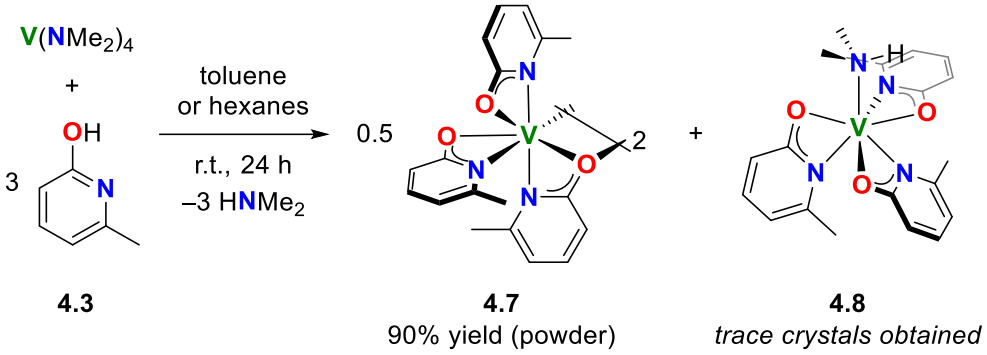

Scheme 4.4 Synthesis of tris(pyridonate)vanadium(III) complexes

Complex **4.8** is seven-coordinate with distorted pentagonal bipyramidal geometry and C_1 symmetry. In this case, the variable C-V-C angles between the pyridonate ligands (C1–V1–C13, 122.96(5)°; C7–V1–C13, 124.39(5)°; C7–V1–C1, 104.56(5)°) render a tetrahedral description unreasonable. The V1−N4 bond distance (2.1885(13) Å) is comparable to the V−N bonds of the pyridonate ligands (V−N_{avg}, 2.1693(13) Å) and significantly longer than the V−N bonds of the π-donating amido ligands in complex **4.6** (V−N_{avg}, 1.861(3) Å). It is also similar in length to the V−N bond of a previously reported V(III) ammine complex (2.1623(8) Å).[278] Furthermore, the geometry about N4 ($\sum\theta_{N4}$ = 338.99(11)°) suggests more sp^3-hybrid character than sp^2-hybrid character. These data support our assignment of a neutral-donor amine ligand versus an anionic amido ligand. Therefore, the oxidation state of V is cautiously assigned as V(III) (S = 1). Sufficient quantities of material for more rigorous characterization could not be obtained. This assignment is also supported by DFT calculations; a thermochemical comparison of the two possible spin states for V(III) complex **4.8** reveals that the triplet spin state is greatly favoured over the diamagnetic singlet spin state by an energy difference of 34.7 kcal/mol (see Appendix B). Once again, the

computed structure of **4.8** shows that all the unpaired spin is localized on the vanadium centre (Figure 4.6). Importantly, the observation of this complex suggests that dimeric **4.7** may be broken up into monomeric species in the presence of neutral amine donors.

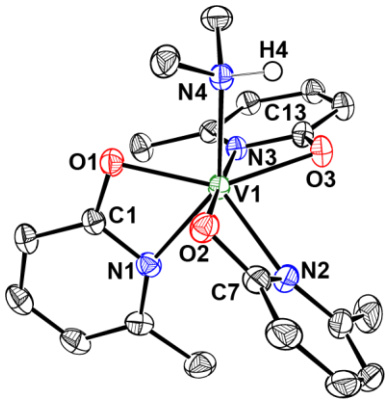

Figure 4.5 ORTEP representation of complex **4.8** with ellipsoids shown at 50% probability and hydrogen atoms (except for the N–H) omitted for clarity. Selected bond lengths (Å) and angles (°): V1–N1, 2.1972(13); V1–O1, 2.0463(11); V1–N4, 2.1885(13); C1–V1–C13, 122.96(5); C7–V1–C13, 124.39(5); C7–V1–C1, 104.56(5)

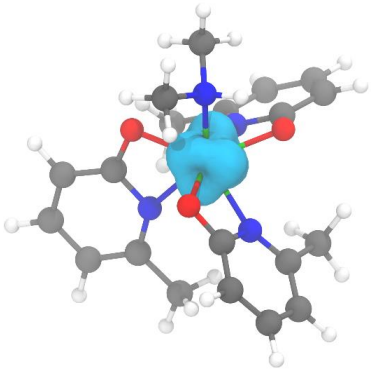

Figure 4.6 Spin density plot of complex **4.8** obtained from its optimized structure (B3LYP/6-311++G(d,p)', spin density = cyan, isovalue = 0.01)

Hypothesizing that the formation of **4.8** resulted from coordination of trace amounts of dimethylamine to a tris(pyridonate)vanadium(III) complex in solution, a route to access such a

species was proposed. Trimesityl complex **4.9**[279] (Scheme 4.5) is a reliable precursor to vanadium(III) complexes[280–282] and would allow direct access to a tris(pyridonate)vanadium(III) species. However, rather than obtaining the expected monomeric product, the protonolysis reaction between complex **4.9** and pyridone **4.3** gave dimeric tris(pyridonate)vanadium(III) complex **4.7** (Scheme 4.5). Complex **4.7** was produced in 87% yield and was fully characterized including by X-ray crystallography, NMR, MS, and EA. Although assignment of the ^{1}H NMR chemical shifts is ambiguous for this paramagnetic complex, the identity of **4.7** was confirmed using X-ray crystallography (*vide infra*). Importantly, the ^{1}H NMR chemical shifts matched those of the pink powder formed in Scheme 4.4, confirming that both routes access dimer **4.7**. Thus, through the simple protonolysis reaction outlined in Scheme 4.4 using commercially available starting materials, the V(IV) starting material is reduced to V(III). The mechanism of this process is explored in a later section.

The reaction of isolated V(IV) complex **4.6** with 1 equiv. **4.3** produces the same result when monitored by ^{1}H NMR spectroscopy. Additionally, performing the same reaction as shown in Scheme 4.4 with pyridones **4.1** and **4.2** did not result in crystalline material, however MS analysis supported the formation of a dimeric tris(pyridonate)vanadium(III) complex for the reaction with **4.2** (750 *m/z*).

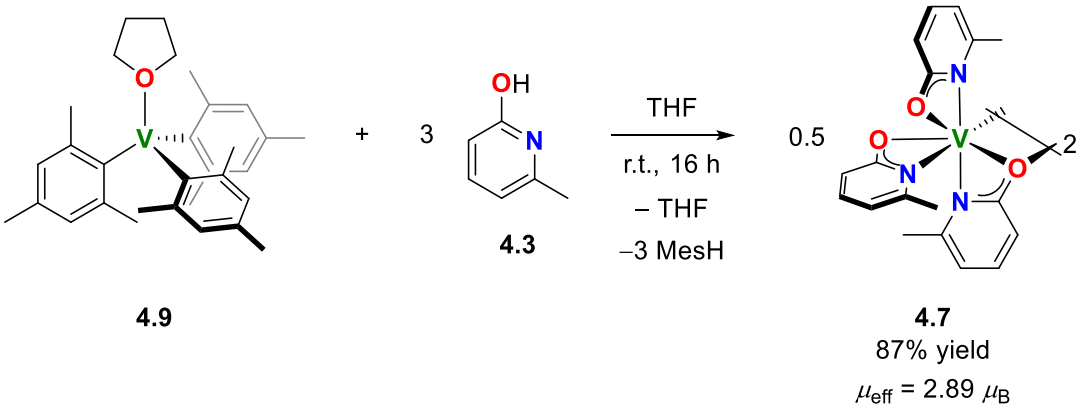

Scheme 4.5 Organometallic synthetic route to dimeric V(III) complex **4.7**

Crystals of **4.7** obtained from a saturated THF solution were suitable for X-ray diffraction and the solid-state molecular structure is depicted (Figure 4.7). Dimeric complex **4.7** is C_2 symmetric, with each V being seven-coordinate and having distorted pentagonal bipyramidal geometry. All six pyridonates are bound κ^2, with the two central ligands also bridging through the oxygen to the adjacent V centre (μ_2-O), exhibiting a κ^2:μ_2 bridging mode.[283–285] The μ_2-O interaction is unsymmetrical (V2−O3, 2.184(3) Å; V1−O3, 2.078(3) Å). The oxidation state of V in **4.7** can be definitively assigned as V(III); this was verified using Evans' Method,[286–288] where paramagnetic **4.7** gives μ_{eff} = 2.89 μ_B (C_6D_6 solution, 25 °C), consistent with two unpaired *d*-electrons ($\mu_{(spin\text{-}only)}$ = 2.83 μ_B). Preliminary electrochemical data for **4.7** in THF solution obtained via cyclic voltammetry (CV) indicate a complex series of redox events, including unidentified, irreversible chemical changes associated with both oxidation and reduction. A more thorough investigation by CV and other electrochemical techniques is needed to assign the redox processes involved and provide experimental insight into possible intermediate species.

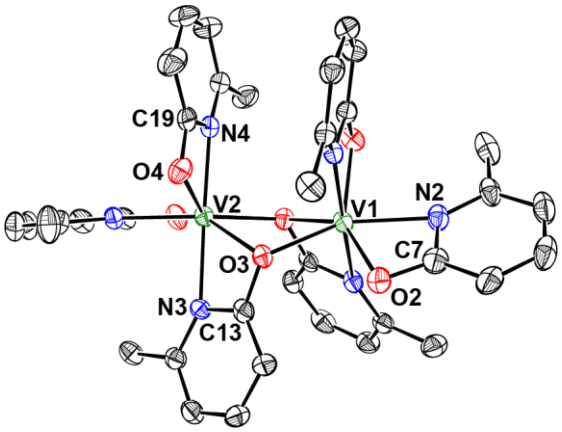

Figure 4.7 ORTEP representation of complex **4.7** with ellipsoids shown at 50% probability and hydrogen atoms omitted for clarity. Selected bond lengths (Å) and angles (°): V1−N2, 2.167(4); V2−N3, 2.170(4); V2−N4, 2.101(4); V1−O2, 2.053(3); V2−O3, 2.184(3); V1−O3, 2.078(3); V2−O4, 2.060(3); O2−V1−N2, 63.18(15); V1−O3−V2, 102.67(13)

To further demonstrate that dimeric **4.7** can be broken up into monomeric species in the presence of neutral donors, 4-dimethylaminopyridine (DMAP) was introduced to a toluene solution of **4.7** to produce complex **4.10** as a poorly soluble, yellow-orange powder (Scheme 4.6). Recrystallization from hot THF gave yellow crystals suitable for X-ray diffraction studies, and the solid-state molecular structure is shown (Figure 4.8). Like **4.8**, complex **4.10** is seven-coordinate with distorted pentagonal bipyramidal geometry, however two of the pyridonate ligands are now co-planar and the molecule is C_s symmetric in the solid state. This change in orientation of the pyridonate ligands further illustrates the flexibility of pyridonates in supporting coordination isomerism. The V1−N4 bond distance (2.1066(10) Å) is shorter than that in **4.8** (2.1885(13) Å) as the pyridyl nitrogen of DMAP has increased anionic character due to electron donation from the *para*-dimethylamine substituent. Complex **4.10** gives μ_{eff} = 3.00 μ_B (C_6D_6 solution, 25 °C), which is consistent with a triplet V(III) centre with two unpaired *d*-electrons ($\mu_{(spin\text{-}only)}$ = 2.83 μ_B). Overall, despite the tendency to aggregate upon reduction, monomeric pyridonate complexes can

be obtained using neutral donors. This is relevant to catalytic processes where incoming substrates need to coordinate the metal centre. In such cases, monomeric intermediates would result.

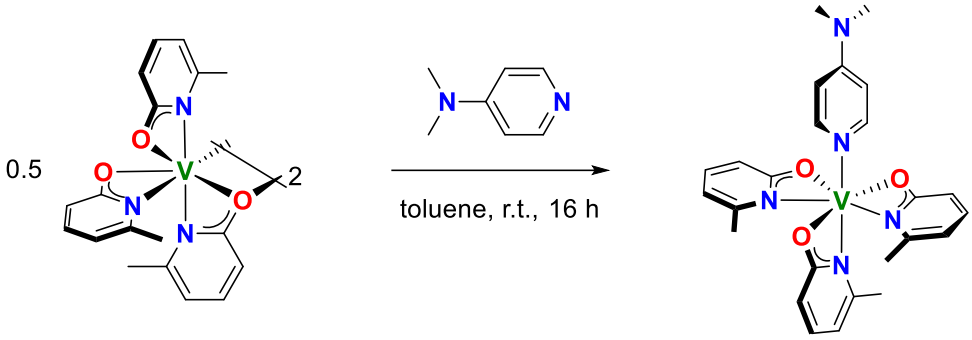

4.7 **4.10**, 84% yield

Scheme 4.6 Synthesis of DMAP-coordinated V(III) complex **4.10**

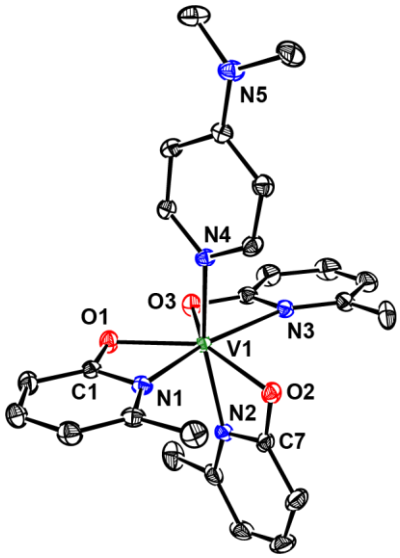

Figure 4.8 ORTEP representation of complex **4.10** with ellipsoids shown at 50% probability and hydrogen atoms omitted for clarity. Selected bond lengths (Å) and angles (°): V1–N1, 2.2350(10); V1–O1, 2.0694(9); V1–N4, 2.1066(10)

4.4 Comparison to a Bis(amidate)vanadium(IV) Complex

After observing facile reduction of V(IV) to V(III) through protonolysis with pyridone, we questioned whether related bis(amidate) vanadium(IV) complexes would exhibit similar reactivity.

To test this, the vanadium analogue of a known Schafer hydroamination catalyst[100] was synthesized: $V(NMe_2)_4$ was reacted with 2 equiv. of amide **4.11** in hexanes to produce bis(amidate) complex **4.12** in quantitative yield (Scheme 4.7). The identity of this complex was confirmed by X-ray crystallography and displays comparable bond and angle metrics to the analogous titanium structure (Figure 4.9).[100] Subsequent reaction of this complex with another equiv. of amide **4.11** and monitoring by ^{1}H NMR spectroscopy shows no reaction at all at room temperature (Scheme 4.8). This shows that reduction occurs more easily in the case of pyridonates, likely due to the comparatively large steric bulk of the amidate ligands preventing protonolysis with the free amide. Nevertheless, the pyridonate complexes show unique behaviour in their tendency to be reduced from V(IV) to V(III).

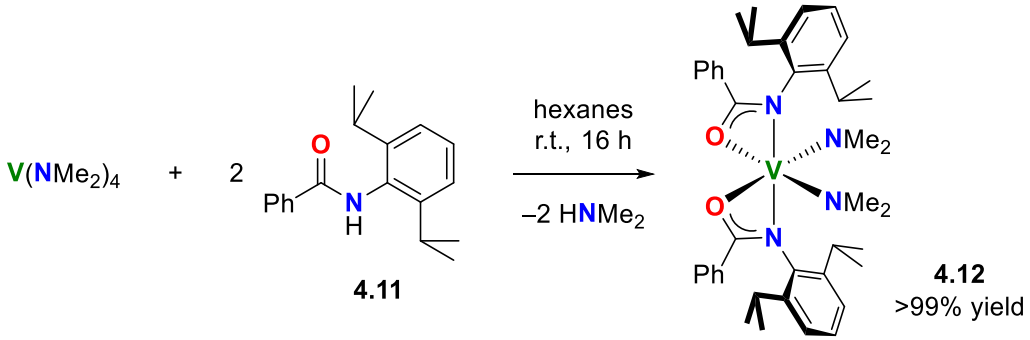

Scheme 4.7 Synthesis of bis(amidate)bis(dimethylamido)vanadium(IV) complex **4.12**

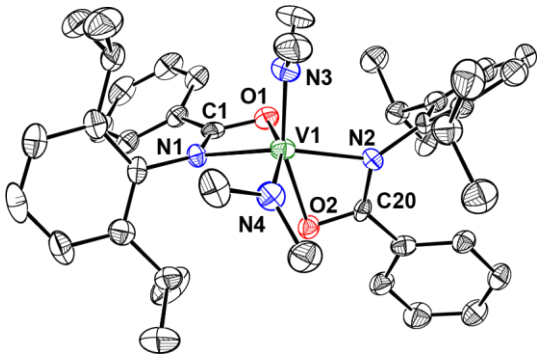

Figure 4.9 ORTEP representation of complex **4.12** with ellipsoids shown at 50% probability and hydrogen atoms omitted for clarity. Selected bond lengths (Å) and angles (°): V1–O1, 2.154(3); V1–N1, 2.072(4); V1–N4, 1.859(4); N1–V1–N2, 145.38(16)

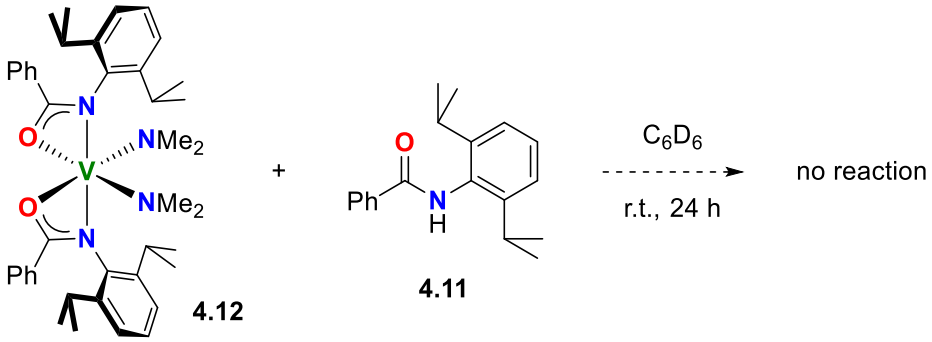

Scheme 4.8 Attempted reaction of **4.12** with 1 equiv. of amide proligand **4.11**

4.5 Comparison to a Bulkier Pyridonate Ligand

As the reduction of the V(IV) pyridonate complexes to V(III) species results in aggregation in the absence of neutral donors, we sought to evaluate if a monomeric tris(pyridonate)vanadium(III) complex could be obtained. It was hypothesized that a more sterically demanding pyridonate ligand would force the complex to form a monomeric species upon reduction. Thus, $V(NMe_2)_4$ was reacted with 3 equiv. of 3-mesityl substituted pyridonate **4.13** in toluene (Scheme 4.9), producing a green solution overnight as observed in the synthesis of **4.7** (*vide supra*). After workup, recrystallization of the brown-yellow solid in toluene at −35 °C

afforded gold crystals suitable for X-ray diffraction; the solid-state molecular structure is shown, confirming reduction to V(III) (Figures 4.10 and 4.11). Interestingly, complex **4.14** is still dimeric but adopts an unsymmetrical paddle-wheel type structure to accommodate the extra steric bulk of the mesityl substituents. Four of the pyridonates bridge the two metal centres via κ^1-*N*, κ^1-*O* binding modes while the other two pyridonates each coordinate to one vanadium centre via the usual κ^2-*N*,*O* binding mode. The large C-O-V angle of the bridging pyridonates (C6−O2−V2, 161.34(18)°) gives rise to the paddle-wheel structure and results in a large V1−V2 distance (3.338 Å (calcd)).[289] Even though the pyridonate ligands are sterically large in this case, the complex still aggregates upon reduction in the absence of neutral donors. Once again, this highlights the flexibility of the pyridonate ligands in adopting different binding modes. With a better understanding of the behaviour of V(IV) and V(III) pyridonate complexes, we then turned our attention to gaining insight into the mechanism of the reduction process.

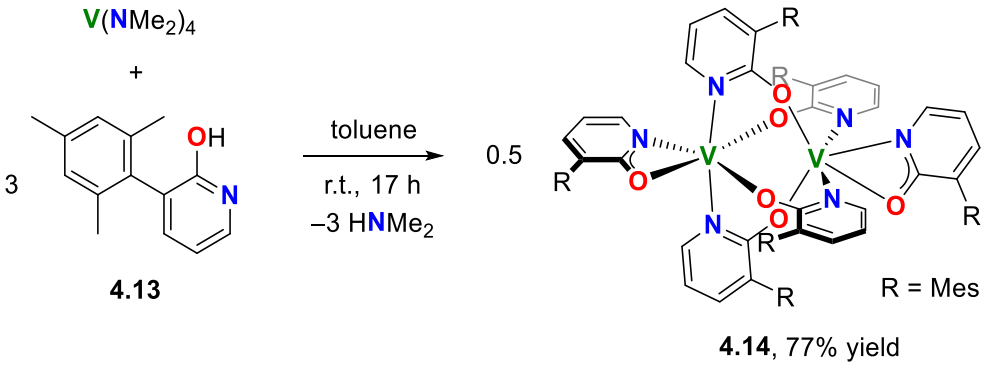

Scheme 4.9 Synthesis of Bulky V(III) Pyridonate Complex **4.14**

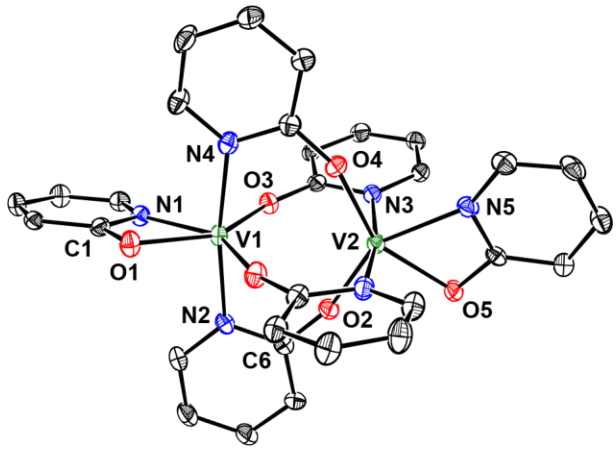

Figure 4.10 ORTEP representation of complex **4.14** with ellipsoids shown at 50% probability and mesityl groups and hydrogen atoms omitted for clarity. Selected bond lengths (Å) and angles (°): V1–N1, 2.141(2); V1–O1, 2.0436(18); V1–N4, 2.117(2); V2–O2, 1.9322(18); C6−O2−V2, 161.34(18)

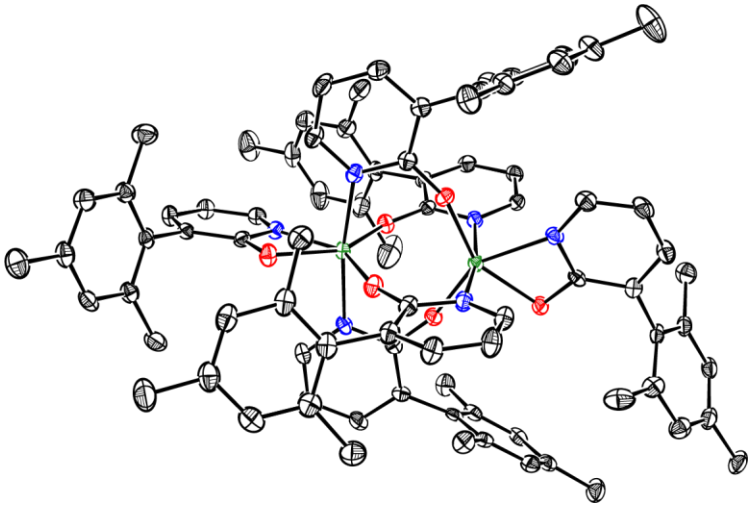

Figure 4.11 ORTEP representation of complex **4.14** with ellipsoids shown at 50% probability and hydrogen atoms omitted for clarity

4.6 Reduction of Vanadium(IV) Pyridonates with Alkylamines

Lastly, the mechanism of 1-electron reduction from V(IV) to V(III) was investigated. The reduction of early-transition-metal complexes with simple amines is known[290] and has been

observed in a related Ti pyridonate complex (Scheme 4.3).[277] Therefore, we hypothesized that the released dimethylamine upon protonolysis with pyridone was acting as the reductant in the subsequent reduction process. As products derived from dimethylamine oxidation were not observed by ^{1}H NMR or GC-MS, pyrrolidine was used as a dimethylamine surrogate. Mildly heating a red hexanes solution of complex **4.6** in the presence of 10 equiv. of pyrrolidine produced an orange solution from which dark orange crystals were obtained (Scheme 4.10). X-ray diffraction studies confirmed the formation of monomeric bis(pyridonate)mono(pyrrolidido)mono(pyrrolidine)vanadium(III) complex **4.15** (Figure 4.12). Complex **4.15** is structurally similar to V(IV) complex **4.6** with distorted octahedral geometry, but with one amine ligand instead of a second amido ligand. This is clearly indicated by the much longer V1−N4 bond distance (2.193(4) Å) compared to V1−N3 (1.891(4) Å), consistent with a neutral amine donor and a π-donating amido ligand, respectively. This V1−N4 distance is also similar to that in dimethylamine complex **4.8** (2.1885(13) Å). Additionally, assignment of **4.15** as a V(III) species is supported by solution phase data giving μ_{eff} = 2.82 μ_B (C_6D_6 solution, 25 °C), consistent with a triplet V(III) centre with two unpaired *d*-electrons ($\mu_{(\text{spin-only})}$ = 2.83 μ_B). Furthermore, carrying out the same reaction in an NMR tube and monitoring by ^{1}H NMR spectroscopy showed the appearance of multiplets at 7.27, 3.70, 1.89, and 1.27 ppm integrating to 1:2:2:2, respectively, supporting the formation of pyrroline as an oxidized byproduct.[291] All these data strongly suggest that the presence of amine in solution is responsible for reducing the V(IV) pyridonate complex to V(III). A plausible mechanism for this process is outlined in Scheme 4.11. First, transamination with pyrrolidine produces another V(IV) bis(amido) complex **F**. Then, another equiv. of pyrrolidine can lose 1 e^- and 1 H^+ × 2 to reduce 2 equiv. of **F** to mono(amido) V(III) complex **G**, releasing pyrroline and 2 equiv. of pyrrolidine. It may be the case that the

reduction of **F** to **G** involves the formation of multimetallic intermediates. Finally, pyrrolidine can coordinate to intermediate **G** to give complex **4.15**. LIFDI-MS data for **4.15** show fragments for both **G** (337 *m/z*) and the corresponding dimer **G'** (674 *m/z*), suggesting these are reasonable intermediates. Notably, elemental analysis after subjecting **4.15** to vacuum overnight showed no decomposition to other species, indicating that the neutral pyrrolidine is bound strongly to the vanadium centre.

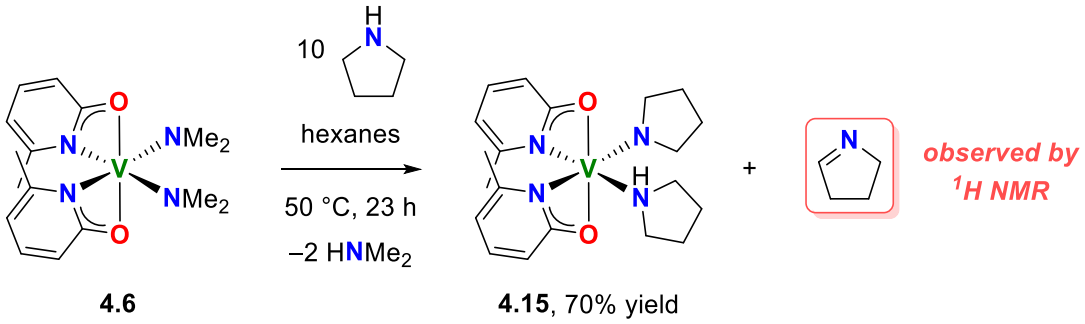

Scheme 4.10 Reduction of V(IV) complex **4.6** via heating with excess pyrrolidine

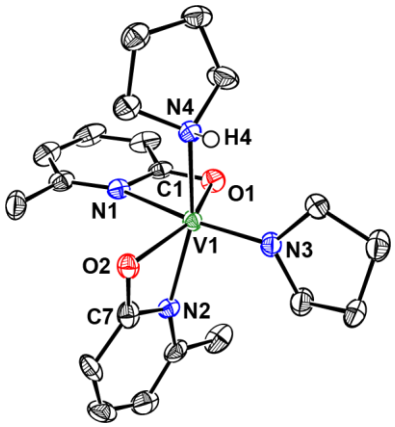

Figure 4.12 ORTEP representation of complex **4.15** with ellipsoids shown at 50% probability and hydrogen atoms (except for N–H) omitted for clarity. Selected bond lengths (Å) and angles (°): V1–N1, 2.225(4); V1–O1, 2.061(3); V1–N3, 1.891(4); V1–N4, 2.193(4)

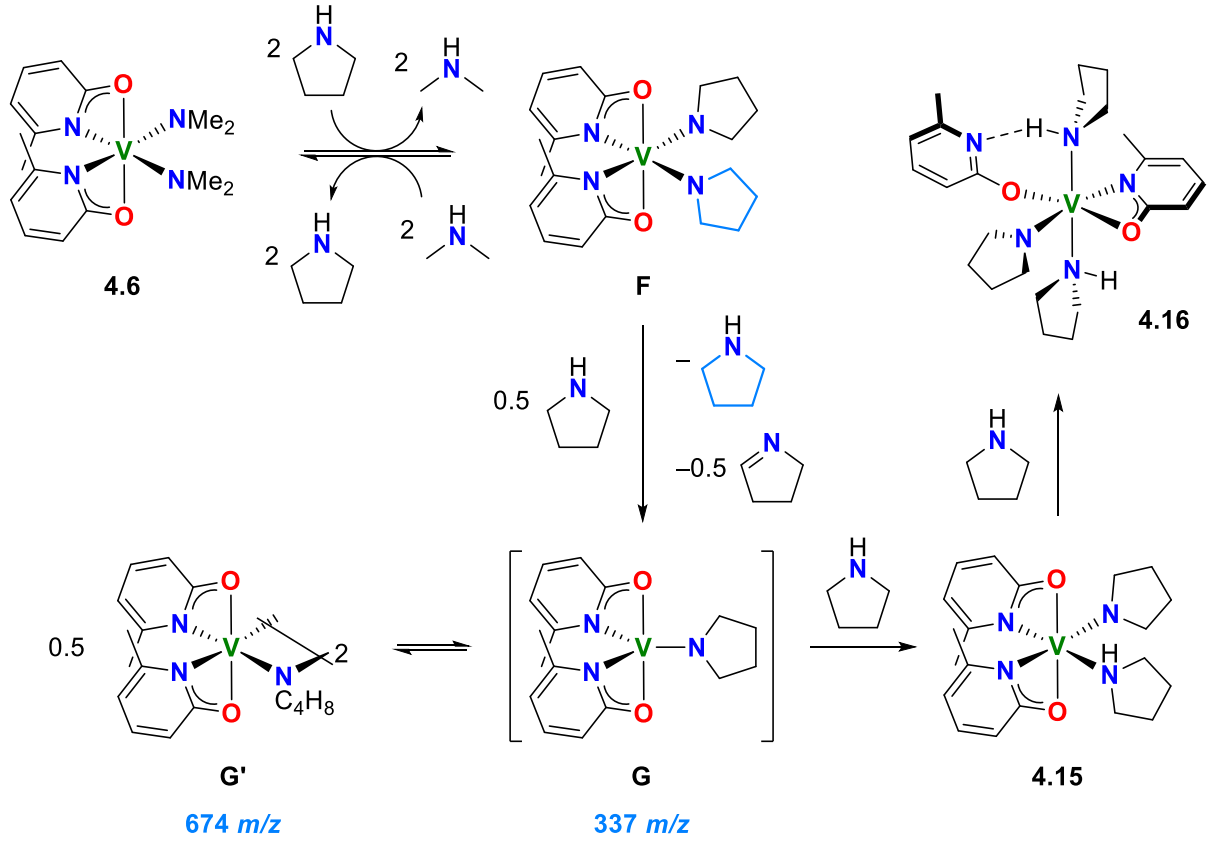

Scheme 4.11 Proposed mechanism of V(IV) reduction by pyrrolidine involving proposed intermediates **F**, **G**, and **G'**

In an attempt to synthesize and isolate proposed intermediate **F**, another reduced product was formed (Scheme 4.12). After repeatedly adding and removing *in vacuo* aliquots of pyrrolidine and hexanes, a mixture of dark orange solids was achieved from which crystals of complex **4.16** suitable for X-ray diffraction could be obtained (Figure 4.13). Complex **4.16** has distorted octahedral geometry and results from coordination of a second equiv. of pyrrolidine to **4.15** (Scheme 4.11). To accommodate the extra neutral donor, one pyridonate ligand adopts a κ^1-*O* binding mode to open a coordination site at vanadium and form a hydrogen-bonding interaction with the neutral amine (N2–H3, 2.185 Å (calcd)). This behaviour once again highlights the hemilability and metal-ligand cooperativity of pyridonates. Both V1−N4 and V1−N3 have

comparable bond distances (2.1781(10) Å and 2.1799(11) Å, respectively) and are significantly longer than V1−N5 (1.8755(11) Å), similar to complex **4.15**. The V1−O2 distance (2.0207(9) Å) is also shorter than V1−O1 (2.1267(9) Å), likely due to increased π-donation from the κ^1-*O* pyridonate. Overall, these data further demonstrate the versatility of pyridonates in forming various binding geometries and assisting in ligand coordination.

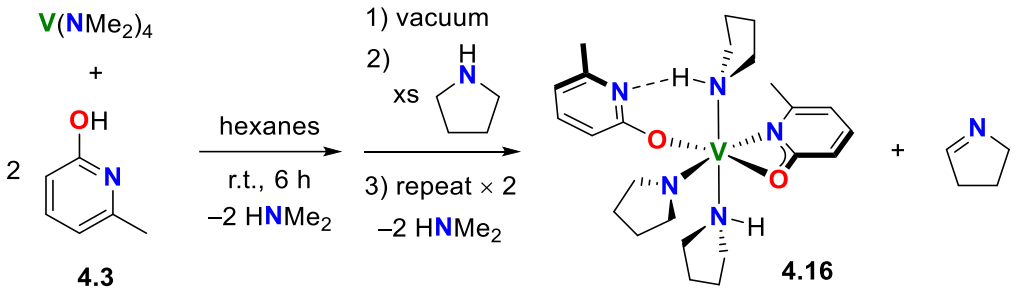

Scheme 4.12 Reduction of V(IV) via sequential additions of excess pyrrolidine

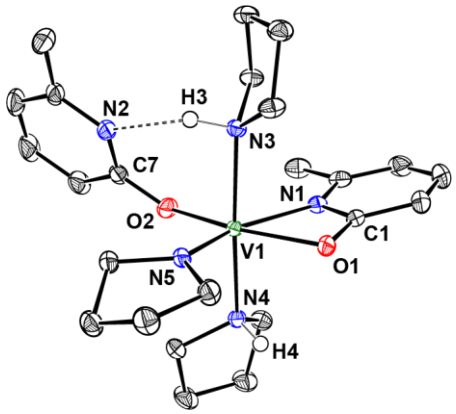

Figure 4.13 ORTEP representation of complex **4.16** with ellipsoids shown at 50% probability and hydrogen atoms (except for N–H) omitted for clarity. Selected bond lengths (Å) and angles (°): V1–N1, 2.2125(11); V1–O1, 2.1267(9); V1–O2, 2.0207(9); V1–N3, 2.1781(10); V1–N4, 2.1799(11); V1–N5, 1.8755(11); C7–O2–V1, 136.24(9)

4.7 Attempts at Catalytic Amine Synthesis with Vanadium

As described in Chapter 1, the Schafer bis(amidate) titanium catalyst in Figure 1.7 is proficient for the hydroamination of alkynes with high *anti*-Markovnikov selectivity.[100–109] Since complex **4.12** is a vanadium analogue of the Schafer catalyst, it was hypothesized that it would also show catalytic activity for alkyne hydroamination. As a benchmark test reaction, the hydroamination of phenylacetylene with aniline was attempted with 10 mol% of catalyst **4.12** (Scheme 4.13). Unfortunately, after heating at 65 °C for 75 h, only 21% conversion to the hydroamination product was achieved; to put this into context, under similar conditions the corresponding titanium catalyst can reach full conversion within 30 min for the same transformation.[105] Likewise, the reaction between alkylamine substrate *tert*-butylamine with an internal alkyne showed no reactivity at all using catalyst **4.12**. The lower activity of vanadium hydroamination catalysts compared to their titanium counterparts is known[275] and is likely due to the increased Lewis acidity of the Ti(IV) centre. Notably, while vanadium catalysts are usually highly regioselective for the Markovnikov product,[275] using catalyst **4.12** resulted in exclusive formation of the *anti*-Markovnikov product, as is observed with the Schafer titanium catalyst. Despite the lower reactivity, this demonstrates the importance and utility of the 1,3-*N*,*O*-chelating ligand in providing exquisite regiocontrol in hydroamination reactions.

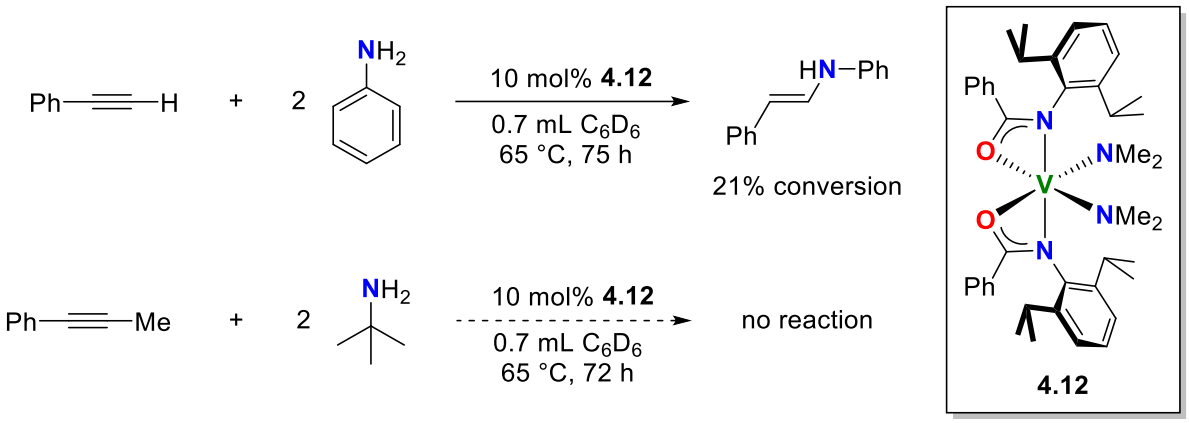

Scheme 4.13 Hydroamination of phenylacetylene using catalyst **4.12**

As mentioned in the introduction, vanadium has been reported to be catalytically active for hydroaminoalkylation as well (Figure 4.2). Specifically, Zi and co-workers reported that simple $V(NMe_2)_4$ was active for the hydroaminoalkylation of norbornene with *N*-methylaniline, achieving 83% conversion to the aminated product after 48 h at 160 °C (Scheme 4.14).[276] It was thus hypothesized that introducing a 1,3-*N*,*O*-chelating ligand would improve the catalytic performance, as has been observed for other group 5 metals.[244,292] However, not only did adding any 1,3-*N*,*O*-chelating ligand not improve the reaction performance, the results described by Zi and co-workers shown in Scheme 4.14 could not be reproduced; using identical conditions, only a 9% conversion to the hydroaminoalkylation product could be achieved. Overall, vanadium does not appear to be an effective metal for use in catalytic hydroaminoalkylation. This may be due to catalyst decomposition at the elevated temperatures required for the reaction, where the excess amine may irreversibly reduce the V(IV) centre to an unreactive species.

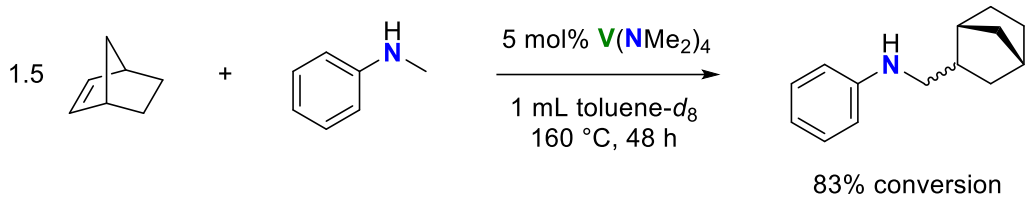

Scheme 4.14 Vanadium-catalyzed hydroaminoalkylation reported by Zi and co-workers

4.8 Conclusions

In summary, several vanadium(IV) and vanadium(III) pyridonate complexes were synthesized and their structures and reactivity were investigated. Bis(amido)bis(pyridonate)vanadium(IV) complexes were easily synthesized via protonolysis of tetrakis(dimethylamido)vanadium(IV) with 2 equiv. of pyridone. When a third equiv. of pyridone was added, an unexpected reduction occurred to produce a tris(pyridonate)vanadium(III) dimer. The identity of the dimer was confirmed through an alternative synthesis utilizing an organometallic V(III) precursor. This species was broken up into a monomeric complex *in situ* by dimethylamine and from the isolated dimer using DMAP as an amine surrogate. In contrast, a bis(amidate)bis(amido) complex did not result in reduction, likely due to steric bulk preventing protonolysis with free amide. Bulky pyridones could also be used to induce reduction, with the resulting species still being dimeric but adopting a paddle-wheel type structure to accommodate the steric bulk of the pyridonate ligands. Reactions of vanadium(IV) precursors with pyrrolidine indicated that the reduction to vanadium(III) is mediated by the free amine present in the protonolysis reactions. This led to bis(pyridonate) vanadium(III) complexes with either one or two neutral pyrrolidines coordinated, highlighting the hemilability and metal-ligand cooperativity of pyridonate ligands. Lastly, vanadium amido complexes displayed poor reactivity as catalysts for hydroamination and hydroaminoalkylation, likely due to deleterious reduction by the amine substrate under catalytic conditions. The insights gained in this study can be exploited by the

organometallic, inorganic, and organic chemistry communities to develop improved catalysts for various transformations. Specifically, catalytic transformations that may benefit from bimetallic intermediates and facile proton shuttling will be most relevant for vanadium pyridonate catalysts. The next chapter will discuss our efforts to apply vanadium pyridonate complexes in catalytic reactions, namely the reductive coupling of alcohols.

Chapter 5: Vanadium Pyridonates for the Catalytic Reductive Coupling of Alcohols

5.1 Introduction

The conversion of oxygen-rich, biomass-derived feedstocks to alternatively functionalized chemicals has been gaining interest due its potential as a renewable source of fuels and chemicals (Figure 5.1).[293–295] Numerous strategies have been developed to this end, including polyol dehydration,[296–298] deoxygenation,[299–308] and deoxydehydration (Scheme 5.1).[293,309–311] Each of these methods effects C−O bond cleavage to produce valuable chemical feedstocks for further functionalization. While the majority of deoxygenation reactions require the use of noble metal catalysts, the use of earth-abundant and inexpensive 3d metal catalysts for these transformations is desirable. To this end, vanadium catalysts have recently found use in catalytic deoxydehydration.[312–314] Key to promoting catalytic turnover is the ability to access reduced V(III) species to carry out the deoxygenation step. In order to generate these reactive intermediates, stoichiometric reductants such as Na_2SO_3, PPh_3, H_2, and CO are usually required, though occasionally the alcohol substrate can promote formation of reduced vanadium intermediates (*vide infra*).[312–314]

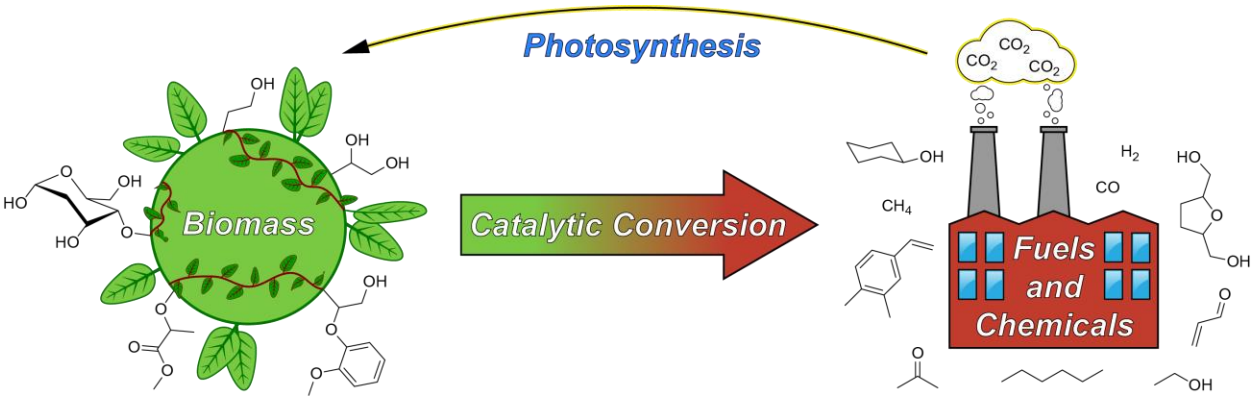

Figure 5.1 Biomass as a renewable source of fuels and chemicals

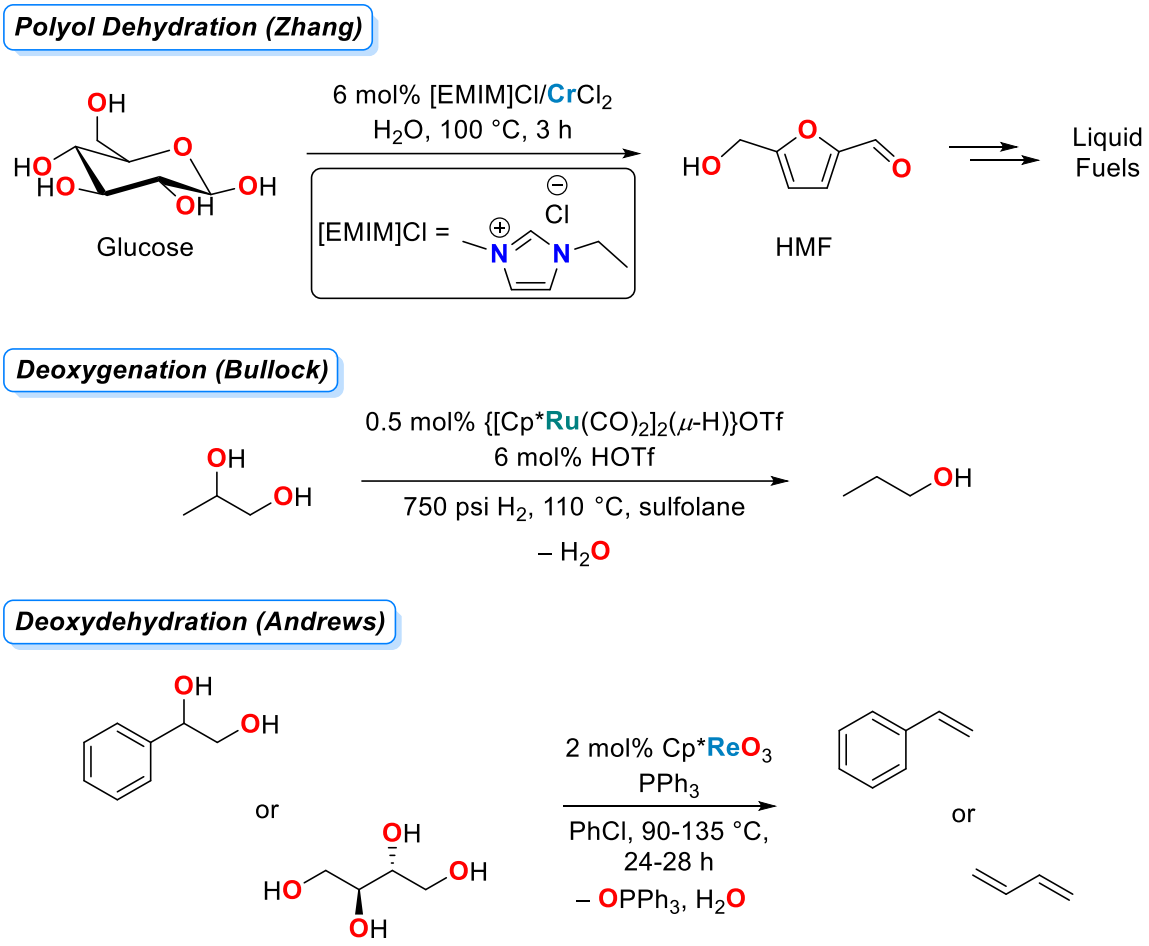

Scheme 5.1 Examples of C–O cleavage reactions towards biomass conversion

Recently, Nicholas and co-workers have reported promising advances in the catalytic reductive coupling of alcohols using oxo-rhenium and oxo-vanadium catalysts (Scheme 5.2).[315–318] This allows for both C–O bond cleavage and subsequent C–C bond formation using readily-available mono-alcohols as the carbon source.[318] While a reductant for oxygen atom transfer is required in the rhenium system,[315,317] the alcohol itself acts as the reductant in the vanadium system, producing the corresponding ketone and water as the byproducts.[316,318] Avoiding the use of external reductant makes the vanadium-catalyzed reaction particularly attractive, though a recent report by Moriuchi and co-workers has shown that hydrazines can also be used as a terminal

reductant for the reaction.[319] Moreover, using earth-abundant vanadium as a catalyst for deoxygenation reactions is both appealing and counter-intuitive; oxygen is often deleterious to early-transition-metal catalysts due to their oxophilic nature.

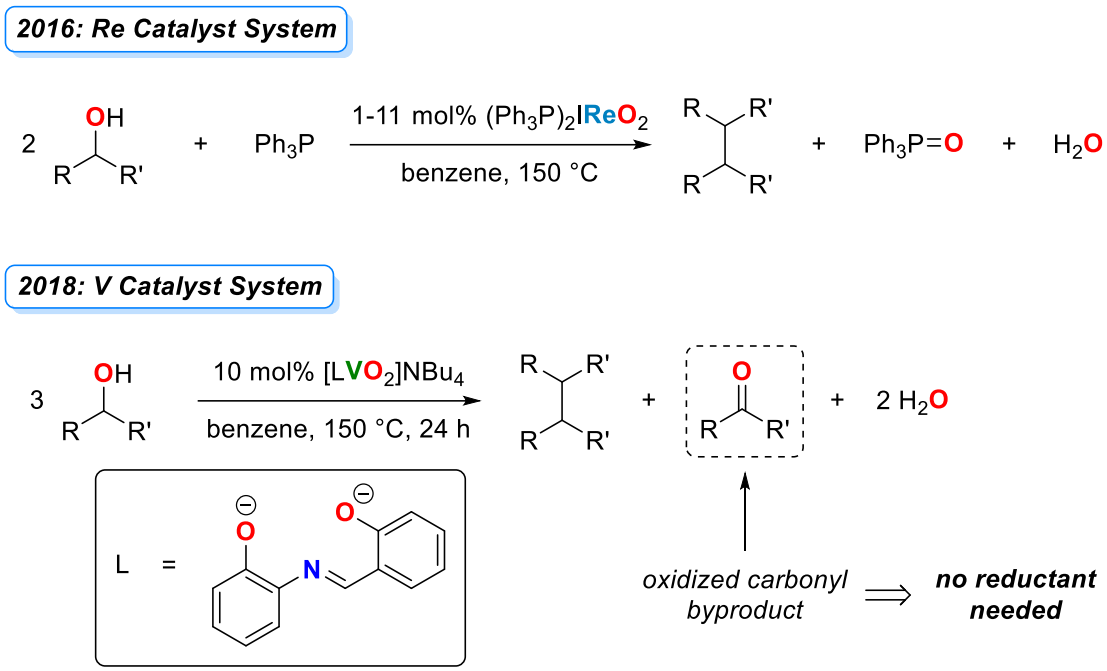

Scheme 5.2 Catalytic reductive coupling of alcohols reported by Nicholas and co-workers

Given our understanding of 1,3-*N*,*O*-chelated early-transition metal catalysts for the functionalization of abundant feedstocks,[82,85,86] we anticipated that such complexes would be well suited for the reductive coupling of alcohols, taking advantage of the established metal-ligand cooperativity of pyridonates for E−H bond activations.[262,264,266,267] Additionally, the knowledge gained on vanadium pyridonate complexes in Chapter 4 could be applied towards the development of efficient catalysts for the reductive coupling of alcohols. Herein we demonstrate that vanadium(III) pyridonate complex **4.7** (*vide supra*) can mediate the catalytic and step-wise stoichiometric reductive coupling of benzyl alcohol derivatives. The stoichiometric reactivity

allowed for the isolation of relevant catalytic intermediates to furnish key insights into the mechanism of this fundamental deoxygenative transformation.

5.2 Catalytic Reductive Coupling of Alcohols with 4.7

First, the catalytic reductive coupling of benzhydrol was attempted using complex **4.7** as the catalyst. Similar reaction conditions to those employed by Nicholas and co-workers were used.[316] Gratifyingly, heating a C_6D_6 solution of benzhydrol with 5 mol% of dimer **4.7** provides full conversion to the desired product with concomitant formation of benzophenone (Table 5.1, entry 1). This is confirmed by the ^{1}H NMR spectrum after the reaction, in which a singlet is observed at 4.68 ppm and a doublet is observed at 7.71 ppm; these signals are diagnostic for the methine Hs of 1,1,2,2-tetraphenylethane and the ortho Hs of benzophenone, respectively.[316] Observation of the ketone byproduct suggests the reaction proceeds through the previously reported mechanism in which the alcohol acts as the reductant. This reaction can be successfully extended to other benzyl alcohol derivatives (Table 5.1, entries 2 and 3), an attractive class of substrates that can be derived from lignin biomass.[320,321] In the case of 1-phenylethanol, a 1:1 mixture of racemic/meso product is observed. No ether byproducts were observed by GC-MS. An explanation of how the yields were calculated and the rationale behind how they are presented can be found in Appendix A.5.

Table 5.1 Catalytic reductive coupling of alcohols using catalyst **4.7**

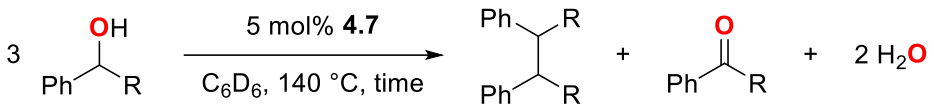

entry	R	time (h)	product yield (%)	carbonyl yield (%)
1	Ph	24	>99	88
2	Me	48	65	66
3	H	48	34	31

Yields determined by ^{1}H NMR using 1,3,5-trimethoxybenzene as an internal standard. A 1:1 mixture of meso/racemic diastereomers was observed for entry 2.

5.3 Stoichiometric Studies

Previous work from the Schafer group and others has shown that 1,3-*N*,*O*-chelating ligands can be used to promote the isolation and characterization of reactive intermediates in catalysis, including the studies presented in Chapters 2 and 3.[108,162,244,258] Reported mechanistic studies of vanadium-catalyzed reductive coupling utilize DFT to predict intermediates in the catalytic cycle.[318] Here we can use the vanadium pyridonate complex advantageously to complete stoichiometric studies and gain complementary mechanistic information.[318]

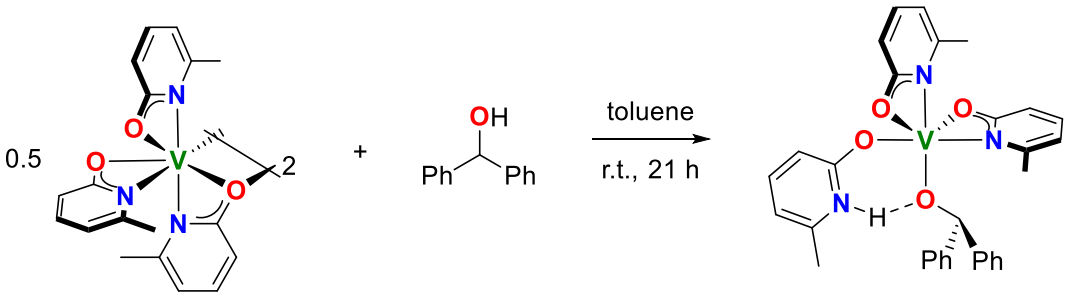

4.7

5.1, 99% yield

μ_{eff} = 2.62 μ_B

Scheme 5.3 Pyridonate-promoted alcohol coordination to catalyst **4.7**

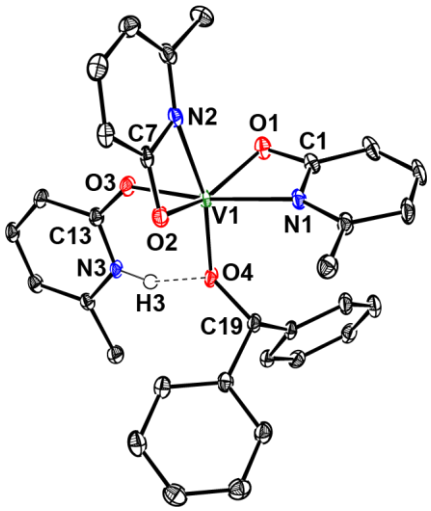

Figure 5.2 ORTEP representation of complex **5.1** with ellipsoids shown at 50% probability and hydrogen atoms omitted for clarity. Selected bond lengths (Å) and angles (°): V1−N1, 2.1482(15); V1−N2, 2.1960(16); V1−O1, 1.9922(14); V1−O2, 2.0081(13); V1−O3, 2.0446(13); V1−O4, 1.8888(14); O4−H3, 1.914 (calcd); O1−V1−N1, 64.55(6); C13−O3−V1, 136.39(12); V1−O4−C19, 128.34(11)

First, the interaction of bimetallic complex **4.7** with 2 equiv. of benzhydrol at room temperature was investigated. Within 21 h at room temperature, the reaction in THF or toluene produced a green solution, which upon removal of volatiles afforded alkoxide complex **5.1** as a green powder in near-quantitative yield (Scheme 5.3). The solid-state molecular structure of **5.1** (Figure 5.2) was obtained by X-ray crystallography using dark green crystals grown from a saturated toluene solution. This structure shows that the hemilability of the pyridonate ligand is advantageous to promote coordination of the alcohol substrate and facilitate deprotonation of the alcohol. This is similar to complex **4.16** (*vide supra*) in which pyridonate hemilability allows coordination of amine. A short hydrogen bonding interaction with the alkoxide (O4−H3, 1.914 Å (calcd)) is present, giving a six-membered vanadacycle within the distorted octahedral complex. Paramagnetic complex **5.1** has C_1 symmetry, consistent with the observation that the ^{1}H NMR

spectrum of **5.1** shows an increased number of signals compared to that of the more symmetric complex **4.7** (see Appendix D). Most importantly, **5.1** provides experimental evidence for the analogous species predicted computationally using DFT.[318] Notably, deprotonation of an alcohol by a pyridonate ligand is the first step in Ir-catalyzed acceptorless alcohol dehydrogenation,[267] and here we show that similar metal-ligand cooperativity is relevant to early-transition-metal reactivity. Evans' Method of **5.1** confirms a d^2 metal (μ_{eff} = 2.62 μ_B; C_6D_6 solution, 25 °C), as expected for this redox-neutral reaction.

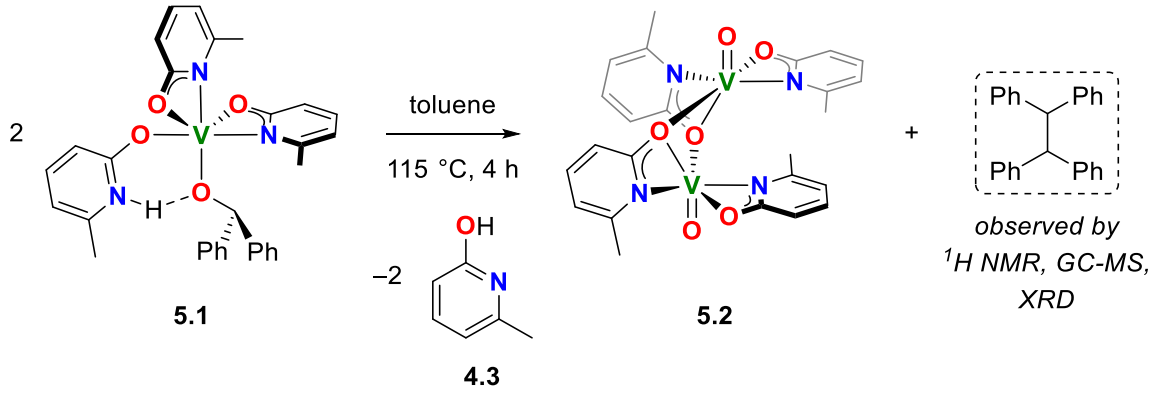

Scheme 5.4 Stoichiometric reductive coupling of benzhydrol to give dimer **5.2**

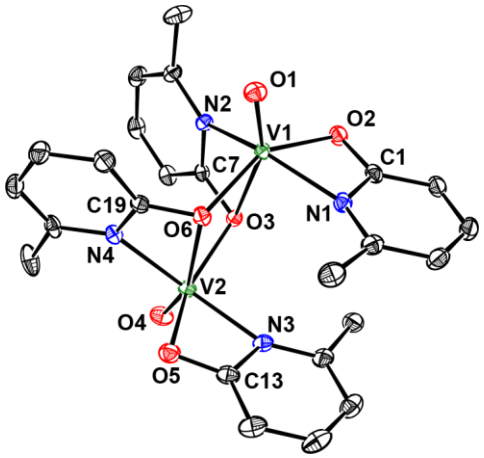

Figure 5.3 ORTEP representation of complex **5.2** with ellipsoids shown at 50% probability and hydrogen atoms omitted for clarity. Selected bond lengths (Å) and angles (°): V1−N1, 2.0840(17);

V1−N2, 2.1096(16); V2−N3, 2.0829(17); V2−N4, 2.0984(17); V1−O1, 1.5931(14); V1−O2, 2.0031(15); V1−O3, 2.4520(14); V2−O3, 2.0039(15); V2−O4, 1.5954(15); V2−O5, 1.9989(16); V2−O6, 2.4454(14); O2−V1−N1, 65.50(7); V1−O6−V2, 107.01(6); O1−V1−O3, 157.02(6)

Complex **5.1** was then heated in toluene to achieve reductive coupling of the bound alcohol (Scheme 5.4). After 4 h, the dark green solution turned turquoise. Following removal of the volatiles and subsequent recrystallization from toluene, blue crystals of **5.2** suitable for X-ray diffraction studies (Figure 5.3) and some colourless crystals (*vide infra*) were obtained. Dimeric terminal oxo-complex **5.2** is C_2 symmetric, with each vanadium being six-coordinate and having distorted octahedral geometry. Similar to **5.1**, all pyridonates bind κ^2 with two having the κ^2:μ_2 bridging mode through a μ_2-*O* to the other vanadium centre. The μ_2-*O*-V interaction is more unsymmetrical in **5.2** compared to **5.1** (V1−O3, 2.4520(14) Å; V2−O3, 2.0039(15) Å) due to the strong *trans* influence of the oxo ligand. Additionally, the vanadium-oxo distances (V1−O1, 1.5931(14) Å; V2−O4, 1.5954(15) Å) are in good agreement with a reported pyridine-2-thiolate oxo-vanadium complex (V−O_{oxo}, 1.583(6) Å).[322] The ^{1}H NMR spectrum of **5.2** gives a diagnostic signal at 13.91 ppm, consistent with an increase in symmetry relative to **5.1**.

Paramagnetic **5** contains two vanadium(IV), d^1 metal centres, as predicted from the solid-state molecular structure. Thus, each vanadium is oxidized by one electron going from **5.1** to **5.2**, consistent with reductive coupling. Indeed, 1,1,2,2-tetraphenylethane was observed by ^{1}H NMR spectroscopy when the reaction was performed in toluene-d_8. Furthermore, the colourless crystals isolated from the reaction were confirmed to be 1,1,2,2-tetraphenylethane. Homolysis of the C−O bond to give the benzhydryl radical (which would dimerize to form the reductively-coupled product) and a vanadium(IV) complex was predicted by DFT to occur; thus the isolation of **5.2** is consistent with the computationally predicted mechanistic proposal. Notably, the pyridone

released during reductive coupling was observed by ^{1}H NMR in both the stoichiometric and catalytic reactions. Moreover, the only vanadium-based signals observed in the ^{1}H NMR spectrum of the catalytic reaction were those of **5.2**, suggesting that **5.2** is the catalyst resting state. Importantly, when crude **5.2** is used as the catalyst, the system still achieves catalytic turnover, giving 46% yield of product after 24 h (Scheme 5.5). This demonstrates that **5.2** is catalytically relevant, while the lower conversion may suggest that the third equivalent of free pyridone is important for catalysis. However, adding 10 mol% of pyridone **4.3** to crude **5.2** prior to catalysis shows no improvement (Scheme 5.5). Therefore, it may be that **5.2** is an off-cycle species that can re-enter the cycle and catalyze the reaction to a lesser extent.

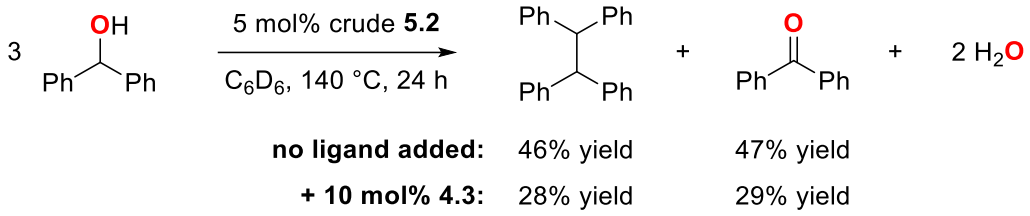

Scheme 5.5 Reductive coupling using catalyst **5.2** with or without added pyridone **4.3**

Given these results, a plausible mechanism for the reductive coupling of benzhydrol with this system is proposed (Scheme 5.6). In the presence of benzhydrol, complex **4.7** would first be converted to **5.1**. Dissociation of a pyridone ligand **4.3** can then give proposed alkoxide complex **H**, which would undergo C−O homolysis to release benzhydryl radical and produce complex **5.2**. The benzhydryl radical would then dimerize to give the C−C coupled product. Importantly, no intermediate is observed during the formation of **5.2** from **5.1** and all efforts to isolate **H** have been unsuccessful. Thus, the nature of **H** is unknown and is proposed to be a bridged species based purely on the observed tendency of these complexes to aggregate. Moreover, a mechanism in which C−O homolysis occurs at **5.1** prior to pyridone dissociation cannot be ruled out. After

reductive coupling, complex **5.2** could undergo reduction with an equiv. of alcohol to give benzophenone as a byproduct and a putative bridged vanadium(III) hydroxide species **I**. This is proposed to proceed through a bimetallic pathway, though efforts to study the formation of benzophenone from **5.2** have proved inconclusive (see Appendix A.5).

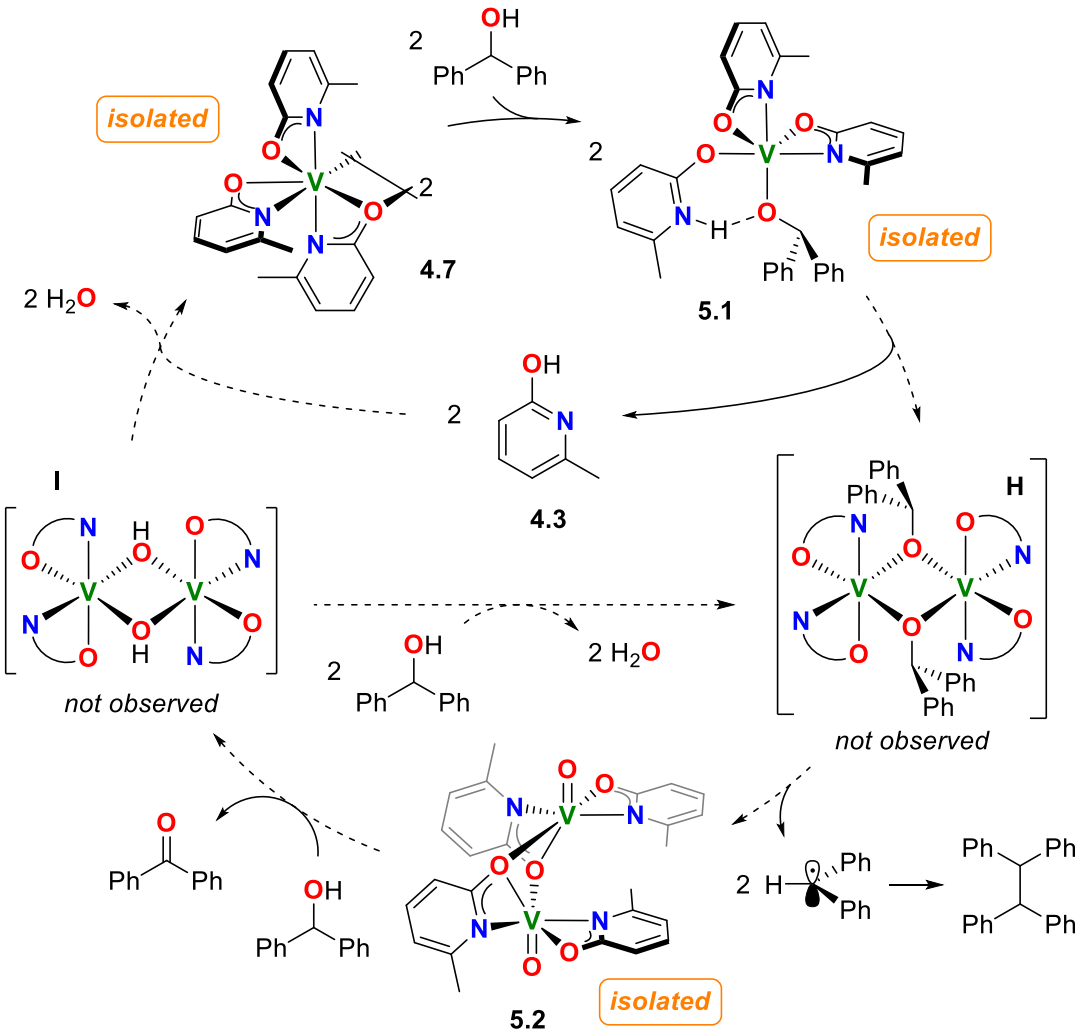

Scheme 5.6 Proposed mechanism of reductive coupling with catalyst **4.7**

While Nicholas and co-workers propose oxidation of benzhydrol via a monomeric vanadium(V) species,[318] no vanadium(V) species have been observed in this system. Moreover, NMR studies on the reaction of dimer **4.7** with 4 equiv. of benzhydrol show that an equiv. of

benzophenone is produced prior to a second reductive coupling event. The fate of the "H_2" equiv. released during alcohol oxidation is the H_2O byproduct (*vide infra*), which is observed by ^{1}H NMR. Similar to **H**, the true nature of **I** is unknown, and this species has not been observed. Nevertheless, we propose that if formed, complex **I** could undergo protonolysis with free pyridone to produce water as a byproduct and regenerate **4.7**. Alternatively, complex **I** could undergo protonolysis with benzhydrol and proceed directly to complex **H**.

Using the DFT studies by Nicholas and co-workers on alcohol oxidation by a monomeric oxo-vanadium catalyst as a guide,[318] a plausible alcohol oxidation pathway by V(IV) dimer **5.2** can be envisioned (Scheme 5.7). First, coordination of benzhydrol to **5.2** to break up the dimer would produce a monomeric, terminal oxo-V(IV) species. As there is no change in the ^{1}H NMR spectrum of **5.2** upon addition of benzhydrol at room temperature, this coordination event likely only occurs at higher temperatures. Intramolecular proton transfer from the coordinated alcohol to the oxo ligand would then result in a mixed hydroxo/alkoxide complex. Re-association of the other half of dimer **5.2**, either through an inner sphere bridging mode as depicted in Scheme 5.7 or an outer sphere process, would place the benzylic C−H bond of the alkoxide ligand in close proximity to the terminal V(IV) oxo ligand. From there, PCET would result in C−H bond cleavage and O−H bond formation with concomitant reduction of V(IV) to V(III) and formation of a radical at the benzylic position of the alkoxide ligand. Finally, V−O homolysis would reduce the other V(IV) centre to V(III) and release the oxidized benzophenone byproduct, with subsequent association of the terminal hydroxyl ligand producing proposed intermediate **I**. Importantly, this pathway is purely speculative and is only informed by analogous steps computed by Nicholas and co-workers on their monomeric catalyst system.[318]

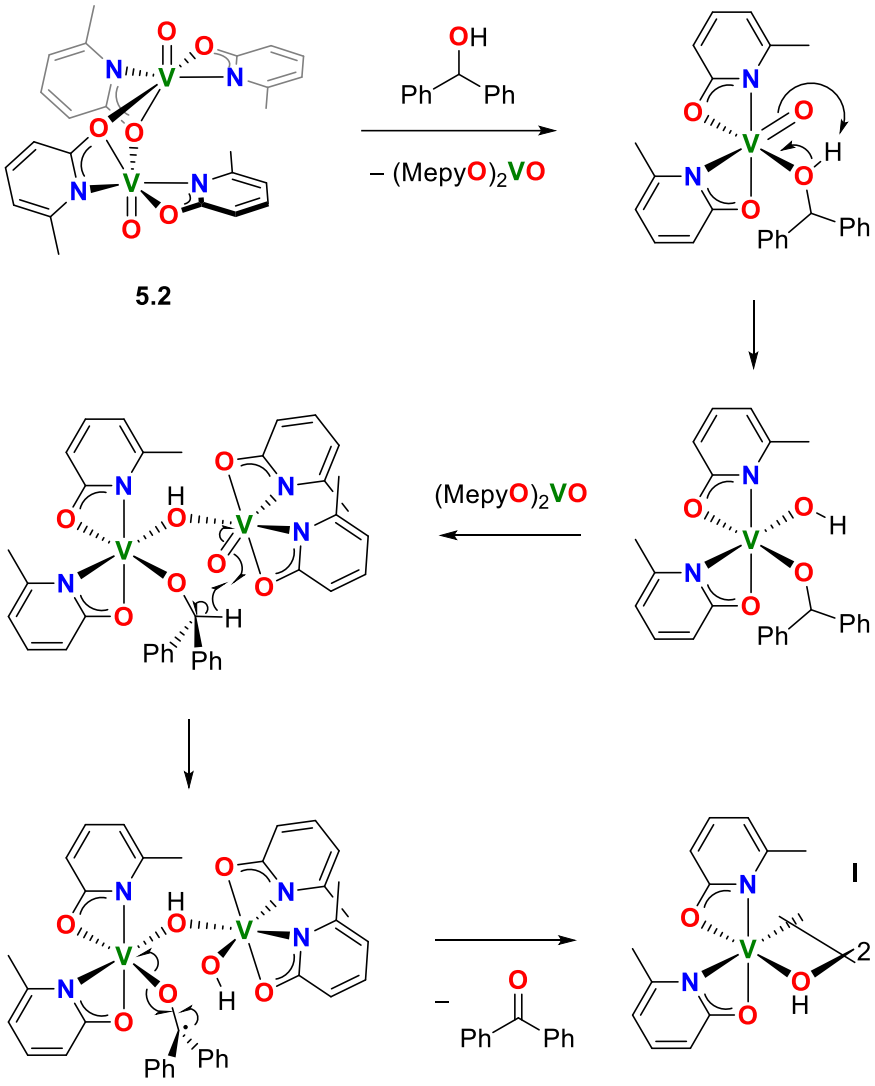

Scheme 5.7 Proposed mechanism of alcohol oxidation by complex **5.2**

5.4 Additional Mechanistic Studies

Evidence for the involvement of radical species has been obtained. A cyclopropyl-substituted alcohol undergoes ring-opening under catalytic conditions, as evidenced by formation of 1,2-dihydronaphthalene (Scheme 5.8). This fused ring forms through a cascade of steps including hydrogen atom transfer (HAT) following ring-opening of the cyclopropyl group next to the benzylic radical. The observed mixture of 1:1 meso/racemic diastereomers for the C−C coupled product using 1-phenylethanol as substrate (Table 5.1, entry 2) also supports a mechanism

involving radical formation. However, radical-trapping agent fluorene does not intercept the benzhydryl radical during the reaction (Scheme 5.9). Additionally, a cross-over experiment between benzhydrol and fluorenol gave very little hetero-coupled product rather than a statistical mixture of homo- and hetero-coupled products (Scheme 5.10). These latter two results contrast observations by Nicholas and co-workers,[318] suggesting that C−C coupling of benzhydryl radicals may occur via a different pathway than in their system. For example, the benzhydryl radicals may combine rapidly within the solvent cage. This would be consistent with the proposed dinuclear intermediate **H**, though further studies are needed to elucidate the exact nature of this process.

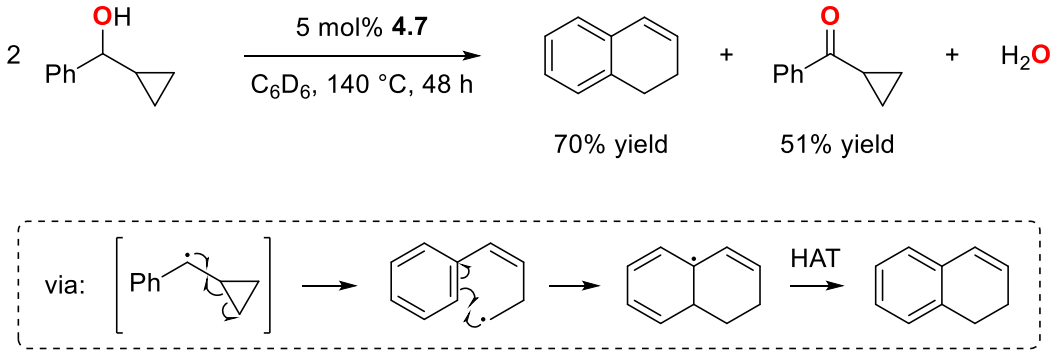

Scheme 5.8 Ring-opening of a cyclopropyl-substituted alcohol under catalytic conditions

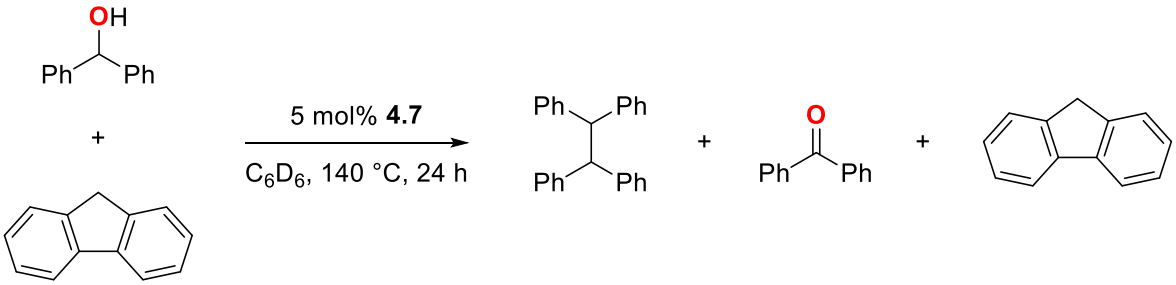

Scheme 5.9 Addition of fluorene to the catalytic reaction with benzhydrol

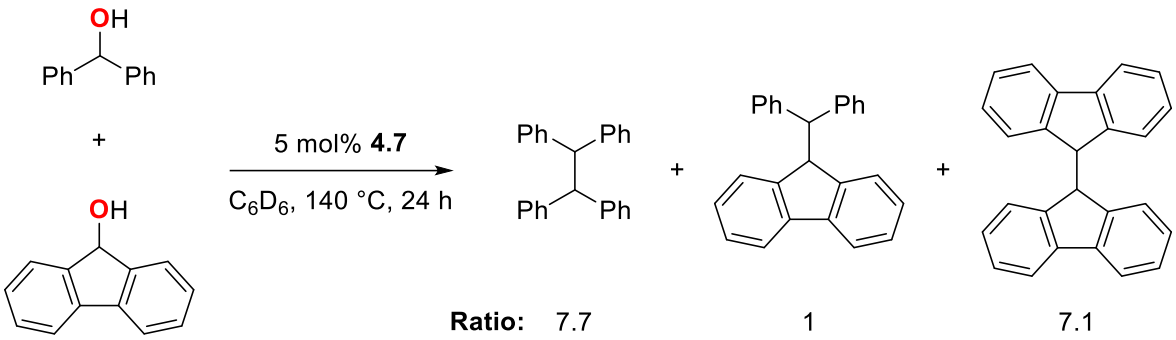

Scheme 5.10 Catalytic cross-over experiment with benzhydrol and fluorenol substrates

5.5 In situ Catalytic Protocol

In order to further demonstrate the convenience of this catalytic protocol, an *in situ* catalyst experiment was attempted. As a control reaction, the catalytic reductive coupling of benzydrol using 5 mol% of isolated catalyst **4.7** was carried out, resulting in a 37% yield of product after 4 h (Scheme 5.11, top). Next, catalyst **4.7** was generated *in situ* via protonolysis by reacting 10 mol% organometallic V(III) precursor **4.9** with 30 mol% pyridone **4.3** before attempting the same reaction. Gratifyingly, the *in situ* protocol produced the desired reductively coupled product in 38% yield after 4 h (Scheme 5.11, bottom). This shows that the *in situ*-generated catalyst **4.7** is equally active to its isolated counterpart and serves as a proof-of-concept for rapid screening of alternative ligands for this transformation. Accordingly, several other 1,3-*N*,*O*-chelating ligands, of which all but one were pyridonates, were evaluated for the catalytic reductive coupling of benzhydrol using this method (Table 5.2). Both unsubstituted pyridone **4.1** and 3-methyl substituted pyridone **4.2** promoted catalytic turnover (entries 1 and 2), but with reduced yields of the C−C coupled product in comparison to the 6-methyl variant. The sterically demanding 6-*iso*-propyl pyridone gave a similar yield to the benchmark reaction (36%, entry 3), though pyridone **4.3** is still more desirable as it is commercially available. Making the steric bulk at this position even larger by using the 6-*tert*-butyl pyridone reduced the yield to 29% (entry 4), possibly due to

more challenging substrate coordination to the bulkier catalyst. Electronic effects were also tested; the electron-withdrawing 5-trifluoromethyl pyridone gave a yield similar to that of unsubstituted pyridone **4.1** (entry 5), suggesting that making the pyridone more electron deficient does not greatly influence the reaction outcome. However, the 5-nitro pyridone gave only stoichiometric reductive coupling product formation and catalytic alcohol oxidation to benzophenone was observed (entry 6). Notably, amidate ligand **4.11** gave no conversion to product at all. Altogether, a scan of several simple pyridonate ligands indicates that the 6-methylpyridonate ligand is most effective in this reductive coupling transformation.

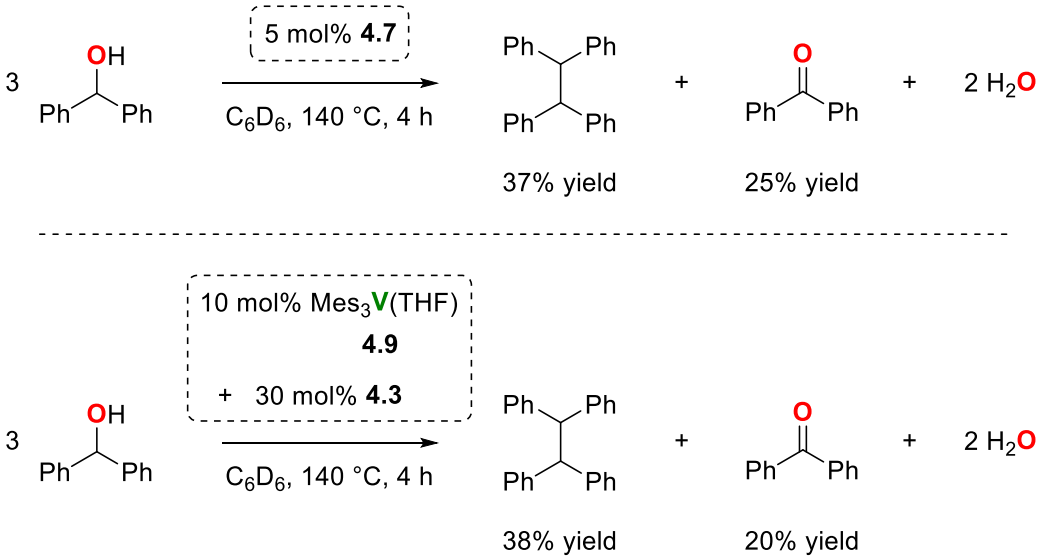

Scheme 5.11 Comparison of isolated and *in situ*-generated **4.7** for catalytic reductive coupling

Table 5.2 Catalytic screening of 1,3-*N*,*O*-chelating ligands for reductive coupling of benzhydrol

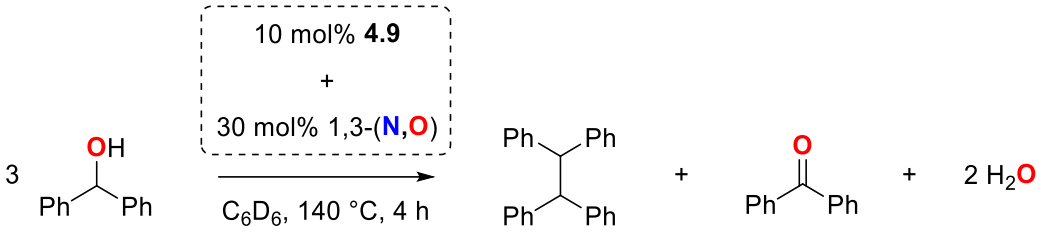

entry	ligand	product yield (%)	carbonyl yield (%)
1	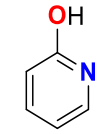	24	10
2	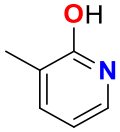	21	8
3	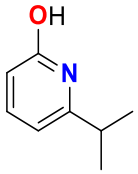	36	25
4	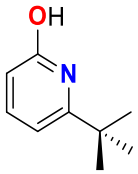	29	21
5	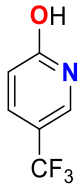	26	15
6	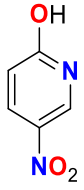	6	25
7	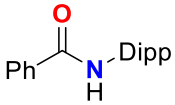	N.D.	N.D.

Yields determined by ^{1}H NMR using 1,3,5-trimethoxybenzene as an internal standard; N.D. = not detected.

5.6 Catalytic Attempts with Alkene Additives

Part of the original motivation for investigating the reactivity of vanadium pyridonate complexes with alcohols was to gauge their potential to catalyze the acceptorless dehydrogenation of alcohols (Scheme 5.12).[323] As mentioned in Chapter 4, pyridonate complexes are particularly useful catalysts for this transformation as metal-ligand cooperativity facilitates the O−H activation step.[262,264–267,269] However, the large majority of catalysts for the acceptorless dehydrogenation of alcohols are based on mid- to late-transition metals,[323] and there is only one, recently reported example utilizing earth-abundant vanadium.[324] Thus, initial catalytic experiments with dimer **4.7** and benzhydrol were carried out in hopes of achieving this transformation and observing benzophenone and H_2 as products. Of course, rather than observing this reactivity, complex **4.7** was found to instead catalyze the reductive coupling of benzhydrol as described above, launching an entirely different investigation. Nevertheless, norbornene and neohexene, which are known H_2 acceptors,[325] were added to the catalytic reaction in an attempt to favour dehydrogenation of benzhydrol (Figure 5.4). Alas, both alkenes remained unchanged over the course of the reductive coupling reaction. Electron-deficient alkenes 2-vinylpyridine and acrylonitrile were also tested as additives (Figure 5.4), as alkyl radicals generated from the reductive coupling of alcohols have been shown to undergo conjugate addition to electron deficient alkenes.[326] However, these electrophiles were also unreactive, consistent with the proposal that the benzhydryl radicals produced with catalyst **4.7** combine rapidly within the solvent cage (*vide supra*).

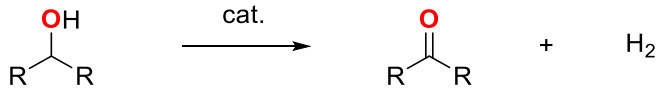

Scheme 5.12 General reaction for the acceptorless dehydrogenation of alcohols

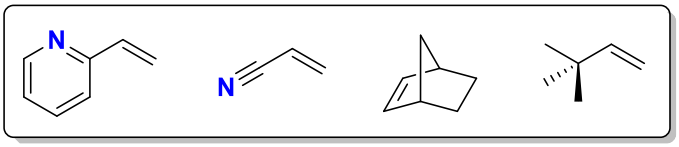

Figure 5.4 Unreactive alkene additives for the reductive coupling of alcohols with catalyst **4.7**

5.7 Conclusions

In summary, the catalytic reductive coupling of alcohols by vanadium pyridonate complexes is reported. Tris(pyridonate) vanadium(III) complex **4.7** was found to be catalytically active for the reductive coupling of benzyl alcohols, showing vanadium(III) to be a viable starting point for the catalytic cycle. Intermediates **5.1** and **5.2** were isolated, providing experimental evidence for bimetallic intermediates in this vanadium-catalyzed transformation, complementary to previous mechanistic studies. Based on these stoichiometric reactions and radical trap experiments, a vanadium(III)/(IV) redox cycle is proposed for this system. Remarkably, an early-transition-metal undergoes catalytic turnover in this deoxygenative reaction despite formation of a terminal oxo-species. The 6-methyl substituted pyridone **4.3** was found to be the most effective ligand for this catalyst system based on ligand screening experiments. This work proposes a new design strategy for developing catalysts for this exciting transformation; the involvement of bimetallic species, coupled with ligand hemilability and metal-ligand cooperativity, should enable further advancements in deoxygenative transformations of renewable feedstocks with 3d early-transition metals. Future directions will focus on related systems for the expansion of the catalyst substrate scope in the redox disproportionation of alcohols.

Chapter 6: Conclusions

6.1 Overview

The aim of this thesis is to exploit the coordination chemistry and catalytic activity of 1,3-*N*,*O*-chelated early-transition-metal complexes, through the development of mechanistic understanding, to tackle challenges in C−E bond making and breaking reactions. It was hypothesized that investigating non-conventional 1,3-*N*,*O*-chelated early-transition-metal complexes for their structure and reactivity would enable the development of improved catalysts for existing transformations or catalysts for new transformations. In studying the chemistry of zirconium ureate complexes and vanadium pyridonate complexes as catalysts and probing the mechanistic features of their reactions, this hypothesis was confirmed as described below.

In Chapter 2, a system in which reversible C−N bond formation could be directly observed was discovered. Specifically, tethered bis(ureate) zirconium bis(amido) complexes **2.3** and **2.6** underwent C−N bond formation in the presence of 2-vinylpyridine to give aza-Michael intermediates **2.4** and **2.7**, respectively. The equilibria between bis(dimethylamido) complex **2.3** and aza-Michael complex **2.4** as well as bis(pyrrolidido) complex **2.6** and aza-Michael complex **2.7** could then be monitored by variable-temperature ^{1}H NMR spectroscopy, allowing for thermal parameters to be obtained for C−N bond formation. This provided insight into why 2-vinylpyridine is such an active and selective substrate for intermolecular *anti*-Markovnikov hydroamination with Lewis acidic metal catalysts. Additionally, steric effects were found to be an important consideration in this bond forming step, as the stoichiometric reaction with 2-vinylpyridine did not proceed when using the bulkier bis(piperidido) complex **2.8**. Finally, the catalytic activity of dimethylamido precatalyst **2.1** for the hydroamination of 2-vinylpyridine and 4-vinylpyridine at room temperature was demonstrated.

In Chapter 3, the first catalytic protocol for the hydroaminoalkylation of alkynes to make *α,β,γ*-allylic amines was uncovered. Using dimethylamido precatalyst **2.1**, several benzylanilines were able to undergo C−H activation and subsequent C−C bond formation with a variety of internal arylacetylenes with 100% atom economy. The ability of the tethered bis(ureate) ligand to support seven-coordinate zirconium complexes, as established previously by the Schafer group as well as in Chapter 2, is a factor in how this system achieves catalytic turnover; previous computational data obtained for alkene hydroaminoalkylation with Ta reported turnover-limiting protonolysis as a result of steric congestion at this key intermediate. This understanding was further emphasized by characterization of model catalytic intermediates, including mixed alkyl/amido complex **3.2**, zirconaaziridine **3.4**, and insertion product **3.5**, providing insight into the C−H activation, insertion, and protonolysis steps of the reaction.

In Chapter 4, these familiar zirconium ureate complexes were set aside in order to investigate vanadium pyridonate complexes, a largely unknown class of compounds. Vanadium(IV) bis(pyridonate) complexes **4.4**-**4.6** were made easily from $V(NMe_2)_4$ and pyridones **4.1**-**4.3**, and underwent reduction to V(III) upon reaction with a third equiv. of pyridone. Through characterization of V(III) amido intermediates **4.15** and **4.16** and the observation of pyrroline as a byproduct when reacting bis(dimethylamido) complex **4.6** with pyrrolidine, it was concluded that the released amine upon protonolysis with the third equiv. of pyridone was responsible for the reduction reaction. This reduction process was used for the synthesis of bimetallic tris(pyridonate) complexes **4.7** and the bulkier **4.14**, the former of which could be synthesized via an alternative protonolysis method using trimesityl V(III) precursor **4.9**. These bimetallic complexes highlighted the various binding modes, including bridging modes, of pyridonate ligands. Additionally, dimer **4.7** could be broken up into monomeric species by neutral donors such as dimethylamine (**4.8**),

DMAP (**4.10**), or as shown in Chapter 5, benzhydrol (**5.1**). The hemilabile character and potential for metal-ligand cooperativity of pyridonate ligands were also shown in the isolation of bis(pyrrolidine) complex **4.16**. Despite relatively poor reactivity compared to its titanium counterpart, V(IV) bis(amidate) complex **4.12** showed catalytic activity for the intermolecular *anti*-Markovnikov hydroamination of alkynes. In contrast to the V(IV) pyridonate complexes, bis(amidate) complex **4.12** did not undergo reduction from V(IV) to V(III) in the presence of proteoligand, possibly due to the large steric bulk of the amidate ligand preventing the formation of aggregate species. This newfound understanding of vanadium pyridonate complexes and their behaviour can be used to advantage for other catalytic applications, as shown in Chapter 5.

In Chapter 5, experimental mechanistic insight into the catalytic reductive coupling of alcohols by vanadium was obtained. Dimeric V(III) complex **4.7** was catalytically active for the reaction with benzyl alcohols to form the C−C coupled product, water, and the corresponding ketone as a byproduct. Catalytic intermediates, namely alkoxide complex **5.1** and bimetallic terminal oxo-V(IV) complex **5.2**, were also synthesized, showcasing once more the hemilability and metal-ligand cooperativity of pyridonate ligands and their ability to support bimetallic complexes relevant to catalysis. Another key feature of this catalytic system was the involvement of bimetallic complexes in order to promote single-electron redox events across two metal centres rather than a two-electron redox event at one metal centre, which contrasts an alternative vanadium catalyst system involving only monomeric intermediates. Studies using a cyclopropyl-substituted substrate, radical trapping agent fluorene, and a mixture of benzhydrol and fluorenol as the substrate provided evidence for a mechanism involving rapid combination of alkyl radicals within the solvent cage of the catalyst, again contrasting the results obtained by the previous monometallic catalyst system. While other 1,3-*N*,*O*-chelating proligands (namely, various pyridones and amide

4.11) did not improve the reaction efficiency, the *in situ* screening method developed here can be used in future studies of other ligands for this transformation. Some early work in this regard is described in the next section.

6.2 Future Directions

6.2.1 Analysis of C−E Bond Formation in Other Hydrofunctionalization Reactions

Beyond hydroamination, catalytic hydrofunctionalization reactions more broadly are important in a number of industries as they generate value-added products from simple feedstock chemicals with 100% atom economy.[135,327] For example, hydroalkoxylation,[135,328] hydrophosphination,[135,329] and hydrothiolation[329] of alkenes provide efficient routes to compounds that are otherwise obtained via less desirable methods involving stoichiometric byproducts and multi-step processes. Gaining insight into the C−E bond forming processes involved can aid in addressing current challenges in hydrofunctionalization reactions.

As the tethered bis(ureate) zirconium system described in Chapter 2 allows for the direct observation of the key bond forming step in the hydroamination of 2-vinylpyridine, it is well-suited for studying the thermal parameters of bond formation in other types of hydrofunctionalization reactions. Therefore, synthesizing analogous species to bis(amido) complex **2.3** bearing non-amido anionic donor ligands could provide interesting comparisons of the reversibility in the bond forming step between donor types. To do this, dibenzyl complex **2.2** can be used as a precursor to ZrX_2 complexes via protonolysis with incoming HX (X = ER', Scheme 6.1). For example, bis(alkoxide), bis(phosphide), and bis(thiolate) complexes could be synthesized using this method by reaction of dibenzyl complex **2.2** with 2 equiv. of alcohol, phosphine, or thiol, respectively. The addition of each of these nucleophiles to 2-vinylpyridine is known.[183,330,331] As such, the reaction with 2-vinylpyridine may produce analogous Michael

addition intermediates to aza-Michael complexes **2.4** and **2.7**, or perhaps the ZrX_2 intermediate would not react with 2-vinylpyridine at all. For instance, a phosphide ligand may be more prone to C−E bond formation than an amido ligand, as the *P*-donor is "softer" than the *N*-donor and thus binds less favourably to Zr. In contrast, the "hard" alkoxide *O*-donor would be strongly bound to Zr, making C−E bond formation less favourable. These differences would influence where the equilibrium for C−E bond formation lies in each case, and thermal parameters might be obtainable by variable-temperature (VT) NMR as demonstrated in Chapter 2, providing key thermodynamic insights into the bond forming step of these hydrofunctionalization reactions.

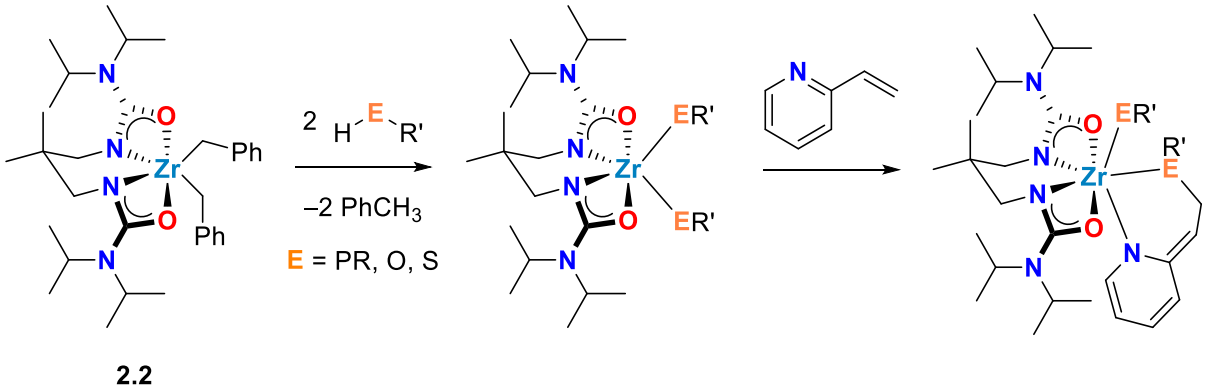

2.2

Scheme 6.1 Possible alternative nucleophilic groups for Michael additions to 2-vinylpyridine

6.2.2 Investigation of Oxidation Reactivity with Dimer 4.7

One of the distinct advantages of vanadium catalysts compared to other earth-abundant 3d metal catalysts, particularly those used for oxidation reactions, is that they are frequently oxygen and moisture stable.[332] Notably, while V(III) dimer **4.7** is air and moisture sensitive, other reported vanadium precatalysts for the reductive coupling of alcohols are air-stable V(V)-oxo species.[316,318,319] In fact, none of the vanadium pyridonate complexes described in this thesis are air stable. Therefore, a systematic study on the electrochemistry of these compounds by CV and the controlled synthesis of high oxidation state vanadium pyridonate complexes may lead to the

development of efficient, air-stable catalysts for the reductive coupling of alcohols and other transformations involving V-oxo intermediates.[332] This investigation would complement the studies in Chapter 4 focused on the reduction of V(IV) pyridonate complexes to their V(III) counterparts.

Preliminary results on the oxidation of V(III) complex **4.7** have been obtained to provide a starting point for this project. When a sealed tube containing a toluene-d_8 solution of **4.7** was exposed to an atmosphere of dioxygen gas, the colour of the solution turned immediately from peach-yellow to dark purple. The ^{1}H NMR spectrum showed new diamagnetic signals consistent with pyridonate ligands, as well as a new paramagnetic signal at 13.88 ppm corresponding to terminal V(IV)-oxo dimer **5.2** as one of the products (see Appendix). After weeks at room temperature, trace amounts of purple crystals precipitated from the solution and were suitable for X-ray diffraction studies, revealing dimeric complex **6.1** as a product (Scheme 6.2, Figure 6.1). Complex **6.1** contains two V(V) centres of distorted octahedral geometry, each having a terminal oxo ligand (V1−O1, 1.528(11) Å) in addition to the μ_2-*O* oxo (V1−O2, 1.7705(6) Å) that bridges the two metal centres together. The O-V-O bond angle is nearly linear (V1*****−O2−V1, 174.6(2)°), while the torsional angle between the two terminal oxo ligands is 65°. The stronger *trans* influence of the terminal oxo ligand in comparison to the bridging oxo donor is reflected in the differences in the corresponding V−N bond lengths of the pyridonate ligands (V1−N2, 2.295(3) Å, and V1−N1, 2.140(3) Å, respectively). For **6.1** to form from **4.7**, 1 equiv. of water likely protonates one pyridonate on each V centre in order to form the bridging oxo ligand, while *O*-atom transfer from dioxygen to each V generates the terminal oxo ligands. Note that this statement addresses mass balance but is not intended to imply reaction mechanism. This suggests that the oxygen source contained trace amounts of water, thus rigorous drying of the oxygen source is needed.

Nevertheless, product **6.1** provides some insight into the initial fate of precatalyst **4.7** upon exposure to the air. It would be worthwhile to test the catalytic activity of **6.1** for the reductive coupling of alcohols, as it could be a potential air-stable precatalyst that enters the catalytic cycle under catalytic conditions.

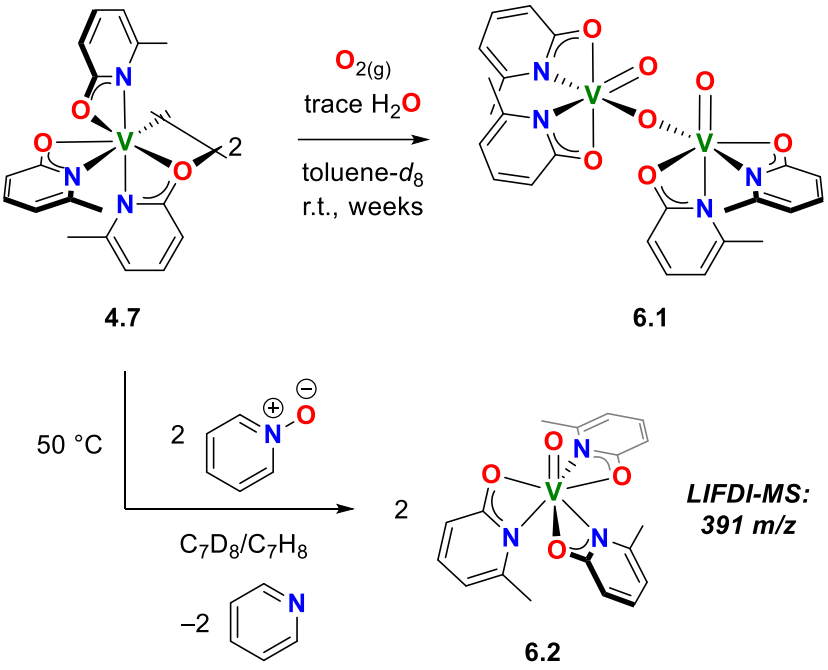

Scheme 6.2 Reaction of dimer **4.7** with dioxygen and pyridine-*N*-oxide

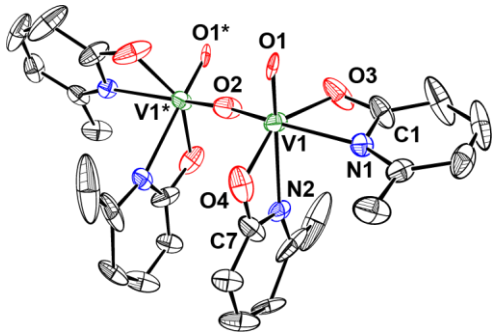

Figure 6.1 ORTEP representation of complex **6.1** with ellipsoids shown at 50% probability and hydrogen atoms omitted for clarity. Selected bond lengths (Å) and angles (°): V1−O1, 1.528(11);

V1−O2, 1.7705(6); V1−O3, 1.955(3); V1−O4, 1.884(3); V1−N1, 2.140(3); V1−N2, 2.295(3); O1−V1−N2, 168.8(3); O1−V1−O2, 101.7(4); V1*−O2−V1, 174.6(2)

Seeking a more controlled oxidation reaction, pyridine-*N*-oxide was also attempted as an *O*-atom transfer agent (Scheme 6.2). This compound is known to cleanly transfer an O atom to V(III) with concomitant release of pyridine.[333] When the oxide was transferred to a solution of **4.7** in toluene-d_8, an immediate colour change to bright orange was observed. As ^{1}H NMR spectroscopy of this solution showed only broad, paramagnetic signals and no signals corresponding to the release of diamagnetic pyridine, the orange colour likely results from oxide adduct formation. Upon heating at 50 °C overnight, the solution turned to the same dark purple colour observed in the reaction with O_2. Crystals suitable for X-ray diffraction could not be obtained from the purple solution in a scaled-up version of this reaction. However, the molecular ion corresponding to V(V)-oxo complex **6.2** (391 *m/z*) was observed by LIFDI-MS, providing preliminary evidence for its formation (Scheme 6.2). Further investigation into the synthesis and characterization of oxo-vanadium pyridonate complexes is needed to understand their air-stability and utility in catalysis.

An alternative approach to the oxidation of reduced pyridonate complexes with oxygen sources would be the synthesis of higher oxidation state, heteroleptic pyridonate/halide complexes, as the halide provides a synthetic handle via salt metathesis to access various oxidized derivatives. The direct oxidation of reduced early-transition metals with I_2 is known to generate M−I species through oxidative addition.[334] Thus, V(III) dimer **4.7** was reacted with I_2 in the hopes of breaking up the dimer and obtaining monomeric V(IV) iodide complex **J** (Scheme 6.3). Immediately upon mixing toluene solutions of **4.7** and iodine, a pale-yellow solid began precipitating from the purple solution. After isolating this powder from the resulting suspension, recrystallization in hot toluene

afforded yellow crystals of trinuclear complex **6.3** suitable for X-ray diffraction, and the solid-state molecular structure is shown in Figure 6.2. Rather than obtaining monometallic product **J**, this complex contains three V centres: two that are seven-coordinate with distorted pentagonal bipyramidal geometry and one central V ion in a six-coordinate, octahedral environment. Both paddle-wheel type binding and the κ^2:μ_2 bridging mode are observed for the pyridonate ligands in this structure. Each V centre is likely in the 3+ oxidation state in order to balance the charge of the eight total pyridonate ligands and the outer-sphere I_3^- counterion. Notably, multinuclear *N*,*O*-chelated vanadium complexes with this counterion have previously been obtained via reaction with I_2.[335]

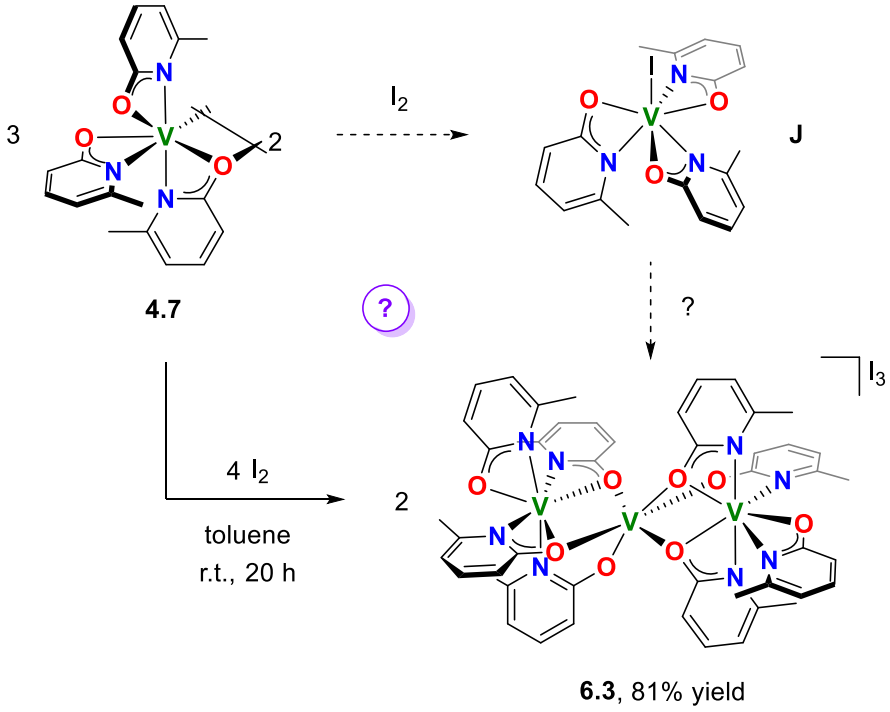

Scheme 6.3 Reaction of dimer **4.7** with iodine to give trimetallic complex **6.3**

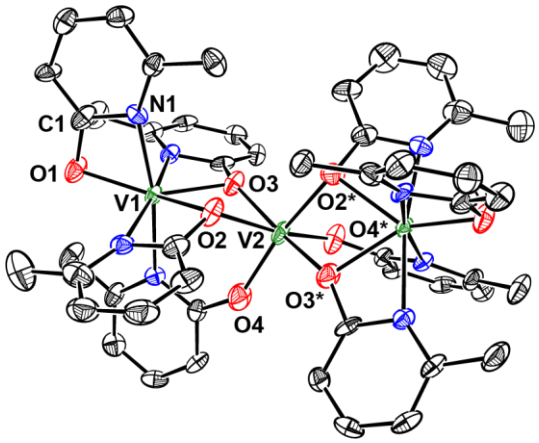

Figure 6.2 ORTEP representation of complex **6.3** with ellipsoids shown at 50% probability and I_3^- counterion and hydrogen atoms omitted for clarity. Selected bond lengths (Å) and angles (°): V1−O2, 2.141(4); V1−O3, 2.089(4); V2−O2, 2.040(4); V2−O3, 1.998(4); V2−O4, 1.904(5); O4−V2−O2*, 167.08(19); O3−V2−O3*, 170.1(2)

The isolation of trimer **6.3** raises questions about the nature of the reaction between **4.7** and I_2. The mass balance for this transformation has not yet been established. Triodide (I_3^-) is the simplest polyiodide and generally forms through complexation of I^- to I_2.[336] Therefore, it is plausible that V(IV) iodide **J** is an intermediate in this transformation, where the generated iodide acts as a Lewis base to I_2 in solution. Indeed, the reaction of ferrocene with I_2 proceeds in this way to produce ferrocenium triiodide.[337] As such, the first step for investigating this reaction would be to isolate **J** through an alternative synthetic route. *N*-iodosuccinimide could be a possible oxidant for the conversion of **4.7** to **J**, though CV studies would aid in choosing an appropriate oxidizing reagent. The stability of **J** in solution and its reactivity with I_2 would then determine whether it is a reasonable intermediate in the synthesis of trimer **6.3**. Subsequent studies would attempt to elucidate the rest of the reaction pathway, as the redox processes involved to produce **6.3** are currently unclear. Evidently, there is much fundamental coordination chemistry to be explored

with mixed pyridonate/halide complexes of vanadium in addition to their potential utility as synthetic intermediates.

6.2.3 Aminopyridinate Ligands for the Catalytic Reductive Coupling of Alcohols

Preliminary results for an improved catalytic system for the reductive coupling of alcohols have also been obtained. DFT studies by Nicholas and co-workers have established that the turnover-limiting step in the vanadium-catalyzed reductive coupling of alcohols is C−O cleavage to produce a *C*-centred radical.[318] As this step involves oxidation of V(III) to V(IV), it was hypothesized that a more electron-rich vanadium complex would lower the barrier for C−O homolysis and increase the reaction rate. Monoanionic aminopyridinate ligands, which are 1,3-*N*,*N*-chelating ligands, are more electron-rich analogues of pyridonates that allow for further steric and electronic tuning via the *N*-substituent.[338] Therefore, aminopyridinates were tested as ligands for the vanadium-catalyzed reductive coupling of alcohols. Using the same *in situ* screening method for pyridonate ligands discussed in Chapter 5, some 2-aminopyridines were evaluated. Initial results showed that using simple, unsubstituted 2-aminopyridine **6.4** was most successful, giving an 86% yield of reductive coupling product within 4 h (Scheme 6.4). This is already a notable improvement over *in situ*-generated catalyst **4.7**, which furnishes the product in a 38% yield under the same conditions (*vide supra*).

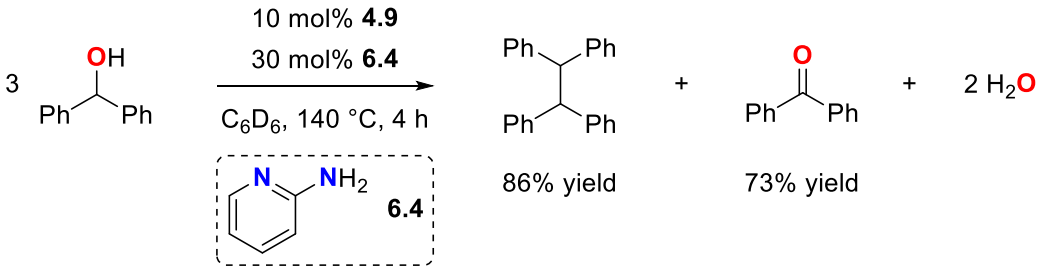

Scheme 6.4 Catalytic reductive coupling of benzhydrol using 2-aminopyridine **6.4** as a ligand

While efforts to isolate the precatalyst corresponding to ligand **6.4** have so far been unsuccessful, a model precatalyst could be synthesized using the same method as used in the synthesis of dimer **4.7**. Organometallic V(III) complex **4.9** was reacted with 3 equiv. of *N*-phenyl-2-pyridinamine **6.5** to give tris(aminopyridine)vanadium(III) complex **6.6** as a red solid via protonolysis (Scheme 6.5). The identity and structure of complex **6.6** was confirmed by X-ray crystallography, using dark red crystals grown from a saturated hexanes solution at −35 °C (Figure 6.3). In contrast to the tris(pyridonate) complexes discussed in Chapter 4, six-coordinate complex **6.6** has distorted octahedral geometry and is monomeric in the solid state even in the absence of any neutral donors. This structure is consistent with a previously reported, sterically bulky tris(aminopyridinate)vanadium(III) complex containing *N*-trimethylsilyl substituents.[339] This difference in catalyst nuclearity could lead to interesting comparisons between the pyridonate and aminopyridinate systems in the reductive coupling of alcohols, especially whether or not bimetallic intermediates are involved and how that influences catalyst activity. After ensuring that isolated **6.6** has comparable catalytic activity to the *in situ*-generated catalyst with ligand **6.5**, analogous stoichiometric experiments to those carried out with the pyridonate system in Chapter 5 would be explored to gain mechanistic insight.

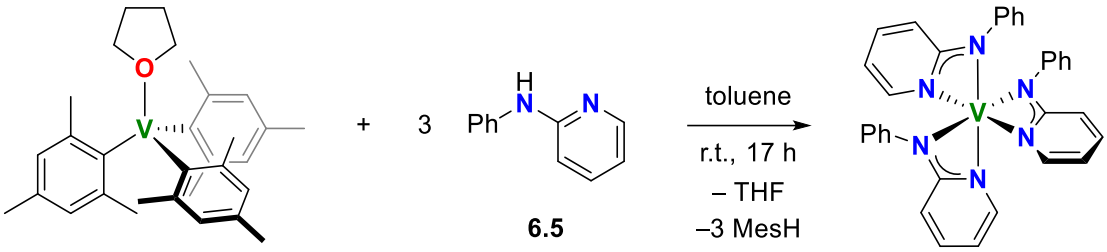

Scheme 6.5 Synthesis of tris(aminopyridinate)vanadium(III) complex **6.6**

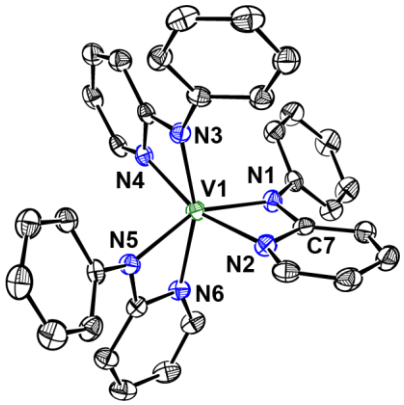

Figure 6.3 ORTEP representation of complex **6.6** with ellipsoids shown at 50% probability and hydrogen atoms omitted for clarity. Selected bond lengths (Å) and angles (°): V1−N1, 1.988(2); V1−N2, 2.092(2); N1−V1−N2, 65.28(8); N2−V1−N4, 162.60(8); N3−V1−N6, 159.47(8); N1−V1−N5, 150.75(8)

6.2.4 Tandem Catalysis for Cross-Electrophile Coupling

Within transition-metal-catalyzed C−C coupling, significant focus has turned towards the development of cross-electrophile coupling reactions,[340–343] as there are far fewer commercially available carbon-based nucleophiles than carbon-based electrophiles due to the reactive nature of nucleophilic organometallic reagents.[341] Recently, alcohols have been used as an abundant and inexpensive source of carbon radicals for cross-electrophile coupling.[344–347] Benzyl alcohols are converted *in situ* to benzylic radicals that can be intercepted by a nickel catalyst to afford C−C coupled products, however these methods require either stoichiometric metal/phosphine reductant or pre-derivatization of the alcohols. The reductive coupling of alcohols has the potential to catalytically generate benzylic radicals from alcohols for cross-electrophile coupling.

Relatedly, Nicholas and co-workers have shown that benzyl radicals produced during the reductive coupling of alcohols can be intercepted by an electron-deficient alkene to undergo conjugate addition.[326] Thus, it is proposed to extend this idea to cross-electrophile coupling with a

nickel co-catalyst (Scheme 6.6). Initial efforts would focus on the stoichiometric reaction between the benzhydryl radical generated from alkoxide complex **5.1** and a nickel complex, such as **6.7**, known to intercept radicals and ultimately give arylated products[348] (Scheme 6.7). Once suitable conditions to promote C−C formation are discovered, subsequent efforts would focus on the translation of this reaction to a catalytic protocol. Key to this project would be fine-tuning the ligand environment around the vanadium centre in order to promote free radical formation and avoid homocoupling. This example highlights the broader impact that the work presented in this thesis may have in the organometallic and organic synthetic communities.

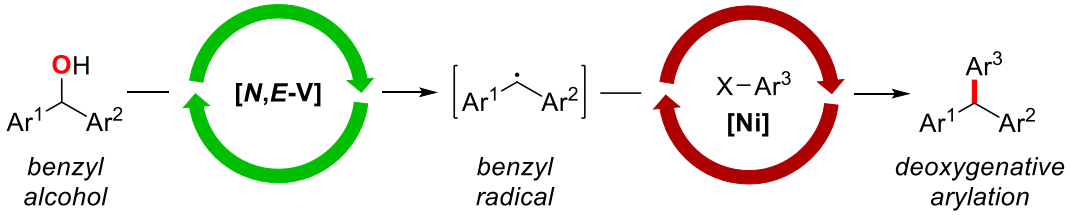

Scheme 6.6 General concept of tandem V-catalyzed radical generation and Ni-catalyzed cross-electrophile coupling

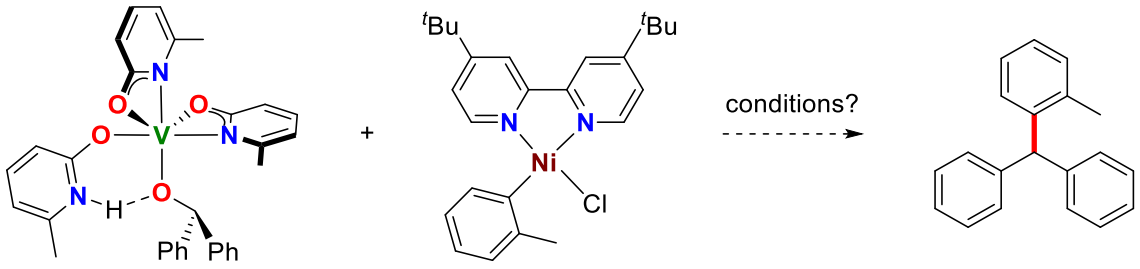

Scheme 6.7 Proposed stoichiometric coupling of benzhydrol and an aryl group

6.3 Concluding Remarks

Altogether, this thesis shows that 1,3-*N*,*O*-chelated early-transition-metal complexes, namely zirconium ureates and vanadium pyridonates, can be used to address longstanding

challenges in the making and breaking of C−E bonds, from hydrofunctionalization reactions to biomass conversion and beyond. While much of the work here is fundamental in nature, the mechanistic groundwork established in this thesis acts as a foundation for developing catalysts with important applications. These 1,3-*N*,*O*-chelated early-transition-metal complexes also provide rich opportunities in fundamental coordination and organometallic chemistry to be explored for years to come. Finally, it is hoped that this foray into vanadium chemistry in the Schafer group will help bolster the idea in the organometallic community at large that pushing the boundaries of underutilized, earth-abundant early-transition-metals in catalysis can lead to exciting and rewarding chemistry.

References

(1) Meijere, A. de.; Bräse, S.; Oestreich, M. *Metal Catalyzed Cross-Coupling Reactions and More*; John Wiley & Sons: Hoboken, 2013; Vol. 1, pp 1–1511.

(2) Hartwig, J. F. *Organotransition Metal Chemistry: From Bonding to Catalysis*; University Science Books: Mill Valley, 2010.

(3) Elschenbroich, C. *Organometallics, 3rd, Completely Revised and Extended Edition*; John Wiley & Sons: Hoboken, 2006.

(4) Crabtree, R. H. *The Organometallic Chemistry of the Transition Metals: Sixth Edition*; Crabtree, R. H., Ed.; John Wiley & Sons, Inc.: Hoboken, 2014.

(5) Togni, A.; Halterman, R. L. *Metallocenes: Synthesis---Reactivity---Applications*; Togni, A., Halterman, R. L., Eds.; John Wiley & Sons, Inc.: Hoboken, 1998.

(6) Evans, W. J. Tutorial on the Role of Cyclopentadienyl Ligands in the Discovery of Molecular Complexes of the Rare-Earth and Actinide Metals in New Oxidation States. *Organometallics* **2016**, *35*, 3088–3100.

(7) Mas-Roselló, J.; Herraiz, A. G.; Audic, B.; Laverny, A.; Cramer, N. Chiral Cyclopentadienyl Ligands: Design, Syntheses, and Applications in Asymmetric Catalysis. *Angew. Chem., Int. Ed.* **2020**, *59*, 2–20.

(8) Okuda, J. Transition Metal Complexes of Sterically Demanding Cyclopentadienyl Ligands. In *Topics in Current Chemistry*; Springer: Berlin, 1992; pp 97–145.

(9) Arndt, S.; Okuda, J. Mono(Cyclopentadienyl) Complexes of the Rare-Earth Metals. *Chem. Rev.* **2002**, *102*, 1953–1976.

(10) Rosenthal, U. Recent Synthetic and Catalytic Applications of Group 4 Metallocene Bis(Trimethylsilyl)Acetylene Complexes. *Eur. J. Inorg. Chem.* **2019**, 895–919.

(11) Janiak, C.; Versteeg, U.; Lange, K. C. H.; Weimann, R.; Hahn, E. The Influence of Electronic and Steric Effects and the Importance of Polymerization Conditions in the Ethylene Polymerization with Zirconocene/MAO Catalysts. *J. Organomet. Chem.* **1995**, *501*, 219–234.

(12) Green, M. L. H. A New Approach to the Formal Classification of Covalent Compounds of the Elements. *J. Organomet. Chem.* **1995**, *500*, 127–148.

(13) Connor, J. M.; Casey, C. P. Ring-Slippage Chemistry of Transition-Metal Cyclopentadienyl and Indenyl Complexes. *Chem. Rev.* **1987**, *87*, 307–318.

(14) Rerek, M. E.; Ji, L. N.; Basolo, F. The Indenyl Ligand Effect on the Rate of Substitution Reactions of Rh(η-C9H7)(CO)2 and Mn(η-C 9H7)(CO)3. *J. Chem. Soc. Chem. Commun.* **1983**, 1208–1209.

(15) Calhorda, M. J.; Romão, C. C.; Veiros, L. F. The Nature of the Indenyl Effect. *Chem. Eur. J.* **2002**, *8*, 868–875.

(16) Calhorda, M. J.; Veiros, L. F. Haptotropic Shifts of Indenyl and Other Related π Ligands. *Comments Inorg. Chem.* **2001**, *22*, 375–391.

(17) Schmid, M. A.; Alt, H. G.; Milius, W. Unverbrückte Indenylkomplexe Mit Metallen Der Vierten Gruppe Als Katalysatoren Bei Der Homogenen Olefinpolymerisation. *J. Organomet. Chem.* **1996**, *514*, 45–49.

(18) Llinas, G. H.; Day, R. O.; Rausch, M. D.; Chien, J. C. W. Ethylidene(1-.Eta.5-Tetramethylcyclopentadienyl)(1-.Eta.5-Indenyl)Dichlorozirconium: Synthesis, Molecular Structure, and Polymerization Catalysis. *Organometallics* **1993**, *12*, 1283–1288.

(19) Borrini, A.; Diviersi, P.; Ingrosso, G.; Lucherini, A.; Serra, G. Highly Active Rhodium Catalysts for the [2+2+2] Cycloaddition of Acetylenes. *J. Mol. Catal.* **1985**, *30*, 181–195.

(20) Garrett, C. E.; Fu, G. C. Exploiting η^5- to η^3-Indenyl Ring Slippage to Access a Directed Reaction: Ether-Directed, Rhodium-Catalyzed Olefin Hydroboration. *J. Org. Chem.* **1998**, *63*, 1370–1371.

(21) Marder, T. B.; Roe, D. C.; Milstein, D. Transition-Metal-Catalyzed C—C Bond Formation via C—H Activation. Intermolecular Hydroacylation: The Addition of Aldehydes to Alkenes. *Organometallics* **1988**, *7*, 1451–1453.

(22) Drover, M. W.; Schild, D. J.; Oyala, P. H.; Peters, J. C. Snapshots of a Migrating H-Atom: Characterization of a Reactive Iron(III) Indenide Hydride and Its Nearly Isoenergetic Ring-Protonated Iron(I) Isomer. *Angew. Chem., Int. Ed.* **2019**, *58*, 15504–15511.

(23) Wolczanski, P. T.; Bercaw, J. E. On the Mechanisms of Carbon Monoxide Reduction with Zirconium Hydrides. *Acc. Chem. Res.* **1980**, *13*, 121–127.

(24) Luinstra, G. A.; Teuben, J. H. The Deceptively Simple Thermolysis of Trivalent Permethyltitanocene Derivatives (η5-C5Me5)2TiR. Formation of a Tetramethylfulvene Titanium Compound (η6-C5Me4CH2)(η5-C5Me5)Ti and RH, Catalyzed by Permethyltitanocene Hydride, (η5-C5Me5)2TiH. *J. Am. Chem. Soc.* **1992**, *114*, 3361–3367.

(25) Schild, D. J.; Drover, M. W.; Oyala, P. H.; Peters, J. C. Generating Potent C-H PCET Donors: Ligand-Induced Fe-to-Ring Proton Migration from a Cp*FeIII-H Complex Demonstrates a Promising Strategy. *J. Am. Chem. Soc.* **2020**, *142*, 18963–18970.

(26) Kealy, T. J.; Pauson, P. L. A New Type of Organo-Iron Compound. *Nature* **1951**, *168*, 1039–1040.

(27) Adams, R. . Foreword | Journal of Organometallic Chemistry - Volumes 637–639. *J. Organomet. Chem.* **2001**, *637–639*, 1.

(28) Zhu, T.; Sha, Y.; Firouzjaie, H. A.; Peng, X.; Cha, Y.; Dissanayake, D. M. M. M.; Smith,

M. D.; Vannucci, A. K.; Mustain, W. E.; Tang, C. Rational Synthesis of Metallo-Cations Toward Redox- And Alkaline-Stable Metallo-Polyelectrolytes. *J. Am. Chem. Soc.* **2020**, *142*, 1083–1089.

(29) Zimmermann, P.; Kilpatrick, A. F. R.; Ar, D.; Demeshko, S.; Cula, B.; Limberg, C. Electron Transfer within β-Diketiminato Nickel Bromide and Cobaltocene Redox Couples Activating CO 2. *Chem. Commun.* **2021**, *57*, 875–878.

(30) Slone, C. S.; Mirkin, C. A.; Yap, G. P. A.; Guzei, I. A.; Rheingold, A. L. Oxidation-State-Dependent Reactivity and Catalytic Properties of a Rh(I) Complex Formed from a Redox-Switchable Hemilabile Ligand. *J. Am. Chem. Soc.* **1997**, *119*, 10743–10753.

(31) Süßner, M.; Plenio, H. Redox-Switchable Phase Tags for Recycling of Homogeneous Catalysts. *Angew. Chem., Int. Ed.* **2005**, *44*, 6885–6888.

(32) Gregson, C. K. A.; Gibson, V. C.; Long, N. J.; Marshall, E. L.; Oxford, P. J.; White, A. J. P. Redox Control within Single-Site Polymerization Catalysts. *J. Am. Chem. Soc.* **2006**, *128*, 7410–7411.

(33) Tennyson, A. G.; Lynch, V. M.; Bielawski, C. W. Arrested Catalysis: Controlling Kumada Coupling Activity via a Redox-Active N-Heterocyclic Carbene. *J. Am. Chem. Soc.* **2010**, *132*, 9420–9429.

(34) Broderick, E. M.; Guo, N.; Wu, T.; Vogel, C. S.; Xu, C.; Sutter, J.; Miller, J. T.; Meyer, K.; Cantat, T.; Diaconescu, P. L. Redox Control of a Polymerization Catalyst by Changing the Oxidation State of the Metal Center. *Chem. Commun.* **2011**, *47*, 9897–9899.

(35) Broderick, E. M.; Guo, N.; Vogel, C. S.; Xu, C.; Sutter, J.; Miller, J. T.; Meyer, K.; Mehrkhodavandi, P.; Diaconescu, P. L. Redox Control of a Ring-Opening Polymerization Catalyst. *J. Am. Chem. Soc.* **2011**, *133*, 9278–9281.

(36) Camara, J. M.; Rauchfuss, T. B. Combining Acid-Base, Redox and Substrate Binding Functionalities to Give a Complete Model for the [FeFe]-Hydrogenase. *Nat. Chem.* **2012**, *4*, 26–30.

(37) Quan, S. M.; Wang, X.; Zhang, R.; Diaconescu, P. L. Redox Switchable Copolymerization of Cyclic Esters and Epoxides by a Zirconium Complex. *Macromolecules* **2016**, *49*, 6768–6778.

(38) Wang, X.; Thevenon, A.; Brosmer, J. L.; Yu, I.; Khan, S. I.; Mehrkhodavandi, P.; Diaconescu, P. L. Redox Control of Group 4 Metal Ring-Opening Polymerization Activity toward l -Lactide and ε-Caprolactone. *J. Am. Chem. Soc.* **2014**, *136*, 11264–11267.

(39) Wei, J.; Diaconescu, P. L. Redox-Switchable Ring-Opening Polymerization with Ferrocene Derivatives. *Acc. Chem. Res.* **2019**, *52*, 415–424.

(40) Lukens, W. W.; Andersen, R. A. Synthesis, Structure, and Reactions of (.Eta.5-C5H5)3Zr. *Organometallics* **1995**, *14*, 3435–3439.

(41) Odian, G. *Principles of Polymerization*; John Wiley & Sons, Inc.: Hoboken, 2004.

(42) Kaminsky, W.; Külper, K.; Brintzinger, H. H.; Wild, F. R. W. P. Polymerization of Propene and Butene with a Chiral Zirconocene and Methylalumoxane as Cocatalyst. *Angew. Chem., Int. Ed.* **1985**, *24*, 507–508.

(43) Rieger, B.; Mu, X.; Mallin, D. T.; Rausch, M. D.; Chien, J. C. W. Degree of Stereochemical Control of Rac-Et[Ind]2ZrCl2/MAO Catalyst and Properties of Anisotactic Polypropylenes. *Macromolecules* **1990**, *23*, 3559–3568.

(44) Razavi, A.; Atwood, J. L. Preparation and Crystal Structures of the Complexes (η^5-C5H4CPh2- η^5-C13H8) MCl2 (M Zr, Hf) and the Catalytic Formation of High Molecular Weight High Tacticity Syndiotactic Polypropylene. *J. Organomet. Chem.* **1993**, *459*, 117–

123.

(45) Broene, R. D.; Buchwald, S. L. Asymmetric Hydrogenation of Unfunctionalized Trisubstituted Olefins with a Chiral Titanocene Catalyst. *J. Am. Chem. Soc.* **1993**, *115*, 12569–12570.

(46) Willoughby, C. A.; Buchwald, S. L. Asymmetric Titanocene-Catalyzed Hydrogenation of Imines. *J. Am. Chem. Soc.* **1992**, *114*, 7562–7564.

(47) Lee, N. E.; Buchwald, S. L. Asymmetric Hydrogenation of Enamines with a Chiral Titanocene Catalyst. *J. Am. Chem. Soc.* **1994**, *116*, 5985–5986.

(48) Pool, J. A.; Lobkovsky, E.; Chirik, P. J. Hydrogenation and Cleavage of Dinitrogen to Ammonia with a Zirconium Complex. *Nature* **2004**, *427*, 527–530.

(49) Shapiro, P. J.; Bunel, E.; Schaefer, W. P.; Bercaw, J. E. Scandium Complex [{(.Eta.5-C5Me4)Me2Si(.Eta.1-NCMe3)}(PMe3)ScH]2: A Unique Example of a Single-Component α-Olefin Polymerization Catalyst. *Organometallics* **1990**, *9*, 867–869.

(50) McKnight, A. L.; Waymouth, R. M. Group 4 Ansa-Cyclopentadienyl-Amido Catalysts for Olefin Polymerization. *Chem. Rev.* **1998**, *98*, 2587–2598.

(51) Liang, Y.; Yap, G. P. A.; Rheingold, A. L.; Theopold, K. H. Constrained Geometry Chromium Catalysts for Olefin Polymerization. *Organometallics* **1996**, *15*, 5284–5286.

(52) Albers, M. O.; Robinson, D. J.; Singleton, E. Ruthenium and Osmium Complexes Containing Cyclopentadienyl and Related Penta Hapto Dienyl Ligands. *Coord. Chem. Rev.* **1987**, *79*, 1–96.

(53) Davies, S. G.; McNally, J. P.; Smallridge, A. J. Chemistry of the Cyclopentadienyl Bisphosphine Ruthenium Auxiliary. *Adv. Organomet. Chem.* **1990**, *30*, 1–76.

(54) Shvo, Y.; Czarkie, D.; Rahamim, Y.; Chodosh, D. F. A New Group of Ruthenium

Complexes: Structure and Catalysis. *J. Am. Chem. Soc.* **1986**, *108*, 7400–7402.

(55) Casey, C. P.; Guan, H. An Efficient and Chemoselective Iron Catalyst for the Hydrogenation of Ketones. *J. Am. Chem. Soc.* **2007**, *129*, 5816–5817.

(56) Yan, T.; Feringa, B. L.; Barta, K. Benzylamines via Iron-Catalyzed Direct Amination of Benzyl Alcohols. *ACS Catal.* **2016**, *6*, 381–388.

(57) Polidano, K.; Allen, B. D. W.; Williams, J. M. J.; Morrill, L. C. Iron-Catalyzed Methylation Using the Borrowing Hydrogen Approach. *ACS Catal.* **2018**, *8*, 6440–6445.

(58) Khusnutdinova, J. R.; Milstein, D. Metal-Ligand Cooperation. *Angew. Chem., Int. Ed.* **2015**, *54*, 12236–12273.

(59) Gibson, V. C.; Spitzmesser, S. K. Advances in Non-Metallocene Olefin Polymerization Catalysis. *Chem. Rev.* **2003**, *103*, 283–315.

(60) Britovsek, G. J. P.; Gibson, V. C.; Wass, D. F. The Search for New-Generation Olefin Polymerization Catalysts: Life beyond Metallocenes. *Angew. Chem., Int. Ed.* **1999**, *38*, 428–447.

(61) Coates, G. W. Polymerization Catalysis at the Millennium: Frontiers in Stereoselective, Metal-Catalyzed Polymerization. *J. Chem. Soc. Dalton Trans.* **2002**, 467–475.

(62) Coates, G. W.; Hustad, P. D.; Reinartz, S. Catalysts for the Living Insertion Polymerization of Alkenes: Access to New Polyolefin Architectures Using Ziegler–Natta Chemistry. *Angew. Chem., Int. Ed.* **2002**, *41*, 2236.

(63) Lamberti, M.; Mazzeo, M.; Pappalardo, D.; Pellecchia, C. Mechanism of Stereospecific Polymerization of α-Olefins by Late-Transition Metal and Octahedral Group 4 Metal Catalysts. *Coord. Chem. Rev.* **2009**, *253*, 2082–2097.

(64) Delferro, M.; Marks, T. J. Multinuclear Olefin Polymerization Catalysts. *Chem. Rev.* **2011**,

111, 2450–2485.

(65) Gragert, M. M.; Tomov, A. K.; Bettonville, S.; Pannier, G.; White, A. J. P.; Britovsek, G. J. P. Biaryl Group 4 Metal Complexes as Non-Metallocene Catalysts for Polyethylene with Long Chain Branching. *Eur. J. Inorg. Chem.* **2020**, 4088–4092.

(66) Bercaw, J. E.; Marvich, R. H.; Bell, L. G.; Brintzinger, H. H. Titanocene as an Intermediate in Reactions Involving Molecular Hydrogen and Nitrogen. *J. Am. Chem. Soc.* **1972**, *94*, 1219–1238.

(67) Lee, A. V.; Schafer, L. L. Modular N,O-Chelating Ligands: Group-4 Amidate Complexes for Catalytic Hydroamination. *Eur. J. Inorg. Chem.* **2007**, 2243–2255.

(68) Drover, M. W.; Love, J. A.; Schafer, L. L. 1,3-N,O-Complexes of Late Transition Metals. Ligands with Flexible Bonding Modes and Reaction Profiles. *Chem. Soc. Rev.* **2017**, *46*, 2913–2940.

(69) Holm, R. H.; Kennepohl, P.; Solomon, E. I. Structural and Functional Aspects of Metal Sites in Biology. *Chem. Rev.* **1996**, *96*, 2239–2314.

(70) Gorelsky, S. I.; Lapointe, D.; Fagnou, K. Analysis of the Concerted Metalation-Deprotonation Mechanism in Palladium-Catalyzed Direct Arylation across a Broad Range of Aromatic Substrates. *J. Am. Chem. Soc.* **2008**, *130*, 10848–10849.

(71) Lapointe, D.; Fagnou, K. Overview of the Mechanistic Work on the Concerted Metallation-Deprotonation Pathway. *Chem. Lett.* **2010**, *39*, 1118–1126.

(72) Wang, W. H.; Himeda, Y.; Muckerman, J. T.; Manbeck, G. F.; Fujita, E. CO2 Hydrogenation to Formate and Methanol as an Alternative to Photo- and Electrochemical CO2 Reduction. *Chem. Rev.* **2015**, *115*, 12936–12973.

(73) Werkema, E. L.; Castro, L.; Maron, L.; Eisenstein, O.; Andersen, R. A. Cleaving Bonds in

CH3OSO2CF3 with [1,2,4-(Me3C)3C5H2]2CeH; An Experimental and Computational Study. *New J. Chem.* **2013**, *37*, 132–142.

(74) Holler, S.; Tüchler, M.; Belaj, F.; Veiros, L. F.; Kirchner, K.; Mösch-Zanetti, N. C. Thiopyridazine-Based Copper Boratrane Complexes Demonstrating the Z-Type Nature of the Ligand. *Inorg. Chem.* **2016**, *55*, 4980–4991.

(75) Yamaguchi, Y.; Nagashima, H. (η^5-C5Me5)Ru(Amidinate): Highly Reactive Ruthenium Complexes Formally Bearing 16 Valence Electrons Showing Signs of Coordinative Unsaturation. *Organometallics* **2000**, *19*, 725–726.

(76) Coles, M. P. Application of Neutral Amidines and Guanidines in Coordination Chemistry. *J. Chem. Soc. Dalton Trans.* **2006**, *60*, 985–1001.

(77) Jones, C.; Mills, D. P.; Stasch, A. Flexible Coordination of Bulky Amidinates and Guanidinates towards Rhodium(i): Conversion of Kinetic to Thermodymanic Isomers. *J. Chem. Soc. Dalton Trans.* **2008**, 4799–4804.

(78) Kelley, M. R.; Rohde, J. U. Guanidinato Complexes of Iridium: Ligand-Donor Strength, O2 Reactivity, and (Alkene)Peroxoiridium(III) Intermediates. *Inorg. Chem.* **2013**, *52*, 2564–2580.

(79) Wu, Y. Y.; Kao, Y. C.; Chen, J. Der; Hung, C. H. Dimolybdenum Complexes with Mixed Formamidinate Ligands. *Inorganica Chim. Acta* **2004**, *357*, 1002–1010.

(80) Werner, D.; Deacon, G. B.; Junk, P. C.; Anwander, R. Cerium(III/IV) Formamidinate Chemistry, and a Stable Cerium(IV) Diolate. *Chem. Eur. J.* **2014**, *20*, 4426–4438.

(81) Mansfield, N. E.; Coles, M. P.; Hitchcock, P. B. Lithium and Aluminium Complexes Supported by Chelating Phosphaguanidinates. *Dalton Trans.* **2005**, 2833–2841.

(82) Ryken, S. A.; Schafer, L. L. N,O-Chelating Four-Membered Metallacyclic Titanium(IV)

Complexes for Atom-Economic Catalytic Reactions. *Acc. Chem. Res.* **2015**, *48*, 2576–2586.

(83) Clarkson, J. M.; Schafer, L. L. Bis(Tert-Butylimido)Bis(N,O-Chelate)Tungsten(VI) Complexes: Probing Amidate and Pyridonate Hemilability. *Inorg. Chem.* **2017**, *56*, 5553–5566.

(84) Jeffrey, J. C.; Rauchfuss, T. B. Metal Complexes of Hemilabile Ligands. Reactivity and Structure of Dichlorobis (o-(Dipheny Lphosphino) Anisole) Ruthenium (II). *Inorg. Chem.* **1979**, *18*, 2658–2666.

(85) Edwards, P. M.; Schafer, L. L. Early Transition Metal-Catalyzed C-H Alkylation: Hydroaminoalkylation for Csp3-Csp3 Bond Formation in the Synthesis of Selectively Substituted Amines. *Chem. Commun.* **2018**, *54*, 12543–12560.

(86) Chong, E.; Garcia, P.; Schafer, L. Hydroaminoalkylation: Early-Transition-Metal-Catalyzed α-Alkylation of Amines. *Synthesis* **2014**, *46*, 2884–2896.

(87) Pearson, R. G. Hard and Soft Acids and Bases. *J. Am. Chem. Soc.* **1963**, *85*, 3533–3539.

(88) Gribkov, D. V.; Hultzsch, K. C. Hydroamination/Cyclization of Aminoalkenes Using Cationic Zirconocene and Titanocene Catalysts. *Angew. Chem., Int. Ed.* **2004**, *43*, 5542–5546.

(89) Wood, M. C.; Leitch, D. C.; Yeung, C. S.; Kozak, J. A.; Schafer, L. L. Chiral Neutral Zirconium Amidate Complexes for the Asymmetric Hydroamination of Alkenes. *Angew. Chem., Int. Ed.* **2007**, *46*, 354–358.

(90) Moore, C. M.; Szymczak, N. K. Redox-Induced Fluoride Ligand Dissociation Stabilized by Intramolecular Hydrogen Bonding. *Chem. Commun.* **2015**, *51*, 5490–5492.

(91) Li, C.; Thomson, R. K.; Gillon, B.; Patrick, B. O.; Schafer, L. L. Amidate Complexes of Titanium and Zirconium: A New Class of Tunable Precatalysts for the Hydroamination of

Alkynes. *Chem. Commun.* **2003**, *0*, 2462–2463.

(92) Leitch, D. C.; Beard, J. D.; Thomson, R. K.; Wright, V. A.; Patrick, B. O.; Schafer, L. L. N,O-Chelates of Group 4 Metals: Contrasting the Use of Amidates and Ureates in the Synthesis of Metal Dichlorides. *Eur. J. Inorg. Chem.* **2009**, 2691–2701.

(93) Chong, E.; Schafer, L. L. 2-Pyridonate Titanium Complexes for Chemoselectivity. Accessing Intramolecular Hydroaminoalkylation over Hydroamination. *Org. Lett.* **2013**, *15*, 6002–6005.

(94) Garcia, P.; Lau, Y. Y.; Perry, M. R.; Schafer, L. L. Phosphoramidate Tantalum Complexes for Room-Temperature C-H Functionalization: Hydroaminoalkylation Catalysis. *Angew. Chem., Int. Ed.* **2013**, *52*, 9144–9148.

(95) Pritchett, S.; Gantzel, P.; Walsh, P. J. Synthesis and Structural Study of Titanium Bis(Sulfonamido) Bis(Amide) Complexes. *Organometallics* **1999**, *18*, 823–831.

(96) Schmidt, S.; Schäper, R.; Schulz, S.; Bläser, D.; Wölper, C. Insertion Reactions of Heterocumulenes into Zn-C Bonds: Synthesis and Structural Characterization of Multinuclear Zinc Amidate Complexes. *Organometallics* **2011**, *30*, 1073–1078.

(97) Lam, H. W.; Wilkinson, G.; Hussain-Bates, B.; Hursthouse, M. B. Reactions of Tert-Butyl Isocyanate and Trimethylsilyl Azide with Imidoamido Compounds of Chromium, Molybdenum and Tungsten. *J. Chem. Soc. Dalton Trans.* **1993**, *78*, 781–788.

(98) Haehnel, M.; Yim, J. C.-H.; Schafer, L. L.; Rosenthal, U. Facile Access to Tuneable Schwartz's Reagents: Oxidative Addition Products from the Reaction of Amide N-H Bonds with Reduced Zirconocene Complexes. *Angew. Chem., Int. Ed.* **2013**, *52*, 11415–11419.

(99) Kim, J. H.; Britten, J.; Chin, J. Kinetics and Mechanism of a Co(III) Complex Catalyzed Hydration of Nitriles. *J. Am. Chem. Soc.* **1993**, *115*, 3618–3622.

(100) Zhang, Z.; Schafer, L. L. Anti-Markovnikov Intermolecular Hydroamination: A Bis(Amidate) Titanium Precatalyst for the Preparation of Reactive Aldimines. *Org. Lett.* **2003**, *5*, 4733–4736.

(101) Lee, A. V.; Schafer, L. L. A Sequential C-N, C-C Bond-Forming Reaction: Direct Synthesis of α-Amino Acids from Terminal Alkynes. *Synlett* **2006**, 2973–2976.

(102) Zhang, Z.; Leitch, D. C.; Lu, M.; Patrick, B. O.; Schafer, L. L. An Easy-To-Use, Regioselective, and Robust Bis(Amidate) Titanium Hydroamination Precatalyst: Mechanistic and Synthetic Investigations toward the Preparation of Tetrahydroisoquinolines and Benzoquinolizine Alkaloids. *Chem. Eur. J.* **2007**, *13*, 2012–2022.

(103) Zhai, H.; Borzenko, A.; Lau, Y. Y.; Ahn, S. H.; Schafer, L. L. Catalytic Asymmetric Synthesis of Substituted Morpholines and Piperazines. *Angew. Chem., Int. Ed.* **2012**, *51*, 12219–12223.

(104) Yim, J. C. H.; Bexrud, J. A.; Ayinla, R. O.; Leitch, D. C.; Schafer, L. L. Bis(Amidate)Bis(Amido) Titanium Complex: A Regioselective Intermolecular Alkyne Hydroamination Catalyst. *J. Org. Chem.* **2014**, *79*, 2015–2028.

(105) Lui, E. K. J.; Schafer, L. L. Facile Synthesis and Isolation of Secondary Amines via a Sequential Titanium(IV)-Catalyzed Hydroamination and Palladium-Catalyzed Hydrogenation. *Adv. Synth. Catal.* **2016**, *358*, 713–718.

(106) Lau, Y. Y.; Zhai, H.; Schafer, L. L. Catalytic Asymmetric Synthesis of Morpholines. Using Mechanistic Insights to Realize the Enantioselective Synthesis of Piperazines. *J. Org. Chem.* **2016**, *81*, 8696–8709.

(107) Hao, H.; Thompson, K. A.; Hudson, Z. M.; Schafer, L. L. Ti-Catalyzed Hydroamination for

the Synthesis of Amine-Containing π-Conjugated Materials. *Chem. Eur. J.* **2018**, *24*, 5562–5568.

(108) Lui, E. K. J.; Brandt, J. W.; Schafer, L. L. Regio- and Stereoselective Hydroamination of Alkynes Using an Ammonia Surrogate: Synthesis of N -Silylenamines as Reactive Synthons. *J. Am. Chem. Soc.* **2018**, *140*, 4973–4976.

(109) Lui, E. K. J.; Hergesell, D.; Schafer, L. L. N-Silylenamines as Reactive Intermediates: Hydroamination for the Modular Synthesis of Selectively Substituted Pyridines. *Org. Lett.* **2018**, *20*, 6663–6667.

(110) Hao, H.; Schafer, L. L. Metal-Ligand Cooperativity in Titanium-Catalyzed Anti-Markovnikov Hydroamination. *ACS Catal.* **2020**, *10*, 7100–7111.

(111) Varela-Álvarez, A.; Yang, T.; Jennings, H.; Kornecki, K. P.; Macmillan, S. N.; Lancaster, K. M.; Mack, J. B. C.; Du Bois, J.; Berry, J. F.; Musaev, D. G. Rh2(II,III) Catalysts with Chelating Carboxylate and Carboxamidate Supports: Electronic Structure and Nitrene Transfer Reactivity. *J. Am. Chem. Soc.* **2016**, *138*, 2327–2341.

(112) Chong, E.; Brandt, J. W.; Schafer, L. L. 2-Pyridonate Tantalum Complexes for the Intermolecular Hydroaminoalkylation of Sterically Demanding Alkenes. *J. Am. Chem. Soc.* **2014**, *136*, 10898–10901.

(113) Daneshmand, P.; Roşca, S. C.; Dalhoff, R.; Yin, K.; Dipucchio, R. C.; Ivanovich, R. A.; Polat, D. E.; Beauchemin, A. M.; Schafer, L. L. Cyclic Ureate Tantalum Catalyst for Preferential Hydroaminoalkylation with Aliphatic Amines: Mechanistic Insights into Substrate Controlled Reactivity. *J. Am. Chem. Soc.* **2020**, *142*, 15740–15750.

(114) Koperniku, A.; Foth, P. J.; Sammis, G. M.; Schafer, L. L. Zirconium Hydroaminoalkylation. An Alternative Disconnection for the Catalytic Synthesis of α-Arylated Primary Amines. *J.*

Am. Chem. Soc. **2019**, *141*, 18944–18948.

(115) DiPucchio, R. C.; Rosca, S.; Athavan, G.; Schafer, L. L. Exploiting Natural Complexity: Synthetic Terpenoid-Alkaloids by Regioselective and Diastereoselective Hydroaminoalkylation Catalysis. *ChemCatChem* **2019**, *11*, 3871–3876.

(116) DiPucchio, R. C.; Roşca, S. C.; Schafer, L. L. Catalytic and Atom-Economic Csp3 −Csp3 Bond Formation: Alkyl Tantalum Ureates for Hydroaminoalkylation. *Angew. Chem., Int. Ed.* **2018**, *57*, 3469–3472.

(117) Wang, P.; Verma, P.; Xia, G.; Shi, J.; Qiao, J. X.; Tao, S.; Cheng, P. T. W.; Poss, M. A.; Farmer, M. E.; Yeung, K. S.; Yu, J. Q. Ligand-Accelerated Non-Directed C-H Functionalization of Arenes. *Nature* **2017**, *551*, 489–493.

(118) Wang, P.; Farmer, M. E.; Huo, X.; Jain, P.; Shen, P. X.; Ishoey, M.; Bradner, J. E.; Wisniewski, S. R.; Eastgate, M. D.; Yu, J. Q. Ligand-Promoted Meta-C-H Arylation of Anilines, Phenols, and Heterocycles. *J. Am. Chem. Soc.* **2016**, *138*, 9269–9276.

(119) Wang, P.; Li, G. C.; Jain, P.; Farmer, M. E.; He, J.; Shen, P. X.; Yu, J. Q. Ligand-Promoted Meta-C-H Amination and Alkynylation. *J. Am. Chem. Soc.* **2016**, *138*, 14092–14099.

(120) Shi, H.; Wang, P.; Suzuki, S.; Farmer, M. E.; Yu, J. Q. Ligand Promoted Meta-C-H Chlorination of Anilines and Phenols. *J. Am. Chem. Soc.* **2016**, *138*, 14876–14879.

(121) Li, G. C.; Wang, P.; Farmer, M. E.; Yu, J. Q. Ligand-Enabled Auxiliary-Free Meta-C−H Arylation of Phenylacetic Acids. *Angew. Chem., Int. Ed.* **2017**, *56*, 6874–6877.

(122) Shi, H.; Herron, A. N.; Shao, Y.; Shao, Q.; Yu, J. Q. Enantioselective Remote Meta-C-H Arylation and Alkylation via a Chiral Transient Mediator. *Nature* **2018**, *558*, 581–585.

(123) Zhu, R. Y.; Li, Z. Q.; Park, H. S.; Senanayake, C. H.; Yu, J. Q. Ligand-Enabled γ-C(Sp3)-H Activation of Ketones. *J. Am. Chem. Soc.* **2018**, *140*, 3564–3568.

(124) Farmer, M. E.; Wang, P.; Shi, H.; Yu, J. Q. Palladium-Catalyzed Meta-C-H Functionalization of Masked Aromatic Aldehydes. *ACS Catal.* **2018**, *8*, 7362–7367.

(125) Liu, L. Y.; Yeung, K. S.; Yu, J. Q. Ligand-Promoted Non-Directed C−H Cyanation of Arenes. *Chem. Eur. J.* **2019**, *25*, 2199–2202.

(126) Hill, D. E.; Yu, J.-Q.; Blackmond, D. G. Insights into the Role of Transient Chiral Mediators and Pyridone Ligands in Asymmetric Pd-Catalyzed C–H Functionalization. *J. Org. Chem.* **2020**, *85*, 13674–13679.

(127) Sankaralingam, M.; Lee, Y. M.; Karmalkar, D. G.; Nam, W.; Fukuzumi, S. A Mononuclear Non-Heme Manganese(III)-Aqua Complex as a New Active Oxidant in Hydrogen Atom Transfer Reactions. *J. Am. Chem. Soc.* **2018**, *140*, 12695–12699.

(128) Rajabimoghadam, K.; Darwish, Y.; Bashir, U.; Pitman, D.; Eichelberger, S.; Siegler, M. A.; Swart, M.; Garcia-Bosch, I. Catalytic Aerobic Oxidation of Alcohols by Copper Complexes Bearing Redox-Active Ligands with Tunable H-Bonding Groups. *J. Am. Chem. Soc.* **2018**, *140*, 16625–16634.

(129) McManus, C.; Mondal, P.; Lovisari, M.; Twamley, B.; McDonald, A. R. Carboxamidate Ligand Noninnocence in Proton Coupled Electron Transfer. *Inorg. Chem.* **2019**, *58*, 4515–4523.

(130) Müller, T. E.; Hultzsch, K. C.; Yus, M.; Foubelo, F.; Tada, M. Hydroamination: Direct Addition of Amines to Alkenes and Alkynes. *Chem. Rev.* **2008**, *108*, 3795–3892.

(131) Michon, C.; Abadie, M. A.; Medina, F.; Agbossou-Niedercorn, F. Recent Metal-Catalysed Asymmetric Hydroaminations of Alkenes. *J. Organomet. Chem.* **2017**, *847*, 13–27.

(132) Lepori, C.; Hannedouche, J. First-Row Late Transition Metals for Catalytic (Formal) Hydro-amination of Unactivated Alkenes. *Synthesis* **2017**, *49*, 1158–1167.

(133) Hill, M. S.; Liptrot, D. J.; Weetman, C. Alkaline Earths as Main Group Reagents in Molecular Catalysis. *Chem. Soc. Rev.* **2016**, *45*, 972–988.

(134) Pirnot, M. T.; Wang, Y. M.; Buchwald, S. L. Copper Hydride Catalyzed Hydroamination of Alkenes and Alkynes. *Angew. Chem., Int. Ed.* **2016**, *55*, 48–57.

(135) Rodriguez-Ruiz, V.; Carlino, R.; Bezzenine-Lafollée, S.; Gil, R.; Prim, D.; Schulz, E.; Hannedouche, J. Recent Developments in Alkene Hydro-Functionalisation Promoted by Homogeneous Catalysts Based on Earth Abundant Elements: Formation of C-N, C-O and C-P Bond. *Dalton Trans.* **2015**, *44*, 12029–12059.

(136) Huang, L.; Arndt, M.; Gooßen, K.; Heydt, H.; Gooßen, L. J. Late Transition Metal-Catalyzed Hydroamination and Hydroamidation. *Chem. Rev.* **2015**, *115*, 2596–2697.

(137) Villa, M.; Jacobi Von Wangelin, A. Hydroaminations of Alkenes: A Radical, Revised, and Expanded Version. *Angew. Chem., Int. Ed.* **2015**, *54*, 11906–11908.

(138) Haggin, J. Chemists Seek Greater Recognition for Catalysis. *Chem. Eng. News* **1993**, *71*, 23–27.

(139) Johns, A. M.; Sakai, N.; Ridder, A.; Hartwig, J. F. Direct Measurement of the Thermodynamics of Vinylarene Hydroamination. *J. Am. Chem. Soc.* **2006**, *128*, 9306–9307.

(140) Musacchio, A. J.; Lainhart, B. C.; Zhang, X.; Naguib, S. G.; Sherwood, T. C.; Knowles, R. R. Catalytic Intermolecular Hydroaminations of Unactivated Olefins with Secondary Alkyl Amines. *Science* **2017**, *355*, 727–730.

(141) Yang, X. H.; Lu, A.; Dong, V. M. Intermolecular Hydroamination of 1,3-Dienes to Generate Homoallylic Amines. *J. Am. Chem. Soc.* **2017**, *139*, 14049–14052.

(142) Ensign, S. C.; Vanable, E. P.; Kortman, G. D.; Weir, L. J.; Hull, K. L. Anti-Markovnikov Hydroamination of Homoallylic Amines. *J. Am. Chem. Soc.* **2015**, *137*, 13748–13751.

(143) Ichikawa, S.; Zhu, S.; Buchwald, S. L. A Modified System for the Synthesis of Enantioenriched N-Arylamines through Copper-Catalyzed Hydroamination. *Angew. Chem., Int. Ed.* **2018**, *57*, 8714–8718.

(144) Lu, G.; Liu, R. Y.; Yang, Y.; Fang, C.; Lambrecht, D. S.; Buchwald, S. L.; Liu, P. Ligand-Substrate Dispersion Facilitates the Copper-Catalyzed Hydroamination of Unactivated Olefins. *J. Am. Chem. Soc.* **2017**, *139*, 16548–16555.

(145) Shi, S. L.; Wong, Z. L.; Buchwald, S. L. Copper-Catalysed Enantioselective Stereodivergent Synthesis of Amino Alcohols. *Nature* **2016**, *532*, 353–356.

(146) Zhu, S.; Niljianskul, N.; Buchwald, S. L. A Direct Approach to Amines with Remote Stereocentres by Enantioselective CuH-Catalysed Reductive Relay Hydroamination. *Nat. Chem.* **2016**, *8*, 144–150.

(147) Gurak, J. A.; Yang, K. S.; Liu, Z.; Engle, K. M. Directed, Regiocontrolled Hydroamination of Unactivated Alkenes via Protodepalladation. *J. Am. Chem. Soc.* **2016**, *138*, 5805–5808.

(148) Xi, Y.; Butcher, T. W.; Zhang, J.; Hartwig, J. F. Regioselective, Asymmetric Formal Hydroamination of Unactivated Internal Alkenes. *Angew. Chem., Int. Ed.* **2016**, *55*, 776–780.

(149) Lardy, S. W.; Schmidt, V. A. Intermolecular Radical Mediated Anti-Markovnikov Alkene Hydroamination Using N-Hydroxyphthalimide. *J. Am. Chem. Soc.* **2018**, *140*, 12318–12322.

(150) Thomas, A. A.; Speck, K.; Kevlishvili, I.; Lu, Z.; Liu, P.; Buchwald, S. L. Mechanistically Guided Design of Ligands That Significantly Improve the Efficiency of CuH-Catalyzed Hydroamination Reactions. *J. Am. Chem. Soc.* **2018**, *140*, 13976–13984.

(151) Hanley, P. S.; Hartwig, J. F. Migratory Insertion of Alkenes into Metal-Oxygen and Metal-

Nitrogen Bonds. *Angew. Chem., Int. Ed.* **2013**, *52*, 8510–8525.

(152) White, P. B.; Stahl, S. S. Reversible Alkene Insertion into the Pd-N Bond of Pd(II)-Sulfonamidates and Implications for Catalytic Amidation Reactions. *J. Am. Chem. Soc.* **2011**, *133*, 18594–18597.

(153) Neukom, J. D.; Perch, N. S.; Wolfe, J. P. Intramolecular Alkene Aminopalladation Reactions of (Dppf)Pd(Ar)[N(Ar 1)(CH2)3CH-CH2] Complexes. Insertion of Unactivated Alkenes into Pd-N Bonds. *J. Am. Chem. Soc.* **2010**, *132*, 6276–6277.

(154) Neukom, J. D.; Perch, N. S.; Wolfe, J. P. Intramolecular Insertion of Alkenes into Pd-N Bonds. Effects of Substrate and Ligand Structure on the Reactivity of (P-P)Pd(Ar)[N(Ar1)(CH 2)3CR=CHR′] Complexes. *Organometallics* **2011**, *30*, 1269–1277.

(155) Hanley, P. S.; Marković, D.; Hartwig, J. F. Intermolecular Insertion of Ethylene and Octene into a Palladium-Amide Bond. Spectroscopic Evidence for an Ethylene Amido Intermediate. *J. Am. Chem. Soc.* **2010**, *132*, 6302–6303.

(156) Hanley, P. S.; Hartwig, J. F. Intermolecular Migratory Insertion of Unactivated Olefins into Palladium-Nitrogen Bonds. Steric and Electronic Effects on the Rate of Migratory Insertion. *J. Am. Chem. Soc.* **2011**, *133*, 15661–15673.

(157) Milstein, D.; Casalnuovo, A. L.; Calabrese, J. C. Rational Design in Homogeneous Catalysis. Ir(I)-Catalyzed Addition of Aniline to Norbornylene via N-H Activation. *J. Am. Chem. Soc.* **1988**, *110*, 6738–6744.

(158) Cowan, R. L.; Trogler, W. C. Regioselective Insertion of Acrylonitrile into the Platinum-Nitrogen Bond of Hydrido(Phenylamido)Bis(Triethylphosphine)Platinum(II). A Model Step for Olefin Amination. *Organometallics* **1987**, *6*, 2451–2453.

(159) Zhao, P.; Krug, C.; Hartwig, J. F. Transfer of Amido Groups from Isolated Rhodium(I)

Amides to Alkenes and Vinylarenes. *J. Am. Chem. Soc.* **2005**, *127*, 12066–12073.

(160) Leitch, D. C.; Platel, R. H.; Schafer, L. L. Mechanistic Elucidation of Intramolecular Aminoalkene Hydroamination Catalyzed by a Tethered Bis(Ureate) Complex: Evidence for Proton-Assisted C-N Bond Formation at Zirconium. *J. Am. Chem. Soc.* **2011**, *133*, 15453–15463.

(161) Leitch, D. C.; Payne, P. R.; Dunbar, C. R.; Schafer, L. L. Broadening the Scope of Group 4 Hydroamination Catalysis Using a Tethered Ureate Ligand. *J. Am. Chem. Soc.* **2009**, *131*, 18246–18247.

(162) Leitch, D. C.; Turner, C. S.; Schafer, L. L. Isolation of Catalytic Intermediates in Hydroamination Reactions: Insertion of Internal Alkynes into a Zirconium-Amido Bond. *Angew. Chem., Int. Ed.* **2010**, *49*, 6382–6386.

(163) Tobisch, S. Intramolecular Aminoalkene Hydroamination Mediated by a Tethered Bis(Ureate)Zirconium Complex: Computational Perusal of Various Pathways for Aminoalkene Activation. *Inorg. Chem.* **2012**, *51*, 3786–3795.

(164) Germain, S.; Schulz, E.; Hannedouche, J. Anti-Markovnikov Hydroamination of Aromatic Alkenes with Secondary Amines Catalyzed by Easily Accessible Yttrium Complexes. *ChemCatChem* **2014**, *6*, 2065–2073.

(165) Ackermann, L.; Bergman, R. G.; Loy, R. N. Use of Group 4 Bis(Sulfonamido) Complexes in the Intramolecular Hydroamination of Alkynes and Allenes. *J. Am. Chem. Soc.* **2003**, *125*, 11956–11963.

(166) Stubbert, B. D.; Marks, T. J. Mechanistic Investigation of Intramolecular Aminoalkene and Aminoalkyne Hydroamination/Cyclization Catalyzed by Highly Electrophilic, Tetravalent Constrained Geometry 4d and 5f Complexes. Evidence for an M-N σ-Bonded Insertive

Pathway. *J. Am. Chem. Soc.* **2007**, *129*, 6149–6167.

(167) Bexrud, J. A.; Li, C.; Schafer, L. L. Enhanced Reactivity Results in Reduced Catalytic Performance: Unexpected Ligand Reactivity of a Bis(N-2,6-Diisopropylphenylperflourophenyl-Amidate)Titanium-Bis(Diethylamido) Hydroamination Precatalyst. *Organometallics* **2007**, *26*, 6366–6372.

(168) Horrillo-Martínez, P.; Hultzsch, K. C.; Gil, A.; Branchadell, V. Base-Catalyzed Anti-Markovnikov Hydroamination of Vinylarenes – Scope, Limitations and Computational Studies. *Eur. J. Org. Chem.* **2007**, *2007*, 3311–3325.

(169) Reznichenko, A. L.; Nguyen, H. N.; Hultzsch, K. C. Asymmetric Intermolecular Hydroamination of Unactivated Alkenes with Simple Amines. *Angew. Chem., Int. Ed.* **2010**, *49*, 8984–8987.

(170) Liu, B.; Roisnel, T.; Carpentier, J.-F.; Sarazin, Y. When Bigger Is Better: Intermolecular Hydrofunctionalizations of Activated Alkenes Catalyzed by Heteroleptic Alkaline Earth Complexes. *Angew. Chem., Int. Ed.* **2012**, *51*, 4943–4946.

(171) Zhang, X.; Tobisch, S.; Hultzsch, K. C. σ-Insertive Mechanism versus Concerted Non-Insertive Mechanism in the Intramolecular Hydroamination of Aminoalkenes Catalyzed by Phenoxyamine Magnesium Complexes: A Synthetic and Computational Study. *Chem. Eur. J.* **2015**, *21*, 7841–7857.

(172) Tobisch, S. Aluminium-Catalysed Intramolecular Hydroamination of Aminoalkenes: Computational Perusal of Alternative Pathways for Aminoalkene Activation. *Dalton Trans.* **2015**, *44*, 12169–12179.

(173) Tobisch, S. Intermolecular Hydroamination of Vinylarenes by Iminoanilide Alkaline-Earth Catalysts: A Computational Scrutiny of Mechanistic Pathways. *Chem. Eur. J.* **2014**, *20*,

8988–9001.

(174) Tobisch, S. Mechanistic Elucidation of the Yttrium(Iii)-Catalysed Intramolecular Aminoalkene Hydroamination: DFT Favours a Stepwise σ-Insertive Mechanism. *Dalton Trans.* **2012**, *41*, 9182.

(175) Tobisch, S. Metal-Ligand Cooperation in Catalytic Intramolecular Hydroamination: A Computational Study of Iridium-Pyrazolato Cooperative Activation of Aminoalkenes. *Chem. Eur. J.* **2012**, *18*, 7248–7262.

(176) Tobisch, S. Does a Concerted Non-Insertive Mechanism Prevail over a σ-Insertive Mechanism in Catalytic Cyclohydroamination by Magnesium Tris(Oxazolinyl) Phenylborate Compounds? A Computational Study. *Chem. Eur. J.* **2011**, *17*, 14974–14986.

(177) López-Gómez, M. J.; Martin, D.; Bertrand, G. Anti-Bredt N-Heterocyclic Carbene: An Efficient Ligand for the Gold(I)-Catalyzed Hydroamination of Terminal Alkynes with Parent Hydrazine. *Chem. Commun.* **2013**, *49*, 4483–4585.

(178) Yoshida, T.; Adachi, T.; Yabunouchi, N.; Ueda, T.; Okamoto, S. Reversible Addition of Carbonyl Compounds to Parent Imido Complex: Preparation and Crystal Structures of Trans-{Mo(NH)(OTf)(Syn-Me 8[16]AneS4)}OTf and Trans-{Mo[NC(OH)RR′](OTf)(Syn- Me8[16]AneS4)}OTf (R=R′=Me; R=H, R′=Ph). *J. Chem. Soc. Chem. Commun.* **1994**, 151–152.

(179) Zhang, J.; Gunnoe, T. B.; Boyle, P. D. Ruthenium(II) Anilido Complex Containing a Bisphosphine Pincer Ligand: Reversible Formation of Amidinate Ligands via Intramolecular C-N Bond Formation. *Organometallics* **2004**, *23*, 3094–3097.

(180) Muller, F.; Van Koten, G.; Vrieze, K.; Heijdenrijk, D.; Krijnen, B. B.; Stam, C. H. Reactions of Dinuclear Metal Carbonyl .Alpha.-Diimine Complexes with Alkynes. Part 3. Reversible

C-N Bond Formation and Fission between an .Alpha.-Diimine Ligand and a Methyl Propynoate Molecule on a Dinuclear Iron Carbonyl Moiety. X-Ray Crystal Structure. *Organometallics* **1989**, *8*, 41–48.

(181) Liu, Z.; Yamamichi, H.; Madrahimov, S. T.; Hartwig, J. F. Rhodium Phosphine-π-Arene Intermediates in the Hydroamination of Alkenes. *J. Am. Chem. Soc.* **2011**, *133*, 2772–2782.

(182) Rahman, M. M.; Smith, M. D.; Peryshkov, D. V. Imido Group Interchange in Reactions of Zwitterionic Tantalum(V) Vinylimido Complexes and Nitriles. *Organometallics* **2018**, *37*, 2945–2949.

(183) Abou-Shehada, S.; Teasdale, M. C.; Bull, S. D.; Wade, C. E.; Williams, J. M. J. Lewis Acid Activation of Pyridines for Nucleophilic Aromatic Substitution and Conjugate Addition. *ChemSusChem* **2015**, *8*, 1083–1087.

(184) Ghasemi, M. H.; Kowsari, E.; Shafiee, A. Aza-Michael-Type Addition Reaction Catalysed by a Supported Ionic Liquid Phase Incorporating an Anionic Heteropoly Acid. *Tetrahedron Lett.* **2016**, *57*, 1150–1153.

(185) Bhanushali, M. J.; Nandurkar, N. S.; Bhor, M. D.; Bhanage, B. M. Cation Exchange Resin Catalyzed Hydroamination of Vinylpyridines with Aliphatic/Aromatic Amines. *Catal. Commun.* **2008**, *9*, 425–430.

(186) Thomas, D.; Baumann, W.; Spannenberg, A.; Kempe, R.; Rosenthal, U. Zirconocene and Rac- 1,2-Ethylene-1,1′-Bis(H5-Tetrahydroindenyl)Zirconium Complexes of 2-Vinylpyridine: Syntheses, x-Ray Crystal Structures, and Reactions with H2C=CH2, H20, HBF4, and CO2. *Organometallics* **1998**, *17*, 2096–2102.

(187) Haynes, W. M. *CRC Handbook of Chemistry and Physics*, 97th ed.; CRC Press: Boca Raton, 2017.

(188) Liang, Q.; Salmon, A.; Kim, P. J.; Yan, L.; Song, D. Unusual Rearrangement of an N-Donor-Functionalized N-Heterocyclic Carbene Ligand on Group 8 Metals. *J. Am. Chem. Soc.* **2018**, *140*, 1263–1266.

(189) Liang, Q.; Song, D. Reactivity of Fe and Ru Complexes of Picolyl-Substituted *N* -Heterocyclic Carbene Ligand: Diverse Coordination Modes and Small Molecule Binding. *Inorg. Chem.* **2017**, *56*, 11956–11970.

(190) Romero, N.; Dufrois, Q.; Vendier, L.; Dinoi, C.; Etienne, M. Coupling and Dearomatization of Pyridines at a Transient H2-Cyclopropene/Bicyclobutane Zirconocene Complex. *Chem. Eur. J.* **2017**, *23*, 15766–15774.

(191) Mukherjee, A.; Nerush, A.; Leitus, G.; Shimon, L. J. W.; Ben David, Y.; Espinosa Jalapa, N. A.; Milstein, D. Manganese-Catalyzed Environmentally Benign Dehydrogenative Coupling of Alcohols and Amines to Form Aldimines and H2: A Catalytic and Mechanistic Study. *J. Am. Chem. Soc.* **2016**, *138*, 4298–4301.

(192) Reiß, F.; Altenburger, K.; Becker, L.; Schubert, K.; Jiao, H.; Spannenberg, A.; Hollmann, D.; Arndt, P.; Rosenthal, U. Reactions of 2-Substituted Pyridines with Titanocenes and Zirconocenes: Coupling versus Dearomatisation. *Chem. Eur. J.* **2016**, *22*, 3361–3369.

(193) Adams, F.; Machat, M. R.; Altenbuchner, P. T.; Ehrmaier, J.; Pöthig, A.; Karsili, T. N. V.; Rieger, B. Toolbox of Nonmetallocene Lanthanides: Multifunctional Catalysts in Group-Transfer Polymerization. *Inorg. Chem.* **2017**, *56*, 9754–9764.

(194) Yan, C.; Xu, T. Q.; Lu, X. B. From Stereochemically Tunable Homopolymers to Stereomultiblock Copolymers: Lewis Base Regulates Stereochemistry in the Coordination Polymerization of 2-Vinylpyridine. *Macromolecules* **2018**, *51*, 2240–2246.

(195) Xu, T. Q.; Yang, G. W.; Lu, X. B. Highly Isotactic and High-Molecular-Weight Poly(2-

Vinylpyridine) by Coordination Polymerization with Yttrium Bis(Phenolate) Ether Catalysts. *ACS Catal.* **2016**, *6*, 4907–4913.

(196) Altenbuchner, P. T.; Adams, F.; Kronast, A.; Herdtweck, E.; Pöthig, A.; Rieger, B. Stereospecific Catalytic Precision Polymerization of 2-Vinylpyridine via Rare Earth Metal-Mediated Group Transfer Polymerization with 2-Methoxyethylamino-Bis(Phenolate)-Yttrium Complexes. *Polym. Chem.* **2015**, *6*, 6796–6801.

(197) Kronast, A.; Reiter, D.; Altenbuchner, P. T.; Vagin, S. I.; Rieger, B. 2-Methoxyethylamino-Bis(Phenolate)Yttrium Catalysts for the Synthesis of Highly Isotactic Poly(2-Vinylpyridine) by Rare-Earth Metal-Mediated Group Transfer Polymerization. *Macromolecules* **2016**, *49*, 6260–6267.

(198) Leitch, D. C.; Schafer, L. L. Zirconium Alkyl Complexes Supported by Ureate Ligands: Synthesis, Characterization, and Precursors to Metal-Element Multiple Bonds. *Organometallics* **2010**, *29*, 5162–5172.

(199) Johannsen, M.; Jørgensen, K. A. Allylic Amination. *Chem. Rev.* **1998**, *98*, 1689–1708.

(200) Trost, B. M.; Crawley, M. L. Asymmetric Transition-Metal-Catalyzed Allylic Alkylations: Applications in Total Synthesis. *Chem. Rev.* **2003**, *103*, 2921–2943.

(201) Hartwig, J. F. Transition Metal Catalyzed Synthesis of Arylamines and Aryl Ethers from Aryl Halides and Triflates: Scope and Mechanism. *Angew. Chem., Int. Ed.* **1998**, *37*, 2046–2067.

(202) Yang, B. H.; Buchwald, S. L. Palladium-Catalyzed Amination of Aryl Halides and Sulfonates. *J. Organomet. Chem.* **1999**, *576*, 125–146.

(203) Dorel, R.; Grugel, C. P.; Haydl, A. M. The Buchwald–Hartwig Amination After 25 Years. *Angew. Chem., Int. Ed.* **2019**, *58*, 17118–17129.

(204) Forero-Cortés, P. A.; Haydl, A. M. The 25th Anniversary of the Buchwald-Hartwig Amination: Development, Applications, and Outlook. *Org. Process Res. Dev.* **2019**, *23*, 1478–1483.

(205) McGuire, R. T.; Paffile, J. F. J.; Zhou, Y.; Stradiotto, M. Nickel-Catalyzed C-N Cross-Coupling of Ammonia, (Hetero)Anilines, and Indoles with Activated (Hetero)Aryl Chlorides Enabled by Ligand Design. *ACS Catal.* **2019**, *9*, 9292–9297.

(206) Lu, Z.; Ma, S. Metal-Catalyzed Enantioselective Allylation in Asymmetric Synthesis. *Angew. Chem., Int. Ed.* **2008**, *47*, 258–297.

(207) Hartwig, J. F.; Stanley, L. M. Mechanistically Driven Development of Iridium Catalysts for Asymmetric Allylic Substitution. *Acc. Chem. Res.* **2010**, *43*, 1461–1475.

(208) Liu, W. B.; Xia, J. B.; You, S. L. Iridium-Catalyzed Asymmetric Allylic Substitutions. *Top. Organomet. Chem.* **2011**, *38*, 155–207.

(209) Cheng, Q.; Tu, H. F.; Zheng, C.; Qu, J. P.; Helmchen, G.; You, S. L. Iridium-Catalyzed Asymmetric Allylic Substitution Reactions. *Chem. Rev.* **2018**, *119*, 1855–1969.

(210) Sandmeier, T.; Goetzke, F. W.; Krautwald, S.; Carreira, E. M. Iridium-Catalyzed Enantioselective Allylic Substitution with Aqueous Solutions of Nucleophiles. *J. Am. Chem. Soc.* **2019**, *141*, 12212–12218.

(211) Yang, X. H.; Dong, V. M. Rhodium-Catalyzed Hydrofunctionalization: Enantioselective Coupling of Indolines and 1,3-Dienes. *J. Am. Chem. Soc.* **2017**, *139*, 1774–1777.

(212) Tran, G.; Shao, W.; Mazet, C. Ni-Catalyzed Enantioselective Intermolecular Hydroamination of Branched 1,3-Dienes Using Primary Aliphatic Amines. *J. Am. Chem. Soc.* **2019**, *141*, 14814–14822.

(213) Adamson, N. J.; Malcolmson, S. J. Catalytic Enantio- And Regioselective Addition of

Nucleophiles in the Intermolecular Hydrofunctionalization of 1,3-Dienes. *ACS Catal.* **2020**, *10*, 1060–1076.

(214) Beccalli, E. M.; Broggini, G.; Christodoulou, M. S.; Giofrè, S. Transition Metal-Catalyzed Intramolecular Amination and Hydroamination Reactions of Allenes. In *Advances in Organometallic Chemistry*; Academic Press Inc., 2018; Vol. 69, pp 1–71.

(215) Kadota, I.; Shibuya, A.; Lutete, L. M.; Yamamoto, Y. Palladium/Benzoic Acid Catalyzed Hydroamination of Alkynes. *J. Org. Chem.* **1999**, *64*, 4570–4571.

(216) Chen, Q. A.; Chen, Z.; Dong, V. M. Rhodium-Catalyzed Enantioselective Hydroamination of Alkynes with Indolines. *J. Am. Chem. Soc.* **2015**, *137*, 8392–8395.

(217) Lutete, L. M.; Kadota, I.; Yamamoto, Y. Palladium-Catalyzed Intramolecular Asymmetric Hydroamination of Alkynes. *J. Am. Chem. Soc.* **2004**, *126*, 1622–1623.

(218) Patil, N. T.; Lutete, L. M.; Wu, H.; Pahadi, N. K.; Gridnev, I. D.; Yamamoto, Y. Palladium-Catalyzed Intramolecular Asymmetric Hydroamination, Hydroalkoxylation, and Hydrocarbonation of Alkynes. *J. Org. Chem.* **2006**, *71*, 4270–4279.

(219) Athira, C.; Changotra, A.; Sunoj, R. B. Rhodium Catalyzed Asymmetric Hydroamination of Internal Alkynes with Indoline: Mechanism, Origin of Enantioselectivity, and Role of Additives. *J. Org. Chem.* **2018**, *83*, 2627–2639.

(220) Yang, S.; Li, Q. Z.; Xu, C.; Xu, Q.; Shi, M. Rhodium-Catalyzed Asymmetric Hydroamination and Hydroindolation of Keto-Vinylidenecyclopropanes. *Chem. Sci.* **2018**, *9*, 5074–5081.

(221) Buchwald, S. L.; Watson, B. T.; Wannamaker, M. W.; Dewan, J. C. Zirconocene Complexes of Imines: General Synthesis, Structure, Reactivity, and in Situ Generation To Prepare Geometrically Pure Allylic Amines. *J. Am. Chem. Soc.* **1989**, *111*, 4486–4494.

(222) Grossman, R. B.; Davis, W. M.; Buchwald, S. L. Enantioselective, Zirconium-Mediated Synthesis of Allylic Amines. *J. Am. Chem. Soc.* **1991**, *113*, 2321–2322.

(223) Broene, R. D.; Buchwald, S. L. Zirconocene Complexes of Unsaturated Organic Molecules: New Vehicles for Organic Synthesis. *Science* **1993**, *261*, 1696–1701.

(224) Kristian, K. E.; Iimura, M.; Cummings, S. A.; Norton, J. R.; Janak, K. E.; Pang, K. Mechanism of the Reaction of Alkynes with a "Constrained Geometry" Zirconaaziridine. PMe 3 Dissociates More Rapidly from the Constrained Geometry Complex than from Its Cp 2 Analogue. *Organometallics* **2009**, *28*, 493–498.

(225) Cummings, S. A.; Tunge, J. A.; Norton, J. R. Synthesis and Reactivity of Zirconaaziridines. *Top. Organomet. Chem.* **2005**, *10*, 1–39.

(226) Zheng, J.; Breit, B. Regiodivergent Hydroaminoalkylation of Alkynes and Allenes by a Combined Rhodium and Photoredox Catalytic System. *Angew. Chem., Int. Ed.* **2019**, *58*, 3392–3397.

(227) Shi, L.; Xia, W. Photoredox Functionalization of C-H Bonds Adjacent to a Nitrogen Atom. *Chem. Soc. Rev.* **2012**, *41*, 7687–7697.

(228) Nakajima, K.; Miyake, Y.; Nishibayashi, Y. Synthetic Utilization of α-Aminoalkyl Radicals and Related Species in Visible Light Photoredox Catalysis. *Acc. Chem. Res.* **2016**, *49*, 1946–1956.

(229) Dong, Z.; Ren, Z.; Thompson, S. J.; Xu, Y.; Dong, G. Transition-Metal-Catalyzed C-H Alkylation Using Alkenes. *Chem. Rev.* **2017**, *117*, 9333–9403.

(230) Roesky, P. W. Catalytic Hydroaminoalkylation. *Angew. Chem., Int. Ed.* **2009**, *48*, 4892–4894.

(231) Hannedouche, J.; Schulz, E. Hydroamination and Hydroaminoalkylation of Alkenes by

Group 3-5 Elements: Recent Developments and Comparison with Late Transition Metals. *Organometallics* **2018**, *37*, 4313–4326.

(232) Bielefeld, J.; Doye, S. Fast Titanium-Catalyzed Hydroaminomethylation of Alkenes and the Formal Conversion of Methylamine. *Angew. Chem., Int. Ed.* **2020**, *59*, 6138–6143.

(233) Kohls, P.; Jadhav, D.; Pandey, G.; Reiser, O. Visible Light Photoredox Catalysis: Generation and Addition of N -Aryltetrahydroisoquinoline-Derived α-Amino Radicals to Michael Acceptors. *Org. Lett.* **2012**, *14*, 672–675.

(234) Ruiz Espelt, L.; Wiensch, E. M.; Yoon, T. P. Brønsted Acid Cocatalysts in Photocatalytic Radical Addition of α-Amino C-H Bonds across Michael Acceptors. *J. Org. Chem.* **2013**, *78*, 4107–4114.

(235) Thullen, S. M.; Rovis, T. A Mild Hydroaminoalkylation of Conjugated Dienes Using a Unified Cobalt and Photoredox Catalytic System. *J. Am. Chem. Soc.* **2017**, *139*, 15504–15508.

(236) Trowbridge, A.; Reich, D.; Gaunt, M. J. Multicomponent Synthesis of Tertiary Alkylamines by Photocatalytic Olefin-Hydroaminoalkylation. *Nature* **2018**, *561*, 522–527.

(237) Leng, L.; Fu, Y.; Liu, P.; Ready, J. M. Regioselective, Photocatalytic α-Functionalization of Amines. *J. Am. Chem. Soc.* **2020**, *142*, 11972–11977.

(238) Manßen, M.; Lauterbach, N.; Dörfler, J.; Schmidtmann, M.; Saak, W.; Doye, S.; Beckhaus, R. Efficient Access to Titanaaziridines by C-H Activation of N-Methylanilines at Ambient Temperature. *Angew. Chem., Int. Ed.* **2015**, *54*, 4383–4387.

(239) Loose, F.; Schmidtmann, M.; Saak, W.; Beckhaus, R. Imines in the Titanium Coordination Sphere: Highly Reactive Titanaaziridines and Larger Titanacycles Formed by Subsequent C-C Coupling Reactions. *Eur. J. Inorg. Chem.* **2015**, *2015*, 5171–5187.

(240) Bielefeld, J.; Doye, S. Dimethylamine as a Substrate in Hydroaminoalkylation Reactions. *Angew. Chem., Int. Ed.* **2017**, *56*, 15155–15158.

(241) Nugent, W. A.; Ovenall, D. W.; Holmes, S. J. Catalytic C-H Activation in Early Transition-Metal Dialkylamides and Alkoxides. *Organometallics* **1983**, *2*, 161–162.

(242) Prochnow, I.; Zark, P.; Müller, T.; Doye, S. The Mechanism of the Titanium-Catalyzed Hydroaminoalkylation of Alkenes. *Angew. Chem., Int. Ed.* **2011**, *50*, 6401–6405.

(243) Brandt, J. W.; Chong, E.; Schafer, L. L. Ligand Effects and Kinetic Investigations of Sterically Accessible 2-Pyridonate Tantalum Complexes for Hydroaminoalkylation. *ACS Catal.* **2017**, *7*, 6323–6330.

(244) Lauzon, J. M.; Eisenberger, P.; Roşca, S. C.; Schafer, L. L. Amidate Complexes of Tantalum and Niobium for the Hydroaminoalkylation of Unactivated Alkenes. *ACS Catal.* **2017**, *7*, 5921–5931.

(245) Gilmour, D. J.; Lauzon, J. M. P.; Clot, E.; Schafer, L. L. Ta-Catalyzed Hydroaminoalkylation of Alkenes: Insights into Ligand-Modified Reactivity Using DFT. *Organometallics* **2018**, *37*, 4387–4394.

(246) Griffin, S. E.; Pacheco, J.; Schafer, L. L. Reversible C-N Bond Formation in the Zirconium-Catalyzed Intermolecular Hydroamination of 2-Vinylpyridine. *Organometallics* **2019**, *38*, 1011–1016.

(247) Platel, R. H.; Schafer, L. L. Zirconium Catalyzed Alkyne Dimerization for Selective Z-Enyne Synthesis. *Chem. Commun.* **2012**, *48*, 10609–10611.

(248) Koperniku, A.; Schafer, L. L. Zirconium Catalyzed Hydroaminoalkylation for the Synthesis of α-Arylated Amines and N-Heterocycles. *Chem. Eur. J.* **2021**, *27*, 6334–6339.

(249) Kaper, T.; Fischer, M.; Warsitz, M.; Zimmering, R.; Beckhaus, R.; Doye, S. Intermolecular

Hydroaminoalkylation of Propadiene. *Chem. Eur. J.* **2020**, *26*, 14300–14304.

(250) Lauzon, J. M. P.; Schafer, L. L. Tantallaaziridines: From Synthesis to Catalytic Applications. *Dalton Trans.* **2012**, *41*, 11539–11550.

(251) Kempe, R.; Spannenberg, A.; Lefeber, C.; Zippel, T.; Rosenthal, U. Crystal Structure of L-Phenyl-2,2-Bis(Eta5-2,4-Cyclopentadiene-1-Yl)-2-Pyridine-2-Zircona-3-Phenyl-3-Methylaziridine, C32H35N2Zr. *Zeitschrift fur Krist.* **1998**, *213*, 791–792.

(252) Chiu, H. C.; See, X. Y.; Tonks, I. A. Dative Directing Group Effects in Ti-Catalyzed [2+2+1] Pyrrole Synthesis: Chemo- and Regioselective Alkyne Heterocoupling. *ACS Catal.* **2019**, *9*, 216–223.

(253) Zhang, W. X.; Zhang, S.; Xi, Z. Zirconocene and Si-Tethered Diynes: A Happy Match Directed toward Organometallic Chemistry and Organic Synthesis. *Acc. Chem. Res.* **2011**, *44*, 541–551.

(254) Rawson, J. M.; Winpenny, R. E. P. The Coordination Chemistry of 2-Pyridone and Its Derivatives. *Coord. Chem. Rev.* **1995**, *139*, 313–374.

(255) Kuanr, N.; Tomkovic, T.; Gilmour, D. J.; Perry, M. R.; Hsiang, S. J.; Van Ruymbeke, E.; Hatzikiriakos, S. G.; Schafer, L. L. Dynamic Cross-Linking of Catalytically Synthesized Poly(Aminonorbornenes). *Macromolecules* **2020**, *53*, 2649–2661.

(256) Braun, C.; Nieger, M.; Bräse, S.; Schafer, L. L. Planar-Chiral [2.2]Paracyclophane-Based Pyridonates as Ligands for Tantalum-Catalyzed Hydroaminoalkylation. *ChemCatChem* **2019**, *11*, 5264–5268.

(257) Edwards, P. M.; Schafer, L. L. *In Situ* Generation of a Regio- and Diastereoselective Hydroaminoalkylation Catalyst Using Commercially Available Starting Materials. *Org. Lett.* **2017**, *19*, 5720–5723.

(258) Bexrud, J. A.; Eisenberger, P.; Leitch, D. C.; Payne, P. R.; Schafer, L. L. Selective C-H Activation α to Primary Amines. Bridging Metallaaziridines for Catalytic, Intramolecular α-Alkylation. *J. Am. Chem. Soc.* **2009**, *131*, 2116–2118.

(259) Yamaguchi, R.; Ikeda, C.; Takahashi, Y.; Fujita, K. I. Homogeneous Catalytic System for Reversible Dehydrogenation-Hydrogenation Reactions of Nitrogen Heterocycles with Reversible Interconversion of Catalytic Species. *J. Am. Chem. Soc.* **2009**, *131*, 8410–8412.

(260) Fujita, K. I.; Tanaka, Y.; Kobayashi, M.; Yamaguchi, R. Homogeneous Perdehydrogenation and Perhydrogenation of Fused Bicyclic N-Heterocycles Catalyzed by Iridium Complexes Bearing a Functional Bipyridonate Ligand. *J. Am. Chem. Soc.* **2014**, *136*, 4829–4832.

(261) Fujita, K. I.; Wada, T.; Shiraishi, T. Reversible Interconversion between 2,5-Dimethylpyrazine and 2,5-Dimethylpiperazine by Iridium-Catalyzed Hydrogenation/Dehydrogenation for Efficient Hydrogen Storage. *Angew. Chem., Int. Ed.* **2017**, *56*, 10886–10889.

(262) Fujita, K. I.; Tanino, N.; Yamaguchi, R. Ligand-Promoted Dehydrogenation of Alcohols Catalyzed by Cp*Ir Complexes. A New Catalytic System for Oxidant-Free Oxidation of Alcohols. *Org. Lett.* **2007**, *9*, 109–111.

(263) Royer, A. M.; Rauchfuss, T. B.; Wilson, S. R. Coordination Chemistry of a Model for the GP Cofactor in the Hmd Hydrogenase: Hydrogen-Bonding and Hydrogen-Transfer Catalysis. *Inorg. Chem.* **2008**, *47*, 395–397.

(264) Fujita, K. I.; Yoshida, T.; Imori, Y.; Yamaguchi, R. Dehydrogenative Oxidation of Primary and Secondary Alcohols Catalyzed by a Cp*Ir Complex Having a Functional C,N-Chelate Ligand. *Org. Lett.* **2011**, *13*, 2278–2281.

(265) Li, H.; Lu, G.; Jiang, J.; Huang, F.; Wang, Z. X. Computational Mechanistic Study on Cp*Ir

Complex-Mediated Acceptorless Alcohol Dehydrogenation: Bifunctional Hydrogen Transfer vs β-H Elimination. *Organometallics* **2011**, *30*, 2349–2363.

(266) Kawahara, R.; Fujita, K. I.; Yamaguchi, R. Dehydrogenative Oxidation of Alcohols in Aqueous Media Using Water-Soluble and Reusable Cp*Ir Catalysts Bearing a Functional Bipyridine Ligand. *J. Am. Chem. Soc.* **2012**, *134*, 3643–3646.

(267) Kawahara, R.; Fujita, K. I.; Yamaguchi, R. Cooperative Catalysis by Iridium Complexes with a Bipyridonate Ligand: Versatile Dehydrogenative Oxidation of Alcohols and Reversible Dehydrogenation-Hydrogenation between 2-Propanol and Acetone. *Angew. Chem., Int. Ed.* **2012**, *51*, 12790–12794.

(268) Sun, X.; Hu, Y.; Nie, S. Z.; Yan, Y. Y.; Zhang, X. J.; Yan, M. Efficient Construction of C=N Double Bonds via Acceptorless Dehydrogenative Coupling. *Adv. Synth. Catal.* **2013**, *355*, 2179–2184.

(269) Yamaguchi, R.; Kobayashi, D.; Shimizu, M.; Fujita, K. ichi. Synthesis of a Series of Iridium Complexes Bearing Substituted 2-Pyridonates and Their Catalytic Performance for Acceptorless Dehydrogenation of Alcohols under Neutral Conditions. *J. Organomet. Chem.* **2017**, *843*, 14–19.

(270) Shima, S.; Ermler, U. Structure and Function of [Fe]-Hydrogenase and Its Iron-Guanylylpyridinol (FeGP) Cofactor. *Eur. J. Inorg. Chem.* **2011**, *2011*, 963–972.

(271) Pan, H. J.; Huang, G.; Wodrich, M. D.; Tirani, F. F.; Ataka, K.; Shima, S.; Hu, X. A Catalytically Active [Mn]-Hydrogenase Incorporating a Non-Native Metal Cofactor. *Nat. Chem.* **2019**, *11*, 669–675.

(272) Yang, X.; Hall, M. B. Monoiron Hydrogenase Catalysis: Hydrogen Activation with the Formation of a Dihydrogen, Fe-Hδ-···Hδ+-O, Bond and Methenyl-H4MPT+ Triggered

Hydride Transfer. *J. Am. Chem. Soc.* **2009**, *131*, 10901–10908.

(273) Geri, J. B.; Szymczak, N. K. A Proton-Switchable Bifunctional Ruthenium Complex That Catalyzes Nitrile Hydroboration. *J. Am. Chem. Soc.* **2015**, *137*, 12808–12814.

(274) Cotton, F. A.; Lewis, G. E.; Mott, G. N. Dinuclear and Polynuclear Oxovanadium(IV) Compounds. 1. Synthesis and Structural Study of V2O2Cl4(μ-Hmhp)3, a Novel Complex Containing Three Neutral Bridging Ligands. *Inorg. Chem.* **1983**, *22*, 378–382.

(275) Lorber, C.; Choukroun, R.; Vendier, L. Hydroamination of Alkynes Catalyzed by Imido Complexes of Titanium and Vanadium. *Organometallics* **2004**, *23*, 1845–1850.

(276) Zhang, F.; Song, H.; Zi, G. Synthesis and Catalytic Activity of Group 5 Metal Amides with Chiral Biaryldiamine-Based Ligands. *Dalton Trans.* **2011**, *40*, 1547–1566.

(277) Chong, E.; Xue, W.; Storr, T.; Kennepohl, P.; Schafer, L. L. Pyridonate-Supported Titanium(III). Benzylamine as an Easy-To-Use Reductant. *Organometallics* **2015**, *34*, 4941–4945.

(278) Smythe, N. C.; Schrock, R. R.; Müller, P.; Weare, W. W. Synthesis of [(HIPTNCH2CH2)3N]V Compounds (HIPT = 3,5-(2,4,6-i-Pr3C6H2)2C 6H3) and an Evaluation of Vanadium for the Reduction of Dinitrogen to Ammonia. *Inorg. Chem.* **2006**, *45*, 9197–9205.

(279) Vivanco, M.; Ruiz, J.; Floriani, C.; Chiesi-Villa, A.; Rizzoli, C. Chemistry of the Vanadium-Carbon .Sigma. Bond. 1. Insertion of Carbon Monoxide, Isocyanides, Carbon Dioxide, and Heterocumulenes into the V-C Bond of Tris(Mesityl)Vanadium(III). *Organometallics* **1993**, *12*, 1794–1801.

(280) Sohn, H.; Camacho-Bunquin, J.; Langeslay, R. R.; Ignacio-De Leon, P. A.; Niklas, J.; Poluektov, O. G.; Liu, C.; Connell, J. G.; Yang, D.; Kropf, J.; Kim, H.; Stair, P. C.;

Ferrandon, M.; Delferro, M. Isolated, Well-Defined Organovanadium(III) on Silica: Single-Site Catalyst for Hydrogenation of Alkenes and Alkynes. *Chem. Commun.* **2017**, *53*, 7325–7328.

(281) Hoang, T. K. A.; Hamaed, A.; Moula, G.; Aroca, R.; Trudeau, M.; Antonelli, D. M. Kubas-Type Hydrogen Storage in V(III) Polymers Using Tri- and Tetradentate Bridging Ligands. *J. Am. Chem. Soc.* **2011**, *133*, 4955–4964.

(282) Thiele, K.; Görls, H.; Imhof, W.; Seidel, W. Mesityl-Phenolato-Vanadium(III)-Komplexe: Synthese, Struktur Und Verhalten. *Zeitschrift fur Anorg. und Allg. Chemie* **2002**, *628*, 107–118.

(283) Brechin, E. K.; Harris, S. G.; Parsons, S.; Winpenny, R. E. P. High Nuclearity Cobalt-Copper and Nickel-Copper Co-Ordination Complexes. *J. Chem. Soc. Dalton Trans.* **1997**, 3403–3404.

(284) Nikiforova, M. E.; Kiskin, M. A.; Bogomyakov, A. S.; Aleksandrov, G. G.; Sidorov, A. A.; Mironov, V. S.; Eremenko, I. L. Synthesis, Structure, and Magnetic Properties of New Pyridonate-Pivalate Nickel(II) Complex, [Ni11(OH)2(Mhp)8(Piv)10(HCO2)2(H2O)2(Hmhp)2(HPiv)2] (Mhp = 6-Methyl-2-Pyridonate), Containing Formate Bridges. *Inorg. Chem. Commun.* **2011**, *14*, 362–365.

(285) Blake, A. J.; Grant, C. M.; Parsons, S.; Rawson, J. M.; Solan, G. A.; Winpenny, R. E. P. Dalton Communications. Syntheses, Structures and Magnetic Studies of Homometallic Manganese and Heterometallic Iron-Sodium One-Dimensional Polymers. *J. Chem. Soc. Dalton Trans.* **1995**, 2311–2313.

(286) Evans, D. F. 400. The Determination of the Paramagnetic Susceptibility of Substances in Solution by Nuclear Magnetic Resonance. *J. Chem. Soc.* **1959**, 2003–2005.

(287) Sur, S. K. Measurement of Magnetic Susceptibility and Magnetic Moment of Paramagnetic Molecules in Solution by High-Field Fourier Transform NMR Spectroscopy. *J. Magn. Reson.* **1989**, *82*, 169–173.

(288) Grant, D. H. Paramagnetic Susceptibility by NMR: The "Solvent Correction" Reexamined. *J. Chem. Educ.* **1995**, *72*, 39.

(289) Liu, Z.; Li, Q. S.; Xie, Y.; King, R. B.; Schaefer, H. F. Binuclear Vanadium Carbonyls: The Limits of the 18-Electron Rule. *Inorg. Chem.* **2007**, *46*, 1803–1816.

(290) Baker, K. L.; Edwards, D. A.; Fowles, G. W. A.; Williams, R. G. The Reduction of Vanadium(V) Oxytrichloride by Aliphatic Amines and Thioethers. *J. Inorg. Nucl. Chem.* **1967**, *29*, 1881–1885.

(291) Poisel, H. Zur Kenntnis Des 1-Pyrrolins. *Monatshefte für Chemie* **1978**, *109*, 925–928.

(292) Eisenberger, P.; Ayinla, R. O.; Lauzon, J. M. P.; Schafer, L. L. Tantalum-Amidate Complexes for the Hydroaminoalkylation of Secondary Amines: Enhanced Substrate Scope and Enantioselective Chiral Amine Synthesis. *Angew. Chem., Int. Ed.* **2009**, *48*, 8361–8365.

(293) *Topics in Current Chemistry: Selective Catalysis for Renewable Feedstocks and Chemicals;* Nicholas, K. M., Ed.; Springer International Publishing, 2014; Vol. 353.

(294) Chheda, J. N.; Huber, G. W.; Dumesic, J. A. Liquid-Phase Catalytic Processing of Biomass-Derived Oxygenated Hydrocarbons to Fuels and Chemicals. *Angew. Chem., Int. Ed.* **2007**, *46*, 7164–7183.

(295) Dhepe, P.; Tomishige, K.; Wu, K. C.-W. Catalytic Conversion of Biomass. *ChemCatChem* **2017**, *9*, 2613–2614.

(296) Agirrezabal-Telleria, I.; Gandarias, I.; Arias, P. L. Heterogeneous Acid-Catalysts for the Production of Furan-Derived Compounds (Furfural and Hydroxymethylfurfural) from

Renewable Carbohydrates: A Review. *Catal. Today* **2014**, *234*, 42–58.

(297) Yang, W.; Sen, A. One-Step Catalytic Transformation of Carbohydrates and Cellulosic Biomass to 2,5-Dimethyltetrahydrofuran for Liquid Fuels. *ChemSusChem* **2010**, *3*, 597–603.

(298) Mascal, M.; Nikitin, E. B. Towards the Efficient, Total Glycan Utilization of Biomass. *ChemSusChem* **2009**, *2*, 423–426.

(299) De Souza, P. M.; Rabelo-Neto, R. C.; Borges, L. E. P.; Jacobs, G.; Davis, B. H.; Sooknoi, T.; Resasco, D. E.; Noronha, F. B. Role of Keto Intermediates in the Hydrodeoxygenation of Phenol over Pd on Oxophilic Supports. *ACS Catal.* **2015**, *5*, 1318–1329.

(300) Tomishige, K.; Nakagawa, Y.; Tamura, M. Selective Hydrogenolysis of C–O Bonds Using the Interaction of the Catalyst Surface and OH Groups. *Top. Curr. Chem.* **2014**, *353*, 127–162.

(301) Hong, Y. K.; Lee, D. W.; Eom, H. J.; Lee, K. Y. The Catalytic Activity of Pd/WOx/γ-Al2O3 for Hydrodeoxygenation of Guaiacol. *Appl. Catal. B Environ.* **2014**, *150–151*, 438–445.

(302) McLaughlin, M. P.; Adduci, L. L.; Becker, J. J.; Gagné, M. R. Iridium-Catalyzed Hydrosilylative Reduction of Glucose to Hexane(S). *J. Am. Chem. Soc.* **2013**, *135*, 1225–1227.

(303) Martin, A.; Armbruster, U.; Gandarias, I.; Arias, P. L. Glycerol Hydrogenolysis into Propanediols Using in Situ Generated Hydrogen - A Critical Review. *Eur. J. Lipid Sci. Technol.* **2013**, *115*, 9–27.

(304) Murru, S.; Nicholas, K. M.; Srivastava, R. S. Ruthenium (II) Sulfoxides-Catalyzed Hydrogenolysis of Glycols and Epoxides. *J. Mol. Catal. A Chem.* **2012**, *363–364*, 460–464.

(305) Schlaf, M.; Ghosh, P.; Fagan, P. J.; Hauptman, E.; Morris Bullock, R. Catalytic

Deoxygenation of 1,2-Propanediol to Give n-Propanol. *Adv. Synth. Catal.* **2009**, *351*, 789–800.

(306) Larson, G. L.; Fry, J. L. *Ionic and Organometallic-Catalyzed Organosilane Reductions*; John Wiley & Sons, Inc.: Hoboken, 2009.

(307) Yasuda, M.; Onishi, Y.; Ueba, M.; Miyai, T.; Baba, A. Direct Reduction of Alcohols: Highly Chemoselective Reducing System for Secondary or Tertiary Alcohols Using Chlorodiphenylsilane with a Catalytic Amount of Indium Trichloride. *J. Org. Chem.* **2001**, *66*, 7741–7744.

(308) Mayr, H.; Dogan, B. Selectivities in Ionic Reductions of Alcohols and Ketones with Triethylsilane/Trifluoroacetic Acid. *Tetrahedron Lett.* **1997**, *38*, 1013–1016.

(309) Petersen, A. R.; Fristrup, P. New Motifs in Deoxydehydration: Beyond the Realms of Rhenium. *Chem. Eur. J.* **2017**, *23*, 10235–10243.

(310) Dethlefsen, J. R.; Fristrup, P. Rhenium-Catalyzed Deoxydehydration of Diols and Polyols. *ChemSusChem* **2015**, *8*, 767–775.

(311) Mao, G.; Jia, B.; Wang, C.; Guoliang, M.; Bing, J.; Congyang, W. Recent Progress in Re-Catalyzed Dehydroxylation Reactions. *Chinese J. Org. Chem.* **2015**, *35*, 284.

(312) Chapman, G.; Nicholas, K. M. Vanadium-Catalyzed Deoxydehydration of Glycols. *Chem. Commun.* **2013**, *49*, 8199–8201.

(313) Gopaladasu, T. V; Nicholas, K. M. Carbon Monoxide (CO)- and Hydrogen-Driven, Vanadium-Catalyzed Deoxydehydration of Glycols. *ACS Catal.* **2016**, *6*, 1901–1904.

(314) Petersen, A. R.; Nielsen, L. B.; Dethlefsen, J. R.; Fristrup, P. Vanadium-Catalyzed Deoxydehydration of Glycerol Without an External Reductant. *ChemCatChem* **2018**, *10*, 769–778.

(315) Kasner, G. R.; Boucher-Jacobs, C.; Michael McClain, J.; Nicholas, K. M. Oxo-Rhenium Catalyzed Reductive Coupling and Deoxygenation of Alcohols. *Chem. Commun.* **2016**, *52*, 7257–7260.

(316) Steffensmeier, E.; Nicholas, K. M. Oxidation-Reductive Coupling of Alcohols Catalyzed by Oxo-Vanadium Complexes. *Chem. Commun.* **2018**, *54*, 790–793.

(317) Boucher-Jacobs, C.; Liu, P.; Nicholas, K. M. Mechanistic Insights into the ReIO2(PPh3)2-Promoted Reductive Coupling of Alcohols. *Organometallics* **2018**, *37*, 2468–2480.

(318) Steffensmeier, E.; Swann, M. T.; Nicholas, K. M. Mechanistic Features of the Oxidation–Reductive Coupling of Alcohols Catalyzed by Oxo-Vanadium Complexes. *Inorg. Chem.* **2019**, *58*, 844–854.

(319) Sakuramoto, T.; Donaka, Y.; Tobisu, M.; Moriuchi, T. Oxovanadium(v)-Catalyzed Deoxygenative Homocoupling Reaction of Alcohols. *New J. Chem.* **2019**, *43*, 17571–17576.

(320) Bulut, S.; Siankevich, S.; Van Muyden, A. P.; Alexander, D. T. L.; Savoglidis, G.; Zhang, J.; Hatzimanikatis, V.; Yan, N.; Dyson, P. J. Efficient Cleavage of Aryl Ether C-O Linkages by Rh-Ni and Ru-Ni Nanoscale Catalysts Operating in Water. *Chem. Sci.* **2018**, *9*, 5530–5535.

(321) Cattelan, L.; Yuen, A. K. L.; Lui, M. Y.; Masters, A. F.; Selva, M.; Perosa, A.; Maschmeyer, T. Renewable Aromatics from Kraft Lignin with Molybdenum-Based Catalysts. *ChemCatChem* **2017**, *9*, 2717–2726.

(322) Reynolds, J. G.; Sendlinger, S. C.; Murray, A. M.; Huffman, J. C.; Christou, G. Synthesis and Characterization of Vanadium(II,III,IV) Complexes of Pyridine-2-Thiolate. *Inorg. Chem.* **1995**, *34*, 5745–5752.

(323) Crabtree, R. H. Homogeneous Transition Metal Catalysis of Acceptorless Dehydrogenative Alcohol Oxidation: Applications in Hydrogen Storage and to Heterocycle Synthesis. *Chem. Rev.* **2017**, *117*, 9228–9246.

(324) Miao, Y.; Samuelsen, S. V.; Madsen, R. Vanadium- and Chromium-Catalyzed Dehydrogenative Synthesis of Imines from Alcohols and Amines. *Organometallics* **2021**, *40*, 1328–1335.

(325) Liu, F.; Pak, E. B.; Singh, B.; Jensen, C. M.; Goldman, A. S. Dehydrogenation of N-Alkanes Catalyzed by Iridium "pincer" Complexes: Regioselective Formation of α-Olefins. *J. Am. Chem. Soc.* **1999**, *121*, 4086–4087.

(326) Bandari, C.; Nicholas, K. M. Oxo-Rhenium-Catalyzed Radical Addition of Benzylic Alcohols to Olefins. *J. Org. Chem.* **2020**, *85*, 3320–3327.

(327) Beller, M.; Seayad, J.; Tillack, A.; Jiao, H. Catalytic Markovnikov and Anti-Markovnikov Functionalization of Alkenes and Alkynes: Recent Developments and Trends. *Angew. Chem., Int. Ed.* **2004**, *43*, 3368–3398.

(328) Hintermann, L. Recent Developments in Metal-Catalyzed Additions of Oxygen Nucleophiles to Alkenes and Alkynes. *Top. Organomet. Chem.* **2010**, *31*, 123–155.

(329) Kawaguchi, S. ichi; Yamamoto, Y.; Ogawa, A. Catalytic Synthesis of Sulfur and Phosphorus Compounds via Atom-Economic Reactions. *Mendeleev Commun.* **2020**, *30*, 129–138.

(330) Ward, B. J.; Hunt, P. A. Hydrophosphination of Styrene and Polymerization of Vinylpyridine: A Computational Investigation of Calcium-Catalyzed Reactions and the Role of Fluxional Noncovalent Interactions. *ACS Catal.* **2017**, *7*, 459–468.

(331) Alunni, S.; De Angelis, F.; Ottavi, L.; Papavasileiou, M.; Tarantelli, F. Evidence of a

Borderline Region between E1cb and E2 Elimination Reaction Mechanisms: A Combined Experimental and Theoretical Study of Systems Activated by the Pyridine Ring. *J. Am. Chem. Soc.* **2005**, *127*, 15151–15160.

(332) Langeslay, R. R.; Kaphan, D. M.; Marshall, C. L.; Stair, P. C.; Sattelberger, A. P.; Delferro, M. Catalytic Applications of Vanadium: A Mechanistic Perspective. *Chem. Rev.* **2019**, *119*, 2128–2191.

(333) Palluccio, T. D.; Rybak-Akimova, E. V.; Majumdar, S.; Cai, X.; Chui, M.; Temprado, M.; Silvia, J. S.; Cozzolino, A. F.; Tofan, D.; Velian, A.; Cummins, C. C.; Captain, B.; Hoff, C. D. Thermodynamic and Kinetic Study of Cleavage of the N-O Bond of N-Oxides by a Vanadium(III) Complex: Enhanced Oxygen Atom Transfer Reaction Rates for Adducts of Nitrous Oxide and Mesityl Nitrile Oxide. *J. Am. Chem. Soc.* **2013**, *135*, 11357–11372.

(334) Morse, D. B.; Rauchfuss, T. B.; Wilson, S. R. Main-Group-Organotransition-Metal Chemistry: The Cyclopentadienylchromium Polyiodides Including [(C5Me5)2Cr2I3+]2[I162-]. *J. Am. Chem. Soc.* **1990**, *112*, 1860–1864.

(335) Choudhary, N. F.; Connelly, N. G.; Hitchcock, P. B.; Leigh, G. J. New Compounds of Tetradentate Schiff Bases with Vanadium(IV) and Vanadium(V). *J. Chem. Soc. Dalton Trans.* **1999**, 4437–4446.

(336) Svensson, P. H.; Kloo, L. Synthesis, Structure, and Bonding in Polyiodide and Metal Iodide-Iodine Systems. *Chem. Rev.* **2003**, *103*, 1649–1684.

(337) Neuse, E. W.; Loonat, M. S. Ferricenium Polyiodides. *J. Organomet. Chem.* **1985**, *286*, 329–341.

(338) Kempe, R. The Strained η^2-Namido-Npyridine Coordination of Aminopyridinato Ligands. *Eur. J. Inorg. Chem.* **2003**, 791–803.

(339) Spannenberg, A.; Tillack, A.; Arndt, P.; Kirmse, R.; Kempe, R. Homoleptic Trisaminopyridinato MIII Complexes (M = Ti, V and Cr), Synthesis, Structure and EPR Investigations. *Polyhedron* **1998**, *17*, 845–850.

(340) Kaga, A.; Chiba, S. Engaging Radicals in Transition Metal-Catalyzed Cross-Coupling with Alkyl Electrophiles: Recent Advances. *ACS Catal.* **2017**, *7*, 4697–4706.

(341) Weix, D. J. Methods and Mechanisms for Cross-Electrophile Coupling of Csp ^{2} Halides with Alkyl Electrophiles. *Acc. Chem. Res.* **2015**, *48*, 1767–1775.

(342) Knappke, C. E. I.; Grupe, S.; Gärtner, D.; Corpet, M.; Gosmini, C.; Jacobi Von Wangelin, A. Reductive Cross-Coupling Reactions between Two Electrophiles. *Chem. Eur. J.* **2014**, *20*, 6828–6842.

(343) Gu, J.; Wang, X.; Xue, W.; Gong, H. Nickel-Catalyzed Reductive Coupling of Alkyl Halides with Other Electrophiles: Concept and Mechanistic Considerations. *Org. Chem. Front.* **2015**, *2*, 1411–1421.

(344) Suga, T.; Ukaji, Y. Nickel-Catalyzed Cross-Electrophile Coupling between Benzyl Alcohols and Aryl Halides Assisted by Titanium Co-Reductant. *Org. Lett.* **2018**, *20*, 7846–7850.

(345) Ackerman, L. K. G.; Anka-Lufford, L. L.; Naodovic, M.; Weix, D. J. Cobalt Co-Catalysis for Cross-Electrophile Coupling: Diarylmethanes from Benzyl Mesylates and Aryl Halides. *Chem. Sci.* **2015**, *6*, 1115–1119.

(346) Guo, P.; Wang, K.; Jin, W. J.; Xie, H.; Qi, L.; Liu, X. Y.; Shu, X. Z. Dynamic Kinetic Cross-Electrophile Arylation of Benzyl Alcohols by Nickel Catalysis. *J. Am. Chem. Soc.* **2021**, *143*, 513–523.

(347) Li, Z.; Sun, W.; Wang, X.; Li, L.; Zhang, Y.; Li, C. Electrochemically Enabled, Nickel-

Catalyzed Dehydroxylative Cross-Coupling of Alcohols with Aryl Halides. *J. Am. Chem. Soc.* **2021**, *143*, 3543.

(348) Shields, B. J.; Doyle, A. G. Direct C(Sp3)-H Cross Coupling Enabled by Catalytic Generation of Chlorine Radicals. *J. Am. Chem. Soc.* **2016**, *138*, 12719–12722.

(349) Zucchini, U.; Albizzati, E.; Giannini, U. Synthesis and Properties of Some Titanium and Zirconium Benzyl Derivatives. *J. Organomet. Chem.* **1971**, *26*, 357–372.

(350) Moorhouse, S.; Wilkinson, G. Bis[(Trimethylsilyl)Methyl]- and Bis(Neopentyl)-Zinc, and Tris[(Trimethylsilyl)Methyl]Aluminium-Diethyl Ether (1/1); Their Use as Alkylating Agents in Forming Niobium and Tantalum Alkyls. *J. Chem. Soc. Dalton Trans.* **1974**, 2187–2190.

(351) Fu, S.; Chen, N. Y.; Liu, X.; Shao, Z.; Luo, S. P.; Liu, Q. Ligand-Controlled Cobalt-Catalyzed Transfer Hydrogenation of Alkynes: Stereodivergent Synthesis of Z- and E-Alkenes. *J. Am. Chem. Soc.* **2016**, *138*, 8588–8594.

(352) Gregori, B. J.; Schwarzhuber, F.; Pöllath, S.; Zweck, J.; Fritsch, L.; Schoch, R.; Bauer, M.; Jacobi von Wangelin, A. Stereoselective Alkyne Hydrogenation by Using a Simple Iron Catalyst. *ChemSusChem* **2019**, *12*, 3864–3870.

(353) William, R.; Wang, S.; Ding, F.; Arviana, E. N.; Liu, X. W. Interrupted Imino-Nazarov Cyclization of 1-Aminopentadienyl Cation and Related Cascade Process. *Angew. Chem., Int. Ed.* **2014**, *53*, 10742–10746.

(354) Liu, Q.; Yu, S.; Hu, L.; Hussain, M. I.; Zhang, X.; Xiong, Y. Cross-Dehydrogenative Coupling Strategy for Phosphonation and Cyanation of Secondary N-Alkyl Anilines by Employing 2,3-Dichloro-5,6-Dicyanobenzoquinone. *Tetrahedron* **2018**, *74*, 7209–7217.

(355) Overman, L. E.; Tsuboi, S.; Rons, J. P.; Taylor, G. F. Preparation of Substituted 2-Pyridones

by Thermal Rearrangement of Propargylic Pyrrolidine Pseudoureas. *J. Am. Chem. Soc.* **1980**, *102*, 747–754.

(356) Hintermann, L.; Dang, T. T.; Labonne, A.; Kribber, T.; Xiao, L.; Naumov, P. The AZARYPHOS Family of Ligands for Ambifunctional Catalysis: Syntheses and Use in Ruthenium-Catalyzed Anti-Markovnikov Hydration of Terminal Alkynes. *Chem. Eur. J.* **2009**, *15*, 7167–7179.

(357) Frisch, M. J.; Trucks, G. W.; Schlegel, H. B.; Scuseria, G. E.; Robb, M. A.; Cheeseman, J. R.; Scalmani, G.; Barone, V.; Mennucci, B.; Petersson, G. A.; Nakatsuji, H.; Caricato, M.; Li, X.; Hratchian, H. P.; Izmaylov, A. F.; Bloino, J.; Zheng, G.; Sonnenberg, J. L.; Hada, M.; Ehara, M.; Toyota, K.; Fukuda, R.; Hasegawa, J.; Ishida, M.; Nakajima, T.; Honda, Y.; Kitao, O.; Nakai, H.; Vreven, T.; Montgomery, J. A.; Peralta, J. E.; Ogliaro, F.; Bearpark, M.; Heyd, J. J.; Brothers, E. .; Kudin, K. N.; Staroverov, V. N. Kobayashi, R.; Normand, J.; Raghavachari, K.; Rendell, A.; Burant, J. C.; Iyengar, S. S.; Tomasi, J.; Cossi, M.; Rega, N.; Millam, M. J.; Klene, M.; Knox, J. E.; Cross, J. B.; Bakken, V.; Adamo, C.; Jaramillo, J.; Gomperts, R.; Stratmann, R. E.; Yazyev, O.; Austin, A. J.; Cammi, R.; Pomelli, C.; Ochterski, J. W.; Martin, R. L.; Morokuma, K.; Zakrzewski, V. G.; Voth, G. A.; Salvador, P.; Dannenberg, J. J. Dapprich, S.; Daniels, A. D.; Farkas, Ö.; Foresman, J. B.; Ortiz, J. V.; Cioslowski, J.; Fox, D. J. Gaussian 09, Revision D.01; Gaussian, Inc.: Wallingford, CT, 2009.

(358) Becke, A. D. Density-Functional Thermochemistry. III. The Role of Exact Exchange. *J. Chem. Phys.* **1993**, *98*, 5648–5652.

(359) Stephens, P. J.; Devlin, F. J.; Chabalowski, C. F.; Frisch, M. J. Ab Initio Calculation of Vibrational Absorption and Circular Dichroism Spectra Using Density Functional Force

Fields. *J. Phys. Chem.* **1994**, *98*, 11623–11627.

(360) Becke, A. D.; Johnson, E. R. A Unified Density-Functional Treatment of Dynamical, Nondynamical, and Dispersion Correlations. *J. Chem. Phys.* **2007**, *127*, 124108.

(361) Marenich, A. V.; Cramer, C. J.; Truhlar, D. G. Universal Solvation Model Based on Solute Electron Density and on a Continuum Model of the Solvent Defined by the Bulk Dielectric Constant and Atomic Surface Tensions. *J. Phys. Chem. B* **2009**, *113*, 6378−6396.

(362) Humphrey, W.; Dalke, A.; Schulten, K. VMD: Visual Molecular Dynamics. *J. Mol. Graph.* **1996**, *14*, 33–38.

(363) Dolomanov, O. V.; Bourhis, L. J.; Gildea, R. J.; Howard, J. A. K.; Puschmann, H. OLEX2: A Complete Structure Solution, Refinement and Analysis Program. *J. Appl. Cryst.* **2009**, *42*, 339.

(364) Sheldrick, G. M. SHELXT - Integrated Space-Group and Crystal-Structure Determination. *Acta Cryst. Sect. A* **2015**, *71*, 3.

(365) Sheldrick, G. M. Crystal Structure Refinement with SHELXL. *Acta Cryst. Sect. C* **2015**, *71*, 3.

(366) Spek, A. L. PLATON SQUEEZE: A Tool for the Calculation of the Disordered Solvent Contribution to the Calculated Structure Factors. *Acta Crystallogr. Sect. C Struct. Chem.* **2015**, *71*, 9–18.

(367) Dowling, G.; Kavanagh, P. V.; Talbot, B.; O'Brien, J.; Hessman, G.; McLaughlin, G.; Twamley, B.; Brandt, S. D. Outsmarted by Nootropics? An Investigation into the Thermal Degradation of Modafinil, Modafinic Acid, Adrafinil, CRL-40,940 and CRL-40,941 in the GC Injector: Formation of 1,1,2,2-Tetraphenylethane and Its Tetra Fluoro Analog. *Drug Test. Anal.* **2017**, *9*, 518–528.

(368) Utsunomiya, M.; Kuwano, R.; Kawatsura, M.; Hartwig, J. F. Rhodium-Catalyzed Anti-Markovnikov Hydroamination of Vinylarenes. *J. Am. Chem. Soc.* **2003**, *125*, 5608–5609.

Appendices

Appendix A Experimental

A.1 General Considerations

All air and moisture sensitive compounds were manipulated under inert N_2 atmosphere using an MBraun LABmaster glovebox or standard Schlenk techniques. Glassware and Teflon® coated magnetic stir bars were dried in a 160 °C oven for at least 4 hours prior to transferring to the glovebox or Schlenk manifold. Toluene and hexanes were passed through an activated alumina column under N_2 gas, collected in a Teflon® sealed Straus flask, and sparged with N_2 for 30 minutes prior to use. THF, benzene-d_6, and toluene-d_8 were dried over sodium metal and distilled under N_2 and collected in a Teflon® sealed Straus flask prior to use. Diatomaceous earth was dried in an oven at 160 °C for at least 24 hours before transferring to the glovebox. J. Young NMR tubes (8" x 5 mm) with Teflon® screw-caps were used for NMR reactions. ^{1}H, ^{13}C{^{1}H}, and ^{19}F{^{1}H} NMR spectra were collected using a Bruker 300 MHz or 400 MHz Avance spectrometer at 298 K unless otherwise noted. Chemical shifts, δ, are reported relative to the corresponding residual protio solvent in parts per million (ppm). Coupling constants, J, are given in Hertz (Hz). Signal multiplicity is reported using the following abbreviations: s = singlet, d = doublet, t = triplet, q = quartet, sep = septet, m = multiplet, and br = broad. For van't Hoff experiments and NMR yield determinations, T_1 relaxation times for the relevant signals were estimated using a spin-echo pulse sequence and relaxation delays were extended accordingly during ^{1}H NMR data collection. The internal standard used for quantitative ^{1}H NMR experiments in Chapters 3 and 5 was 1,3,5-trimethoxybenzene and the chemical shifts associated with it are the following: ^{1}H NMR (C_6D_6, 400 MHz) δ = 6.25 (s, 3H), 3.32 (s, 9H). Effective magnetic moments were determined using the Evans Method,[286–288] using coaxial inserts containing 1 mol% cyclooctane in benzene-d_6. Mass

spectra were collected using one of the following: a Kratos MS-50 spectrometer equipped with an electron impact (EI, 70 eV) source; a Jeol AccuTOF GCv 4G spectrometer equipped with a Liquid Injection Field Desorption Ionization (LIFDI) probe; or an Agilent 6545 QTOF spectrometer equipped with an electrospray or field desorption ionization source. The fragments are given in mass per charge number (*m/z*). GC-MS experiments were performed using an Agilent 7890A GC equipped with a 5975C inert XL EI/CI mass detector, operated in positive CI mode and using methane as the reagent gas. Elemental analysis (EA) was performed with a Thermo Flash 2000 Elemental Analyzer. The elemental composition values are given in percentages (%). Single crystal X-ray diffraction data were collected using a Bruker X8 APEX or Bruker APEX DUO diffractometer. All chemicals were purchased from commercial sources and used without further purification, and those which were not already dried and stored under inert atmosphere were either dried over calcium hydride and degassed via the freeze-pump-thaw method or sublimed or dried under high vacuum before use.

For Chapter 2, all amines and 2-vinylpyridine were dried over calcium hydride and distilled under N_2 before degassing via the freeze-pump-thaw method and bringing them into the glovebox or using them on the Schlenk manifold. Tetrabenzylzirconium(IV)[349] and compounds **2.1**,[161] **2.2**,[198] and **2.3**[160] were prepared according to literature methods. Crystals of **2.2** suitable for X-ray diffraction studies were grown from a concentrated toluene solution at −35 °C.

For Chapter 3, all liquid amines were dried over molecular sieves before degassing via the freeze-pump-thaw method and bringing them into the glovebox. All solid amines were dried and degassed in a drying tube before bringing them into the glovebox. All solid alkynes were sublimed or dried under high vacuum before use. All liquid alkynes were dried over calcium hydride and distilled under vacuum before degassing via the freeze-pump-thaw method and bringing them into

the glovebox. The bis(urea) proligand $H_2(N,O)_2$,[92] dibenzyl complex **2.2**,[198] sodium ureate salt **D**,[116] $Ta(CH_2SiMe_3)_3Cl_2$,[350] and titanium formamidinate complex **E**[240] were prepared according to literature procedures. All alkynes[351,352] and amines[353,354] that were not commercially available were synthesized according to literature methods.

For Chapter 4, trimesitylvanadium(III)-tetrahydrofuran (complex **4.9**),[279] amide **4.11**,[109] and pyridone **4.13**[93] were synthesized according to literature procedures.

For Chapter 5, trimesitylvanadium(III)-tetrahydrofuran (complex **4.9**),[279] amide **4.11**,[109] 6-isopropyl-2-hydroxypyridine,[355] and 6-tertbutyl-2-hydroxypyridine[356] were synthesized according to literature procedures.

A.2 Experimental Data for Chapter 2

Synthesis of Complexes

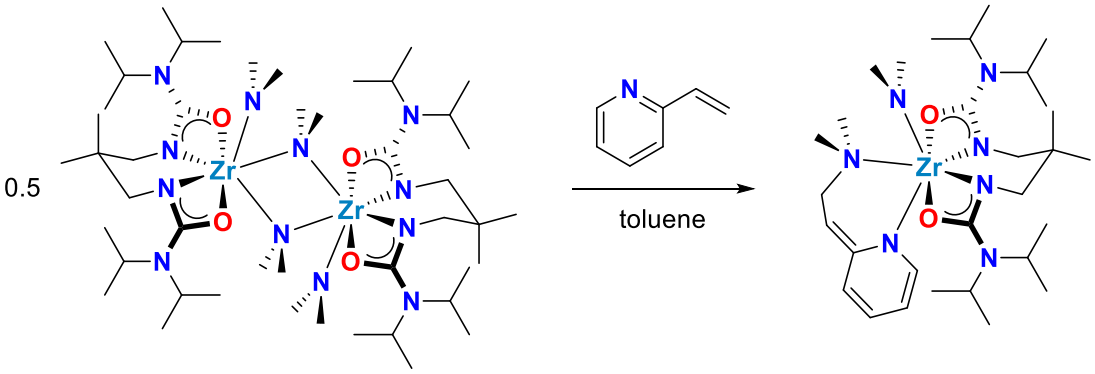

2.3 **2.4** 61% yield

Synthesis of 2.4: A 20 mL vial was charged with bis(amido) complex **2.3** (0.165 g, 0.155 mmol) before dissolving in ~5 mL toluene via gentle heating and vigorous swirling to give a clear, colourless solution. 2-Vinylpyridine (0.033 g, 0.31 mmol) was then added directly to the concentrated solution of **2.3** using ~0.5 mL toluene for quantitative transfer, causing an immediate colour change to bright orange. The vial was then placed in a freezer at –35 °C for several days, during which time bright orange crystals suitable for X-ray diffraction precipitated out of solution. After removing the supernatant, the crystals were washed with cold hexanes (5 x ~0.25 mL) and the residual solvent was allowed to evaporate, giving 0.120 g of material (61% yield). ^{1}H NMR (C_6D_6, 400 MHz) δ = 7.04 (br d, 6.5 Hz, 1H), 6.23 (br d, J = 9.0 Hz, 1H), 6.21 (ddd, J = 9.0, 5.4, 1.6 Hz, 1H), 5.20 (ddd, J = 6.5, 5.4, 1.6 Hz, 1H), 4.19 (t, J = 7.1 Hz, 1H), 3.62 (br sep, J = 6.7 Hz, 4H), 3.44 (d, J = 11.5 Hz, 2H), 3.25 (d, J = 11.5 Hz, 2H), 3.22 (br m, 2H), 3.11 (br s, 6H), 2.61 (br s, 6H), 1.25 (d, J = 6.7 Hz, 12H), 1.22 (br s, 3H), 1.17 (d, J = 6.7 Hz, 12H), 0.90 (br s, 3H); ^{13}C NMR (C_6D_6, 100 MHz) δ = 167.3, 156.3, 146.9, 127.4, 121.1, 96.3, 79.9, 59.2, 57.8, 57.3, 46.6, 45.4, 36.8, 28.2, 22.2, 22.1, 21.5. The molecular ion was not observed by MS, instead the ion corresponding to a loss of 2-vinylpyridine was observed: MS(EI) *m/z* 532 $[M - C_7H_7N]^+$, *m/z* 488

[M − C_7H_7N − $N(CH_3)_2$]$^+$; Anal Calcd for $C_{30}H_{57}N_7O_2Zr$: N, 15.34; C, 56.38; H, 8.99. Found: N, 14.99; C, 56.50; H, 8.92.

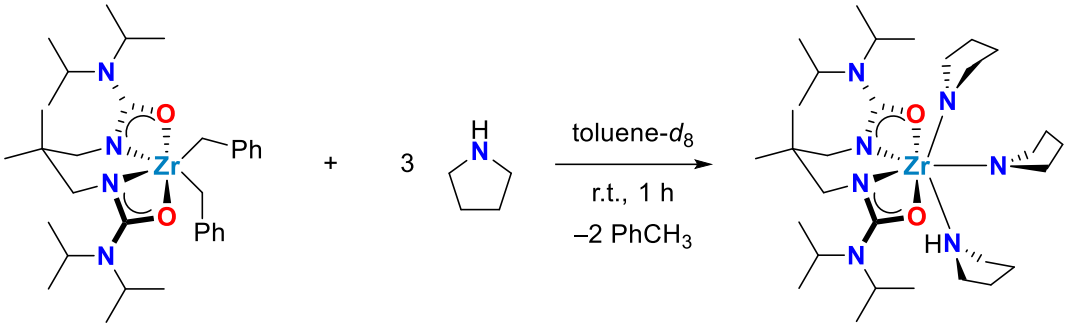

2.2 **2.5**

Synthesis of 2.5 *in situ*: To a ~250 μL toluene-d_8 solution of dibenzyl complex **2.2** (0.011 g, 0.017 mmol), pyrrolidine (0.004 g, 0.05 mmol) was added using ~250 μL toluene-d_8 for quantitative transfer, causing a change to bright yellow before turning to pale yellow and then colourless over a period of 10 minutes. The reaction was found to be complete after 1 hour by ^{1}H NMR spectroscopy. ^{1}H NMR (C_7D_8, 400 MHz) δ = 3.58 (sep, 6.7 Hz, 4H), 3.48 (br m, 12H), 3.19 (br s, 4H), 2.06 (br s, 1H), 1.62 (br m, 12H), 1.28 (d, J = 6.7 Hz, 24H), 0.96 (br s, 6H); ^{13}C NMR (C_7D_8, 100 MHz) δ = 168.8, 57.6, 51.2, 46.7, 36.7, 26.9, 25.5, 22.4.

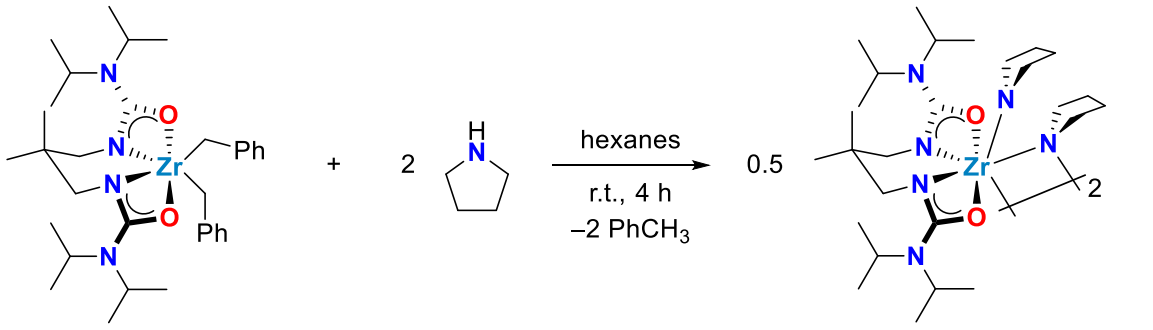

2.2 **2.6** 82% yield

Synthesis of 2.6: A 20 mL vial was charged with dibenzyl complex **2.2** (0.099 g, 0.16 mmol) before dissolving in ~7 mL hexanes via gentle heating and vigorous swirling to give a clear, pale

yellow solution. Pyrrolidine (0.024 g, 0.33 mmol) was then added dropwise to the concentrated solution of **2.2** while stirring using ~2 mL hexanes for quantitative transfer, immediately turning it bright yellow and then gradually to pale yellow over a period of an hour. After stirring for a total of 4 hours, the volatiles were removed *in vacuo* to give a colourless powder with a small amount of highly soluble pale-yellow solid (pyrrolidine adduct **2.5**). Recrystallization in hexanes at –35 °C for several days and isolation of the colourless crystals resulted in 0.076 g of **2.6** (82% yield). Similar recrystallization in toluene was carried out to achieve crystals suitable for X-ray diffraction. ^{1}H NMR (C_6D_6, 300 MHz) δ = 3.96 (m, 8H), 3.52 (sep, 6.7 Hz, 4H), 3.03 (br s, 4H), 1.70 (m, 8H), 1.28 (d, J = 6.7 Hz, 24H), 0.88 (br s, 6H); ^{13}C NMR (C_6D_6, 75 MHz) δ = 171.0, 57.8, 52.7, 46.8, 36.8, 27.2, 24.8, 22.2; MS(EI) *m/z* 584 $[M]^+$, *m/z* 514 $[M - N(CH_2)_4]^+$. Satisfactory elemental analysis could not be obtained: Anal Calcd for $C_{54}H_{108}N_{12}O_4Zr_2$: N, 14.34; C, 55.34; H, 9.29. Found: N, 14.47; C, 55.94; H, 9.72.

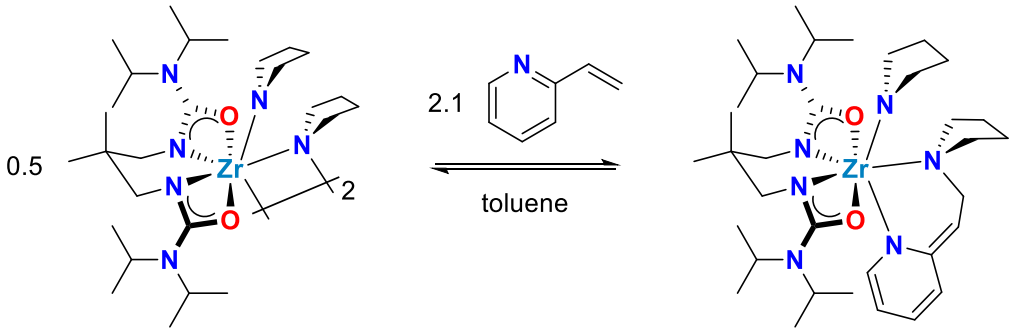

2.6 **2.7**

Synthesis of 2.7: A 20 mL vial was charged with dibenzyl complex **2.2** (0.202 g, 0.322 mmol) and suspended in ~3 mL toluene. Pyrrolidine (0.046 g, 0.64 mmol) was then added dropwise to the colourless solution using ~3 mL toluene for quantitative transfer, turning it bright yellow and then gradually to pale yellow over 15 minutes. The vial was shaken to assist dissolving. The volatiles were then removed *in vacuo* to give **2.6** as a colourless powder. 2-Vinylpyridine (0.071

g, 0.68 mmol) was then dissolved in ~3.5 mL toluene and added to the solid, turning the solution bright orange. Immediate formation of insoluble material, suspected to be poly(vinylpyridine), was also observed. The vial was then placed in the freezer at –35 °C for several days, during which time orange crystals suitable for X-ray diffraction precipitated out of solution in addition to crude, insoluble material. X-ray crystallography revealed **2.7**, but efforts to isolate it on a suitable scale to characterize it by NMR spectroscopy were futile as decomposition to **2.6** and polymer involving unidentified intermediates occurred spontaneously in solution. Extraction of the orange compound from the insoluble material with toluene, filtration through diatomaceous earth, and rapid removal of the volatiles *in vacuo* resulted in an orange-yellow material that was subjected to mass spectrometry: MS(EI) *m/z* 584 $[M - C_7H_7N]^+$, *m/z* 514 $[M - C_7H_7N - N(CH_2)_4]^+$. Elemental analysis could not be obtained.

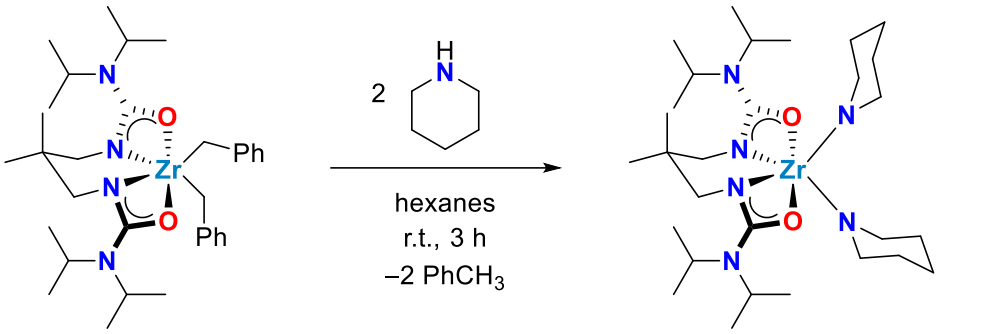

2.2 **2.8** 61% yield

Synthesis of 2.8: A 20 mL vial was charged with dibenzyl complex **2.2** (0.104 g, 0.165 mmol) before dissolving in ~7 mL hexanes via gentle heating and vigorous swirling to give a clear, pale yellow solution. Piperidine (0.028 g, 0.33 mmol) was then added dropwise to the concentrated solution of **2.2** while stirring using ~1 mL hexanes for quantitative transfer, immediately turning it bright yellow and then gradually to colourless over a period of 5 minutes. After stirring for a total of 3 hours, the vial was placed in a freezer at –35 °C for several days and isolation of the

colourless crystals suitable for X-ray diffraction resulted in 0.061 g of **2.8** (61% yield). ^{1}H NMR (C_6D_6, 300 MHz) δ = 3.82 (br m, 8H), 3.50 (sep, 6.7 Hz, 4H), 3.04 (s, 4H), 1.72 (br m, 12H), 1.25 (d, J = 6.7 Hz, 24H), 0.91 (br s, 6H); ^{13}C NMR (C_6D_6, 75 MHz) δ = 171.0, 57.9, 52.4, 46.8, 36.6, 30.2, 26.8, 25.0, 22.3; MS(EI) *m/z* 612 $[M]^+$, *m/z* 528 $[M - N(CH_2)_5]^+$; Anal Calcd for $C_{29}H_{58}N_6O_2Zr$: N, 13.69; C, 56.73; H, 9.52. Found: N, 13.83; C, 56.69; H, 9.63.

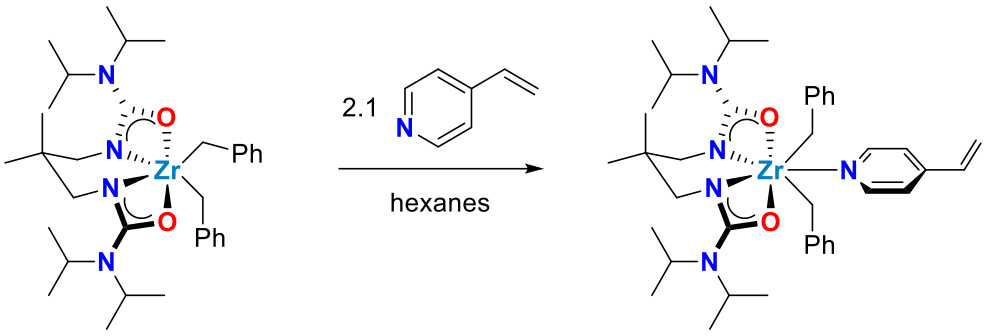

2.2 **2.9** 93% yield

Synthesis of 2.9: A 20 mL vial was charged with dibenzyl complex **2.2** (0.104 g, 0.165 mmol) and dissolved in ~2 mL hexanes with gentle heating and swirling. 4-Vinylpyridine (0.037 g, 0.35 mmol) was then added directly to this colourless solution, causing an immediate change to dark red. Swirling the solution resulted in the precipitating of dark red, needle-shaped crystals suitable for X-ray diffraction. After letting stand at room temperature for 2 hours, the vial was placed in the freezer at –35 °C for several days. Removal of the supernatant before allowing residual solvent to evaporate resulted in 0.123 g of dark red needles (87% yield). X-ray crystallography revealed co-crystallized toluene, but it was removed (as observed by ^{1}H NMR spectroscopy) by crushing into a red powder, washing with hexanes (3 x ~1 mL), and removing the volatiles *in vacuo* to give 0.113 g of isolated **2.9** (93% yield). ^{1}H NMR (C_6D_6, 300 MHz) δ = 8.99 (br m, 2H), 7.10 (t, J = 7.5 Hz, 4H), 6.88 (d, J = 7.4 Hz, 4H), 6.78 (d, J = 6.3 Hz, 2H), 6.71 (t, J = 7.2 Hz, 2H), 6.20 (dd,

J = 17.5, 10.9 Hz, 1H), 5.52 (d, J = 17.5 Hz, 1H), 5.05 (d, J = 10.9 Hz, 1H), 3.66 (br sep, J = 6.6 Hz, 4H), 2.95 (br s, 4H), 2.08 (br s, 4H), 1.31 (d, J = 6.6 Hz, 24H), 0.99 (br s, 4H).

NMR Tube Experiments

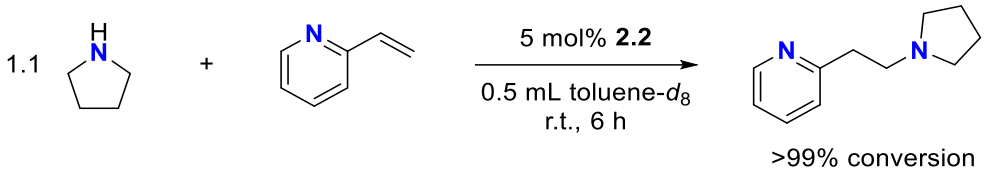

Catalytic Hydroamination of 2-Vinylpyridine with Pyrrolidine: To separate small vials, toluene-d_8 (0.4715 g), dibenzyl complex **2.2** (0.025 mmol), 2-vinylpyridine (0.5 mmol), and pyrrolidine (0.55 mmol) were all weighed. Using the toluene-d_8 for quantitative transfer, the amine was transferred to the complex before adding 2-vinylpyridine to the mixture. The solution was then stirred at room temperature for 6 hours before transferring to a J. Young tube to determine the conversion by ^{1}H NMR spectroscopy.

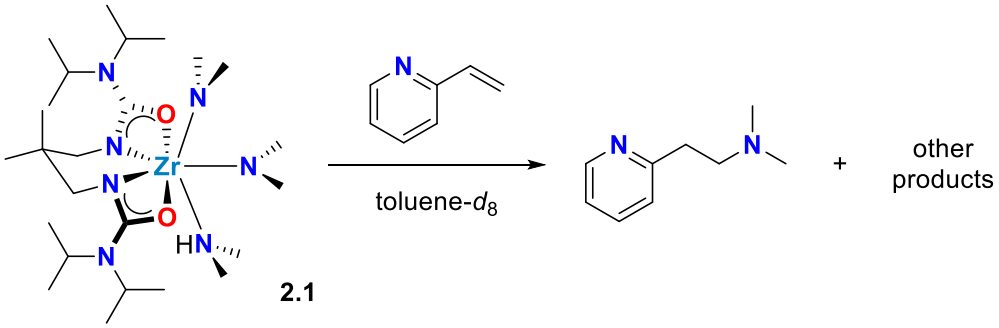

Stoichiometric Hydroamination of 2-Vinylpyridine with Dimethylamine: Complex **2.1** (0.016 g, 0.027 mmol) was transferred to a J. Young tube with ~1.25 mL toluene-d_8 before transferring 2-vinylpyridine (0.003 g, 0.03 mmol) to the same tube with ~150 μL toluene-d_8, turning the solution bright orange. The J. Young tube was then inverted continuously at room temperature and checked by ^{1}H NMR spectroscopy periodically.

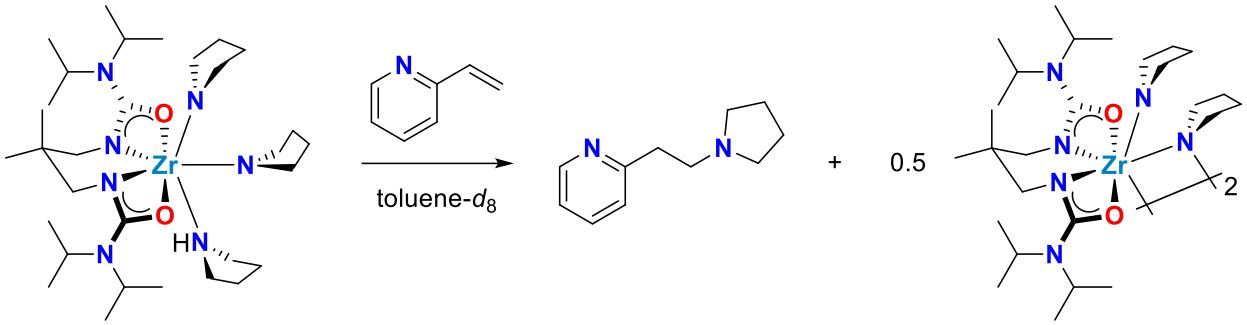

2.5 **2.6**

Stoichiometric Hydroamination of 2-Vinylpyridine with Pyrrolidine: After taking the ^{1}H NMR spectrum of the *in situ*-generated **2.5** after 1 hour (*vide supra*), 2-vinylpyridine (0.002 g, 0.02 mmol) was added, turning the colourless solution orange. After 2 hours, the reaction was determined to be complete by ^{1}H NMR spectroscopy.

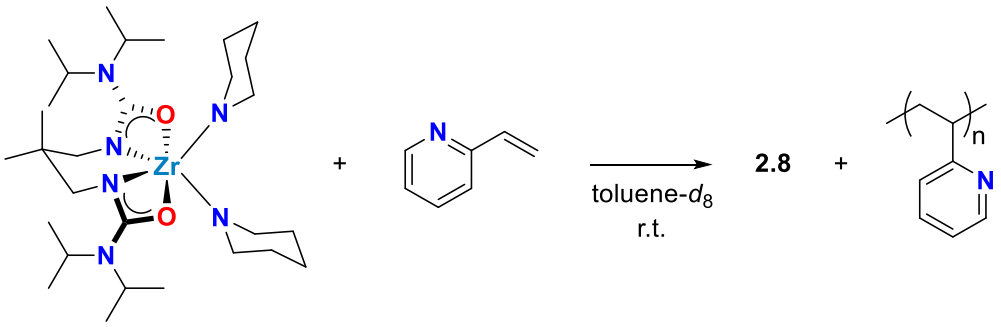

2.8

Reaction of 2-Vinylpyridine with 2.8: Bis(amido) complex **2.8** (0.008 g, 0.01 mmol) was transferred to a J. Young tube with ~250 μL toluene-d_8 before transferring 2-vinylpyridine (0.001 g, 0.01 mmol) to the same tube with ~450 μL toluene-d_8; no colour change was observed. The J. Young tube was then checked by ^{1}H NMR spectroscopy periodically. The only new signals observed were those resulting from the polymerization of 2-vinylpyridine.

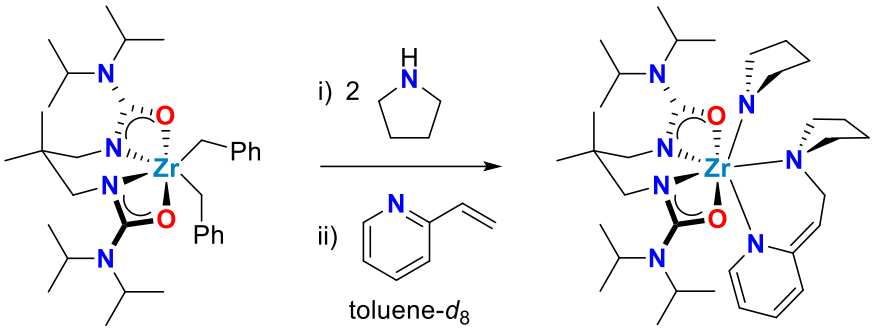

2.2 **2.7**

Generation of 2.7 *in situ*: To a small vial, **2.2** (0.011 g, 0.018 mmol) was added and then dissolved in ~250 μL toluene-d_8. Pyrrolidine (0.003 g, 0.04 mmol) was then added, turning it bright yellow immediately and then pale yellow over 10 minutes. After transferring the solution to a J. Young tube, 2-vinylpyridine (0.002 g, 0.02 mmol) was added, turning it bright orange. VT ^{1}H NMR was then performed on the solution.

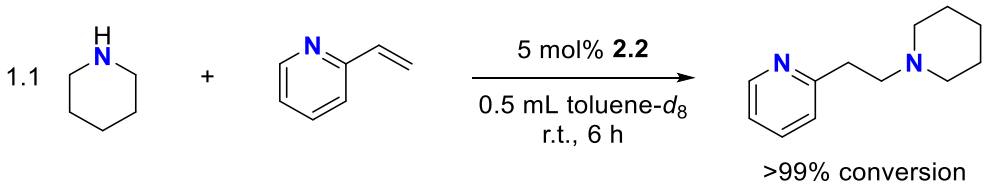

Catalytic Hydroamination of 2-Vinylpyridine with Piperidine: To separate small vials, toluene-d_8 (0.4712 g), dibenzyl complex **2.2** (0.025 mmol), 2-vinylpyridine (0.5 mmol), and piperidine (0.55 mmol) were all weighed. Using the toluene-d_8 for quantitative transfer, the amine was transferred to the complex before adding 2-vinylpyridine to the mixture. The solution was then stirred at room temperature for 6 hours before transferring to a J. Young tube to determine the conversion by ^{1}H NMR spectroscopy.

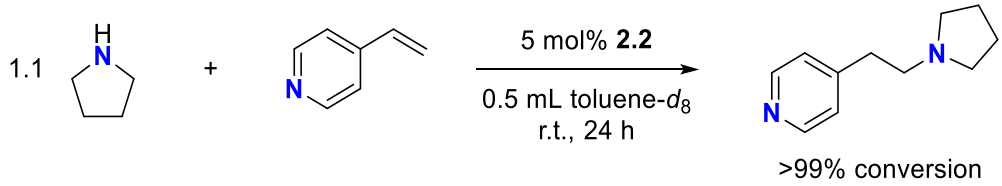

Catalytic Hydroamination of 4-Vinylpyridine with Pyrrolidine: To separate small vials, toluene-d_8 (0.4715 g), precatalyst **2.2** (0.025 mmol), 4-vinylpyridine (0.5 mmol), and pyrrolidine (0.55 mmol) were all weighed. Using the toluene-d_8 for quantitative transfer, pyrrolidine was transferred to the complex before adding 4-vinylpyridine to the mixture. The solution was then stirred at room temperature for 24 hours before transferring to a J. Young tube to determine the conversion by ^{1}H NMR spectroscopy.

Van't Hoff Data

Complex 2.4: To determine the K_{eq} values at each temperature, the relative integrations of the H_c proton of **2.4** and the H_b proton of 2-vinylpyridine (Figure 2.5) were measured and used to calculate the equilibrium constants (Table A.1). Only the largest three temperatures are used as the integration of H_b is zero at the other three temperatures.

Table A.1 Relevant parameters for construction of the van't Hoff plot for complex **2.4**

T **(°C)**	$\mathbf{H_c}$ **Integration**	$\mathbf{H_b}$ **Integration**	K_{eq}	***T*** **(K)**	**1/*T*** **(1/K)**	**ln(K_{eq})**
25.5	1.00	0.76	1.7	298.7	0.003348	0.55
13.8	1.00	0.32	9.8	286.9	0.003485	2.28
2.2	1.00	0.11	83	275.4	0.003631	4.41

Sample calculation for K_{eq} (T = 25.54 °C):

$$K_{eq} = \frac{1.00}{(0.76 \times 0.76)} = 1.7$$

Next, ln(K_{eq}) was plotted versus 1/T to obtain the van't Hoff plot (Figure A.1). The equation of the line and associated errors were determined using the LINEST equation in Excel.

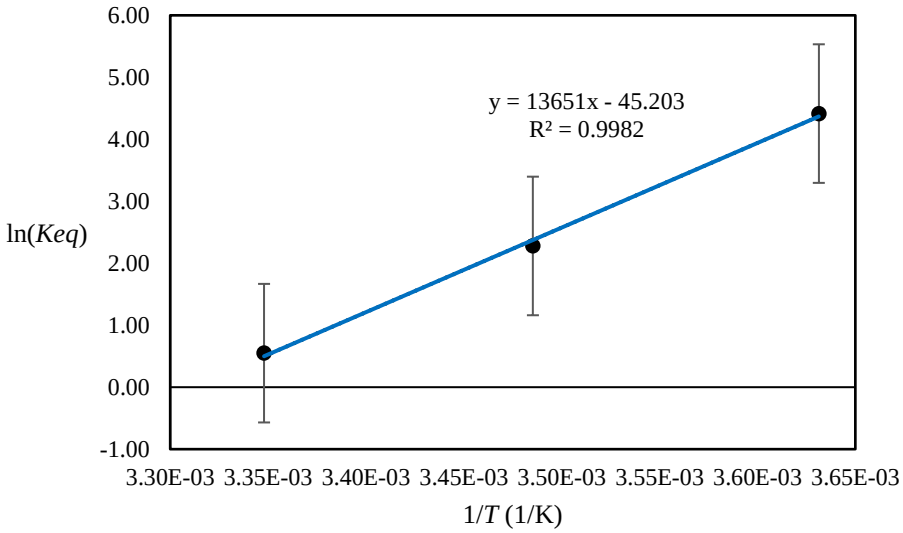

Figure A.1 Plot of ln(K_{eq}) versus 1/T (van't Hoff plot) for complex **2.4**

Using the van't Hoff equation, $\ln(K_{eq}) = -\Delta H°/RT + \Delta S°/R$ where R = 8.3145 × 10^{-3} kJ/mol•K, the enthalpy of reaction $\Delta H°$ can be determined from the slope of the line in Figure A.1 and the standard error in the slope (600 K, obtained from the LINEST equation):

$\Delta H° = -1 \bullet \text{slope} \bullet R = -113. \pm 5.$ kJ/mol

Similarly, the entropy of reaction $\Delta S°$ can be determined from the intercept of the line in Figure A.1 and the standard error in the intercept (2, obtained from the LINEST equation):

$\Delta S°$ = intercept•R = −0.38 ± 0.02 kJ/mol•K

Using the Gibbs free energy equation, $\Delta G° = \Delta H° - T\Delta S°$, the free energy can be calculated for T = 298 K to compare to the computed free energy for a reversible C−N bond forming step in Mg-catalyzed hydroamination ($\Delta G°$ = 9.2 kcal/mol).[171] The calculated errors in $\Delta H°$ and $\Delta S°$ can be used and converting to kcal/mol gives the free energy:

$\Delta G°$ = −0.36 ± 0.03 kcal/mol at 298 K; computed $\Delta G°$ = 9.2 kcal/mol at 298 K

These values are quite different, with this Zr system showing slightly exergonic C−N bond formation compared to an endergonic process in the Mg system.

Complex 2.7: To determine the K_{eq} values at each temperature, the relative integrations of the H_c proton of **2.7** (analogous to that of **2.4**) and the H_b proton of 2-vinylpyridine (Figure 2.8) were measured and used to calculate the equilibrium constants (Table A.2). The lowest temperature is excluded as the integration of H_b is zero.

Table A.2 Relevant parameters for construction of the van't Hoff plot for complex **2.7**

T **(°C)**	**H_c Integration**	**H_b Integration**	K_{eq}	***T*** **(K)**	**1/*T*** **(1/K)**	**ln(K_{eq})**
25.54	1.00	10.90	0.00842	298.7	0.003348	-4.778
13.77	1.00	2.41	0.172	286.9	0.003485	-1.759
2.23	1.00	0.91	1.2	275.4	0.003631	0.19
-9.14	1.00	0.34	8.7	264.0	0.003788	2.16
-19.21	1.00	0.10	1.0×10^2	253.9	0.003938	4.61

Next, ln(K_{eq}) was plotted versus 1/*T* to obtain the van't Hoff plot (Figure A.2). The equation of the line and associated errors were determined using the LINEST equation in Excel.

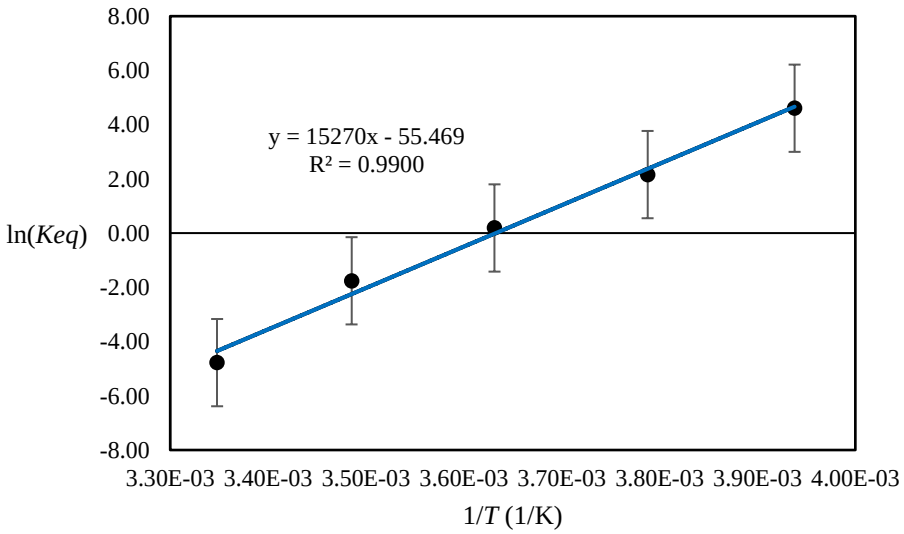

Figure A.2 Plot of ln(K_{eq}) versus 1/*T* (van't Hoff plot) for complex **2.7**

Using the van't Hoff equation, $\ln(K_{eq}) = -\Delta H°/RT + \Delta S°/R$ where $R = 8.3145 \times 10^{-3}$ kJ/mol•K, the enthalpy of reaction $\Delta H°$ can be determined from the slope of the line in Figure A.2 and the standard error in the slope (900 K, obtained from the LINEST equation):

$\Delta H° = -1 \bullet \text{slope} \bullet R = -127. \pm 7.$ kJ/mol

Similarly, the entropy of reaction $\Delta S°$ can be determined from the intercept of the line in Figure A.2 and the standard error in the intercept (3, obtained from the LINEST equation):

$\Delta S° = \text{intercept} \bullet R = -0.46 \pm 0.03$ kJ/mol•K

Using the Gibbs free energy equation, $\Delta G° = \Delta H° - T\Delta S°$, the free energy can be calculated for $T = 298$ K to compare to the computed free energy for a reversible C−N bond forming step in Mg-catalyzed hydroamination.[171] The calculated errors in $\Delta H°$ and $\Delta S°$ can be used, and converting to kcal/mol gives the free energy:

$\Delta G° = 2.5 \pm 0.3$ kcal/mol at 298 K; computed $\Delta G° = 9.2$ kcal/mol at 298 K

This value compares more favourably to the computed free energy than does the free energy determined for complex **2.4** above, as both values show an endergonic process for C−N bond formation. However, C−N bond formation in the Mg system is still less favourable than in this Zr system.

A.3 Experimental Data for Chapter 3

Synthesis of Complexes

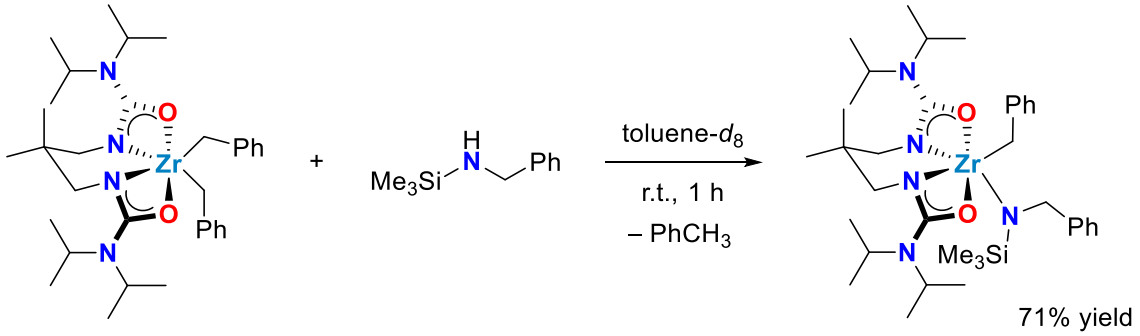

2.2 **3.2**

Synthesis of 3.2: A 20 mL vial was charged with dibenzyl complex **2.2** (0.104 g, 0.166 mmol) before dissolving in ~5 mL toluene with vigorous swirling to give a yellow solution. Then, a solution of *N*-(trimethylsilyl)benzylamine (0.030 g, 0.17 mmol) in ~3 mL toluene was added dropwise while stirring. The solution turned gradually to pale yellow over a period of 1 h. After this time, the volatiles were removed under vacuum and a white powder contaminated with a yellow impurity was obtained. This reaction mixture was redissolved in ~5 mL hexanes with gentle heating, resulting in a yellow solution. Cooling this solution to −35 °C for 24 h afforded 0.084 g of **3.2** as colourless crystals (71% yield). These crystals were suitable for X-ray diffraction. ^{1}H NMR (C_6D_6, 400 MHz) δ = 7.64 (m, 2H), 7.48 (m, 2H), 7.27 (m, 2H), 7.20 (m, 2H), 7.13 (m, 1H), 6.83 (m, 1H), 4.78 (s, 2H), 3.46 (sep, J = 6.7 Hz, 4H), 3.03 (d, J = 11.4 Hz, 2H), 2.87 (d, J = 11.4 Hz, 2H), 2.83 (s, 2H), 1.31 (d, J = 6.6 Hz, 12H), 1.21 (d, J = 6.7 Hz, 12H), 0.72 (s, 3H), 0.54 (s, 3H), 0.11 (s, 9H); ^{13}C NMR (C_6D_6, 100 MHz) δ =170.3, 149.8, 145.2, 128.7, 126.9, 128.4 – 127.8 (2C), 126.3, 120.1, 61.1, 57.4, 47.1, 45.0, 36.0, 27.0, 22.7, 22.6, 21.8, 1.4. The molecular ion was not observed by MS, instead the ion corresponding to a loss of a benzyl group was observed: MS(LIFDI) *m/z* 622 $[M - CH_2Ph]^+$, *m/z* 535 $[M - N(SiMe_3)(CH_2Ph)]^+$. Satisfactory elemental

analysis could not be obtained: Anal Calcd for $C_{36}H_{61}N_5O_2SiZr$: N, 9.79; C, 60.46; H, 8.60. Found: N, 9.81; C, 59.36; H, 8.39.

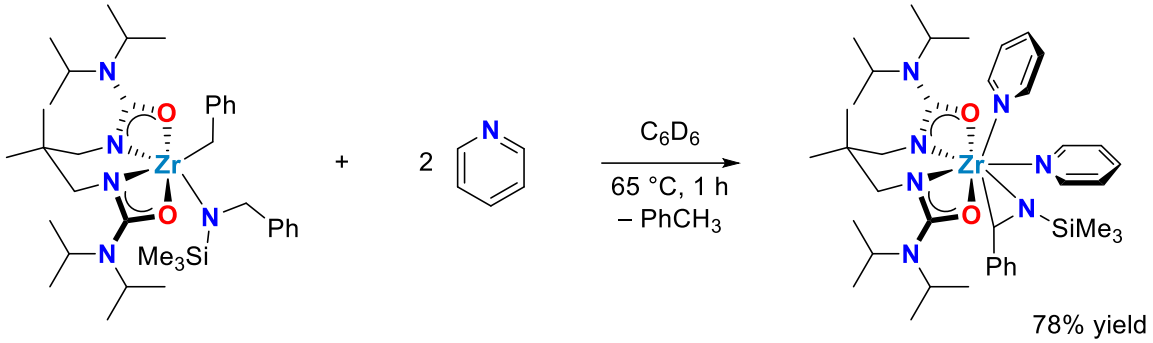

3.2 **3.4**

Synthesis of 3.4: To a ~2 mL C_6D_6 solution of complex **3.2** (0.093 g, 0.13 mmol), pyridine (0.022 g, 0.28 mmol) was added using ~0.5 mL C_6D_6 for quantitative transfer, causing a change from colourless to bright yellow. ^{1}H NMR spectroscopy revealed the formation of a pyridine adduct of **3.2**. Heating the reaction to 65 °C resulted in a gradual change of colour to dark red over a period of 30 min. The reaction was found to be complete after 1 h by ^{1}H NMR spectroscopy. Next, the solution was transferred to a 20 mL vial and the volatiles were removed *in vacuo*. The resulting dark red powder was dissolved in ~5 mL hexanes and the solution was cooled down to −35 °C overnight, during which time dark red crystals suitable for X-ray diffraction precipitated. The supernatant was then removed to give 0.079 g of isolated **3.4** (78% yield). ^{1}H NMR (C_6D_6, 300 MHz) δ = 9.26 (br m, 2H), 8.74 (br m, 2H), 7.29 (m, 4H), 6.85 (m, 3H), 6.65 (br m, 4H), 4.18 (s, 1H), 3.55 (br m, 5H), 3.20 (br d, J = 11.7 Hz, 1H), 2.97 (br d, J = 11.7 Hz, 1H), 2.83 (br d, J = 11.7 Hz, 1H), 1.36 (br m, 12H), 1.17 (br m, 12H), 0.80 (br s, 3H), 0.77 (br s, 3H), 0.24 (s, 9H). ^{13}C NMR (C_6D_6, 100 MHz) δ = 165.8, 159.7, 150.12, 128.6-127.6 (1C), 127.2, 123.5, 121.1, 116.4, 73.8, 56.7, 56.3, 46.8, 46.7, 36.8, 35.0, 34.9, 25.7, 22.9, 22.4, 20.9, 2.5. MS(LIFDI) *m/z* 779 $[M]^+$, *m/z* 621 $[M - (NC_5H_5)_2]^+$. Satisfactory elemental analysis could not be obtained, possibly due to

loss of pyridine when removing volatiles: Anal Calcd for $C_{39}H_{63}N_7O_2SiZr$: N, 12.55; C, 59.96; H, 8.13. Found: N, 11.86; C, 60.36; H, 8.47.

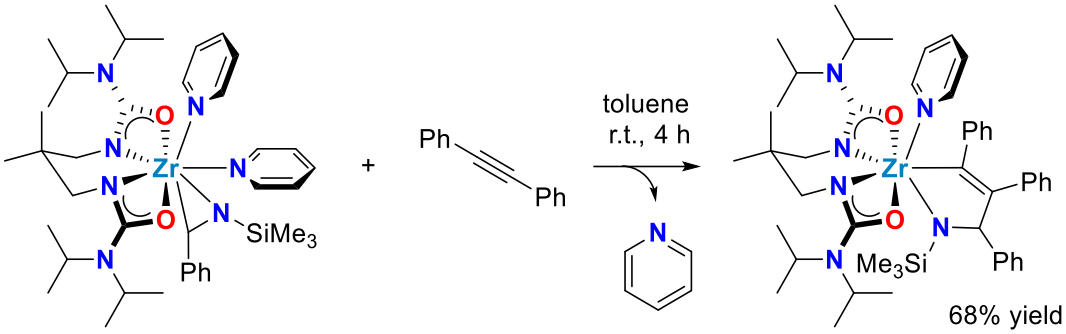

3.4 **3.5**

Synthesis of 3.5: A 20 mL vial was charged with complex **3.4** (0.084 g, 0.11 mmol) before dissolving in ~5 mL toluene with vigorous swirling to give a dark red solution. Then, a solution of diphenylacetylene (0.019 g, 0.11 mmol) in ~5 mL toluene was added to the solution of **3.4** while stirring. The solution turned gradually to orange over a period of 1.5 h and then turned pale yellow after a total of 3.5 h. The volatiles were then removed *in vacuo* and a white powder contaminated with an orange impurity was obtained. This reaction mixture was redissolved in ~8 mL hexanes at room temperature to give a clear, yellow solution. Cooling this solution to –35 °C for 24 h afforded 0.065 g of **3.5** (68% yield) as colourless crystals suitable for X-ray diffraction. ^{1}H NMR (C_6D_6, 300 MHz) δ = 8.70 (d, J = 7.5 Hz, 2H), 7.92 (d, J = 7.5 Hz, 2H), 7.25 (t, J = 7.4 Hz, 2H), 7.11 (m, 1H), 7.03 (m, 2H), 6.95 (m, 2H), 6.89 (m, 2H), 6.76 (m, 4H), 6.48 (m, 3H), 5.72 (s, 1H), 3.56 (br m, 4H), 3.00 (br m, 4H), 1.35 (br m, 24H), 0.67 (br s, 3H), 0.45 (br s, 3H), 0.26 (s, 9H). ^{13}C NMR (C_6D_6, 100 MHz) δ = 191.1, 150.9, 150.3, 144.8, 137.0, 130.3, 130.2, 129.3, 128.6, 127.4, 126.9, 126.4, 126.1, 125.7, 124.6, 123.1, 120.0, 74.5, 56.9, 47.1, 37.1, 32.0, 22.2, 14.4, 3.0. The molecular ion was not observed by MS, instead the ion corresponding to a loss of pyridine was observed: MS(LIFDI) *m/z* 799 $[M - (NC_5H_5)]^+$. Satisfactory elemental analysis could not be obtained,

possibly due to loss pyridine during removal of volatiles: Anal Calcd for $C_{48}H_{68}N_6O_2SiZr$: N, 9.55; C, 65.48; H, 7.79. Found: N, 9.03; C, 63.65; H, 8.30.

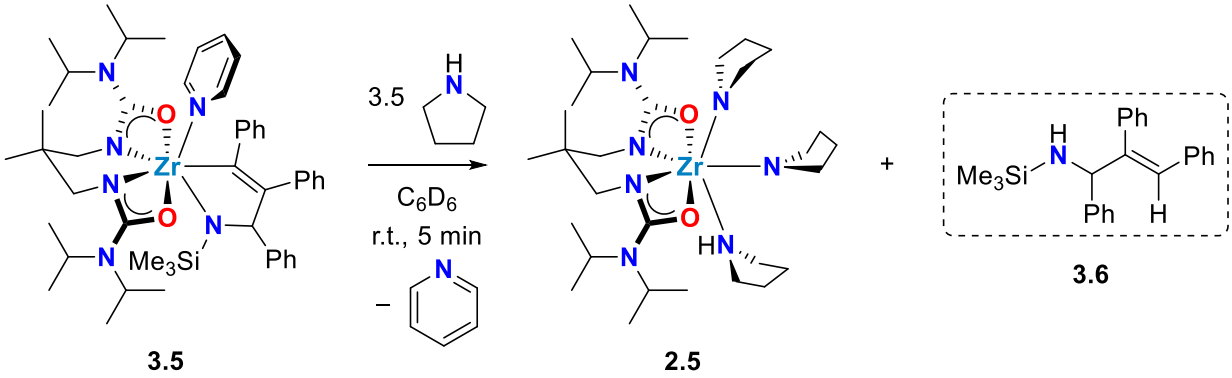

3.5 **2.5** **3.6**

Synthesis of 3.6 *in situ*: To a solution of complex **3.5** (0.010 g, 0.011 mmol) in ~1 mL C_6D_6, pyrrolidine was added (0.003 g, 0.04 mmol) with ~0.5 mL C_6D_6 to ensure quantitative transfer, turning the solution from pale yellow to colourless. After 5 min, ^{1}H NMR spectroscopy revealed the formation of complex **2.5**,[246] free pyridine, and allylic amine **3.6**. Characterization of **3.6** was performed *in situ*. ^{1}H NMR (C_6D_6, 300 MHz) δ = 7.37 (m, 2H), 7.19 (m, 2H), 7.07 (m, 3H), 6.96 (m, 8H), 6.84 (s, 1H), 4.90 (d, J = 10.8 Hz, 1H), 0.08 (s, 9H); ^{13}C NMR (C_6D_6, 100 MHz) δ = 147.3, 145.3, 140.3, 137.6, 129.8, 129.6, 128.6, 128.5, 128.4-127.8 (2C), 127.4, 127.3, 127.0, 126.9, 64.2, 0.5.

Initial Catalytic Results and Evaluation of Reported Hydroaminoalkylation Catalysts

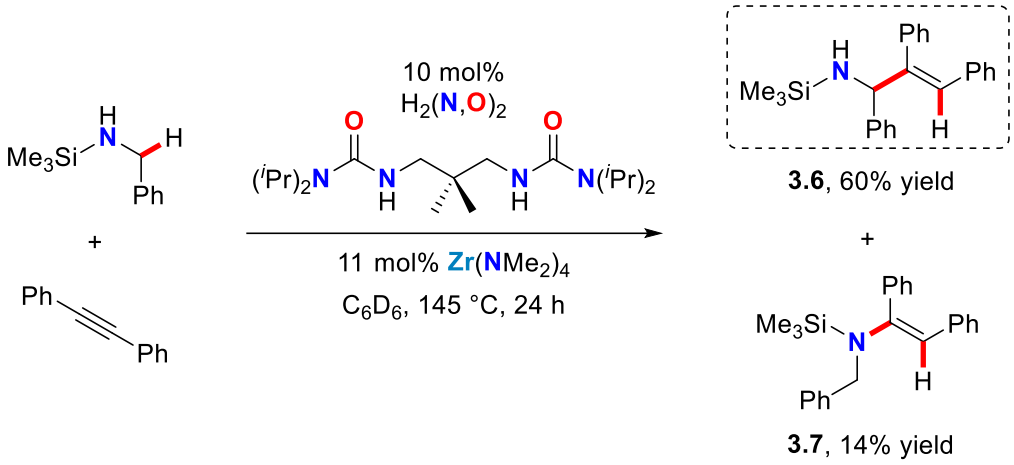

Hydroaminoalkylation with *N*-(trimethylsilyl)benzylamine: To a small vial containing ligand $H_2(N,O)_2$ (0.004 g, 0.01 mmol), a solution of $Zr(NMe_2)_4$ (0.003 g, 0.01 mmol) in ~0.25 mL C_6D_6 was added and mixed thoroughly to form the precatalyst. After 20 min, solutions of *N*-(trimethylsilyl)benzylamine (0.018 g, 0.10 mmol) and diphenylacetylene (0.018 g, 0.10 mmol) in ~0.25 mL C_6D_6 were added separately to the precatalyst solution, using a total of ~0.25 mL C_6D_6 for quantitative transfer. The solution was then transferred into a J. Young tube and a t = 0 ^{1}H NMR spectrum was obtained before heating to 145 °C for 24 h. After the reaction, a ^{1}H NMR spectrum was obtained (*vide infra*). A solution of 1,3,5-trimethoxybenzene in ~0.15 mL C_6D_6 was then transferred to the reaction mixture and a ^{1}H NMR spectrum was obtained for NMR yield determination.

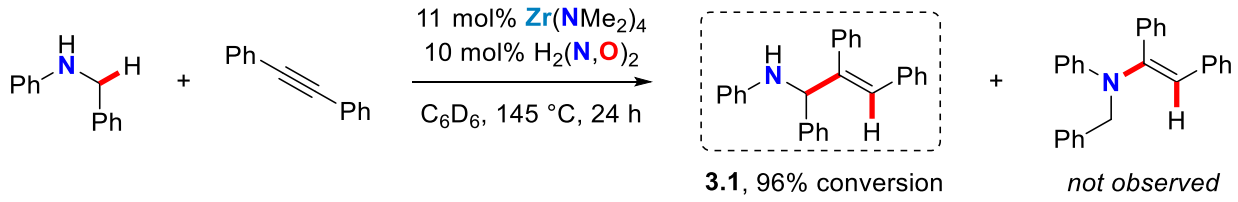

Hydroaminoalkylation with *N*-benzylaniline: To a small vial containing ligand $H_2(N,O)_2$ (0.001 g, 0.004 mmol), a solution of $Zr(NMe_2)_4$ (0.001 g, 0.004 mmol) in ~0.25 mL C_6D_6 was added and

mixed thoroughly to form the precatalyst. After 20 min, solutions of *N*-benzylaniline (0.007 g, 0.04 mmol) and diphenylacetylene (0.007 g, 0.04 mmol) in ~0.25 mL C_6D_6 were added separately to the precatalyst solution, using a total of ~0.25 mL C_6D_6 for quantitative transfer. The solution was then transferred into a J. Young tube and a t = 0 ^{1}H NMR spectrum was obtained before heating to 145 °C for 24 h. After the reaction, a ^{1}H NMR spectrum was obtained to determine the conversion to the allylic amine product. Note: changing the solvent (for example to toluene) and/or lowering the reaction temperature (for example to 140 °C) dramatically reduced the conversion by approximately 20% in either case.

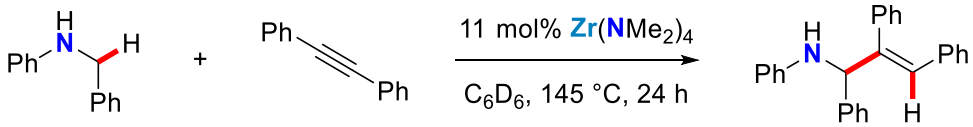

3.1, 15% conversion

Hydroaminoalkylation with *N*-benzylaniline (No Ligand): To a small vial containing a solution of $Zr(NMe_2)_4$ (0.001 g, 0.004 mmol) in ~0.25 mL C_6D_6, solutions of *N*-benzylaniline (0.007 g, 0.04 mmol) and diphenylacetylene (0.007 g, 0.04 mmol) in ~0.25 mL C_6D_6 were added separately using a total of ~0.25 mL C_6D_6 for quantitative transfer. The resulting solution was then transferred into a J. Young tube and a t = 0 ^{1}H NMR spectrum was obtained before heating to 145 °C for 24 h. After the reaction, a ^{1}H NMR spectrum was obtained to determine the conversion to the allylic amine product.

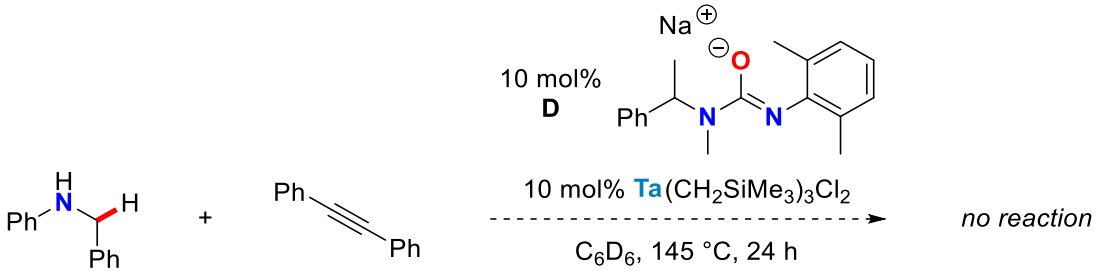

Hydroaminoalkylation with *N*-benzylaniline (Ta Catalyst): To a small vial containing ureate ligand **D** (0.001 g, 0.004 mmol), a solution of $Ta(CH_2SiMe_3)_3Cl_2$ (0.002 g, 0.004 mmol) in ~0.25 mL C_6D_6 was added and mixed thoroughly to form the precatalyst. After 20 min, solutions of *N*-benzylaniline (0.007 g, 0.04 mmol) and diphenylacetylene (0.007 g, 0.04 mmol) in ~0.25 mL C_6D_6 were added separately to the precatalyst solution, using a total of ~0.25 mL C_6D_6 for quantitative transfer. The solution was then transferred into a J. Young tube and a $t = 0$ ^{1}H NMR spectrum was obtained before heating to 145 °C for 24 h. After the reaction, a ^{1}H NMR spectrum was obtained and revealed that no reaction occurred between the two substrates.

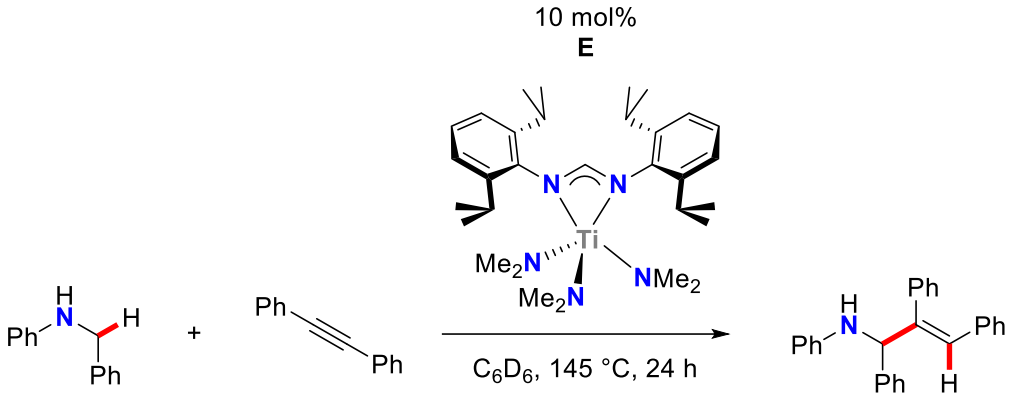

3.1, 25% conversion

Hydroaminoalkylation with *N*-benzylaniline (Ti Catalyst): To a small vial containing a solution of Ti catalyst **E** (0.002 g, 0.004 mmol) in ~0.25 mL C_6D_6, solutions of *N*-benzylaniline (0.007 g, 0.04 mmol) and diphenylacetylene (0.007 g, 0.04 mmol) in ~0.25 mL C_6D_6 were added separately using a total of ~0.25 mL C_6D_6 for quantitative transfer. The resulting solution was then transferred into a J. Young tube and a $t = 0$ ^{1}H NMR spectrum was obtained before heating to 145 °C for 24 h. After the reaction, a ^{1}H NMR spectrum was obtained to determine the conversion to the allylic amine product.

Catalytic Hydroaminoalkylation of Alkynes

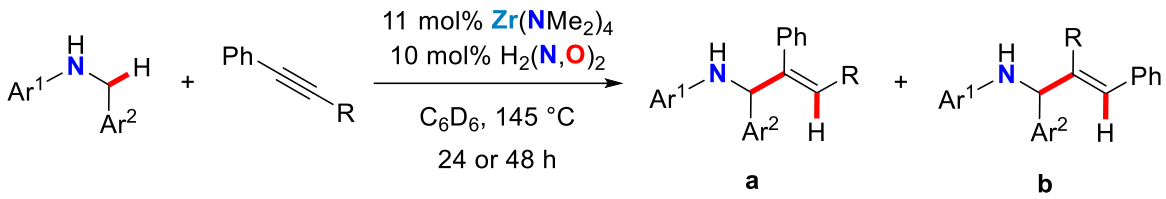

General Procedure for Alkyne Hydroaminoalkylation: To a small vial containing ligand $H_2(N,O)_2$ (0.004 g, 0.01 mmol), a solution of $Zr(NMe_2)_4$ (0.003 g, 0.01 mmol) in ~0.25 mL C_6D_6 was added and mixed thoroughly to form the precatalyst. After 20 min, solutions of the respective amine (0.10 mmol) and alkyne (0.10 mmol) in ~0.25 mL C_6D_6 were added separately to the precatalyst solution, using a total of ~0.25 mL C_6D_6 for quantitative transfer. The solution was then transferred into a J. Young tube and a $t = 0$ ^{1}H NMR spectrum was obtained before heating to 145 °C for 24 or 48 h. After the reaction, a ^{1}H NMR spectrum was obtained for *in situ* characterization (*vide infra*). A solution of 1,3,5-trimethoxybenzene in ~0.15 mL C_6D_6 was then transferred to the reaction mixture and a ^{1}H NMR spectrum was obtained for NMR yield determination and regioisomeric ratio (a:b). Each reaction was run in duplicate. For product characterization, the crude reaction mixture without internal standard was quenched with ~2 mL DCM and filtered through diatomaceous earth. The volatiles were then removed *in vacuo* and the resulting residue was purified by silica column chromatography (hexanes/ethyl acetate). In some cases, the product decomposed during solvent removal after column purification. Thus, to preserve the NMR signals of the product for characterization, some solvent impurities can be observed in select NMR spectra. In cases where multiple regioisomers are produced, the isomers were isolated as a mixture.

Hydroaminoalkylation of Diphenylacetylene with *N*-benzylaniline (3.1)

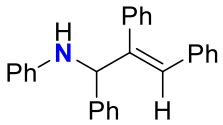

This reaction was carried out according to the general procedure (24 h, 82% NMR yield, 58% isolated yield). ^{1}H NMR ($CDCl_3$, 400 MHz) δ = 7.38-7.31 (m, 5H), 7.22 (m, 3H), 7.16 (m, 2H), 7.06 (m, 3H), 6.98 (m, 2H), 6.91 (m, 2H), 6.86 (s, 1H), 6.71 (m, 1H), 6.67 (m, 2H), 5.18 (s, 1H), 4.32 (br s, 1H); ^{13}C NMR ($CDCl_3$, 100 MHz) δ = 147.2, 141.8, 141.1, 139.4, 136.7, 129.5, 129.4, 129.3, 129.2, 128.8, 128.7, 128.3, 128.0, 127.8, 127.5, 126.9, 117.9, 113.8, 66.2. HRMS(ESI) *m/z* Calcd for $C_{27}H_{22}N$ $[M]^+$: 360.1752; found: 360.1758.

Hydroaminoalkylation of 1-Methyl-4-(phenylethynyl)benzene with *N*-benzylaniline (3.8)

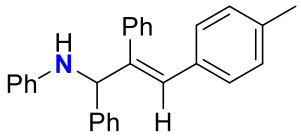

+ regioisomer

This reaction was carried out according to the general procedure (48 h, 75% NMR yield, 1.1:1, 51% isolated yield). ^{1}H NMR ($CDCl_3$, 400 MHz) δ = 7.37 (m, 4H), 7.32-7.25 (m, 6H), 7.21 (m, 2H), 7.15 (m, 4H), 7.06-7.00 (m, 6H), 6.98-6.92 (m, 4H), 6.87-6.78 (m, 8H), 6.70 (m, 2H), 6.65 (m, 4H), 5.16 (br s, 2H), 4.27 (br s, 2H), 2.29 (s, 3H), 2.20 (s, 3H); ^{13}C NMR ($CDCl_3$, 100 MHz) δ = 147.2, 141.7, 141.2, 140.8, 139.6, 137.1, 136.9, 136.7, 136.2, 133.8, 129.4, 129.3, 129.3, 129.2, 129.0, 128.7, 128.7, 128.1, 128.2, 128.0, 128.0, 128.0, 127.7, 127.4, 126.8, 117.9, 113.8, 66.3, 21.4, 21.2. HRMS(ESI) *m/z* Calcd for $C_{28}H_{24}N$ $[M]^+$: 374.1909; found: 374.1912.

Hydroaminoalkylation of 1-Methoxy-4-(phenylethynyl)benzene with *N*-benzylaniline (3.9)

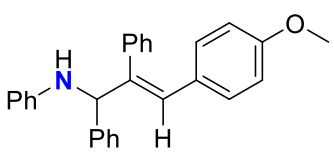

+ regioisomer

This reaction was carried out according to the general procedure (48 h, 76% NMR yield, 1.4:1, 66% isolated yield; some *E*/*Z*-isomerization also occurred during purification). ^{1}H NMR ($CDCl_3$, 400 MHz) δ = 7.48-7.41 (m, 2H), 7.40-7.26 (m, 4H), 7.21 (m, 2H), 7.17-7.08 (m, 2H), 7.06-6.86 (m, 5H), 6.86-6.62 (m, 5H), 5.22 (s, 1H), 5.16 (s, 1H), 4.34 (br s, 1H), 3.84 (s, 3H), 3.82 (s, 3H), 3.75 (s, 3H); ^{13}C NMR ($CDCl_3$, 100 MHz) δ = 159.2, 159.0, 158.5, 147.3, 141.9, 141.4, 141.3, 141.3, 139.8,

139.7, 139.6, 137.0, 136.8, 131.4, 130.7, 130.4, 129.4, 129.3, 129.2, 128.8, 128.7, 128.7, 128.2, 128.0, 128.0, 127.7, 127.7, 127.4, 126.8, 126.8, 117.9, 114.1, 113.8, 113.5, 66.3, 65.7, 55.4, 55.2. HRMS(FD) *m/z* Calcd for $C_{28}H_{25}NO$ $[M]^+$: 391.19361; found: 391.19472.

Hydroaminoalkylation of 1-(Phenylethynyl)-4-(trifluoromethyl)benzene with *N*-benzylaniline (3.10)

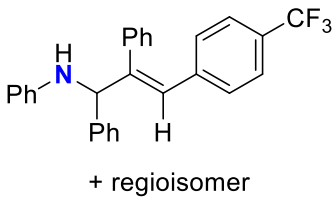

+ regioisomer

This reaction was carried out according to the general procedure (48 h, 63% NMR yield, 1:1, 61% isolated yield). ^{1}H NMR ($CDCl_3$, 300 MHz) δ = 7.48 (m, 2H), 7.42-7.30 (m, 13H), 7.30-7.18 (m, 7H), 7.15-6.82 (m, 12H), 6.78 (m, 2H) 6.73 (m, 4H), 5.20 (s, 1H), 5.19 (s, 1H), 4.36 (br s, 2H); ^{13}C NMR (C_6D_6, 100 MHz) δ = 147.0, 147.0, 144.4, 143.4, 140.6, 140.4, 138.8, 136.1, 129.7, 129.5, 129.5, 129.4, 129.4, 129.4, 129.3, 129.0, 128.9, 128.9, 128.8, 128.7, 128.4, 128.1, 128.0, 128.0, 127.9, 127.3, 126.6, 125.6 (q, J = 3.8 Hz), 124.9 (q, J = 3.8 Hz), 122.9, 118.2, 118.2, 113.8, 66.3, 66.0; ^{19}F NMR ($CDCl_3$, 282 MHz) δ = 63.0, 62.9. HRMS(ESI) *m/z* Calcd for $C_{28}H_{21}F_3N$ $[M]^+$: 428.1626; found: 428.1631.

Hydroaminoalkylation of 1-Chloro-4-(phenylethynyl)benzene with *N*-benzylaniline (3.11)

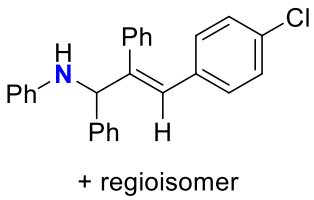

+ regioisomer

This reaction was carried out according to the general procedure (48 h, 74% NMR yield, 1:1.2, 51% isolated yield). ^{1}H NMR ($CDCl_3$, 400 MHz) δ = 7.37-7.28 (m, 11H), 7.24-7.13 (m, 11H), 7.11-7.05 (m, 4H), 7.00 (m, 2H), 6.97-6.86 (m, 4H), 6.82 (s, 1H), 6.80 (s, 1H), 6.74 (m, 2H), 6.69 (m, 4H), 5.15 (s, 1H), 5.13 (s, 1H), 4.24 (br s, 2H); ^{13}C NMR ($CDCl_3$, 100 MHz) δ = 146.9, 146.9, 142.4, 140.6, 140.4, 139.0, 137.8, 136.4, 135.5, 133.4, 132.5, 130.7, 130.7, 129.5, 129.3, 129.3, 129.1, 128.9, 128.9, 128.8, 128.8, 128,1, 128.0, 128.0, 127.9, 127.7, 127.1, 126.9, 118.3, 118.3, 114.0, 114.0, 66.5, 66.3. HRMS(ESI) *m/z* Calcd for $C_{27}H_{21}ClN$ $[M]^+$: 394.1363; found: 394.1373.

Hydroaminoalkylation of 2-(Phenylethynyl)pyridine with *N*-benzylaniline (3.12)

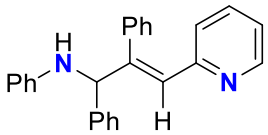

This reaction was carried out according to the general procedure (48 h, 49% NMR yield, 36% isolated yield). ^{1}H NMR ($CDCl_3$, 400 MHz) δ = 8.49 (m, 1H), 7.38 (m, 2H), 7.32-7.24 (m, 7H), 7.18 (m, 3H), 7.05-7.00 (m, 3H), 6.71 (m, 3H), 6.64 (m, 1H), 5.28 (d, J = 2.9 Hz, 1H), 4.28 (d, J = 2.9 Hz, 1H); ^{13}C NMR ($CDCl_3$, 100 MHz) δ = 154.8, 146.9, 146.6, 139.9, 138.2, 137.8, 129.4, 129.0, 129.0, 128.7, 128.2, 128.0, 128.0, 124.5, 122.0, 118.1, 113.6, 66.0. HRMS(ESI) *m/z* Calcd for $C_{26}H_{22}N_2$ $[M]^+$: 362.1783; found: 362.1789.

Hydroaminoalkylation of 1-Phenyl-1-propyne with *N*-benzylaniline (3.13)[319]

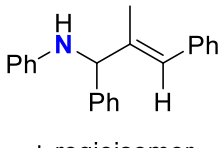

+ regioisomer

This reaction was carried out according to the general procedure (48 h, 40% NMR yield, 1:4.7, 40% isolated yield). ^{1}H NMR ($CDCl_3$, 400 MHz) δ = 7.45 (m, 2H), 7.36-7.13 (m, 10H), 6.98 (m, 1H), 6.86-6.70 (m, 4H), 6.04 (br s, 1H), 5.07 (s, 1H), 1.83 (s, 3H), 1.57 (m, 3H). HRMS(ESI) *m/z* Calcd for $C_{22}H_{20}N$ $[M]^+$: 298.1596; found: 298.1600.

Hydroaminoalkylation of (Cyclohexylethynyl)benzene with *N*-benzylaniline (3.14)

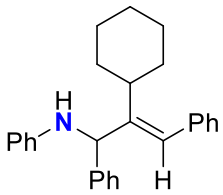

+ regioisomer

This reaction was carried out according to the general procedure (48 h, 76% NMR yield, 1:1.2, 38% isolated yield). ^{1}H NMR ($CDCl_3$, 400 MHz) δ = 7.43 (m, 2H), 7.36-7.20 (m, 16H), 7.15 (m, 6H), 6.93 (m, 2H), 6.72 (m, 2H), 6.61 (m, 3H), 6.43 (br s, 1H), 5.69 (m, 1H), 5.09 (s, 1H), 5.06 (s, 1H), 4.02 (br s, 1H), 2.87 (m, 1H), 1.95 (m, 1H), 1.85-0.94 (m, 20H); ^{13}C NMR ($CDCl_3$, 100 MHz) δ = 148.2, 147.2, 139.3, 137.9, 136.4, 129.2, 129.1, 129.1, 128.8, 128.6, 128.5, 128.2, 128.1, 127.9, 127.4, 127.3, 127.0, 126.5, 117.6, 113.6, 65.2, 59.3, 40.3, 37.6, 33.3, 33.1, 32.8, 31.7, 26.5, 26.5, 26.0, 25.7, 25.6. HRMS(ESI) *m/z* Calcd for $C_{27}H_{28}N$ $[M]^+$: 366.2222; found: 366.2226.

Hydroaminoalkylation of 1-Phenyl-2-trimethylsilylacetylene with *N*-benzylaniline (3.15)

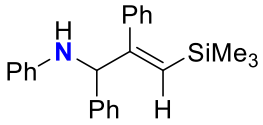

This reaction was carried out according to the general procedure (48 h, 31% NMR yield, 11% isolated yield). ^{1}H NMR ($CDCl_3$, 400 MHz) δ = 7.37-7.25 (m, 5H), 7.22-7.14 (m, 5H), 6.92 (m, 2H), 6.71 (m, 1H), 6.62 (m, 2H), 6.05 (s, 1H), 5.05 (s, 1H), 4.12 (br s, 1H), −0.22 (s, 9H)); ^{13}C NMR ($CDCl_3$, 100 MHz) δ = 157.0, 147.4, 141.8, 129.2, 129.0, 128.7, 128.7, 127.9, 127.8, 127.8, 127.6, 127.4, 117.7, 113.7, 67.3, 0.0. HRMS(ESI) *m/z* Calcd for $C_{24}H_{26}NSi$ $[M]^+$: 356.1835; found: 356.1838.

Hydroaminoalkylation of Diphenylacetylene with *N*-benzyl-4-methylaniline (3.16)

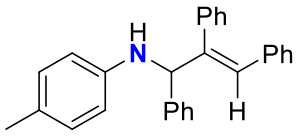

This reaction was carried out according to the general procedure (24 h, 84% NMR yield, 69% isolated yield). ^{1}H NMR ($CDCl_3$, 300 MHz) δ = 7.41 (m, 2H), 7.38-7.30 (m, 3H), 7.30-7.23 (m, 3H), 7.12-7.05 (m, 3H), 7.05-6.92 (m, 4H), 6.96-6.90 (m, 3H), 6.68 (m, 2H), 5.18 (s, 1H), 4.33 (br s, 1H), 2.27 (s, 3H); ^{13}C NMR ($CDCl_3$, 75 MHz) δ = 144.6, 141.8, 140.9, 139.4, 136.7, 133.0, 129.8, 129.4, 129.2, 128.7, 128.7, 128.3, 128.0, 128.0, 127.7, 127.4, 126.8, 114.2, 66.8, 20.6. HRMS(ESI) *m/z* Calcd for $C_{28}H_{24}N$ $[M]^+$: 374.1909; found: 374.1914.

Hydroaminoalkylation of Diphenylacetylene with *N*-benzyl-4-chloroaniline (3.17)

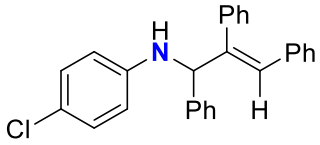

This reaction was carried out according to the general procedure (48 h, 42% NMR yield, 25% isolated yield). ^{1}H NMR ($CDCl_3$, 400 MHz) δ = 7.43-7.32 (m, 5H), 7.30-7.23 (m, 3H), 7.17-7.06 (m, 5H), 6.96 (m, 4H), 6.85 (s, 1H), 6.62 (m, 2H), 5.18 (s, 1H), 4.24 (br s, 1H); ^{13}C NMR ($CDCl_3$, 100 MHz) δ = 145.6, 141.3, 140.6, 139.1, 136.5, 129.4, 129.2, 129.2, 128.9, 128.8, 128.6, 128.1, 128.0, 127.6, 127.0, 122.6, 115.0, 66.3. HRMS(FD) *m/z* Calcd for $C_{27}H_{22}ClN$ $[M]^+$: 395.14408; found: 395.14280.

Hydroaminoalkylation of Diphenylacetylene with *N*-benzyl-4-fluoroaniline (3.18)

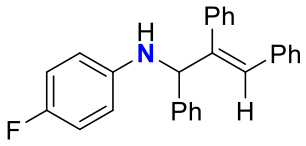

This reaction was carried out according to the general procedure (48 h, 78% NMR yield, 66% isolated yield). ^{1}H NMR ($CDCl_3$, 400 MHz) δ = 7.37 (m, 2H), 7.33-7.26 (m, 3H), 7.20 (m, 3H), 7.05 (m, 3H), 6.95-6.83 (m, 7H), 6.59 (br m, 2H), 5.11 (s, 1H), 4.08 (br s, 1H); ^{13}C NMR ($CDCl_3$, 100 MHz) δ = 156.2 (d, J = 235.4 Hz), 143.4, 141.6, 140.8, 139.2, 136.6, 129.4, 129.2, 128.8, 128.7, 128.4, 128.0, 128.0, 127.9, 127.6, 127.0, 115.8 (d, J = 22.3 Hz), 114.7, 66.9; ^{19}F NMR ($CDCl_3$, 282 MHz) δ = 127.9. HRMS(ESI) *m/z* Calcd for $C_{27}H_{21}FN$ $[M]^+$: 378.1658; found: 378.1663.

Hydroaminoalkylation of Diphenylacetylene with *N*-(4-methylbenzyl)aniline (3.19)

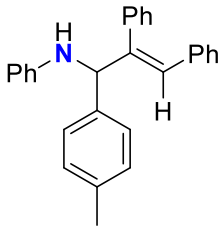

This reaction was carried out according to the general procedure (24 h, 41% NMR yield; 48 h, 72% NMR yield, 56% isolated yield). ^{1}H NMR ($CDCl_3$, 400 MHz) δ = 7.28-7.21 (m, 5H), 7.16 (m, 2H), 7.12 (m, 2H), 7.04 (m, 3H), 6.97 (m, 2H), 6.91 (m, 3H), 6.72 (m, 3H), 5.12 (s, 1H), 4.22 (br s, 1H), 2.33 (s, 3H); ^{13}C NMR ($CDCl_3$, 100 MHz) δ = 146.5, 139.6, 139.5, 137.6, 136.7, 136.7, 133.7, 129.5, 129.3, 129.2 128.7, 128.7, 128.0, 128.0, 127.4, 126.8, 118.5, 114.5, 66.7, 21.3. HRMS(ESI) *m/z* Calcd for $C_{28}H_{24}N$ $[M]^+$: 374.1909; found: 374.1911.

Hydroaminoalkylation of Diphenylacetylene with *N*-(4-chlorobenzyl)aniline (3.20)

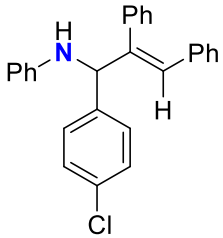

This reaction was carried out according to the general procedure (24 h, 79% NMR yield, 40% isolated yield). ^{1}H NMR ($CDCl_3$, 400 MHz) δ = 7.40-7.28 (m, 7H), 7.22 (m, 2H), 7.12 (m, 3H), 7.02 (m, 2H), 6.96 (m, 2H), 6.89 (s, 1H), 6.80 (m, 1H) 6.72 (m, 2H), 5.23 (s, 1H), 4.45 (br s, 1H); ^{13}C NMR ($CDCl_3$, 100 MHz) δ = 146.6, 141.4, 139.5, 139.0, 136.4, 133.5, 130.2, 129.4, 129.4, 129.3, 129.2, 129.0,

128.8, 128.1, 127.7, 127.1, 118.5, 114.2, 65.9. HRMS(ESI) *m/z* Calcd for $C_{27}H_{21}ClN$ $[M]^+$: 394.1363; found: 394.1365.

Catalytic Hydroaminoalkylation of Diphenylacetylene with *N*-(4-fluorobenzyl)aniline (3.21)

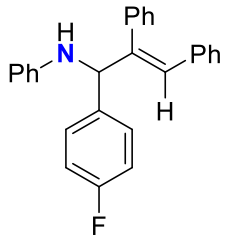

This reaction was carried out according to the general procedure (24 h, 80% NMR yield, 61% isolated yield). ^{1}H NMR ($CDCl_3$, 400 MHz) δ = 7.41 (m, 2H), 7.30 (m, 3H), 7.22 (m, 2H), 7.12 (m, 3H), 7.09-7.00 (m, 4H), 6.97 (m, 2H), 6.88 (s, 1H), 6.79 (m, 1H), 6.72 (m, 2H), 5.23 (s, 1H), 4.19 (br s, 1H); ^{13}C NMR ($CDCl_3$, 100 MHz) δ = 162.4 (d, J = 245.9 Hz), 147.0, 141.6, 139.2, 136.8, 136.5, 129.6 (d, J = 8.3 Hz), 129.4, 129.4, 129.2, 128.8, 128.5, 128.1, 127.6, 127.0, 118.2, 115.6 (d, J = 21.5 Hz), 113.9, 65.6; ^{19}F NMR ($CDCl_3$, 282 MHz) δ = 115.3. HRMS(ESI) *m/z* Calcd for $C_{27}H_{21}FN$ $[M]^+$: 378.1658; found: 378.1664.

A.4 Experimental Data for Chapter 4

Synthesis of Complexes

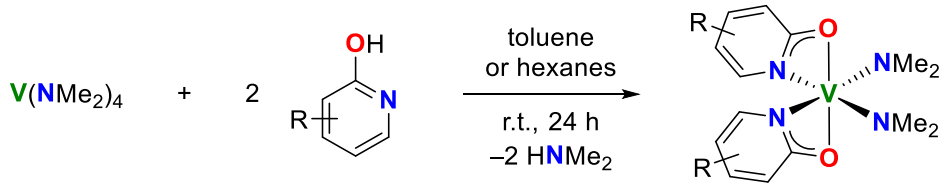

4.1: R = H
4.2: R = 3-Me
4.3: R = 6-Me

4.4: 70% yield; μ_{eff} = 2.04 μ_B
4.5: 55% yield; μ_{eff} = 1.97 μ_B
4.6: 66% yield; μ_{eff} = 2.07 μ_B

Synthesis of complexes 4.4-4.6: A 20 mL vial was charged with pyridone (0.50 mmol) and ~3 mL of hexanes (pyridones **4.2** and **4.3**) or toluene (pyridone **4.1**), giving a cloudy suspension of the colourless solid. Tetrakis(dimethylamido)vanadium(IV) or TDMAV (0.057 g, 0.25 mmol) was then added to the stirring suspension using a total of ~3 mL hexanes; the dark green TDMAV solution became crimson immediately upon contact with the suspension with concomitant solubilization of the pyridone. After stirring the solution at room temperature for 24 h, the volatiles were removed *in vacuo* to give a red powder/residue. The solid/residue was then extracted with ~3 mL of the reaction solvent and filtered through diatomaceous earth. Cooling to −35 °C resulted in the precipitation of dark red crystals of the product suitable for X-ray diffraction. **Complex 4.4:** 0.058 g (70% yield). Effective magnetic moment (Evans' method, 400 MHz, C_6D_6, 25 °C): μ_{eff} = 2.04 μ_B; ^{1}H NMR (C_6D_6, 300 MHz) δ = 4, 3, 2.2. The molecular ion was observed: MS(LIFDI) *m/z* 327 $[M]^+$; Satisfactory elemental analysis could not be obtained. Anal Calcd for $C_{14}H_{20}N_4O_2V$: N, 17.12; C, 51.38; H, 6.16. Found: N, 16.63; C, 51.21; H, 6.19. **Complex 4.5:** 0.049 g, (55% yield). Effective magnetic moment (Evans' method, 400 MHz, C_6D_6, 25 °C): μ_{eff} = 1.97 μ_B; ^{1}H NMR (C_6D_6, 300 MHz) δ = 2.2. The molecular ion was observed: MS(LIFDI) *m/z* 355 $[M]^+$; Anal Calcd for $C_{16}H_{24}N_4O_2V$: N, 15.77; C, 54.08; H, 6.81. Found: N, 15.50; C, 53.98; H, 6.99. **Complex**

4.6: 0.059 g, (66% yield). Effective magnetic moment (Evans' method, 400 MHz, C_6D_6, 25 °C): μ_{eff} = 2.07 μ_B; ^{1}H NMR (C_6D_6, 300 MHz) δ = 5, 2. The molecular ion was observed: MS(LIFDI) *m/z* 355 $[M]^+$; Satisfactory elemental analysis could not be obtained. Anal Calcd for $C_{16}H_{24}N_4O_2V$: N, 15.77; C, 54.08; H, 6.81. Found: N, 14.29; C, 53.95; H, 6.50.

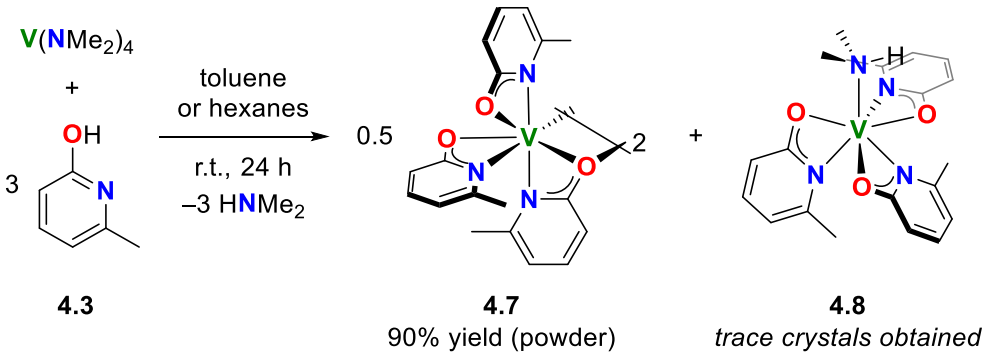

Synthesis of complexes 4.7 and 4.8: A 20 mL vial was charged with pyridone **4.3** (0.082 g, 0.75 mmol) and ~3 mL of hexanes, giving a cloudy suspension of the colourless solid. TDMAV (0.057 g, 0.25 mmol) was then added to the stirring suspension using a total of ~3 mL hexanes; the dark green TDMAV solution became crimson immediately upon contact with the suspension with concomitant solubilization of the pyridone, before turning brown-red over the course of ~5 min. After stirring the solution at room temperature for 24 h, the solution had changed to dark green. Concentrating this solution *in vacuo* to ~4 mL and cooling to −35 °C for several months produced trace amounts of pink crystals of **4.8** suitable for X-ray diffraction. Alternatively, removal of all volatiles *in vacuo* resulted in a viscous, green oil/residue. Repeated trituration of this residue with hot hexanes followed by removal of the volatiles *in vacuo* (three repetitions total) resulted in precipitation of a pink solid and a change in solution colour from green to faint orange. The pink solid was then washed with ~3 mL hexanes and the volatiles were removed *in vacuo*, giving **4.7**

as a pink powder (0.085 g, 90% yield). The characterization data of **4.7** matched those for the alternative synthetic method described below.

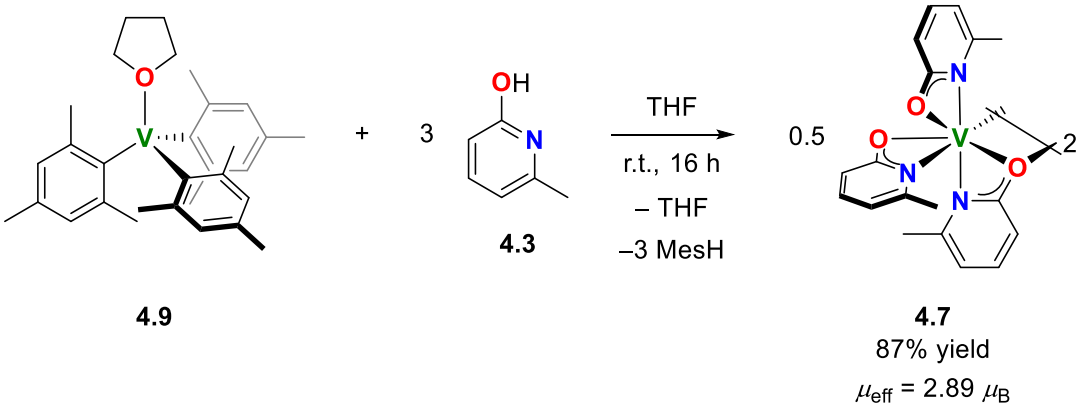

4.9 **4.7**
87% yield
μ_{eff} = 2.89 μ_B

Alternative synthesis of complex 4.7: A 20 mL vial was charged with tris(mesityl) complex **4.9** (0.100 g, 0.214 mmol) before transferring pyridone **4.3** (0.070 g, 0.64 mmol) to the same vial with ~5 mL THF, producing a clear, dark amber-pink solution. The solution was then stirred at room temperature. After 16 h, the volatiles were removed *in vacuo* to give an amorphous pink residue. To this residue, ~3 mL hexanes were added and the suspension was triturated to induce precipitation of a pink powder before removal of the volatiles *in vacuo*; this trituration/removal of volatiles procedure was repeated once more. Finally, the sample was put under high vacuum for 14 h to remove residual mesitylene and give 0.070 g of **4.7** as a pink powder (87% yield). Recrystallization from a saturated THF solution at room temperature for 24 h gave pink crystals suitable for X-ray diffraction. Effective magnetic moment (Evans' method, 400 MHz, C_6D_6, 25 °C): μ_{eff} = 2.89 μ_B; ^{1}H NMR (C_7D_8, 300 MHz) δ = 25, 13, 0, −18. The molecular ions of the dimeric complex and the corresponding monomeric complex were observed: MS(LIFDI) *m/z* 750 $[M]^+$, *m/z* 375 $[M – V(C_6H_6NO)_3]^+$; Anal Calcd for $C_{36}H_{36}N_6O_6V_2$: N, 11.20; C, 57.61; H, 4.83. Found: N, 11.03; C, 57.64; H, 4.86.

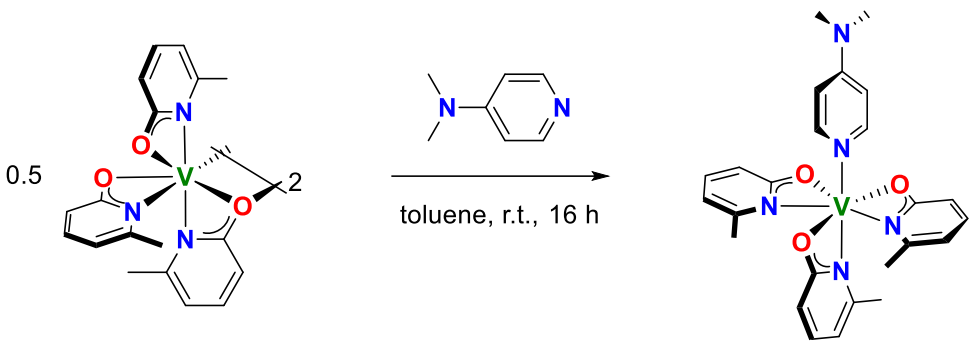

4.7 **4.10**, 84% yield

Synthesis of complex 4.10: A 20 mL vial was charged with complex **4.7** (0.020 g, 0.027 mmol) and ~4 mL of toluene, producing a gold-yellow solution upon stirring for several minutes. A ~1 mL toluene solution of DMAP (0.007 g, 0.06 mmol) was then added dropwise to the stirring solution, gradually changing the solution colour to sage green over the course of ~5 min. After stirring at room temperature for 16 h, the solution had become a yellow-orange, cloudy suspension. The supernatant was then decanted, and the orange precipitate was washed with 3 x ~3 mL hexanes. Finally, the volatiles were removed *in vacuo* to give **4.10** as a poorly soluble, orange powder (0.022 g, 84% yield). Recrystallization in hot THF afforded orange crystals suitable for X-ray diffraction. Effective magnetic moment (Evans' method, 400 MHz, C_6D_6, 25 °C): μ_{eff} = 3.00 μ_B; ^{1}H NMR (C_6D_6, 400 MHz, cyclooctane added) δ = 26, 14.1, 12, 11, −0.8, −21. The molecular ions of **4.10**, **4.7** (corresponding to a loss of DMAP from **4.10**), and DMAP were observed: MS(LIFDI) *m/z* 497 $[M]^+$, *m/z* 375 $[M - C_7H_{10}N_2]^+$, *m/z* 122 $[M - V(C_6H_6NO)_3]^+$; Satisfactory elemental analysis could not be obtained. Anal Calcd for $C_{25}H_{28}N_5O_3V$: N, 14.08; C, 60.36; H, 5.67. Found: N, 13.71; C, 59.34; H, 5.57.

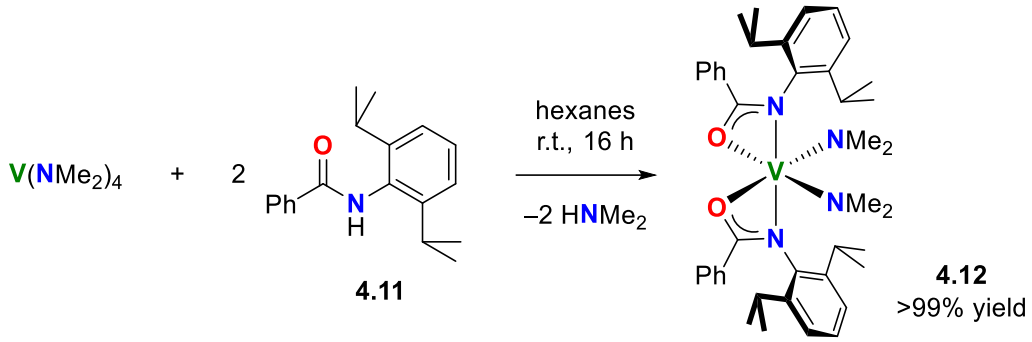

Synthesis of complex 4.12: A 20 mL vial was charged with amide **4.11** (0.141 g, 0.50 mmol) and ~3 mL of hexanes, giving a cloudy suspension of the colourless solid. TDMAV (0.057 g, 0.25 mmol) was then added to the stirring suspension using a total of ~3 mL hexanes; the dark green TDMAV solution became dark yellow upon contact with the suspension, then gradually turned yellow-red and finally crimson as the ligand dissolved. After stirring the solution at room temperature for 16 h, at which point it had become a red-orange suspension, the volatiles were removed *in vacuo* to give the product as an orange-red powder (0.175 g, >99% yield). The solid was then extracted with ~2 mL of toluene and filtered through diatomaceous earth. Layering with pentane before cooling to −35 °C resulted in the precipitation of red-orange crystals suitable for X-ray diffraction. Effective magnetic moment (Evans' method, 400 MHz, C_6D_6, 25 °C): μ_{eff} = 1.74 μ_B; ^{1}H NMR (C_6D_6, 300 MHz) δ = 10, 6, 1. The molecular ion was observed: MS(LIFDI) *m/z* 699 $[M]^+$; Satisfactory elemental analysis could not be obtained. Anal Calcd for $C_{42}H_{56}N_4O_2V$: N, 8.01; C, 72.08; H, 8.07. Found: N, 7.93; C, 71.97; H, 8.64.

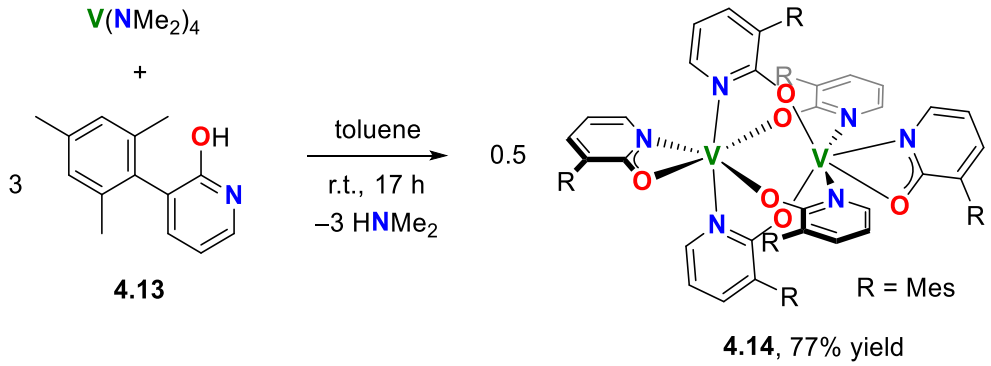

Synthesis of complex 4.14: A 20 mL vial was charged with pyridone **4.13** (0.160 g, 0.75 mmol) and ~3 mL of toluene, giving a cloudy suspension of the colourless solid. TDMAV (0.057 g, 0.25 mmol) was then added to the stirring suspension using a total of ~2 mL toluene; the dark green TDMAV solution became brown-red within ~1 min of addition to the suspension. After stirring the solution at room temperature for 17 h, the solution had changed to dark green. Removal of the volatiles *in vacuo* resulted in a viscous, green oil/residue. Repeated trituration of this residue with hot hexanes followed by removal of the volatiles *in vacuo* (four repetitions total) resulted in precipitation of a yellow-gold solid and a change in solution colour from green to orange-brown. After the final removal of volatiles *in vacuo*, product **4.14** was isolated as a yellow-gold powder (0.133 g, 77% yield). Recrystallization in toluene at −35 °C afforded yellow-gold crystals suitable for X-ray diffraction. Effective magnetic moment (Evans' method, 400 MHz, C_6D_6, 25 °C): μ_{eff} = 3.20 μ_B; ^{1}H NMR (C_6D_6, 300 MHz) δ = 6.7, 6.4, 2.6, 2.26, 2.10, −7, −23, −32. The molecular ion was observed: MS(LIFDI) *m/z* 1375 $[M]^+$; Satisfactory elemental analysis could not be obtained. Anal Calcd for $C_{84}H_{84}N_6O_6V_2$: N, 6.11; C, 73.35; H, 6.16. Found: N, 5.70; C, 73.37; H, 7.15.

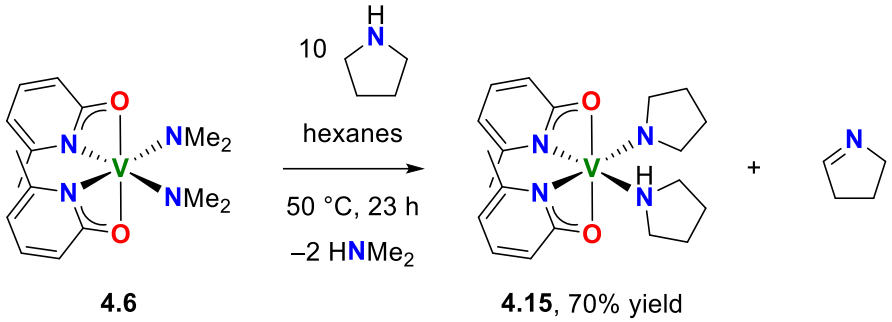

4.6 **4.15**, 70% yield

Synthesis of complex 4.15: Complex **4.6** (0.084 g, 0.24 mmol) was transferred to a 50 mL bomb using ~6 mL of hexanes, producing a dark crimson solution. Pyrrolidine (0.1664 g, 2.34 mmol) was then added to the solution using ~2 mL of hexanes; no colour change was observed. Next, the bomb was sealed, and the solution was stirred at 50 °C for 23 h, becoming dark orange in colour over the course of the reaction. The volatiles were then removed *in vacuo* to give the product as a dark orange powder (0.068 g, 70% yield). Recrystallization in hexanes at −35 °C afforded dark orange crystals suitable for X-ray diffraction. Effective magnetic moment (Evans' method, 400 MHz, C_6D_6, 25 °C): μ_{eff} = 2.82 μ_B; ^{1}H NMR (C_6D_6, 300 MHz) δ = 36, 32, 25, 24, 21, 17, 12, 3, 2.65, 1.40, −8, −26, −30, −32, −35. The molecular ions of **4.15**, **G** (corresponding to a loss of pyrrolidine from **4.15**), and **G'** (corresponding to dimerization of **G**) were observed: MS(LIFDI) *m/z* 408 $[M]^+$, *m/z* 337 $[M - C_4H_9N]^+$, *m/z* 674 $[M - C_4H_9N + C_{16}H_{20}N_3O_2V]^+$; Anal Calcd for $C_{20}H_{29}N_4O_2V$: N, 13.72; C, 58.82; H, 7.16. Found: N, 13.34; C, 58.70; H, 7.13.

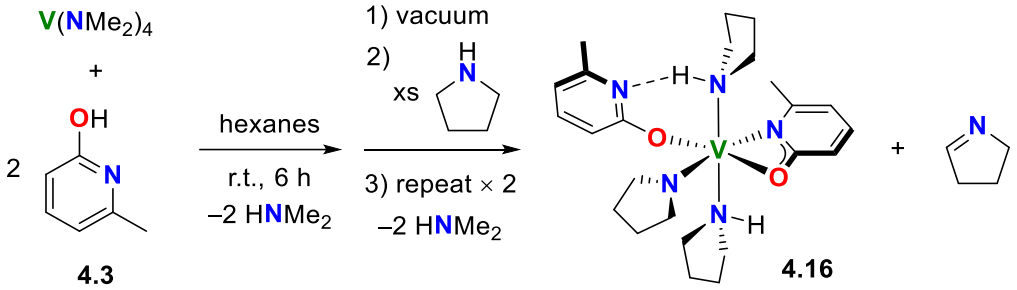

4.3 **4.16**

Synthesis of complex 4.16: A 20 mL vial was charged with pyridone **4.3** (0.055 g, 0.50 mmol) and ~3 mL of hexanes, giving a cloudy suspension of the colourless solid. Tetrakis(dimethylamido)vanadium(IV) or TDMAV (0.057 g, 0.25 mmol) was then added to the stirring suspension using a total of ~3 mL hexanes; the dark green TDMAV solution became crimson immediately upon contact with the suspension with concomitant solubilization of the pyridone. After stirring the solution at room temperature for 6 h, the volatiles were removed *in vacuo* to give a dark red solid/residue. Pyrrolidine (0.181 g, 2.54 mmol) was then transferred to the solution using ~6 mL of hexanes, producing a dark red solution. After stirring for 10 min, the volatiles were removed *in vacuo* and pyrrolidine and hexanes were again added as previously. The solution was then stirred at room temperature for 15 h. Once more, the volatiles were removed *in vacuo* and pyrrolidine was added in the same way as before before stirring at room temperature for 1 h. Finally, removal of volatiles *in vacuo* resulted in a dark orange solid/residue. Unfortunately, only a crude mixture could be obtained for the bulk material. However, recrystallization in hexanes at −35 °C afforded trace amounts of dark orange crystals suitable for X-ray diffraction. In addition to unidentified higher masses and the corresponding monomer of complex **4.7**, **G** (corresponding to a loss of two pyrrolidines from **4.16**), and **G'** (corresponding to dimerization of **G**) were observed, while the molecular ion itself was not observed: MS(LIFDI) *m/z* 337 $[M - 2(C_4H_9N)]^+$, *m/z* 674 $[M - 2(C_4H_9N) + C_{16}H_{20}N_3O_2V]^+$.

NMR Tube Experiments

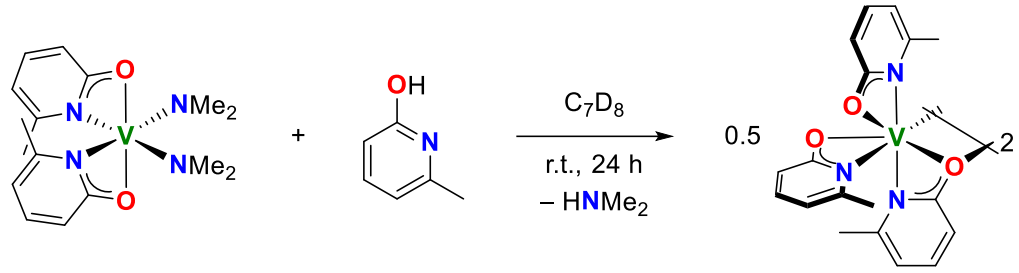

4.6 **4.3** **4.7**

Reduction of 4.6 to 4.7 on NMR scale: Complex **4.6** (0.003 g, 0.009 mmol) was first weighed into a small vial and then quantitatively transferred to a J. Young tube using ~0.75 mL C_7D_8, giving a crimson solution. A *t* = 0 ^{1}H NMR spectrum was then obtained before pyridone **4.3** (0.001 g, 0.009 mmol) was transferred to the J. Young tube using ~0.4 mL C_7D_8; the colour took on a slight brown hue. The tube was then continuously inverted at room temperature for 24 h and periodically monitored by ^{1}H NMR spectroscopy, during which time the solution became orange-yellow in colour. After 24 h, the signals due to pyridone **4.3** had disappeared from the ^{1}H NMR spectrum and signals matching that of isolated complex **4.7** were observed.

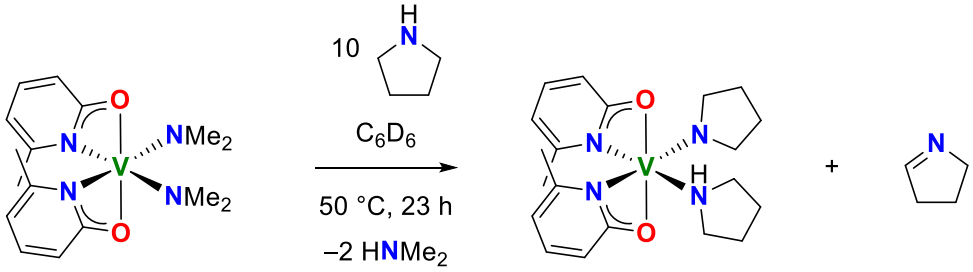

4.6 **4.15**

Reduction of 4.6 to 4.15 on NMR scale: Complex **4.6** (0.005 g, 0.01 mmol) was first weighed into a small vial and then quantitatively transferred to a J. Young tube using ~0.5 mL C_6D_6, giving a crimson solution. A *t* = 0 ^{1}H NMR spectrum was then obtained before pyrrolidine (0.010 g, 0.14 mmol) was transferred to the J. Young tube using ~0.3 mL C_6D_6; no colour change was observed.

Once again, a ^{1}H NMR spectrum was obtained, showing little change beyond the new signals of pyrrolidine. The tube was then heated to 50 °C for 23 h. After the reaction, the solution had become a lighter red-orange colour. Another ^{1}H NMR spectrum was then obtained, showing signals matching that of isolated complex **4.15** and confirming the formation of pyrroline as a byproduct.[291]

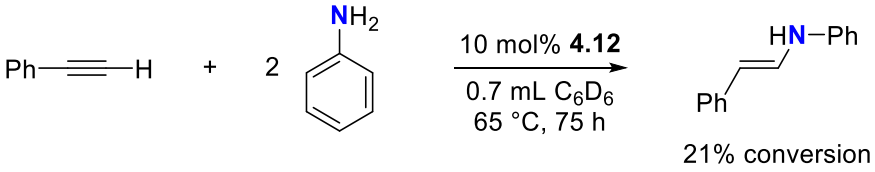

Catalytic hydroamination of phenylacetylene: Complex **4.12** (0.006 g, 0.009 mmol) was first weighed into a small vial and dissolved in ~0.3 mL C_6D_6, giving a red solution. Next, aniline (17 μL, 0.017 g, 0.19 mmol) was added to the vial via microsyringe, causing a gradual colour change from red to orange. Phenylacetylene (10 μL, 0.009 g, 0.09 mmol) was then added via microsyringe, with no accompanying change in colour. The solution was then quantitatively transferred to a J. Young tube using ~0.4 mL C_6D_6. A t = 0 ^{1}H NMR spectrum was then obtained before heating the tube to 65 °C for 75 h. After the reaction, the solution had become a dark red-brown colour. Another ^{1}H NMR spectrum was then obtained, showing 21% conversion to the *anti*-Markovnikov product.[105]

A.5 Experimental Data for Chapter 5

Synthesis of Complexes

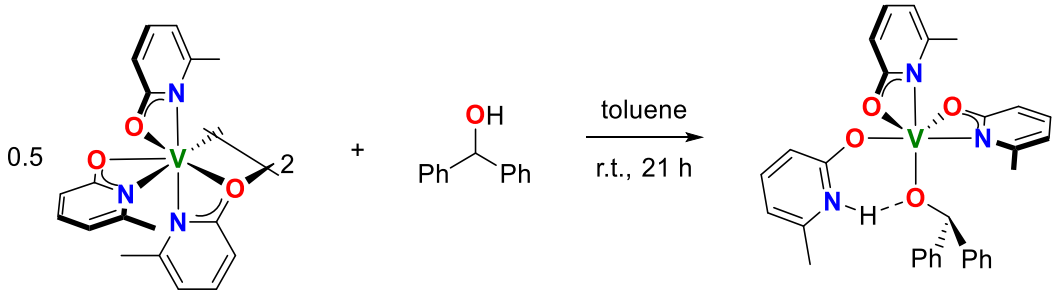

4.7

5.1, 99% yield

μ_{eff} = 2.62 μ_B

Synthesis of 5.1: A 20 mL vial was charged with tris(pyridonate) dimer **4.7** (0.066 g, 0.088 mmol) before adding ~2 mL toluene to give a pale-yellow suspension of the pink solid. Benzhydrol (0.032 g, 0.18 mmol) was then transferred to the suspension using ~2 mL toluene, immediately producing a clear, moss green solution. After stirring at room temperature for 21 h, the solution was filtered through diatomaceous earth and ~3 mL hexanes were added. The solution was then concentrated *in vacuo* to ~1 mL of solvent, and ~3 mL hexanes were added once again, causing a small amount of green solid to precipitate out. This concentration/hexanes addition procedure was repeated two more times before completely removing the volatiles *in vacuo* to give 0.098 g of **5.1** as a light green powder (99% yield). Dissolving the solid in ~2 mL hot toluene and letting the solution cool to room temperature for 24 h gave dark green crystals suitable for X-ray diffraction. Effective magnetic moment (Evans' method, 400 MHz, C_6D_6, 25 °C): μ_{eff} = 2.62 μ_B; ^{1}H NMR (C_7D_8, 300 MHz) δ = 30, 27, 16, 12, −3, −5, −23, −24; The molecular ion was observed, however higher masses were also observed including that of dimer **4.7**: MS(LIFDI) *m/z* 559 $[M]^+$; Anal Calcd for $C_{31}H_{30}N_3O_4V$: N, 7.51; C, 66.54; H, 5.40. Found: N, 7.44; C, 66.79; H, 5.40.

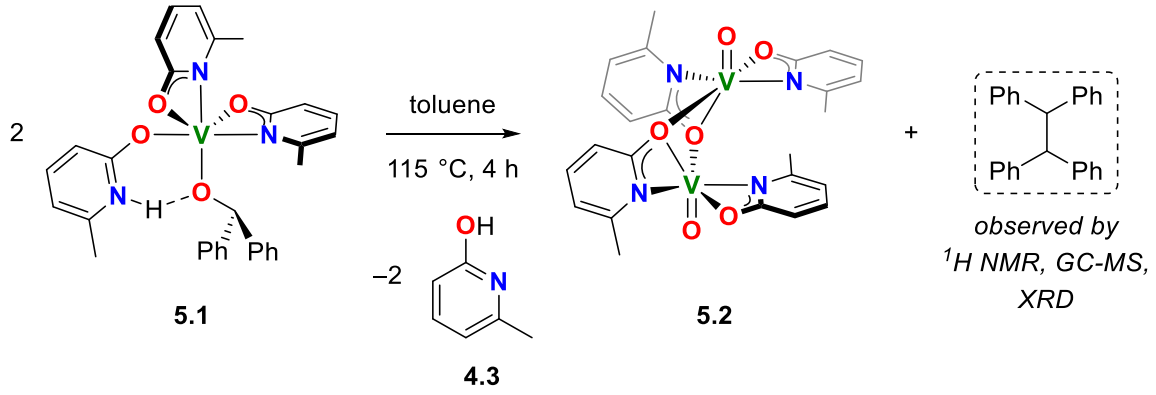

5.1 **5.2** **4.3**

Synthesis of 5.2: A 2 mL bomb was charged with alkoxide complex **5.1** (0.030 g, 0.054 mmol) and a stir bar before adding ~1.5 mL toluene and gently heating to give a dark green solution. The bomb was then sealed, placed in an oil bath set to 115 °C, and stirred for 4 hours. During this time the solution turned to dark turquoise. The solution was then filtered through diatomaceous earth and the volatiles were removed *in vacuo* to give a mixture of colourless and seafoam green solids. The mixture was then dissolved in a minimum amount of hot toluene (~0.5 mL) and left to stand at room temperature. After 48 hours, a mixture of colourless and sky-blue crystals formed, both of which were suitable for X-ray diffraction. The colourless and blue crystals corresponded to 1,1,2,2-tetraphenylethane and complex **5.2**, respectively. Repeated attempts to separate these two products were unsuccessful, thus a yield for complex **5.2** could not be obtained. ^{1}H NMR (C_7D_8, 300 MHz) δ = 14. The molecular ions of the dimeric complex and the corresponding monomeric complex were observed: MS(LIFDI) *m/z* 566 $[M]^+$, *m/z* 283 $[M - VO(C_6H_6NO)_2]^+$. Satisfactory elemental analysis could not be obtained due to persistent co-crystallization of organic product.

NMR Tube Reactions

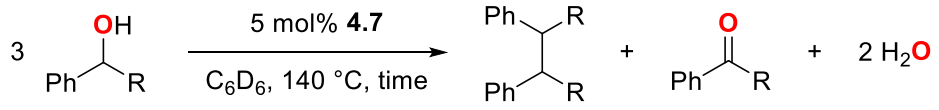

General Procedure for the Catalytic Reductive Coupling of Alcohols with 4.7: To separate small vials, catalyst **4.7** (0.0013 mmol), alcohol substrate (0.026 mmol), and 1,3,5-trimethoxybenzene (0.0083 mmol) were all weighed. Using 800 μL C_6D_6, the contents of the vials were mixed thoroughly to produce a light green solution. The solution was then transferred to a J. Young tube and placed in an oil bath set to 140 °C for 24 or 48 hours (CAUTION: As 140 °C is well above the boiling point of C_6D_6, a blast shield should be used in case the J. Young tube bursts. Though these tubes are designed to withstand pressure, the blast shield should still be used as a precaution). The yields were determined based on the average of two runs, using the relative integrations of the benzylic protons in the product and ortho protons in the aryl ketone byproduct compared to those of the methyl protons in the 1,3,5-trimethoxybenzene internal standard. The solutions were then quenched with methanol, filtered through diatomaceous earth, and diluted in methanol prior to GC-MS analysis to confirm formation of all products.

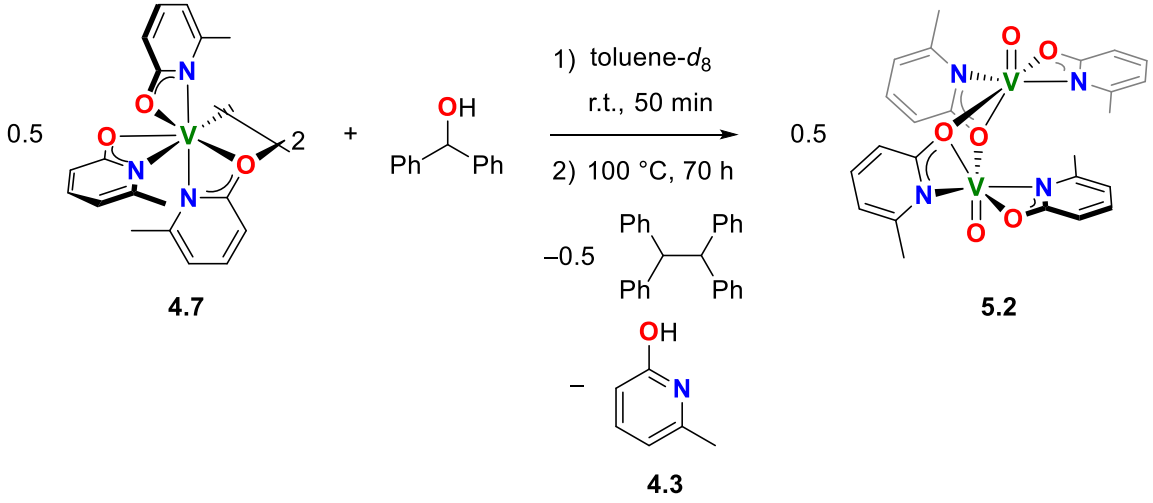

Generation of 5.2 *in situ*: To separate small vials, complex **4.7** (0.002 g, 0.003 mmol) and benzhydrol (0.001 g, 0.005 mmol) were weighed. The alcohol was transferred quantitively to the complex using toluene-d_8 to give a peach-coloured solution, which was transferred to a J. Young

tube. The total volume of toluene-d_8 used was ~1.5 mL. After 50 minutes at room temperature, during which time the ^{1}H NMR spectrum was obtained, the tube was placed in an oil bath set to 100 °C for 70 hours. The ^{1}H NMR spectrum was obtained once more after the heating was finished.

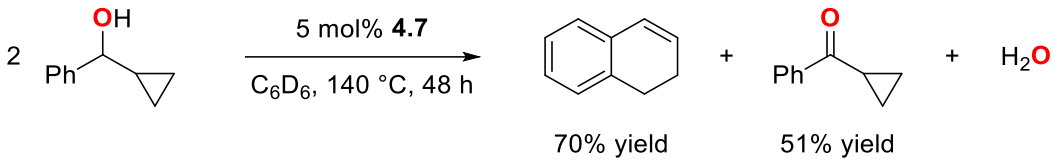

Catalysis with *α*-Cyclopropylbenzyl Alcohol: This reaction was carried out in the same way as the catalytic reductive coupling of 1-phenylethanol except that α-cyclopropylbenzyl alcohol (0.026 mmol) was used as the substrate. The ^{1}H NMR spectrum after the reaction showed the formation of 1,2-dihydronapthalene in 70% yield, which results from the ring-opening reaction of a benzylic radical with the cyclopropyl substituent;[316] thus, this is indicative of a radical process.

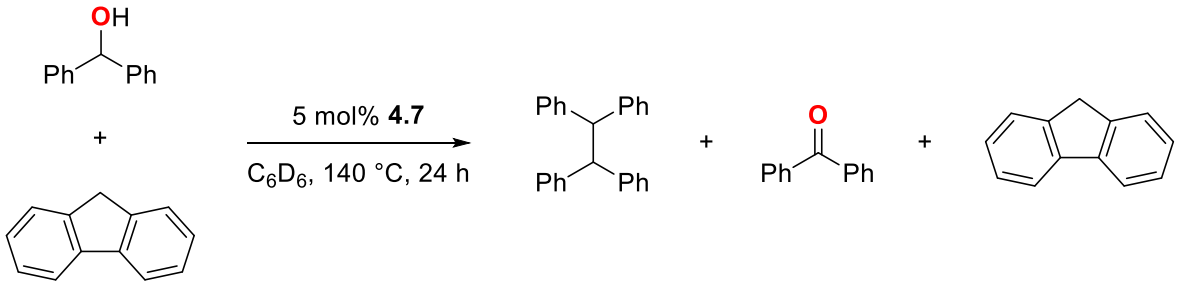

Radical Trap Test with Fluorene: This reaction was carried out in the same way as the catalytic reductive coupling of benzhydrol except that one equivalent of fluorene (0.026 mmol) was included in the reaction mixture. The ^{1}H NMR spectrum after the reaction showed no difference to that of the catalytic reductive coupling of benzhydrol other than the presence of completely unreacted fluorene.

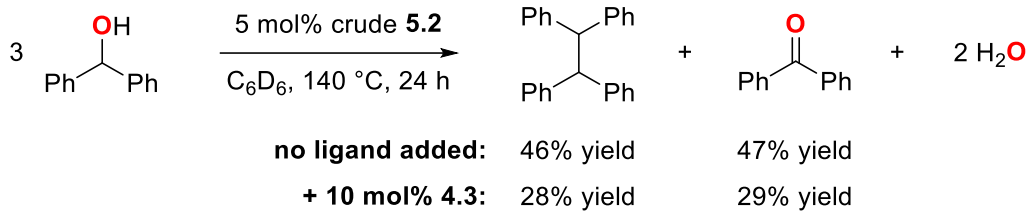

Catalysis using Crude 5.2: This reaction was carried out in the same way as the catalytic reductive coupling of benzhydrol except that a crude sample of dimer **5.2**, containing 1,1,2,2-tetraphenylethane impurity, was used as the catalyst (0.0013 mmol). The moles of product already present at t = 0 were subtracted from the total after the reaction when calculating the yield. This reaction was then repeated in the same way except with 10 mol% of pyridone **4.3** added to the reaction.

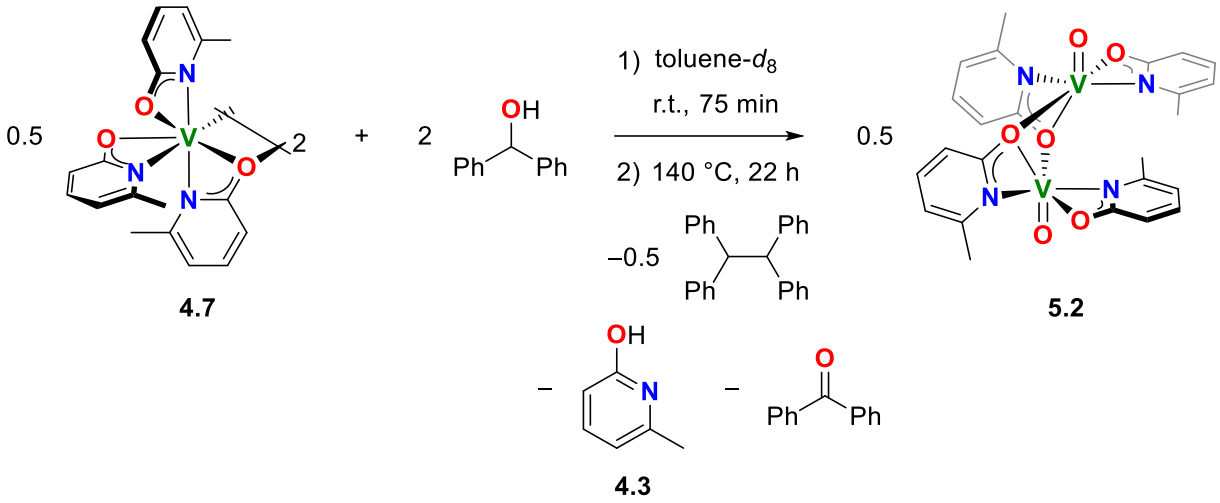

Reaction of 4.7 with 4 Equiv. of Benzhydrol: To separate small vials, complex **4.7** (0.002 g, 0.003 mmol) and benzhydrol (0.002 g, 0.011 mmol) were weighed. The alcohol was transferred quantitively to the complex using toluene-d_8 to give a green coloured solution, which was transferred to a J. Young tube. The total volume of toluene-d_8 used was ~1 mL. After 75 minutes at room temperature, during which time the ^{1}H NMR spectrum was obtained, the tube was placed

in an oil bath set to 140 °C for 22 hours. The ^{1}H NMR spectrum was obtained once more after the heating was finished, revealing that benzophenone had formed.

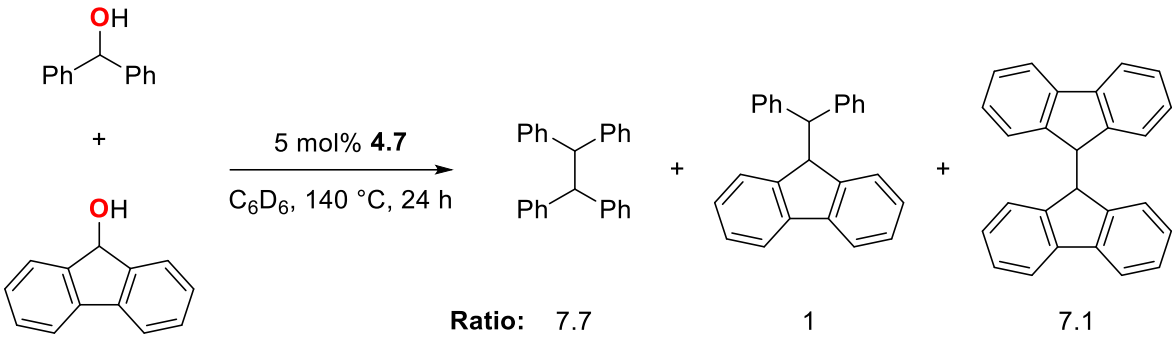

Cross-Over Experiment with Fluorenol: This reaction was carried out in the same way as the catalytic reductive coupling of benzhydrol except that a 1:1 mixture of benzhydrol/fluorenol was used as the substrate (0.013 mmol of each alcohol). The ratio of products was estimated by ^{1}H NMR spectroscopy, using the diagnostic benzylic protons for each product.[315]

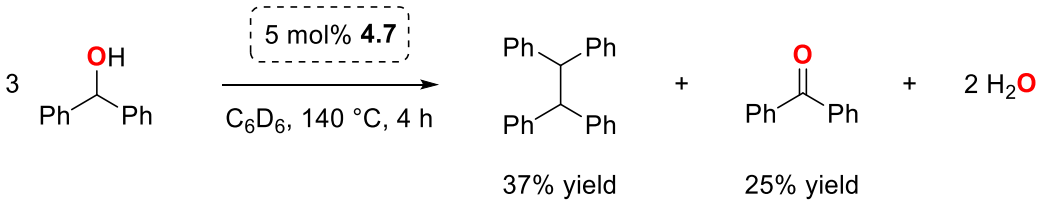

Shortened Catalytic Reaction with Benzhydrol: This reaction was carried out in the same way as the catalytic reductive coupling of benzhydrol except that the reaction was stopped after 4 h rather than 24 h.

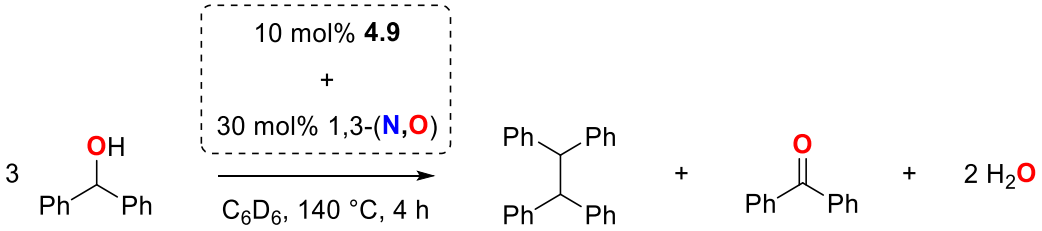

Ligand Screen for Catalytic Reductive Coupling of Benzhydrol: To separate small vials, complex **4.9** (0.0026 mmol), 1,3-*N*,*O*-chelate proligand (0.0079 mmol), alcohol substrate (0.026

mmol), and 1,3,5-trimethoxybenzene (0.0083 mmol) were all weighed. Using 800 μL C_6D_6, the contents of the vials were mixed thoroughly to produce a light yellow or green solution depending on the ligand used. The solution was then transferred to a J. Young tube and placed in an oil bath set to 140 °C for 4 h. The yields were determined by ^{1}H NMR spectroscopy using 1,3,5-trimethoxybenzene as an internal standard.

Calculation of Yields for the Reductive Coupling of Alcohols

The calculation used to obtain the yield of product in the reaction shown in Table 5.1, entry 1 and Figure D.34 is as follows:

1. Given that 3 equiv. of benzhydrol starting material produce 1 equiv. of 1,1,2,2-tetraphenylethane product, the theoretical yield of product for the reaction is:

   0.027 mmol benzhydrol × (1 mol product)/(3 mol benzhydrol) = 0.0090 mmol

2. The signal for the three methyl Hs of 1,3,5-trimethoxybenzene (internal standard) has been integrated to 9.00, which corresponds to one relative mole of internal standard. The signal for the methine Hs of the product integrates to 2.17 as a result, which must be divided by two to give the relative moles of product. The actual amount of internal standard used was 0.0083 mmol. Thus, the actual yield of product based on the integration ratio with the internal standard is:

   0.0083 mmol internal standard × [(2.17/2) mol product]/[(9.00/9) mol internal standard] =

   0.0090 mmol product

3. Thus, the NMR yield is:

   (0.0090 mmol product)/(0.0090 mmol) × 100% = 100%, or >99%

The yield of benzophenone byproduct produced can be calculated analogously using the signal at 7.71 ppm for the ortho Hs of the phenyl substituents integrating to 3.75.

Presentation of Yields for the Reductive Coupling of Alcohols

The yields of product and ketone byproduct reported in Table 5.1 and elsewhere in this thesis may initially appear confusing, as they sum to greater than 100%. This section is meant to clarify why this is reasonable. The reaction with benzhydrol is used as an example.

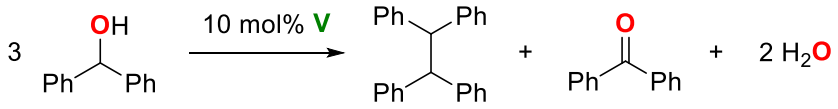

The pathway to produce 1,1,2,2-tetraphenylethane is coupled with the production of benzophenone. In other words, benzophenone does *not* result from an independent reaction that competes with product formation (the only exception to this is entry 5 in Table 5.2, where more benzophenone is produced than 1,1,2,2-tetraphenylethane, indicating an independent alcohol oxidation pathway).

Since the precatalyst for reductive coupling is already in the reduced V(III) oxidation state, no alcohol oxidation is needed for the first reductive coupling event to occur to generate 1,1,2,2-tetraphenylethane. Therefore, as 10 mol% V is used, the yield of 1,1,2,2-tetraphenylethane is generally 10% higher than that of benzophenone. As such, if a 100% yield of 1,1,2,2-tetraphenylethane is achieved, a ~90% yield of benzophenone would be expected.

An alternative way to conceptualize this reaction is to consider the third equiv. of benzhydrol that acts as the reductant separately from the other 2 equiv. of benzhydrol (the substrate). The scheme below shows the third equiv. of alcohol over the arrow, which could be interchanged with any other stoichiometric reductant able to reduce the oxidized V catalyst back to V(III). This is conceptually no different than any generic reaction requiring a reductant; full conversion of the reductant to its corresponding oxidized product is needed to achieve full conversion to the desired product, so both products could have yields approaching 100%. Since

benzhydrol is the reductant, it is redundant to show it both above and beside the arrow as represented below, thus the 3:1 stoichiometry of benzhydrol to each organic product results. Importantly, whichever way the reaction is represented has no impact on the results when calculating the yields.

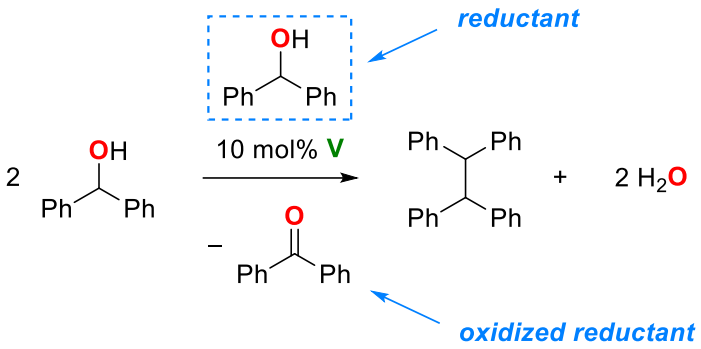

A.6 Experimental Data for Chapter 6

Synthesis of Complexes

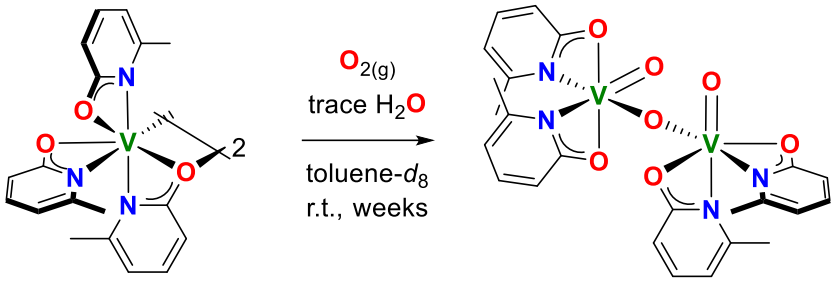

4.7 **6.1**

Synthesis of 6.1: A small vial was charged with tris(pyridonate) dimer **4.7** (0.015 g, 0.020 mmol) before quantitative transfer to a J. Young tube using ~1 mL toluene-d_8. Gentle heating was applied to aid in dissolving the complex, producing a peach-yellow solution. A t = 0 ^{1}H NMR spectrum was then collected. Next, the tube was connected to a Schlenk line and the solution was degassed via three freeze-pump-thaw cycles and backfilled with oxygen gas at room temperature. After sealing and shaking the tube, the solution immediately turned dark purple and a ^{1}H NMR spectrum was collected. This solution was left for weeks at room temperature before the tube was degassed again using the same procedure and backfilled with nitrogen to bring into the glovebox. After removal of the solution, trace amounts of dark purple crystals remained in the J. Young tube that were suitable for X-ray diffraction studies, revealing **6.1** as a product.

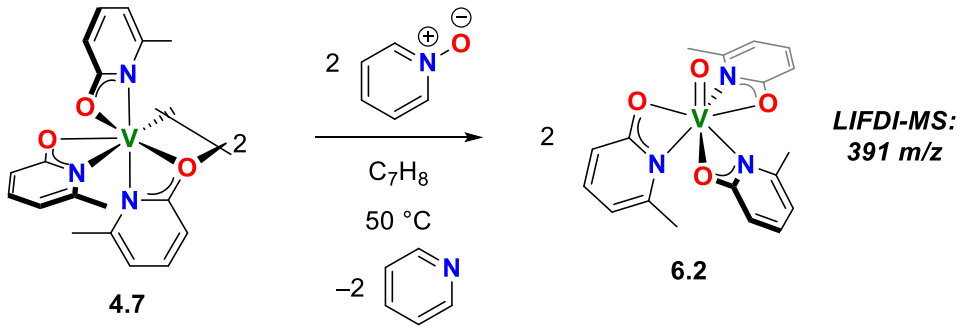

4.7 **6.2**

Synthesis of 6.2: To separate small vials, tris(pyridonate) dimer **4.7** (0.030 g, 0.040 mmol) and pyridine-*N*-oxide (0.008 g, 0.08 mmol) were weighed. The complex was then quantitatively transferred to a 50 mL bomb using ~5 mL toluene, before the same was done with the oxide using ~3 mL toluene. Upon addition of the oxide, the peach-yellow solution turned bright orange. The bomb was then sealed, placed in an oil bath set to 50 °C, and stirred for 16 h. During this time the solution turned to dark purple. The solution was then transferred to a 20 mL vial and the volatiles were removed *in vacuo* to give a very viscous, dark purple oil. As efforts to recrystallize this oil to get a crystal structure of **6.2** were unsuccessful, a dilute toluene solution of the sample was prepared for LIFDI-MS analysis. The molecular ions of complex **6.2**, the corresponding monomeric complex of dimer **5.2**, and pyridone **4.3** were observed: MS(LIFDI) *m/z* 391 $[M]^+$, *m/z* 283 $[VO(C_6H_6NO)_2]^+$, *m/z* 109 $[C_6H_6NO]^+$.

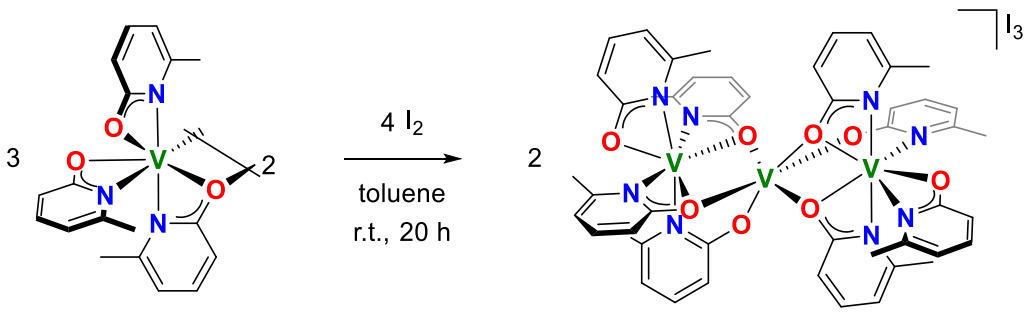

4.7 **6.3**, 81% yield

Synthesis of 6.3: A small vial was charged with iodine (0.013 g, 0.051 mmol) and dissolved in ~2 mL toluene to give a red-violet solution. Next, a 20 mL vial was charged with tris(pyridonate) dimer **4.7** (0.028 g, 0.038 mmol) before adding ~4 mL toluene to give a pale-yellow suspension of the pink solid. While stirring, the iodine solution was then transferred to the suspension, causing the purple colour to change to brown-orange with concomitant precipitation of a yellow powder. After stirring at room temperature for 20 h, the volatiles were removed *in vacuo* to give a mixture

of the yellow solid and some brown-orange residue. The yellow solid was then washed with toluene several times at room temperature until the brown-orange residue was no longer present. Removal of the volatiles *in vacuo* once more gave 0.029 g of complex **6.3** as a yellow powder (81% yield). Recrystallization in a minimum amount of hot toluene and letting the solution cool to room temperature for 24 h gave bright yellow crystals suitable for X-ray diffraction. LIFDI-MS analysis revealed a complex mixture of fragments, with no observation of the molecular ion. Satisfactory elemental analysis could not be obtained. Anal Calcd for $C_{48}H_{48}I_3N_8O_8V_3$: N, 8.01; C, 41.22; H, 3.46. Found: N, 7.65; C, 40.30; H, 3.99.

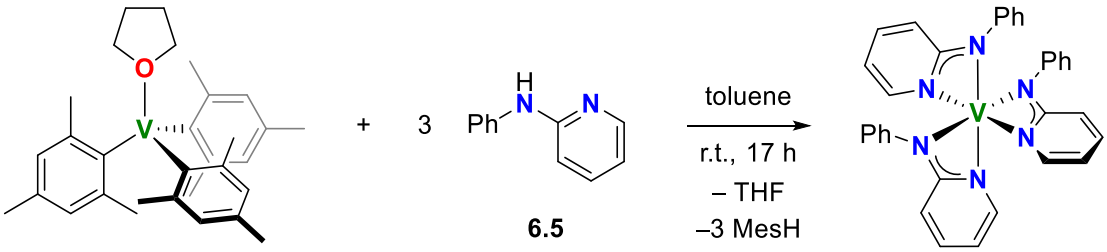

4.9 **6.5** **6.6**, 71% yield

Synthesis of 6.6: A 20 mL vial was charged with tris(mesityl) complex **4.9** (0.015 g, 0.031 mmol) and dissolved in ~2 mL toluene, producing a deep blue solution. While stirring, aminopyridine **6.5** (0.016 g, 0.093 mmol) was then transferred to the same vial dropwise with ~3 mL toluene. During addition, the solution first turned plum-purple, then burgundy-red, and finally pink-red over the course of 5 min. The solution was then stirred at room temperature. After 17 h, the volatiles were removed *in vacuo* to give an amorphous red residue. The residue was then dissolved in ~5 mL hot hexanes and filtered through diatomaceous earth using an additional ~3 mL hexanes before concentrating *in vacuo* to a volume of ~2 mL. After cooling to −35 °C for several days, a small amount of dark red crystals suitable for X-ray diffraction crystallized from the solution. Finally,

the volatiles were removed from the supernatant *in vacuo* to give 0.012 g of **6.6** as a red solid (71% yield).

NMR Tube Reactions

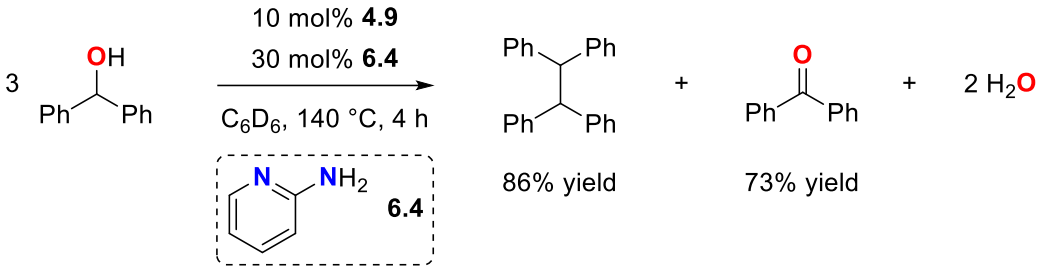

Catalytic Reductive Coupling of Alcohols with Ligand 6.4: To separate small vials, complex **4.9** (0.005 mmol), proligand **6.4** (0.015 mmol), benzhydrol substrate (0.053 mmol), and ferrocene (1.3417% wt./wt. in toluene, 0.009 mmol) were all weighed. Using 800 μL C_6D_6 (including the volume of ferrocene solution added), the contents of the vials were mixed thoroughly to produce a bright yellow solution. The solution was then transferred to a J. Young tube and placed in an oil bath set to 140 °C for 4 h. The yields were determined by ^{1}H NMR spectroscopy using ferrocene as an internal standard.

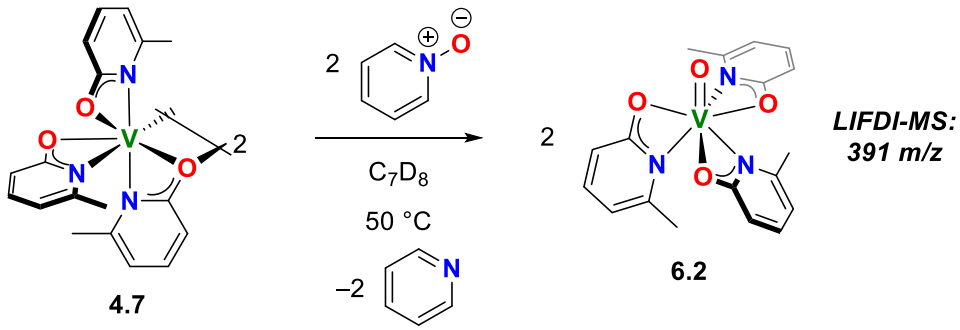

NMR Scale Synthesis of Complex 6.2: To separate small vials, tris(pyridonate) dimer **4.7** (0.004 g, 0.005 mmol) and pyridine-*N*-oxide (0.001 g, 0.01 mmol) were weighed. The complex was then dissolved in ~0.2 mL toluene-d_8, giving a peach-yellow solution. Next, the oxide was quantitatively transferred to the complex using ~0.4 mL toluene-d_8, causing a colour change to

light orange. The solution was then transferred to a J. Young tube using ~0.2 mL toluene-d_8 and a ^{1}H NMR spectrum was collected. The tube was then placed in an oil bath set to 50 °C and stirred for 17 h. During this time, the solution turned to dark purple. After heating, a second ^{1}H NMR spectrum was collected.

Appendix B Computational Details

B.1 Computational Data for Chapter 4

General Computational Methods

Density functional theory calculations were carried out using the Gaussian 09 package (Revision D.01)[357] and the B3LYP functional.[358,359] All geometry optimizations were performed using the 6-311++G(d,p)' basis set for all atoms and the GD3BJ[360] dispersion correction with inclusion of solvent effects (*n*-hexane, SMD model).[361] Frequency calculations were performed at the same level of theory to verify that each optimized structure was a true stationary point. The calculated spin-densities from the optimized structures were plotted using VMD.[362]

Spin State Determination of Complex 4.8

To distinguish between the triplet and singlet spin states for complex 4.8, both structures were calculated, and their optimized energies were compared:

Table B.1 Thermochemical comparison of the two possible spin states for V(III) complex **4.8**

Spin State	Electronic Energy (EE) (Hartrees)	Thermal Free Energy Correction (Hartrees)	EE + Thermal Free Energy Correction (Hartrees)	EE + Thermal Free Energy Correction (kcal/mol)	Relative Free Energy (kcal/mol)
triplet (S = 1)	−2166.576438	0.368611	−2166.207827	−1359315.990	0.0
singlet (S = 0)	−2166.521597	0.369066	−2166.152531	−1359281.292	34.7

Thus, the triplet spin state of complex **4.8** is much more energetically favourable compared to the singlet spin state.

XYZ Coordinates of Optimized Geometries

Complex **4.4**

V	0.000000	0.818400	-0.000000
O	1.100800	0.221200	-1.560800
O	-1.100800	0.221200	1.560800
N	1.453300	-0.871900	0.327000
N	-1.453400	-0.871800	-0.327000
N	-1.137800	2.031300	-0.820500
N	1.137900	2.031200	0.820500
C	-2.772000	-1.531600	1.571400
H	-3.023200	-1.391700	2.614600
C	2.054500	-1.796000	1.080800
H	1.732100	-1.860500	2.114800
C	-1.787500	-0.722800	0.974100
C	-2.054600	-1.795900	-1.080900
H	-1.732300	-1.860300	-2.114900
C	-3.033000	-2.632900	-0.568400
H	-3.502500	-3.378100	-1.196700
C	2.772100	-1.531600	-1.571400
H	3.023400	-1.391500	-2.614600
C	-3.387600	-2.486600	0.781200
H	-4.150500	-3.127200	1.210200
C	1.787500	-0.722800	-0.974100
C	-1.729200	1.749800	-2.116600
H	-1.624700	2.617100	-2.783600
H	-2.801500	1.523400	-2.027100
H	-1.231300	0.899600	-2.582400
C	3.387600	-2.486600	-0.781200
H	4.150500	-3.127100	-1.210200
C	3.033000	-2.632900	0.568300
H	3.502400	-3.378100	1.196700
C	-1.682600	3.221500	-0.196300
H	-1.171100	3.424900	0.744200
H	-2.752700	3.091100	0.020800
H	-1.583500	4.096200	-0.854800
C	1.729300	1.749600	2.116600
H	1.231300	0.899400	2.582400
H	1.624800	2.616800	2.783700

H	2.801600	1.523100	2.027100
C	1.682700	3.221400	0.196400
H	2.752800	3.091000	-0.020500
H	1.583500	4.096100	0.855000
H	1.171200	3.424800	-0.744100

Complex **4.5**

V	0.000000	0.926100	0.000000
N	-0.831200	2.140600	-1.129900
N	0.831600	2.140300	1.130100
C	-0.997100	1.858600	-2.544600
H	-0.378800	1.009500	-2.835100
H	-0.695500	2.726400	-3.148100
H	-2.044700	1.629300	-2.787900
C	1.542300	3.329700	0.703400
H	2.627600	3.198600	0.824400
H	1.247400	4.204900	1.299900
H	1.343500	3.533600	-0.348500
C	-1.541400	3.330300	-0.703100
H	-2.626800	3.199700	-0.824200
H	-1.246100	4.205500	-1.299500
H	-1.342600	3.534000	0.348800
C	0.997400	1.858100	2.544800
H	0.696100	2.726000	3.148300
H	2.044900	1.628400	2.788100
H	0.378700	1.009300	2.835200
O	1.525100	0.329000	-1.146800
N	1.279900	-0.761100	0.760300
C	1.994800	-0.615600	-0.371900
C	3.122400	-1.418800	-0.661500
C	1.619500	-1.684300	1.666000
H	0.997200	-1.747900	2.552000
C	3.454700	-2.369200	0.291000
H	4.312000	-3.012000	0.116800
C	3.879300	-1.212400	-1.939700
H	3.228500	-1.349000	-2.808800
H	4.713300	-1.912900	-2.018800
H	4.275200	-0.194100	-2.003200
C	2.707300	-2.516500	1.470700

H	2.968200	-3.263200	2.209100
O	-1.525100	0.329100	1.146900
N	-1.280100	-0.760700	-0.760500
C	-1.995000	-0.615400	0.371800
C	-3.122600	-1.418500	0.661400
C	-1.620000	-1.683800	-1.666200
H	-0.997700	-1.747300	-2.552300
C	-3.879400	-1.212100	1.939800
H	-3.228400	-1.349100	2.808700
H	-4.713400	-1.912500	2.018800
H	-4.274900	-0.193800	2.003500
C	-3.455100	-2.368700	-0.291200
H	-4.312500	-3.011400	-0.116900
C	-2.707800	-2.515900	-1.471000
H	-2.968900	-3.262500	-2.209400

Complex **4.6**

V	-0.000100	1.003300	-0.000000
N	-1.242000	2.222100	0.641400
N	1.241800	2.222200	-0.641400
C	1.693500	3.401400	0.071200
H	1.051100	3.595300	0.929800
H	1.693600	4.285100	-0.583000
H	2.720300	3.263300	0.440100
C	2.010200	1.958400	-1.844600
H	3.053700	1.704700	-1.607500
H	2.021700	2.844100	-2.495500
H	1.567000	1.132800	-2.399700
C	-1.693700	3.401400	-0.071200
H	-1.693900	4.285000	0.583100
H	-2.720500	3.263300	-0.440200
H	-1.051200	3.595300	-0.929800
C	-2.010400	1.958300	1.844500
H	-1.567400	1.132500	2.399500
H	-3.054000	1.704800	1.607400
H	-2.021800	2.843900	2.495600
O	-0.866100	0.423400	-1.703800
N	-1.475500	-0.709800	0.093500
C	-1.617100	-0.542200	-1.240200

C	-2.131400	-1.679000	0.747800
C	-2.472800	-1.360600	-1.996000
H	-2.572700	-1.202100	-3.061600
C	-1.906400	-1.784600	2.228300
H	-0.868500	-1.558100	2.475200
H	-2.157200	-2.781600	2.594000
H	-2.534600	-1.063800	2.761500
C	-2.987400	-2.533500	0.057500
H	-3.507500	-3.322000	0.586000
C	-3.154400	-2.359300	-1.321400
H	-3.820700	-3.018300	-1.867900
O	0.866000	0.423500	1.703800
N	1.475600	-0.709700	-0.093500
C	1.617100	-0.542100	1.240200
C	2.131600	-1.678800	-0.747800
C	2.472900	-1.360300	1.996100
H	2.572800	-1.201800	3.061600
C	2.987700	-2.533200	-0.057400
H	3.507900	-3.321600	-0.585900
C	1.906600	-1.784500	-2.228300
H	0.868600	-1.558200	-2.475100
H	2.157600	-2.781500	-2.593900
H	2.534500	-1.063600	-2.761500
C	3.154700	-2.358900	1.321500
H	3.821100	-3.017800	1.868000

Complex **4.8** (triplet)

V	0.106300	-0.134900	0.790600
O	0.705000	1.761300	1.374600
N	-0.647600	1.593000	-0.361400
C	0.042100	2.411400	0.471500
C	0.014000	3.811600	0.310500
H	0.574500	4.439500	0.990300
C	-1.386800	2.089300	-1.370600
C	-1.445600	3.461700	-1.583400
H	-2.039500	3.854800	-2.398000
C	-0.738400	4.319700	-0.728400
H	-0.784200	5.391900	-0.888000
C	-2.126700	1.124200	-2.248100

H	-1.442600	0.386400	-2.672000
H	-2.622400	1.649200	-3.065700
H	-2.881400	0.578800	-1.677700
O	-1.736900	-0.143800	1.783300
N	-1.483200	-1.243300	-0.107200
C	-2.329800	-0.853700	0.879000
C	-1.875500	-2.035400	-1.117200
C	-3.691500	-1.222200	0.838000
H	-4.363500	-0.884900	1.616000
C	-3.200800	-2.441900	-1.199100
H	-3.523100	-3.076500	-2.014100
C	-4.105300	-2.019700	-0.211200
H	-5.143800	-2.327600	-0.273400
C	-0.833900	-2.445900	-2.113700
H	-0.229100	-1.589400	-2.419300
H	-1.288400	-2.894500	-2.998000
H	-0.152300	-3.172700	-1.664100
O	1.022100	-2.035200	0.637300
N	1.799600	-0.343900	-0.543900
C	1.891400	-1.666500	-0.246400
C	2.631700	0.236300	-1.430400
C	2.853200	-2.487300	-0.872500
H	2.904400	-3.539100	-0.623900
C	3.599600	-0.523600	-2.074900
H	4.268000	-0.055200	-2.785100
C	3.699900	-1.893800	-1.787200
H	4.454500	-2.490900	-2.288300
C	2.473400	1.706800	-1.675200
H	1.480400	1.930500	-2.071700
H	3.221100	2.066200	-2.383200
H	2.578000	2.260700	-0.739800
N	0.950700	-0.523300	2.790000
H	0.795600	-1.525100	2.873800
C	2.407200	-0.286600	2.833200
H	2.902600	-0.894800	2.078700
H	2.817700	-0.539800	3.817600
H	2.596300	0.766100	2.626400
C	0.268300	0.165600	3.902600
H	0.380100	1.240400	3.765600

H	0.704200	-0.126000	4.865400
H	-0.790400	-0.080300	3.881500

Complex **4.8** (singlet)

V	-0.189100	-0.311000	0.768300
O	0.386200	-2.168900	0.612400
N	1.709100	-0.779100	-0.462600
C	1.486900	-2.055600	-0.103500
C	2.340400	-3.105400	-0.452800
H	2.111400	-4.117800	-0.148400
C	2.824800	-0.451700	-1.135500
C	3.728300	-1.445000	-1.519200
H	4.618100	-1.173600	-2.072100
C	3.474200	-2.775000	-1.180600
H	4.171100	-3.550800	-1.478400
C	3.068100	0.991100	-1.464800
H	2.305100	1.369700	-2.147900
H	4.043000	1.117100	-1.937400
H	3.032700	1.606800	-0.564700
O	0.795300	0.776500	2.196400
N	0.369800	1.679900	0.235500
C	0.910000	1.845200	1.467700
C	0.335500	2.670700	-0.667300
C	1.495700	3.070900	1.837600
H	1.925600	3.187100	2.823700
C	0.906500	3.900200	-0.361500
H	0.894200	4.698300	-1.092200
C	1.488800	4.088000	0.901300
H	1.936100	5.045700	1.145600
C	-0.328800	2.390700	-1.983400
H	-0.049700	1.403800	-2.355400
H	-0.059500	3.143900	-2.725500
H	-1.416600	2.395100	-1.872200
O	-1.984900	0.814100	1.078100
N	-1.660400	-0.409600	-0.715900
C	-2.477200	0.462500	-0.064100
C	-1.971400	-0.898200	-1.930800
C	-3.686900	0.888900	-0.645800
H	-4.320700	1.587300	-0.115200

C	-3.157600	-0.517900	-2.546200
H	-3.412400	-0.918000	-3.518800
C	-4.012500	0.382300	-1.891200
H	-4.938600	0.683600	-2.369100
C	-0.991600	-1.845500	-2.554500
H	-0.009200	-1.374200	-2.644000
H	-1.322700	-2.160500	-3.544900
H	-0.862600	-2.731400	-1.927100
N	-1.227600	-1.289600	2.441500
H	-1.708800	-0.465900	2.793500
C	-2.236200	-2.286400	2.050300
H	-2.951100	-1.832200	1.365400
H	-2.775800	-2.675700	2.922700
H	-1.736500	-3.111400	1.542700
C	-0.323300	-1.803000	3.484900
H	0.240200	-2.643900	3.080300
H	-0.884000	-2.139200	4.365400
H	0.370800	-1.015500	3.774700

Appendix C Crystallographic Details

C.1 Data Collection and Processing Information

The summaries of the crystallographic data for all compounds are shown in the tables below. The automatic data collection strategy was determined using *COSMO* and the cell determination and integration processes were carried out using *SAINT*. Using *Olex2*,[363] the structures were solved with the *ShelXT*[364] structure solution program using Intrinsic Phasing and the structures were refined using the *ShelXL*[365] refinement package using the Least Squares method.

For Chapter 3, *PLATON/SQUEEZE*[366] was used in the structural refinement of **3.5** to remove disordered hexanes. Complex **3.2** was poorly-diffracting, resulting in relatively poor resolution and two unusually shaped ellipsoids. This could not be improved to resolve the A- and B-alerts in the checkCIF for **3.2**. Complex **3.5** was also poorly-diffracting, resulting in relatively poor resolution and four unusually shaped ellipsoids. Additionally, **3.5** crystallizes as a racemic twin in a non-centrosymmetric space group ($P2_1$), where most of the molecule is related by inversion symmetry except for the chiral carbon. This further contributes to the disorder and could not be improved to resolve the A- and B-alerts in the checkCIF for **3.5**. These facts should be taken into consideration when examining the bond metrics for complexes **3.2** and **3.5**.

For Chapter 4, the crystals of complex **4.10** were found to undergo a phase change and crack at 90 K, thus the data was collected at 120 K to avoid cracking during data collection. However, this had no detrimental effect on the quality of the data. In the crystal structure of complex **4.14**, some of the toluene molecules present in the lattice were modelled, but others were highly disordered and could not be modelled; these disordered toluene molecules were removed using the *Olex2* solvent mask command. Additionally, the checkCIF for complex **4.14** produces a

B-alert as the coordinates do not form a properly connected set. Unfortunately, this alert could not be resolved as the structure sits on a symmetry element with half a molecule in the asymmetric unit. Complex **4.15** was poorly-diffracting, resulting in relatively poor resolution. This could not be improved to resolve the B-alert in the checkCIF for **4.15**, although the model still refined well.

For Chapter 5, the unit cell determined for the colourless crystals obtained during the synthesis of **5.2** matched that of 1,1,2,2-tetraphenylethane from a previous report.[367]

For Chapter 6, the crystals of **6.3** were poorly-diffracting, resulting in relatively poor resolution and giving an A-alert in the checkCIF. This should be taken into consideration when examining the bond metrics for complex **6.3**.

C.2 Tabulated Crystallographic Parameters for Chapter 2

Table C.1 List of crystallographic parameters for compounds **2.2**, **2.4**, **2.6**, **2.7**, **2.8**, and **2.9**

Compound	**2.2**	**2.4**
Empirical formula	$C_{33}H_{52}N_4O_2Zr$	$C_{30}H_{57}N_7O_2Zr$
Formula weight	628.00	639.04
Temperature/K	90	100
Crystal system	monoclinic	triclinic
Space group	$P2_1/n$	P-1
a/Å	11.411(2)	11.0212(8)
b/Å	20.388(4)	11.6924(9)
c/Å	14.842(3)	14.0264(10)
α/°	90	76.133(3)
β/°	106.342(4)	77.447(4)
γ/°	90	80.581(4)
Volume/Å^3	3313.4(10)	1701.0(2)
Z	4	2
ρ_{calc}g/cm^3	1.259	1.248
μ/mm^{-1}	0.365	0.359
F(000)	1336.0	684.0
Crystal size/mm^3	0.44 × 0.2 × 0.12	0.25 × 0.14 × 0.13
Radiation	MoKα (λ = 0.71073)	MoKα (λ = 0.71073)
2Θ range for data collection/°	3.488 to 61.174	3.812 to 61.084
Index ranges	$-16 \le h \le 16$, $-29 \le k \le 29$, $-20 \le l \le 20$	$-15 \le h \le 13$, $-16 \le k \le 16$, $-19 \le l \le 19$
Reflections collected	38688	37732
Independent reflections	10051 [R_{int} = 0.0401, R_{sigma} = 0.0374]	10263 [R_{int} = 0.0299, R_{sigma} = 0.0310]
Data/restraints/parameters	10051/0/371	10263/0/375
Goodness-of-fit on F^2	1.037	1.062
Final R indexes [I>=2σ (I)]	R_1 = 0.0336, wR_2 = 0.0763	R_1 = 0.0345, wR_2 = 0.0858
Final R indexes [all data]	R_1 = 0.0454, wR_2 = 0.0813	R_1 = 0.0404, wR_2 = 0.0886
Largest diff. peak/hole / e Å^{-3}	0.88/-0.61	1.01/-0.41

Compound	**2.6**	**2.7**
Empirical formula	$C_{61}H_{116}N_{12}O_4Zr_2$	$C_{34}H_{61}N_7O_2Zr$
Formula weight	1264.09	691.11
Temperature/K	90	100
Crystal system	triclinic	monoclinic
Space group	P-1	$P2_1/c$
a/Å	11.103(2)	19.2374(14)
b/Å	11.619(2)	9.9154(8)
c/Å	13.843(3)	20.1776(14)
α/°	80.868(4)	90
β/°	66.762(4)	109.871(4)
γ/°	82.283(4)	90
Volume/$Å^3$	1615.2(5)	3619.6(5)
Z	1	4
$\rho_{calc}g/cm^3$	1.300	1.268
μ/mm^{-1}	0.376	0.343
F(000)	678.0	1480.0
Crystal size/mm^3	0.14 × 0.07 × 0.04	0.32 × 0.21 × 0.16
Radiation	MoKα (λ = 0.71073)	MoKα (λ = 0.71073)
2Θ range for data collection/°	3.224 to 56.018	4.114 to 60.906
Index ranges	$-14 \le h \le 14$, $-15 \le k \le 15$, $-18 \le l \le 18$	$-27 \le h \le 27$, $-14 \le k \le 10$, $-28 \le l \le 28$
Reflections collected	29659	35882
Independent reflections	7777 [R_{int} = 0.0570, R_{sigma} = 0.0522]	10890 [R_{int} = 0.0392, R_{sigma} = 0.0412]
Data/restraints/parameters	7777/0/384	10890/0/407
Goodness-of-fit on F^2	1.024	1.029
Final R indexes [I>=2σ (I)]	R_1 = 0.0369, wR_2 = 0.0803	R_1 = 0.0331, wR_2 = 0.0779
Final R indexes [all data]	R_1 = 0.0499, wR_2 = 0.0855	R_1 = 0.0424, wR_2 = 0.0823
Largest diff. peak/hole / e $Å^{-3}$	0.97/-0.36	0.51/-0.39

Compound	**2.8**	**2.9**
Empirical formula	$C_{29}H_{58}N_6O_2Zr$	$C_{43.5}H_{63}N_5O_2Zr$
Formula weight	614.03	779.21
Temperature/K	100	100
Crystal system	monoclinic	monoclinic
Space group	$P2_1/c$	$P2_1/n$
a/Å	13.7581(7)	9.6978(5)
b/Å	16.4217(8)	36.393(2)
c/Å	15.2414(8)	12.4350(7)
α/°	90	90
β/°	100.6780(13)	96.7460(18)
γ/°	90	90
Volume/Å^3	3383.9(3)	4358.3(4)
Z	4	4
ρ_{calc}g/cm^3	1.205	1.188
μ/mm^{-1}	0.357	0.291
F(000)	1320.0	1660.0
Crystal size/mm^3	0.32 × 0.11 × 0.10	0.35 × 0.11 × 0.09
Radiation	MoKα (λ = 0.71073)	MoKα (λ = 0.71073)
2Θ range for data collection/°	3.68 to 59.856	3.482 to 48.262
Index ranges	$-18 \leq h \leq 19$, $-12 \leq k \leq 23$, $-21 \leq l \leq 20$	$-11 \leq h \leq 11$, $-41 \leq k \leq 41$, $-12 \leq l \leq 14$
Reflections collected	38083	27103
Independent reflections	9778 [R_{int} = 0.0418, R_{sigma} = 0.0425]	6909 [R_{int} = 0.0540, R_{sigma} = 0.0563]
Data/restraints/parameters	9778/0/353	6909/1/503
Goodness-of-fit on F^2	1.055	1.035
Final R indexes [I>=2σ (I)]	R_1 = 0.0382, wR_2 = 0.0921	R_1 = 0.0420, wR_2 = 0.0955
Final R indexes [all data]	R_1 = 0.0521, wR_2 = 0.0981	R_1 = 0.0645, wR_2 = 0.1036
Largest diff. peak/hole / e Å^{-3}	1.13/-0.36	0.57/-0.48

C.3 Tabulated Crystallographic Parameters for Chapter 3

Table C.2 List of crystallographic parameters for compounds **3.2**, **3.4**, **3.5**, and **3.20**

Compound	**3.2**	**3.4**
Empirical formula	$C_{36}H_{61}N_5O_2SiZr$	$C_{39}H_{63}N_7O_2SiZr$
Formula weight	715.20	781.27
Temperature/K	100	100
Crystal system	orthorhombic	monoclinic
Space group	Pbca	$P2_1/n$
a/Å	13.6685(5)	10.8676(3)
b/Å	16.3427(7)	20.4389(6)
c/Å	35.6325(14)	18.9581(6)
α/°	90	90
β/°	90	90.480(2)
γ/°	90	90
Volume/Å^3	7959.6(5)	4210.9(2)
Z	8	4
ρ_{calc}g/cm^3	1.194	1.232
μ/mm^{-1}	0.341	0.330
F(000)	3056.0	1664.0
Crystal size/mm^3	0.36 × 0.22 × 0.07	0.34 × 0.29 × 0.14
Radiation	MoKα (λ = 0.71073)	MoKα (λ = 0.71073)
2Θ range for data collection/°	3.756 to 48.312	2.93 to 61.196
Index ranges	-15 ≤ h ≤ 11, -18 ≤ k ≤ 18, -40 ≤ l ≤ 40	-15 ≤ h ≤ 14, -28 ≤ k ≤ 29, -26 ≤ l ≤ 27
Reflections collected	39455	50758
Independent reflections	6362 [R_{int} = 0.0766, R_{sigma} = 0.0574]	12929 [R_{int} = 0.0419, R_{sigma} = 0.0399]
Data/restraints/parameters	6362/0/423	12929/0/464
Goodness-of-fit on F^2	1.275	1.022
Final R indexes [I>=2σ (I)]	R_1 = 0.0703, wR_2 = 0.1211	R_1 = 0.0487, wR_2 = 0.1136
Final R indexes [all data]	R_1 = 0.0953, wR_2 = 0.1275	R_1 = 0.0631, wR_2 = 0.1224
Largest diff. peak/hole / e Å^{-3}	0.82/-1.35	1.90/-1.81
Flack parameter	-	-

Compound	**3.5**	**3.20**
Empirical formula	$C_{48}H_{68}N_6O_2SiZr$	$C_{27}H_{22}ClN$
Formula weight	880.39	395.90
Temperature/K	100	90
Crystal system	monoclinic	monoclinic
Space group	$P2_1$	C2/c
a/Å	11.8111(7)	33.6107(19)
b/Å	39.5535(19)	7.1095(4)
c/Å	12.1276(7)	17.5870(10)
α/°	90	90
β/°	93.288(3)	108.2629(17)
γ/°	90	90
Volume/$Å^3$	5656.3(5)	3990.8(4)
Z	4	8
$\rho_{calc}g/cm^3$	1.034	1.318
μ/mm^{-1}	0.252	0.205
F(000)	1872.0	1664.0
Crystal size/mm^3	0.21 × 0.17 × 0.11	0.18 × 0.15 × 0.14
Radiation	MoKα (λ = 0.71073)	MoKα (λ = 0.71073)
2Θ range for data collection/°	3.364 to 47.158	4.744 to 61.144
Index ranges	$-13 \leq h \leq 11$, $-44 \leq k \leq 44$, $-13 \leq l \leq 12$	$-48 \leq h \leq 41$, $-10 \leq k \leq 10$, $-25 \leq l \leq 25$
Reflections collected	54817	27057
Independent reflections	16833 [R_{int} = 0.0494, R_{sigma} = 0.0604]	6097 [R_{int} = 0.0448, R_{sigma} = 0.0415]
Data/restraints/parameters	16833/1759/1059	6097/0/262
Goodness-of-fit on F^2	1.032	1.033
Final R indexes [I>=2σ (I)]	R_1 = 0.0603, wR_2 = 0.1471	R_1 = 0.0441, wR_2 = 0.1131
Final R indexes [all data]	R_1 = 0.0683, wR_2 = 0.1514	R_1 = 0.0554, wR_2 = 0.1205
Largest diff. peak/hole / e $Å^{-3}$	2.22/-1.93	0.64/-0.62
Flack parameter	0.5	-

C.4 Tabulated Crystallographic Parameters for Chapter 4

Table C.3 List of crystallographic parameters for compounds **4.4**, **4.5**, **4.6**, **4.7**, **4.8**, **4.10**, **4.12**, **4.14**, **4.15**, and **4.16**.

Compound	**4.4**	**4.5**
Empirical formula	$C_{14}H_{20}N_4O_2V$	$C_{16}H_{24}N_4O_2V$
Formula weight	327.28	355.33
Temperature/K	100	100
Crystal system	monoclinic	triclinic
Space group	$P2_1/c$	P-1
a/Å	8.7947(4)	8.9184(5)
b/Å	12.8162(5)	9.1750(5)
c/Å	14.5558(6)	11.3271(6)
α/°	90	77.6800(10)
β/°	105.5090(10)	87.3910(10)
γ/°	90	89.4980(10)
Volume/Å^3	1580.91(12)	904.57(9)
Z	4	2
ρ_{calc}g/cm^3	1.375	1.305
μ/mm^{-1}	0.637	0.562
F(000)	684.0	374.0
Crystal size/mm^3	0.15 × 0.11 × 0.07	0.31 × 0.2 × 0.14
Radiation	MoKα (λ = 0.71073)	MoKα (λ = 0.71073)
2Θ range for data collection/°	4.306 to 61.042	3.684 to 61.13
Index ranges	$-12 \leq h \leq 12$, $-18 \leq k \leq 15$, $-13 \leq l \leq 20$	$-12 \leq h \leq 12$, $-13 \leq k \leq 13$, $-16 \leq l \leq 16$
Reflections collected	23754	22197
Independent reflections	4820 [R_{int} = 0.0416, R_{sigma} = 0.0355]	5531 [R_{int} = 0.0303, R_{sigma} = 0.0274]
Data/restraints/parameters	4820/0/194	5531/0/214
Goodness-of-fit on F^2	1.036	1.062
Final R indexes [I>=2σ (I)]	R_1 = 0.0316, wR_2 = 0.0727	R_1 = 0.0321, wR_2 = 0.0801
Final R indexes [all data]	R_1 = 0.0460, wR_2 = 0.0791	R_1 = 0.0392, wR_2 = 0.0840
Largest diff. peak/hole / e Å^{-3}	0.50/-0.31	0.48/-0.38

Compound	**4.6**	**4.7**
Empirical formula	$C_{16}H_{24}N_4O_2V$	$C_{18}H_{18}N_3O_3V$
Formula weight	355.33	375.29
Temperature/K	100	100
Crystal system	monoclinic	monoclinic
Space group	$P2_1/n$	Pn
a/Å	7.6250(9)	12.3071(6)
b/Å	29.317(4)	10.3510(6)
c/Å	8.7682(10)	13.5916(7)
α/°	90	90
β/°	111.566(6)	91.199(3)
γ/°	90	90
Volume/Å^3	1822.9(4)	1731.07(16)
Z	4	4
ρ_{calc}g/cm^3	1.295	1.440
μ/mm^{-1}	0.558	0.595
F(000)	748.0	776.0
Crystal size/mm^3	0.21 × 0.11 × 0.06	0.14 × 0.08 × 0.05
Radiation	MoKα (λ = 0.71073)	MoKα (λ = 0.71073)
2Θ range for data collection/°	2.778 to 51.304	3.934 to 52.69
Index ranges	$-7 \leq h \leq 9$, $-29 \leq k \leq 35$, $-10 \leq l \leq 9$	$-13 \leq h \leq 15$, $0 \leq k \leq 12$, $-16 \leq l \leq 16$
Reflections collected	11780	6177
Independent reflections	3434 [R_{int} = 0.0614, R_{sigma} = 0.0735]	6177 [R_{int} = 0.0505, R_{sigma} = 0.0510]
Data/restraints/parameters	3434/0/214	6177/2/457
Goodness-of-fit on F^2	1.019	1.065
Final R indexes [I>=2σ (I)]	R_1 = 0.0540, wR_2 = 0.1098	R_1 = 0.0396, wR_2 = 0.0862
Final R indexes [all data]	R_1 = 0.0876, wR_2 = 0.1219	R_1 = 0.0507, wR_2 = 0.0912
Largest diff. peak/hole / e Å^{-3}	0.36/-0.30	0.33/-0.35
Flack parameter	-	-0.036(15)

Compound	**4.8**	**4.10**
Empirical formula	$C_{20}H_{25}N_4O_3V$	$C_{25}H_{28}N_5O_3V$
Formula weight	420.38	497.46
Temperature/K	100	120
Crystal system	triclinic	triclinic
Space group	P-1	P-1
a/Å	8.9979(5)	8.1620(10)
b/Å	9.5099(6)	9.0032(11)
c/Å	12.4283(8)	16.663(2)
α/°	83.967(2)	86.475(4)
β/°	80.205(2)	81.945(4)
γ/°	78.645(2)	86.385(4)
Volume/Å^3	1024.64(11)	1208.3(3)
Z	2	2
ρ_{calc}g/cm^3	1.363	1.367
μ/mm^{-1}	0.512	0.447
F(000)	440.0	520.0
Crystal size/mm^3	0.3 × 0.15 × 0.14	0.28 × 0.27 × 0.09
Radiation	MoKα (λ = 0.71073)	MoKα (λ = 0.71073)
2Θ range for data collection/°	3.334 to 59.434	2.472 to 61.112
Index ranges	$-12 \leq h \leq 12$, $-13 \leq k \leq 13$, $-17 \leq l \leq 17$	$-11 \leq h \leq 11$, $-12 \leq k \leq 12$, $-23 \leq l \leq 23$
Reflections collected	10140	30734
Independent reflections	5809 [R_{int} = 0.0247, R_{sigma} = 0.0371]	7395 [R_{int} = 0.0309, R_{sigma} = 0.0284]
Data/restraints/parameters	5809/0/258	7395/0/312
Goodness-of-fit on F^2	1.073	0.947
Final R indexes [I>=2σ (I)]	R_1 = 0.0419, wR_2 = 0.1097	R_1 = 0.0331, wR_2 = 0.1134
Final R indexes [all data]	R_1 = 0.0518, wR_2 = 0.1149	R_1 = 0.0406, wR_2 = 0.1223
Largest diff. peak/hole / e Å^{-3}	0.59/-0.37	0.46/-0.29

Compound	**4.12**	**4.14**
Empirical formula	$C_{42}H_{56}N_4O_2V$	$C_{40}H_{40.57}N_{2.57}O_{2.57}V_{0.86}$
Formula weight	699.84	642.12
Temperature/K	100	90
Crystal system	monoclinic	monoclinic
Space group	$P2_1/c$	C2/c
a/Å	13.2954(10)	27.9809(19)
b/Å	30.480(2)	18.6624(13)
c/Å	10.2846(8)	47.284(3)
α/°	90	90
β/°	108.269(4)	94.0449(10)
γ/°	90	90
Volume/$Å^3$	3957.6(5)	24630(3)
Z	4	28
$\rho_{calc}g/cm^3$	1.175	1.212
μ/mm^{-1}	0.289	0.285
F(000)	1500.0	9488.0
Crystal size/mm^3	0.44 × 0.11 × 0.08	0.18 × 0.14 × 0.13
Radiation	MoKα (λ = 0.71073)	MoKα (λ = 0.71073)
2Θ range for data collection/°	3.492 to 48.368	2.626 to 50.808
Index ranges	$-15 \leq h \leq 15$, $-35 \leq k \leq 35$, $-11 \leq l \leq 11$	$-33 \leq h \leq 33$, $-22 \leq k \leq 22$, $-57 \leq l \leq 57$
Reflections collected	24373	129460
Independent reflections	6264 [R_{int} = 0.0569, R_{sigma} = 0.0634]	22644 [R_{int} = 0.0658, R_{sigma} = 0.0489]
Data/restraints/parameters	6264/0/454	22644/0/1479
Goodness-of-fit on F^2	1.093	1.071
Final R indexes [I>=2σ (I)]	R_1 = 0.0786, wR_2 = 0.1563	R_1 = 0.0530, wR_2 = 0.1451
Final R indexes [all data]	R_1 = 0.1156, wR_2 = 0.1677	R_1 = 0.0781, wR_2 = 0.1593
Largest diff. peak/hole / e $Å^{-3}$	0.32/-0.44	1.49/-0.63

Compound	**4.15**	**4.16**
Empirical formula	$C_{20}H_{29}N_4O_2V$	$C_{24}H_{38}N_5O_2V$
Formula weight	408.41	479.53
Temperature/K	100	90
Crystal system	monoclinic	triclinic
Space group	$P2_1/n$	P-1
a/Å	9.5832(7)	9.1787(4)
b/Å	12.8300(9)	10.7455(5)
c/Å	16.4657(12)	13.7121(6)
α/°	90	67.9103(11)
β/°	102.278(4)	79.1333(11)
γ/°	90	80.9407(12)
Volume/Å^3	1978.2(2)	1225.10(10)
Z	4	2
ρ_{calc}g/cm^3	1.371	1.300
μ/mm^{-1}	0.524	0.435
F(000)	864.0	512.0
Crystal size/mm^3	0.15 × 0.1 × 0.05	0.18 × 0.18 × 0.08
Radiation	MoKα (λ = 0.71073)	MoKα (λ = 0.71073)
2Θ range for data collection/°	4.06 to 47.75	3.238 to 61.074
Index ranges	$-10 \le h \le 10$, $-14 \le k \le 14$, $-18 \le l \le 18$	$-13 \le h \le 13$, $-15 \le k \le 15$, $-19 \le l \le 19$
Reflections collected	15217	29777
Independent reflections	3048 [R_{int} = 0.0973, R_{sigma} = 0.0808]	7494 [R_{int} = 0.0278, R_{sigma} = 0.0279]
Data/restraints/parameters	3048/0/246	7494/0/295
Goodness-of-fit on F^2	0.958	0.969
Final R indexes [I>=2σ (I)]	R_1 = 0.0520, wR_2 = 0.1346	R_1 = 0.0368, wR_2 = 0.1154
Final R indexes [all data]	R_1 = 0.0959, wR_2 = 0.1603	R_1 = 0.0495, wR_2 = 0.1283
Largest diff. peak/hole / e Å^{-3}	0.28/-0.33	0.46/-0.34

C.5 Tabulated Crystallographic Parameters for Chapter 5

Table C.4 List of crystallographic parameters for compounds **5.1** and **5.2**.

Compound	**5.1**	**5.2**
Empirical formula	$C_{31}H_{30}N_3O_4V$	$C_{24}H_{24}N_4O_6V_2$
Formula weight	559.52	566.35
Temperature/K	90	90
Crystal system	triclinic	monoclinic
Space group	P-1	Pn
a/Å	9.0669(16)	7.9562(6)
b/Å	10.4121(19)	9.7274(7)
c/Å	14.970(3)	16.0900(11)
α/°	96.110(5)	90
β/°	98.347(4)	95.631(2)
γ/°	101.792(5)	90
Volume/Å^3	1355.2(4)	1239.25(15)
Z	2	2
ρ_{calc}g/cm^3	1.371	1.518
μ/mm^{-1}	0.408	0.801
F(000)	584.0	580.0
Crystal size/mm^3	0.17 × 0.1 × 0.04	0.25 × 0.24 × 0.14
Radiation	MoKα (λ = 0.71073)	MoKα (λ = 0.71073)
2Θ range for data collection/°	2.778 to 61.346	4.188 to 61.154
Index ranges	$-12 \leq h \leq 12$, $-14 \leq k \leq 14$, $-21 \leq l \leq 21$	$-11 \leq h \leq 11$, $-13 \leq k \leq 13$, $-23 \leq l \leq 23$
Reflections collected	48010	37824
Independent reflections	8308 [R_{int} = 0.0642, R_{sigma} = 0.0430]	7323 [R_{int} = 0.0281, R_{sigma} = 0.0256]
Data/restraints/parameters	8308/0/355	7323/2/330
Goodness-of-fit on F^2	1.076	1.049
Final R indexes [I>=2σ (I)]	R_1 = 0.0520, wR_2 = 0.1385	R_1 = 0.0235, wR_2 = 0.0576
Final R indexes [all data]	R_1 = 0.0660, wR_2 = 0.1485	R_1 = 0.0252, wR_2 = 0.0584
Largest diff. peak/hole / e Å^{-3}	1.41/-0.93	0.38/-0.20
Flack parameter	-	0.147(13)

C.6 Tabulated Crystallographic Parameters for Chapter 6

Table C.5 List of crystallographic parameters for compounds **6.1**, **6.3**, and **6.6**.

Compound	**6.1**	**6.3**
Empirical formula	$C_{24}H_{24}N_4O_7V_2$	$C_{24}H_{24}I_{1.5}N_4O_4V_{1.5}$
Formula weight	582.35	699.23
Temperature/K	90	90
Crystal system	monoclinic	monoclinic
Space group	C2/c	C2/c
a/Å	13.4151(9)	22.2392(14)
b/Å	8.8641(6)	8.6813(5)
c/Å	21.4000(15)	28.841(2)
α/°	90	90
β/°	98.195(2)	111.919(2)
γ/°	90	90
Volume/Å^3	2518.7(3)	5165.6(6)
Z	4	8
ρ_{calc}g/cm^3	1.536	1.798
μ/mm^{-1}	0.794	2.384
F(000)	1192.0	2736.0
Crystal size/mm^3	0.2 × 0.11 × 0.08	0.25 × 0.06 × 0.04
Radiation	MoKα (λ = 0.71073)	MoKα (λ = 0.71073)
2Θ range for data collection/°	3.846 to 53.496	3.044 to 45.484
Index ranges	-13 ≤ h ≤ 16, -11 ≤ k ≤ 11, -26 ≤ l ≤ 26	-24 ≤ h ≤ 19, -9 ≤ k ≤ 9, -30 ≤ l ≤ 31
Reflections collected	15370	13195
Independent reflections	2570 [R_{int} = 0.0395, R_{sigma} = 0.0323]	3439 [R_{int} = 0.0495, R_{sigma} = 0.0528]
Data/restraints/parameters	2570/0/206	3439/0/322
Goodness-of-fit on F^2	1.150	1.076
Final R indexes [I>=2σ (I)]	R_1 = 0.0472, wR_2 = 0.0967	R_1 = 0.0413, wR_2 = 0.0761
Final R indexes [all data]	R_1 = 0.0719, wR_2 = 0.1164	R_1 = 0.0653, wR_2 = 0.0824
Largest diff. peak/hole / e Å^{-3}	0.76/-0.87	0.68/-0.63
Flack parameter	-	-

Compound	**6.6**	-
Empirical formula	$C_{33}H_{27}N_6V$	-
Formula weight	558.54	-
Temperature/K	100	-
Crystal system	triclinic	-
Space group	P-1	-
a/Å	11.7861(10)	-
b/Å	14.1065(12)	-
c/Å	16.5718(14)	-
α/°	90.417(3)	-
β/°	90.580(3)	-
γ/°	96.025(3)	-
Volume/Å^3	2739.8(4)	-
Z	4	-
ρ_{calc}g/cm^3	1.354	-
μ/mm^{-1}	0.396	-
F(000)	1160.0	-
Crystal size/mm^3	0.27 × 0.18 × 0.13	-
Radiation	MoKα (λ = 0.71073)	-
2Θ range for data collection/°	2.458 to 52.21	-
Index ranges	$-14 \leq h \leq 14$, $-17 \leq k \leq 17$, $-20 \leq l \leq 16$	-
Reflections collected	44526	-
Independent reflections	10843 [R_{int} = 0.0617, R_{sigma} = 0.0581]	-
Data/restraints/parameters	10843/0/721	-
Goodness-of-fit on F^2	0.971	-
Final R indexes [I>=2σ (I)]	R_1 = 0.0472, wR_2 = 0.1310	-
Final R indexes [all data]	R_1 = 0.0741, wR_2 = 0.1505	-
Largest diff. peak/hole / e Å^{-3}	0.69/-0.55	-
Flack parameter	-	-

Appendix D Selected NMR Spectra

D.1 Inclusion Criteria for NMR Spectra

The following sections include various NMR spectra for the compounds described in each respective chapter. However, the lists of spectra below are not exhaustive. The spectra presented below are included to provide a reference for the purity of a compound or for some other purpose that is beneficial to the reader. For any spectra that are not present in this thesis, please refer to the corresponding publication for each chapter.

D.2 Selected NMR Spectra for Chapter 2

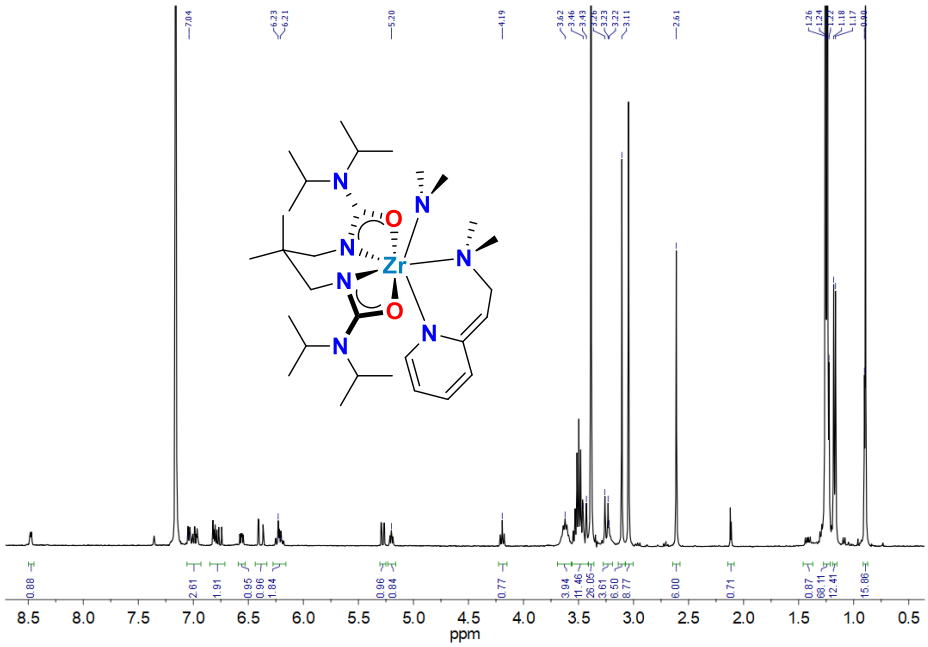

Figure D.1 ^{1}H NMR spectrum of **2.4** (C_6D_6, 400 MHz, 298 K)

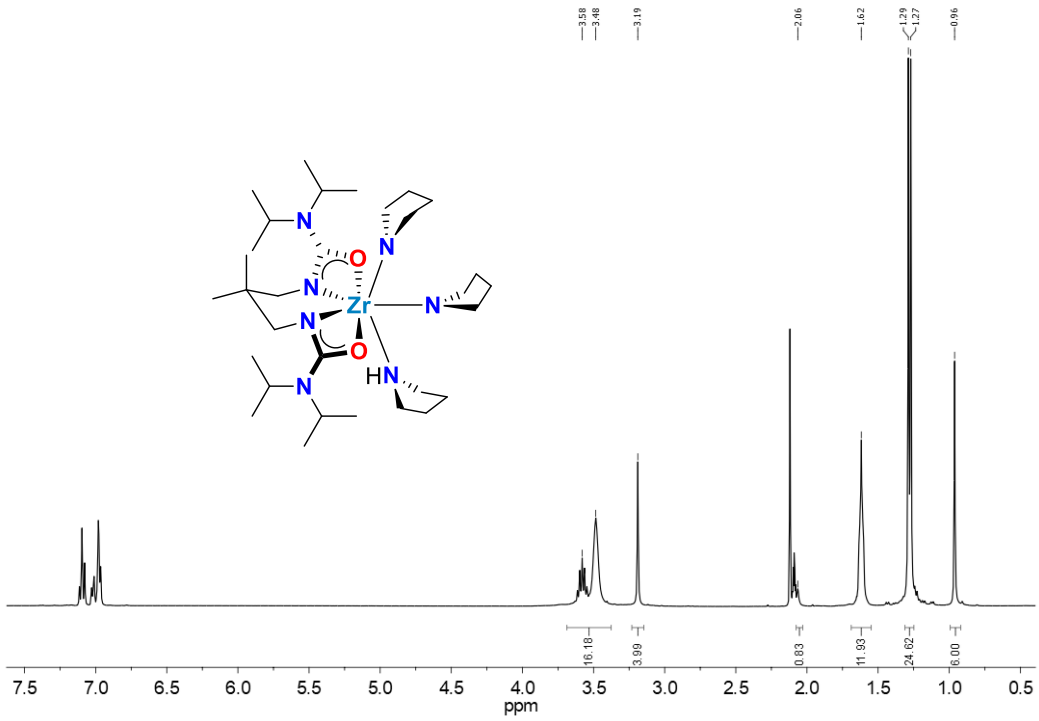

Figure D.2 ^{1}H NMR spectrum of **2.5** (toluene-d_8, 400 MHz, 298 K)

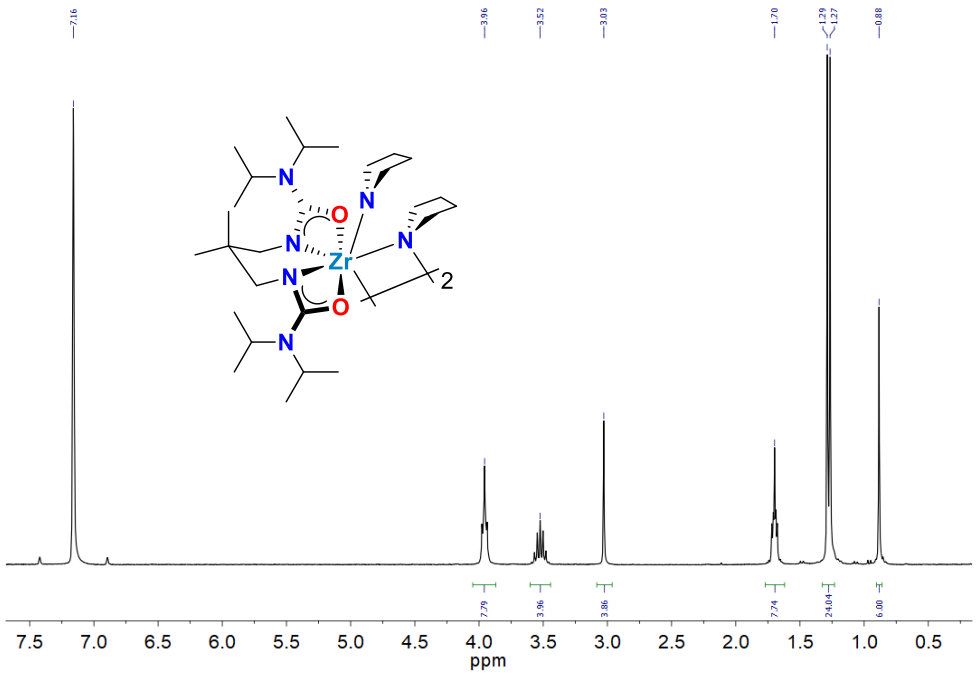

Figure D.3 ^{1}H NMR spectrum of **2.6** (C_6D_6, 300 MHz, 298 K)

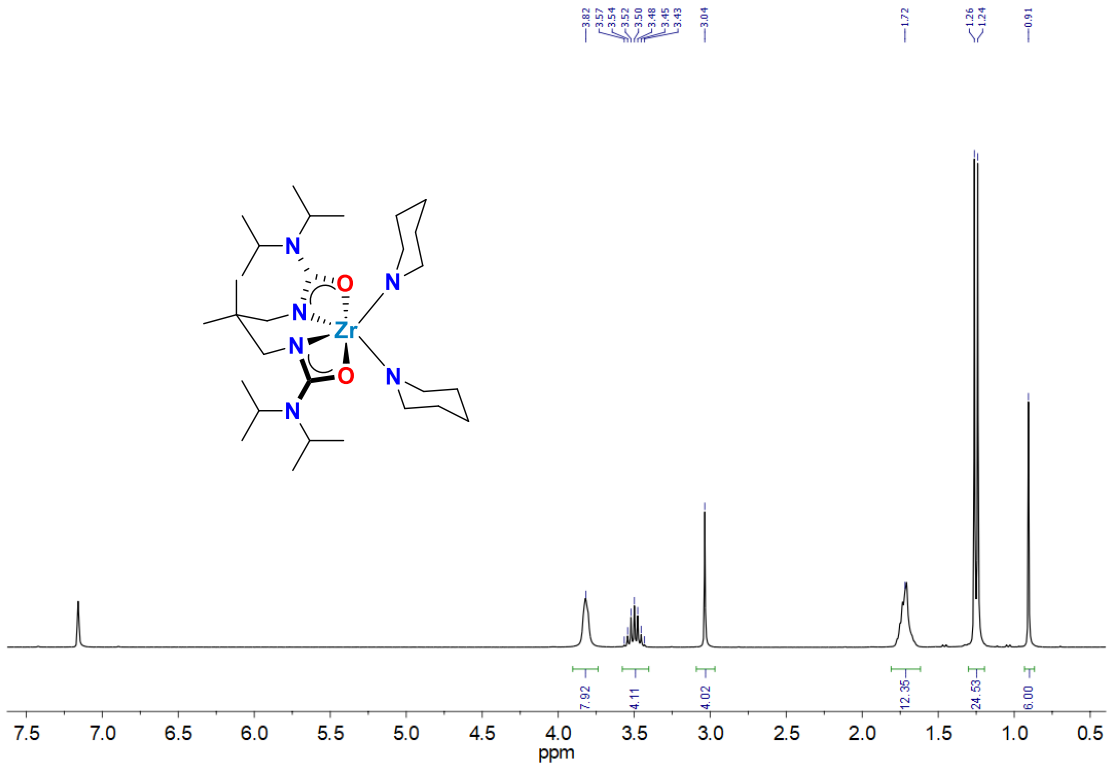

Figure D.4 ^{1}H NMR spectrum of **2.8** (C_6D_6, 300 MHz, 298 K)

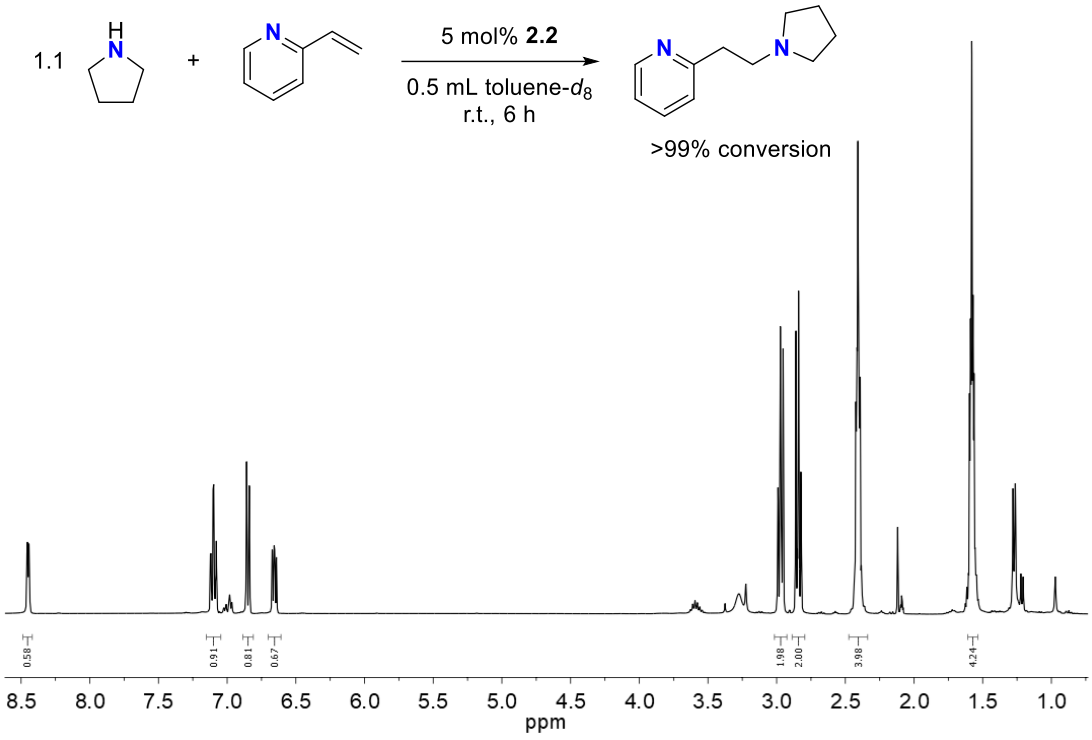

Figure D.5 ^{1}H NMR spectrum of hydroamination catalysis (toluene-d_8, 400 MHz, 298 K)[164]

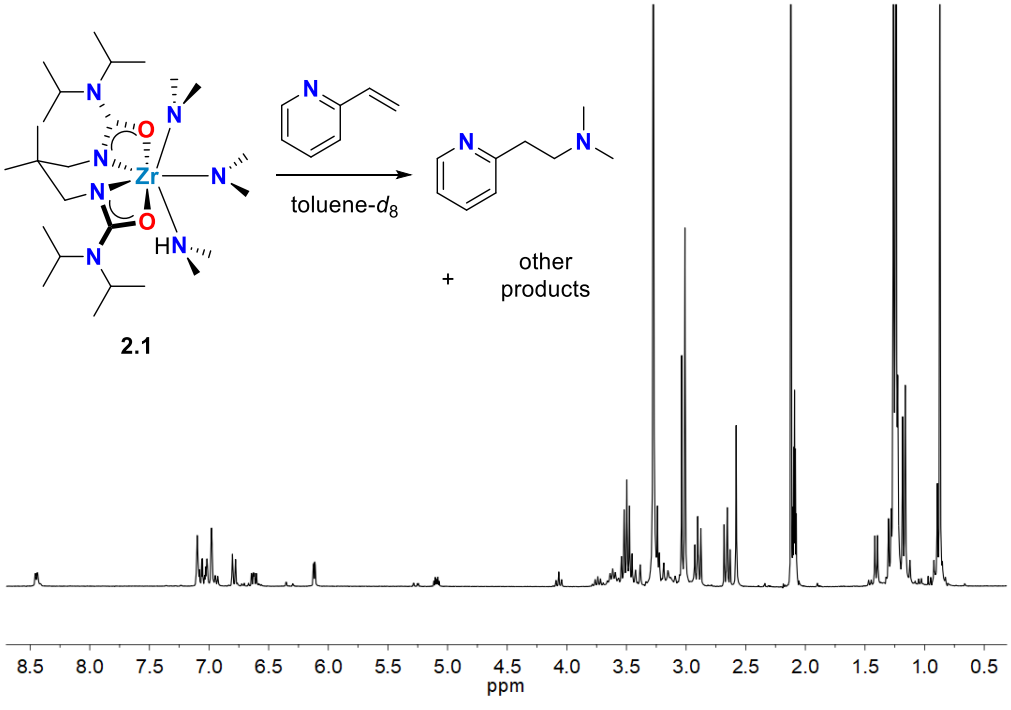

Figure D.6 ^{1}H NMR spectrum of **2.1** and 2-vinylpyridine (toluene-d_8, 400 MHz, 298 K)[368]

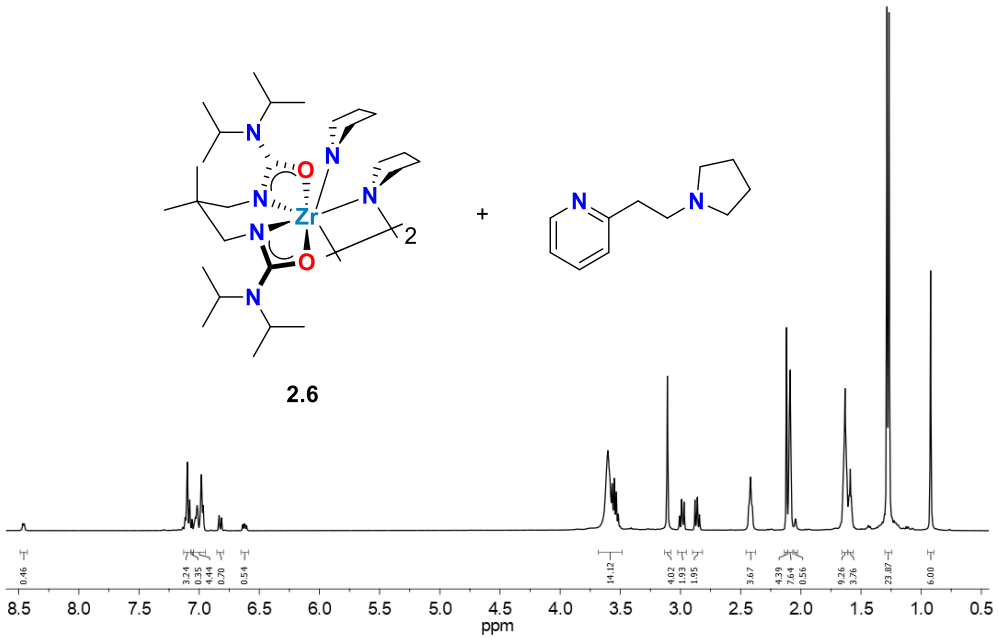

Figure D.7 ^{1}H NMR spectrum of **2.6** and hydroamination product (toluene-d_8, 400 MHz, 298 K)

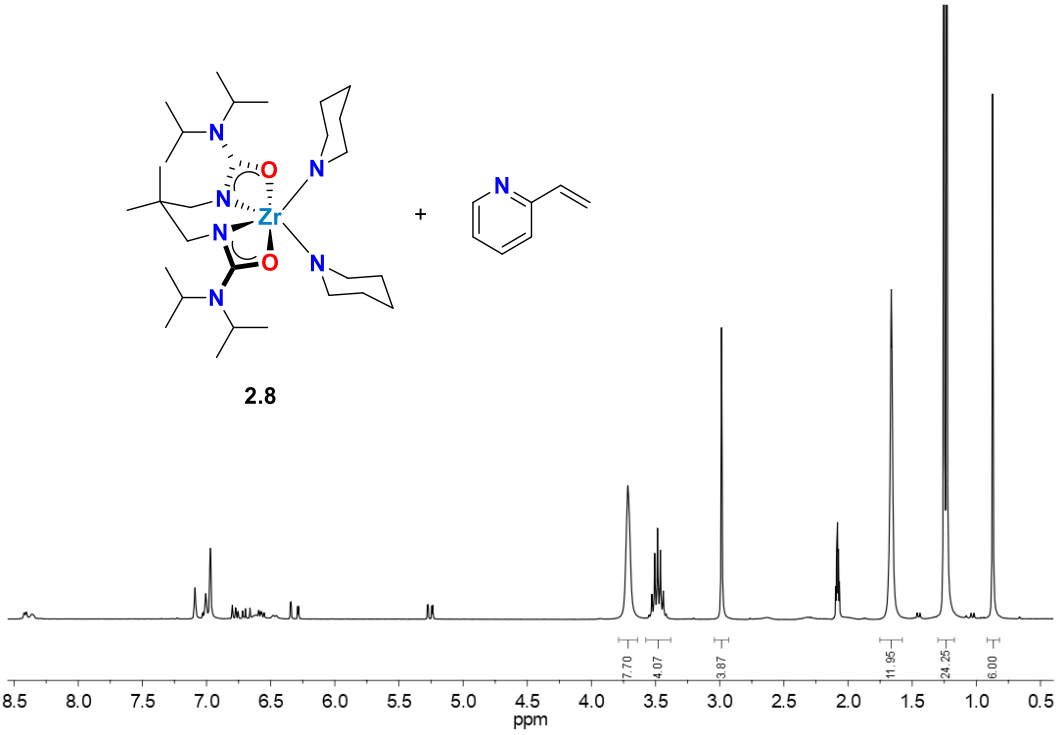

Figure D.8 ^{1}H NMR spectrum of **2.8** and 2-vinylpyridine (toluene-d_8, 300 MHz, 298 K)

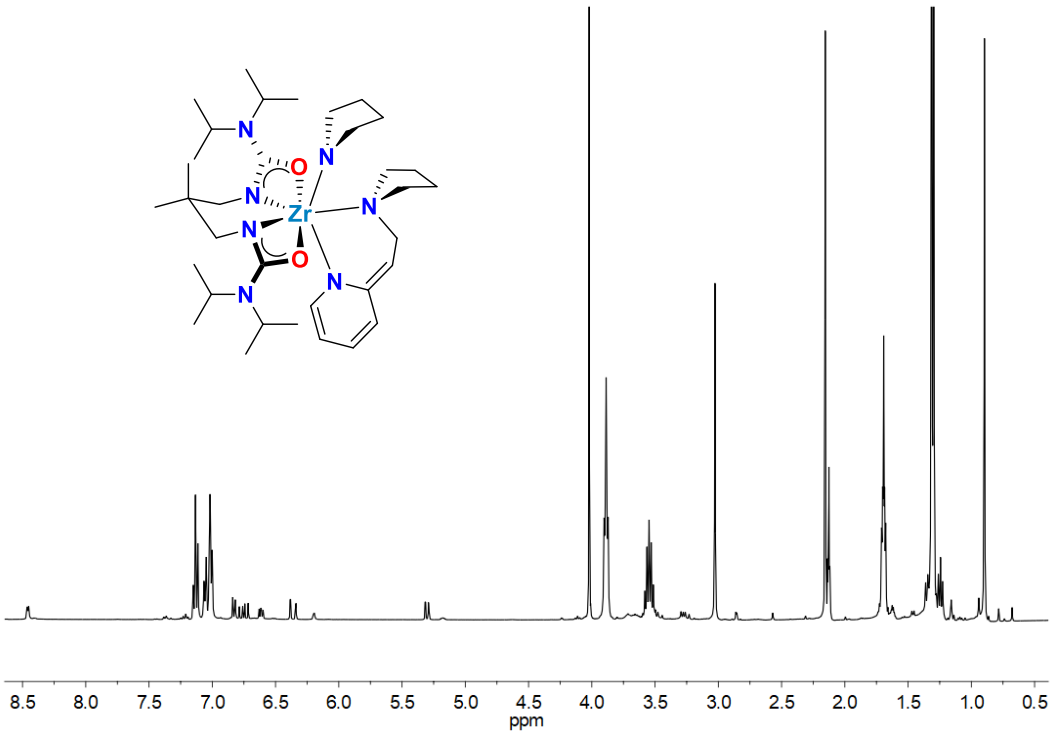

Figure D.9 ^{1}H NMR spectrum of **2.7** and ferrocene (toluene-d_8, 400 MHz, 298 K)

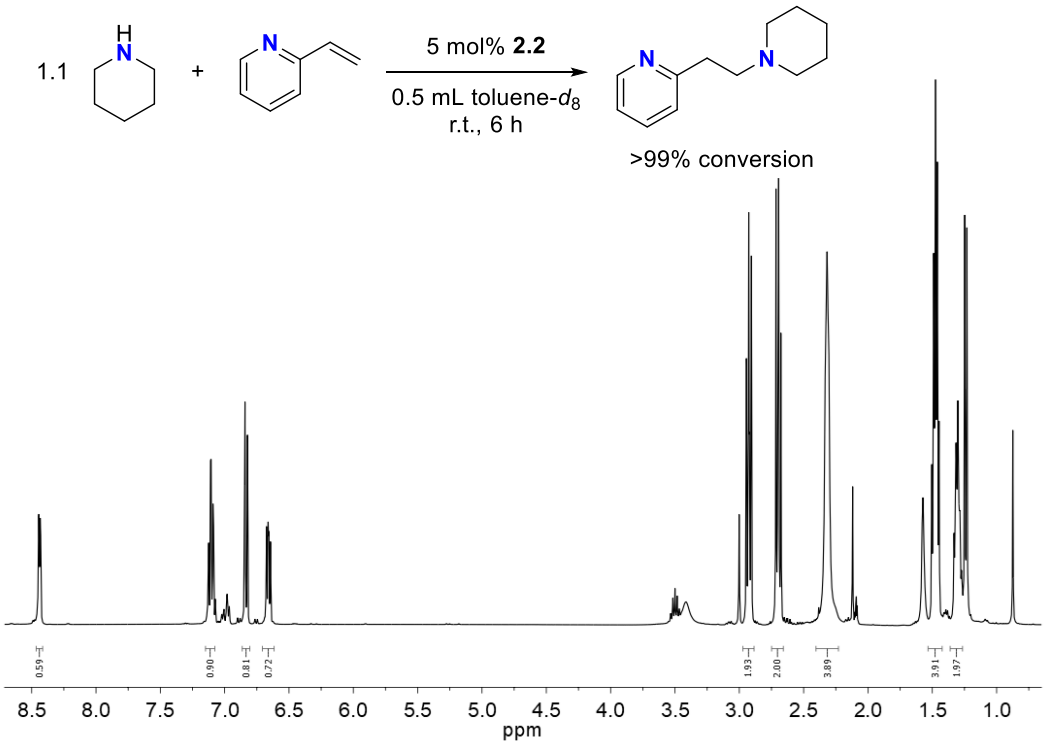

Figure D.10 ^{1}H NMR spectrum of hydroamination catalysis (toluene-d_8, 400 MHz, 298 K)[183]

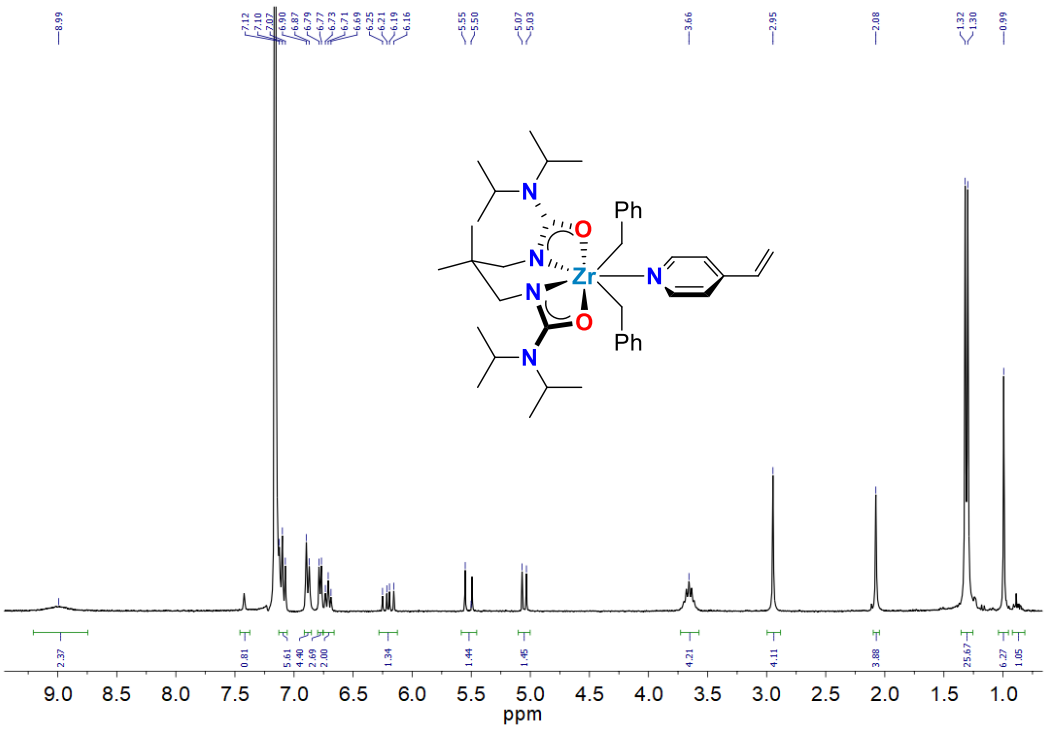

Figure D.11 ^{1}H NMR spectrum of **2.9** (C_6D_6, 300 MHz, 298 K)

D.3 Selected NMR Spectra for Chapter 3

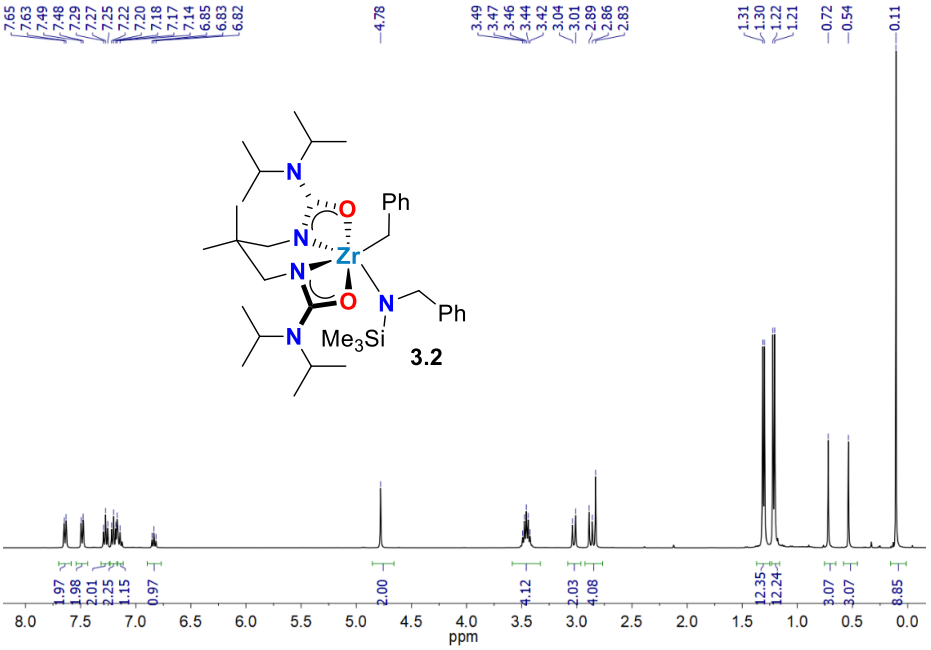

Figure D.12 ^{1}H NMR spectrum of **3.2** (C_6D_6, 400 MHz, 298 K)

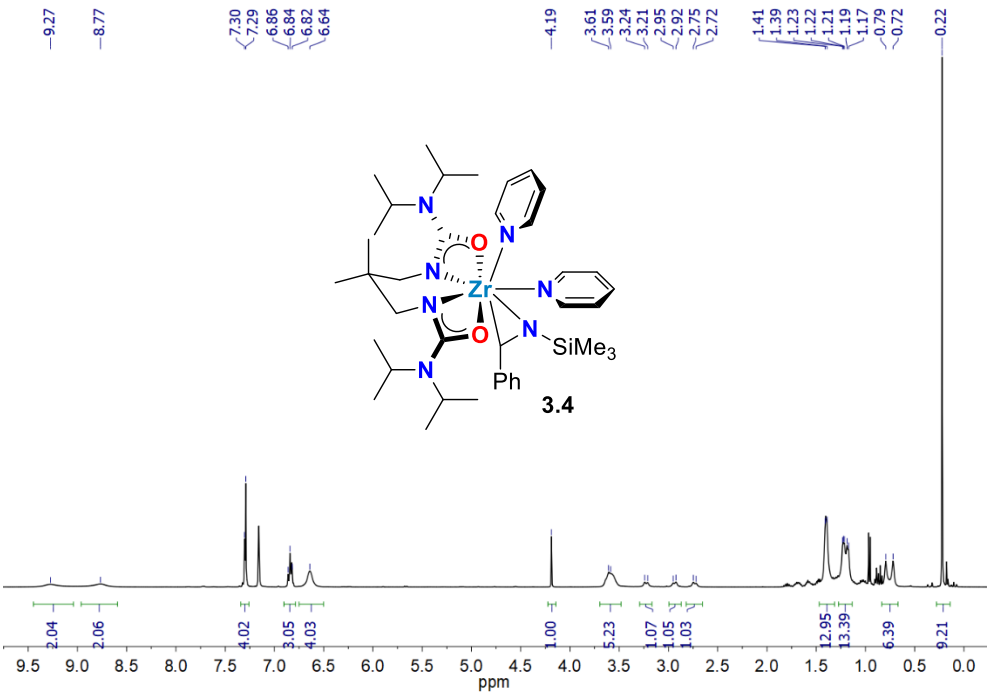

Figure D.13 ^{1}H NMR spectrum of **3.4** (C_6D_6, 400 MHz, 298 K)

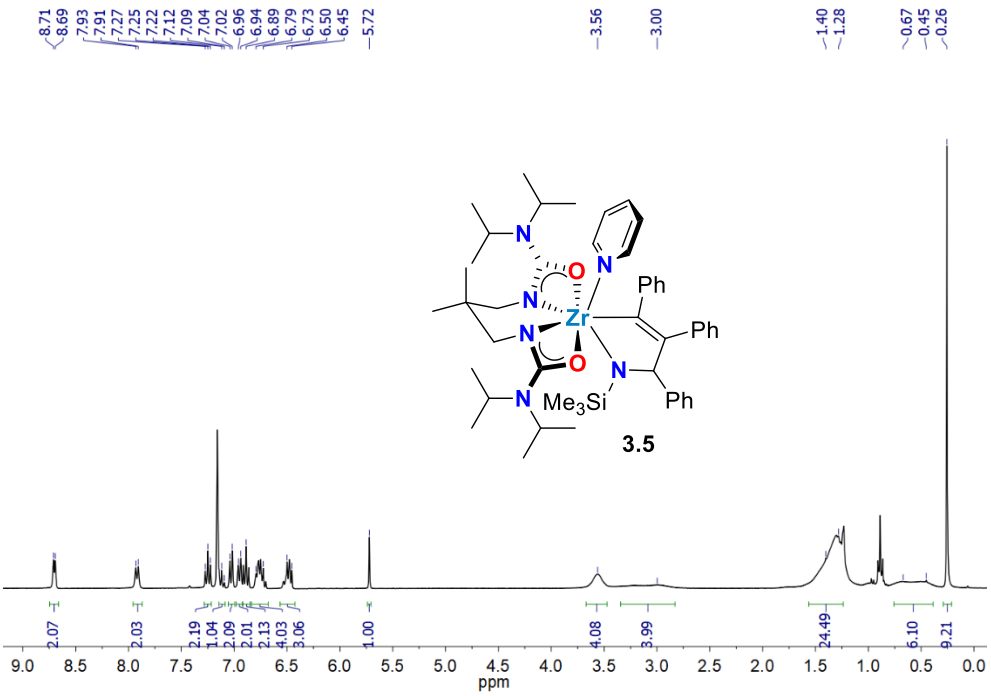

Figure D.14 ^{1}H NMR spectrum of **3.5** (C_6D_6, 300 MHz, 298 K)

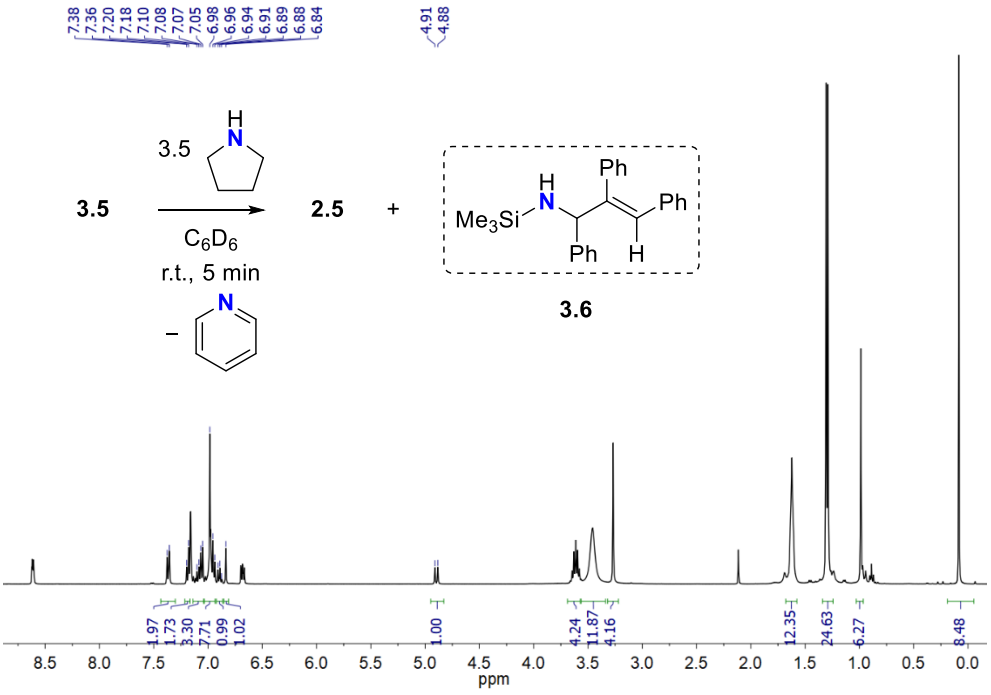

Figure D.15 ^{1}H NMR spectrum of **3.6** *in situ* (C_6D_6, 400 MHz, 298 K)

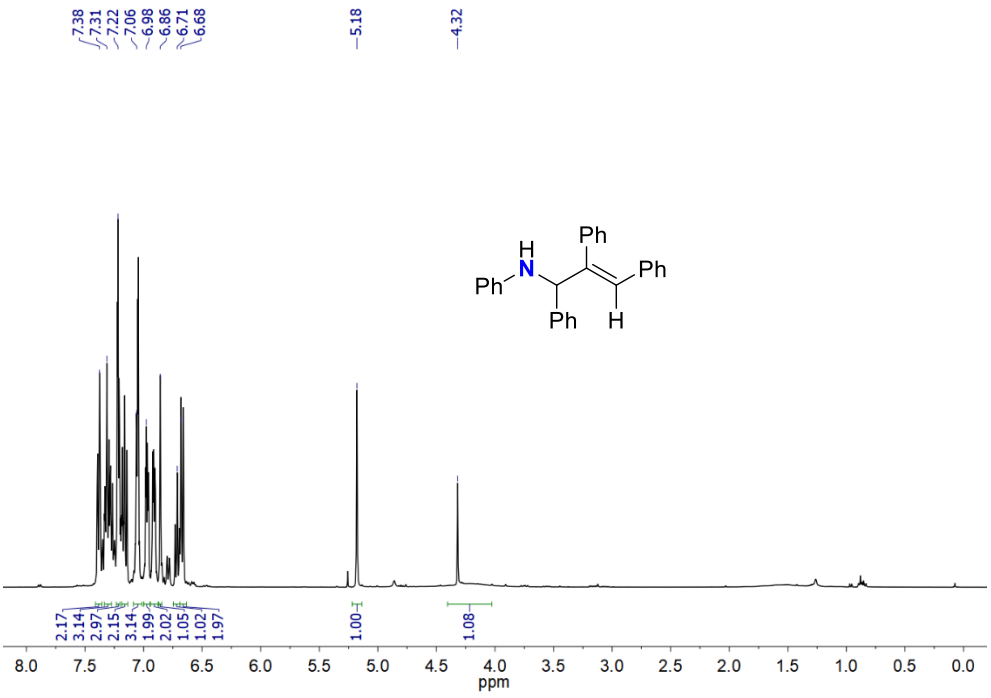

Figure D.16 ^{1}H NMR spectrum of **3.1** ($CDCl_3$, 400 MHz, 298 K)

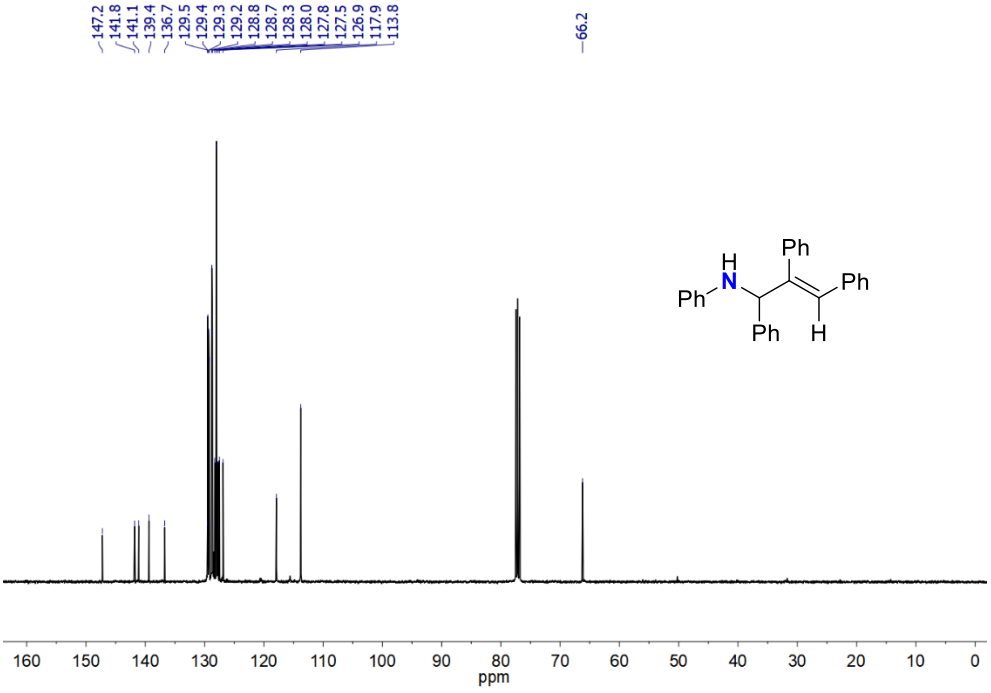

Figure D.17 $^{13}C\{^{1}H\}$ NMR spectrum of **3.1** ($CDCl_3$, 100 MHz, 298 K)

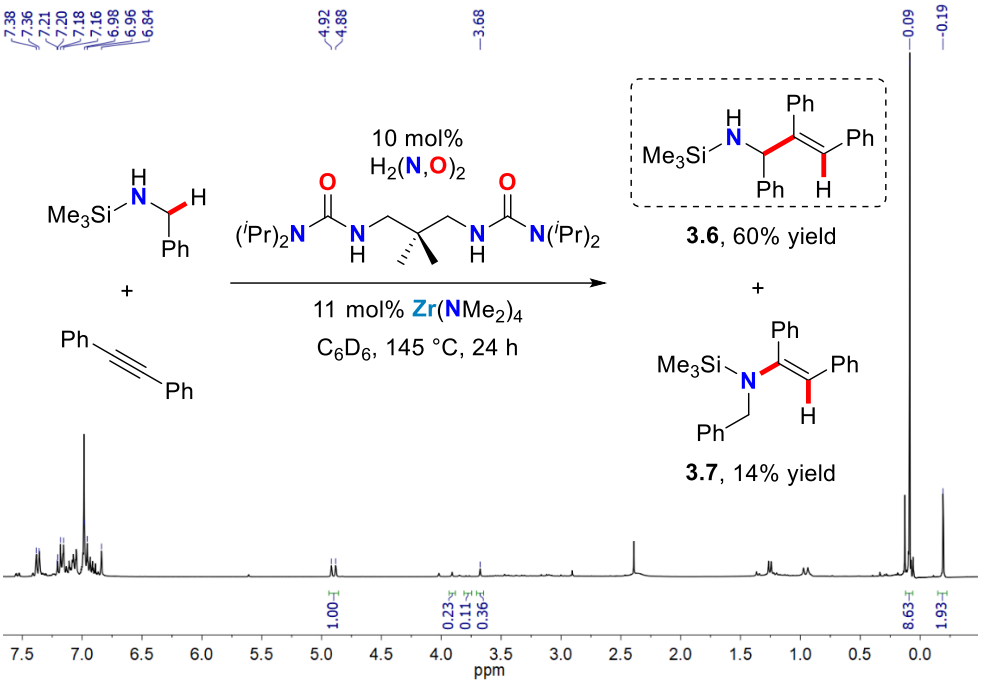

Figure D.18 ^{1}H NMR of the catalytic reaction with *N*-(trimethylsilyl)benzylamine (C_6D_6, 300 MHz, 298 K)

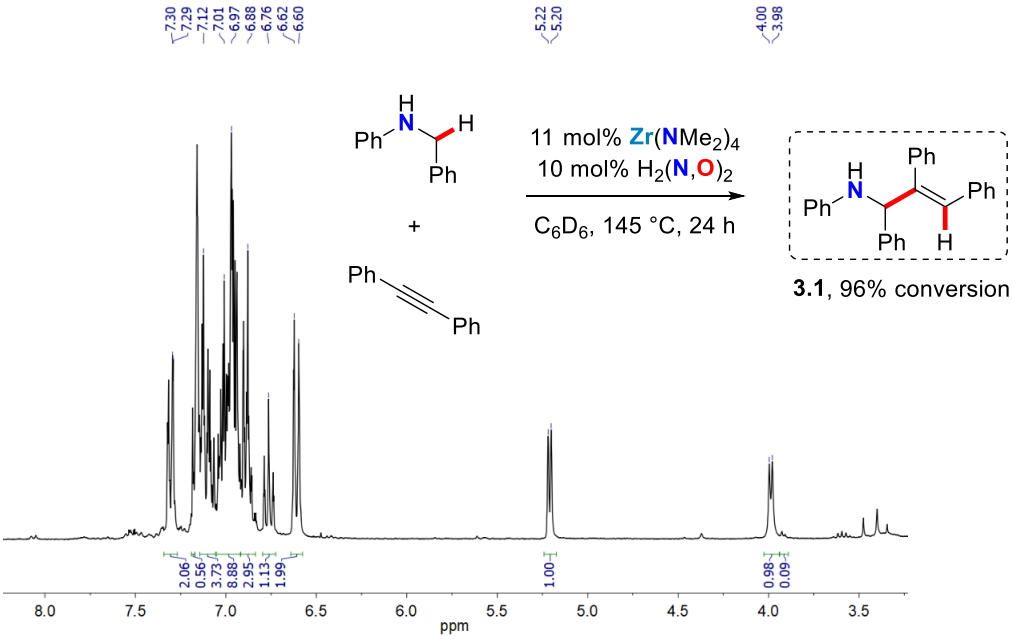

Figure D.19 ^{1}H NMR of the initial catalytic reaction with *N*-benzylaniline (C_6D_6, 300 MHz, 298 K)

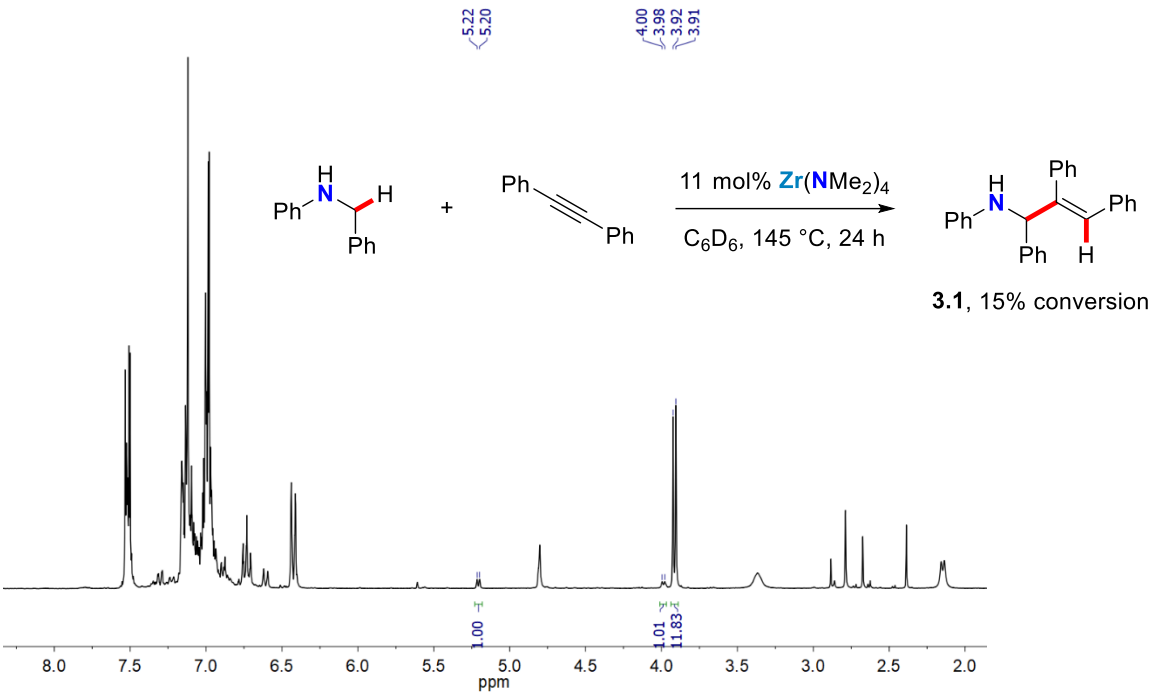

Figure D.20 ^{1}H NMR of the catalytic reaction in the absence of ligand (C_6D_6, 300 MHz, 298 K)

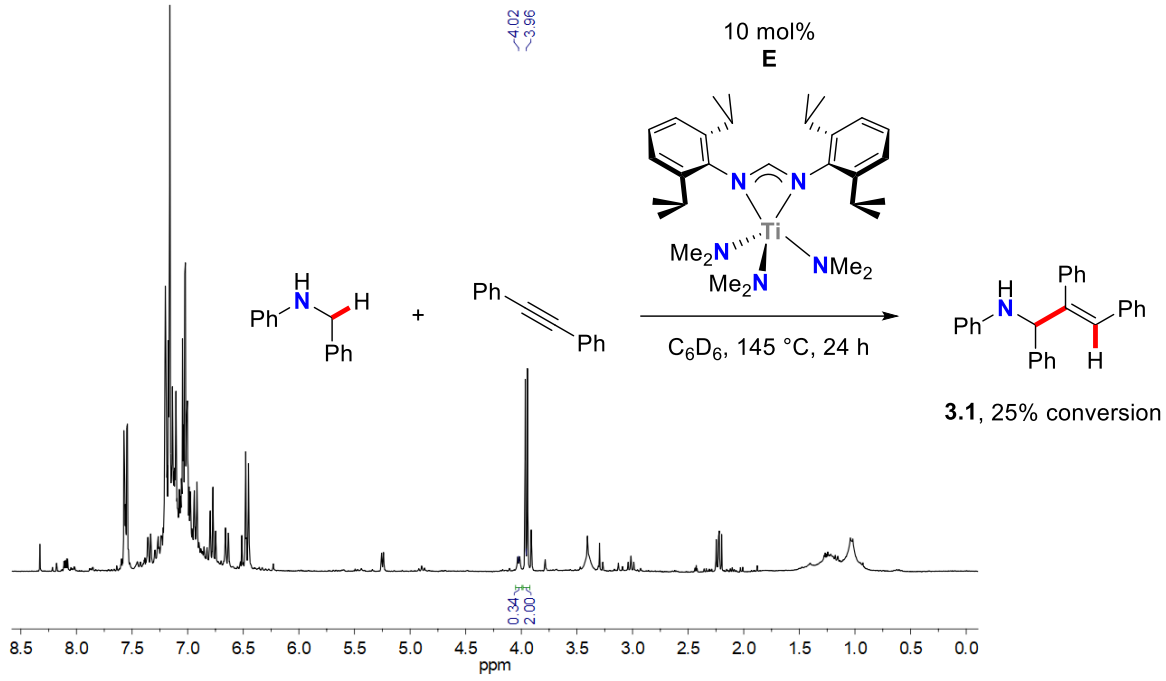

Figure D.21 ^{1}H NMR of the catalytic reaction using the Ti catalyst (C_6D_6, 300 MHz, 298 K)

D.4 Selected NMR Spectra for Chapter 4

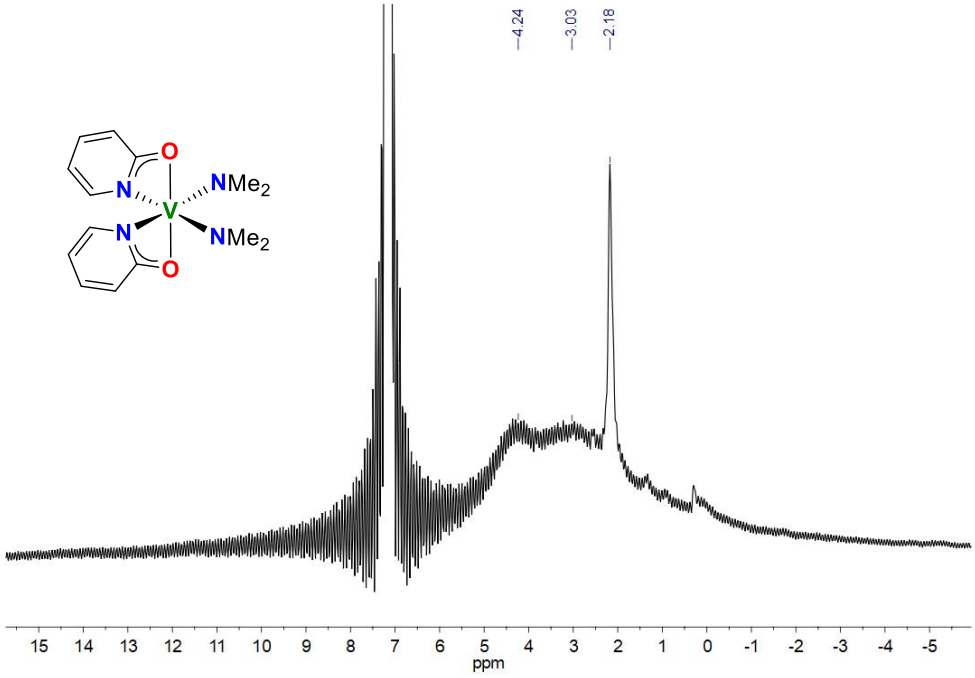

Figure D.22 ^{1}H NMR spectrum of **4.4** (C_6D_6, 300 MHz, 298 K)

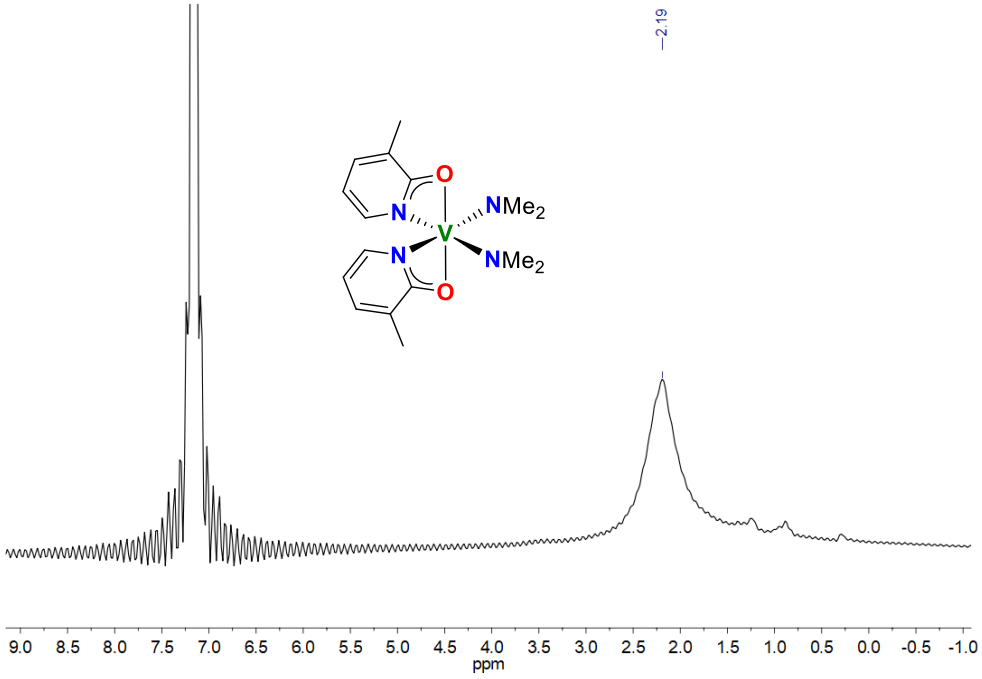

Figure D.23 ^{1}H NMR spectrum of **4.5** (C_6D_6, 300 MHz, 298 K)

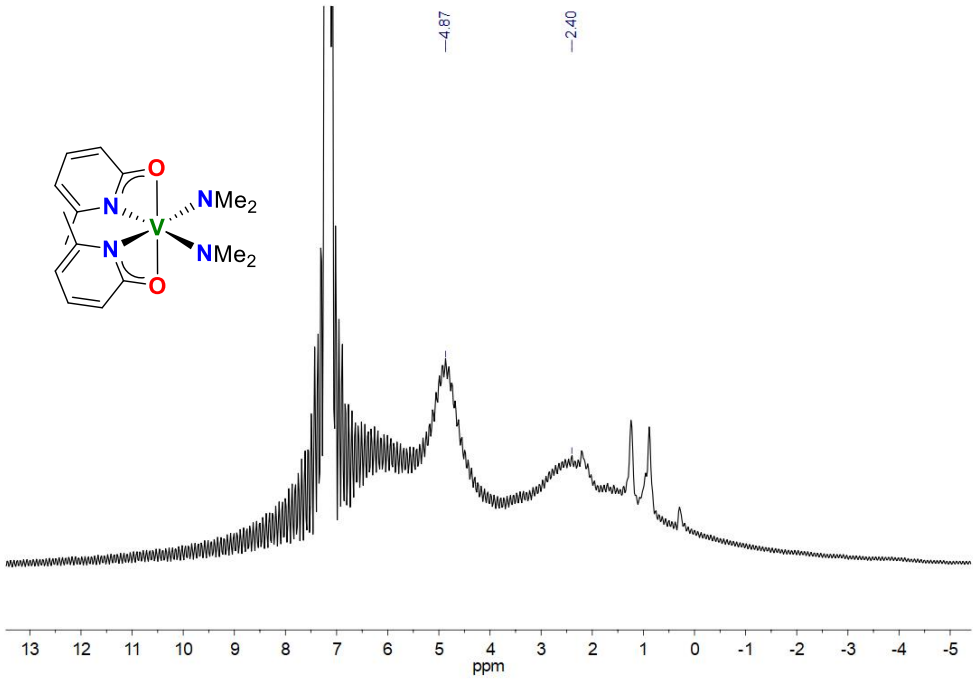

Figure D.24 ^{1}H NMR spectrum of **4.6** (C_6D_6, 300 MHz, 298 K)

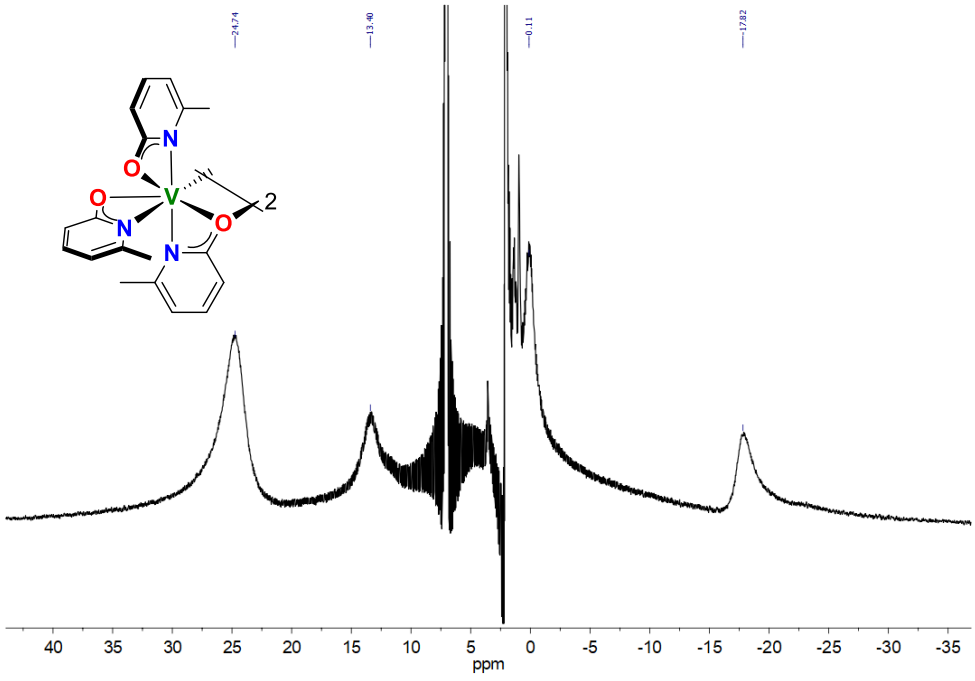

Figure D.25 ^{1}H NMR spectrum of **4.7** (C_7D_8, 300 MHz, 298 K)

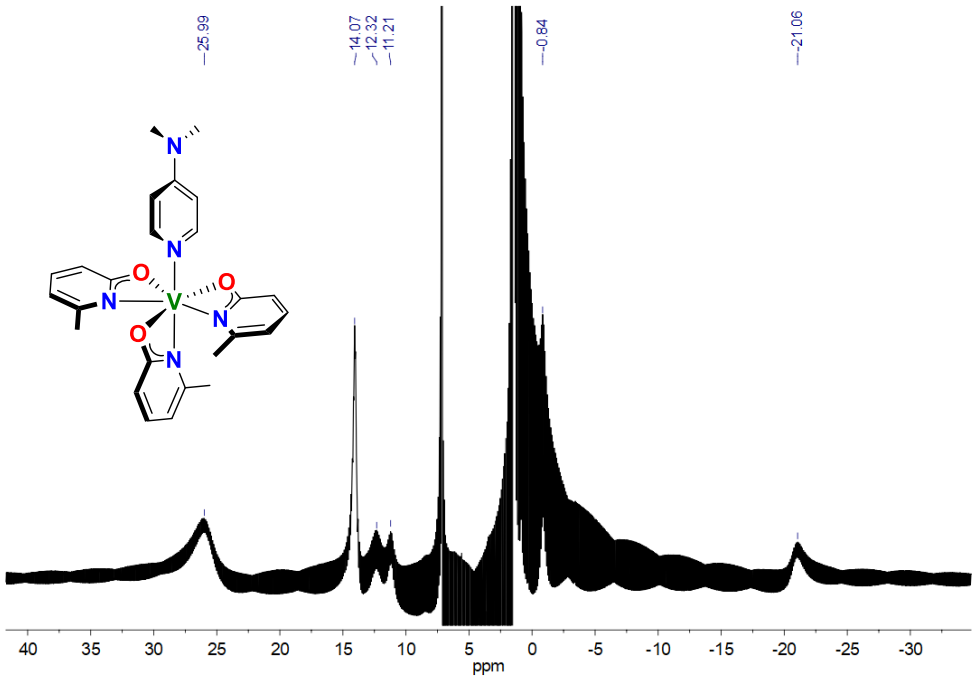

Figure D.26 ^{1}H NMR spectrum of **4.10** and cyclooctane (C_6D_6, 400 MHz, 298 K)

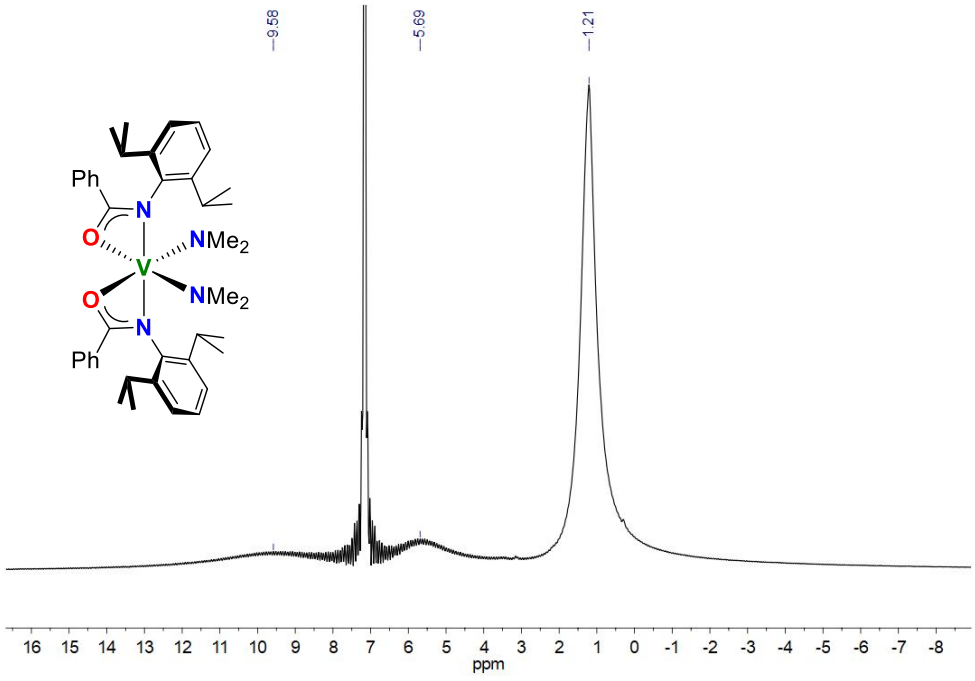

Figure D.27 ^{1}H NMR spectrum of **4.12** (C_6D_6, 300 MHz, 298 K)

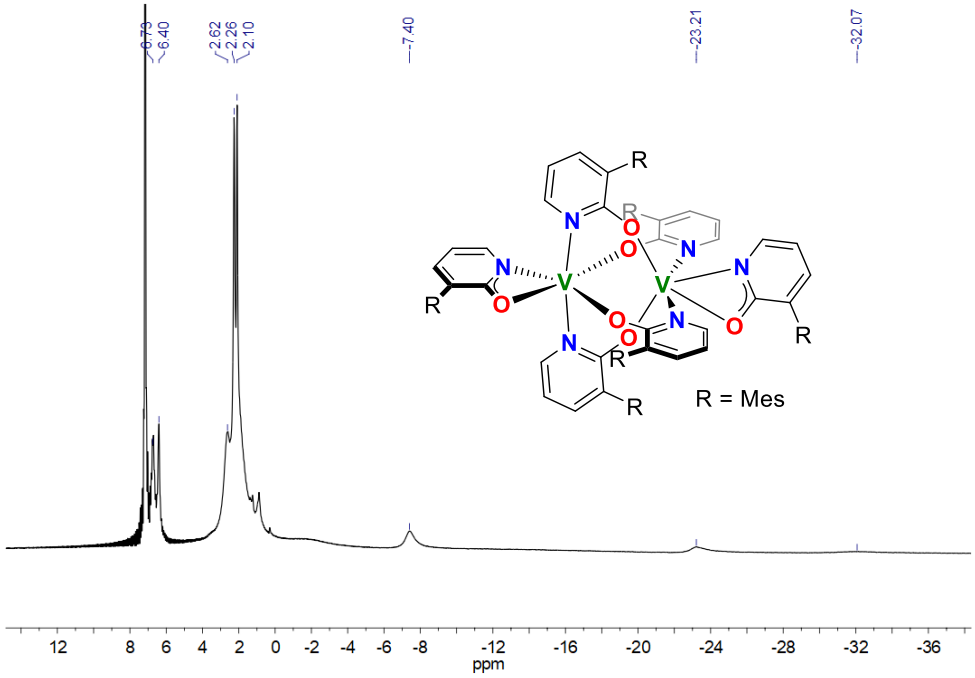

Figure D.28 ^{1}H NMR spectrum of **4.14** (C_6D_6, 300 MHz, 298 K)

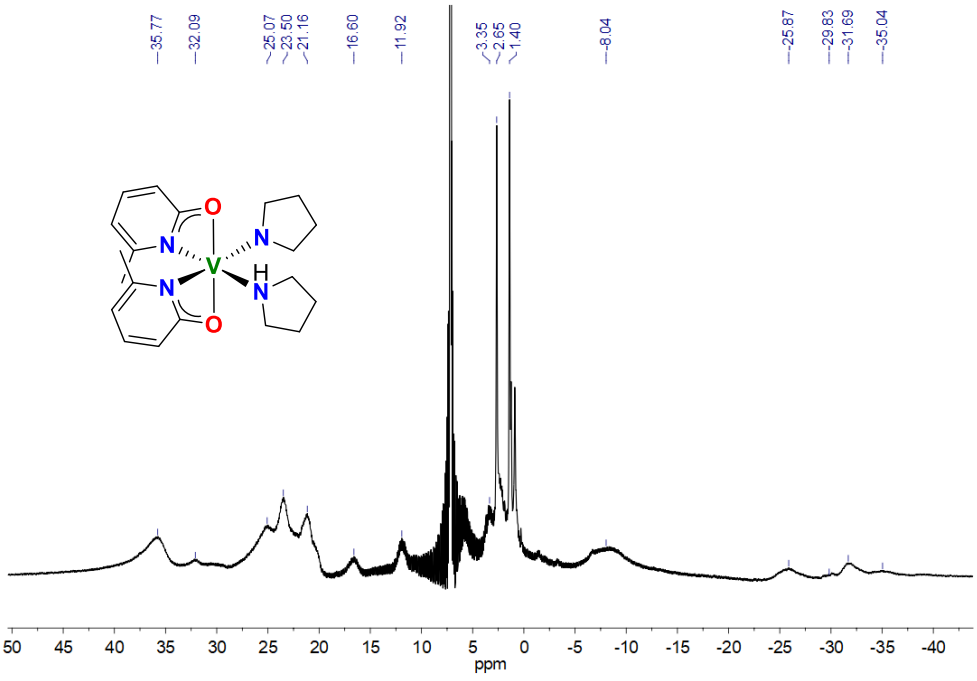

Figure D.29 ^{1}H NMR spectrum of **4.15** (C_6D_6, 300 MHz, 298 K)

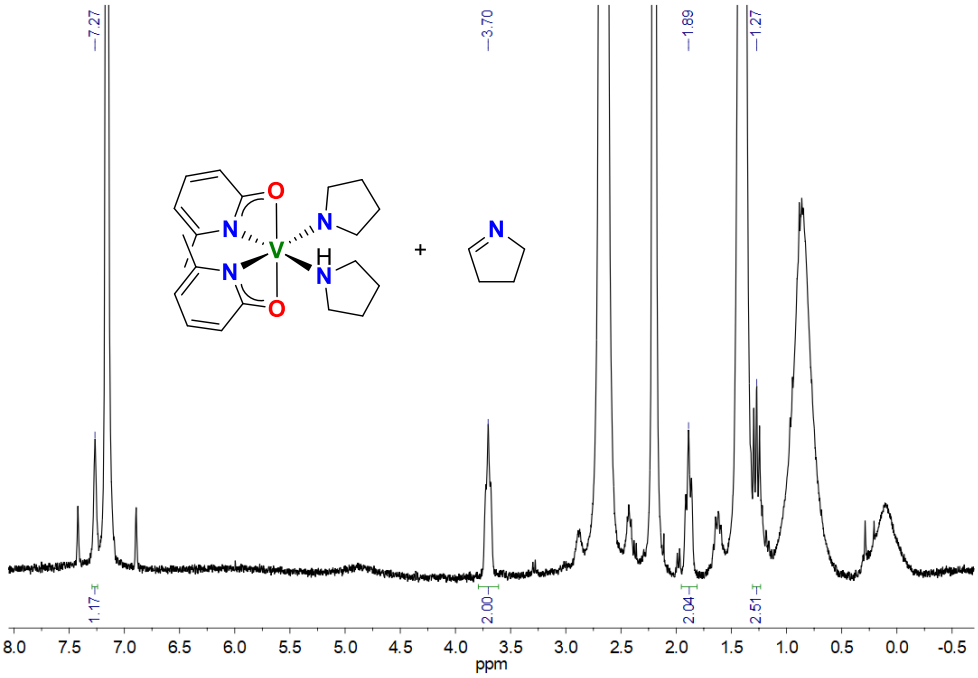

Figure D.30 ^{1}H NMR spectrum of **4.15** and pyrroline *in situ* (C_6D_6, 300 MHz, 298 K)[291]

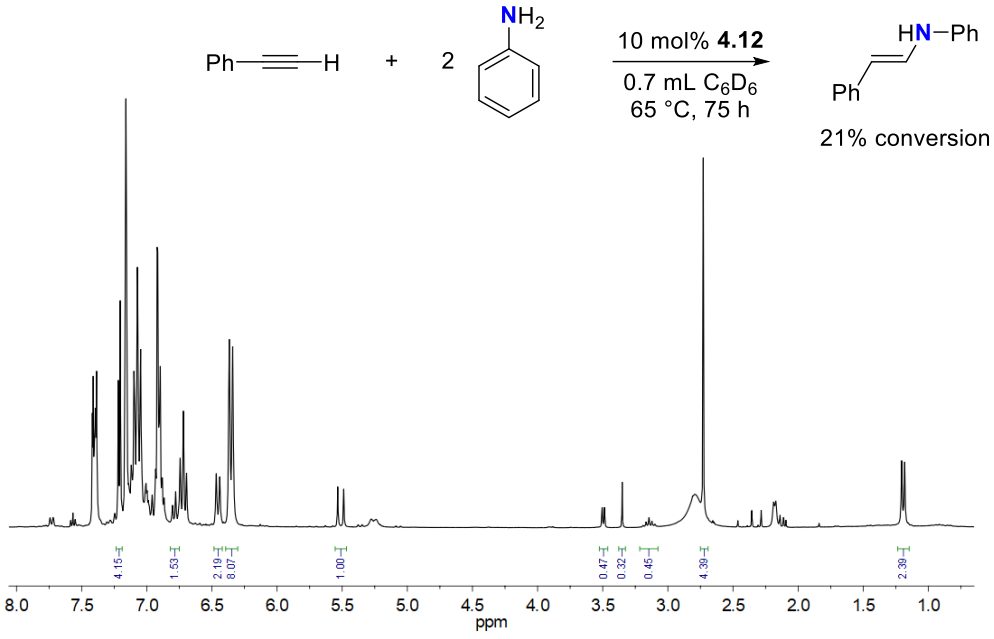

Figure D.31 ^{1}H NMR spectrum of **4.12**-catalyzed hydroamination of phenylacetylene with aniline (C_6D_6, 300 MHz, 298 K)[105]

D.5 Selected NMR Spectra for Chapter 5

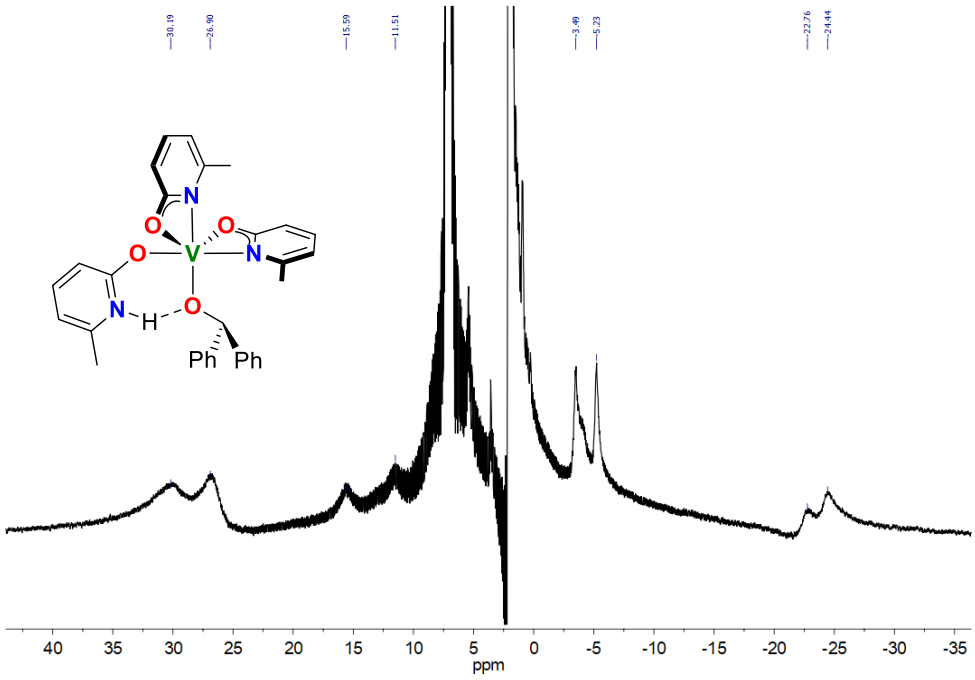

Figure D.32 ^{1}H NMR spectrum of **5.1** (C_7D_8, 300 MHz, 298 K)

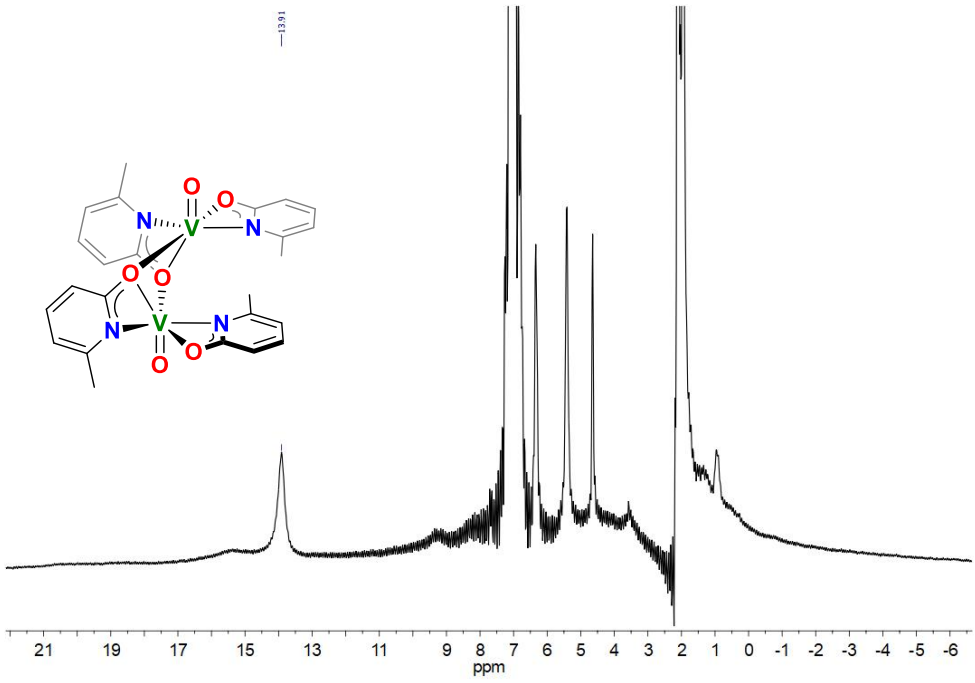

Figure D.33 ^{1}H NMR spectrum of **5.2** (C_7D_8, 300 MHz, 298 K)

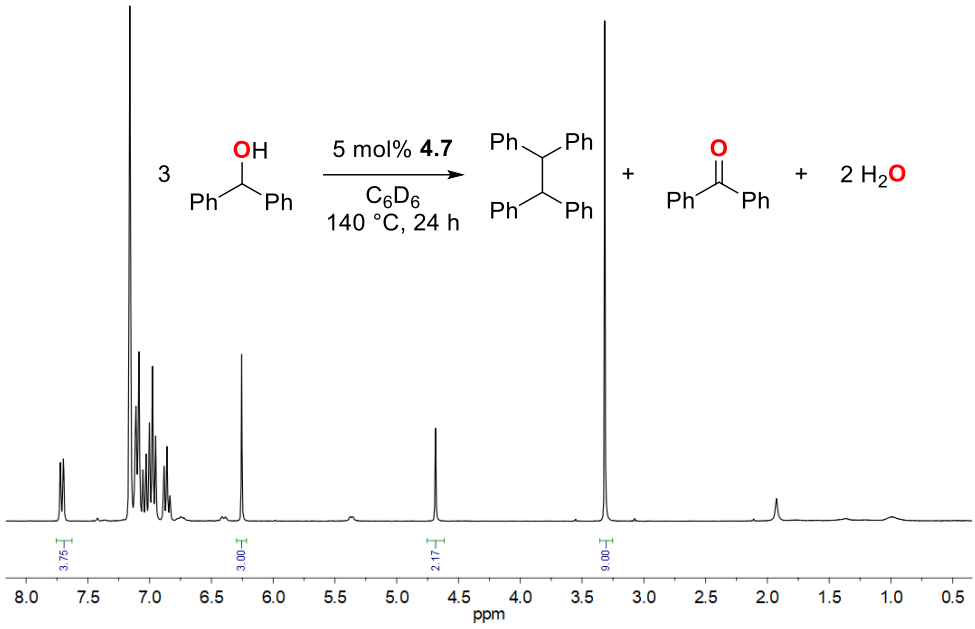

Figure D.34 ^{1}H NMR spectrum of catalysis with benzhydrol (C_6D_6, 300 MHz, 298 K)[316]

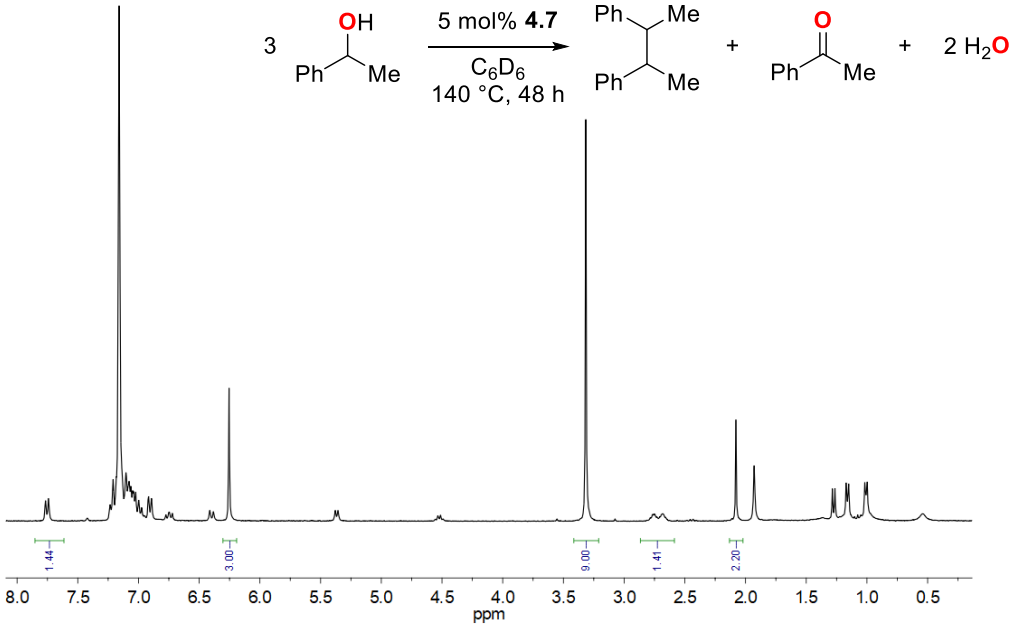

Figure D.35 ^{1}H NMR spectrum of catalysis with 1-phenylethanol (C_6D_6, 300 MHz, 298 K)[316]

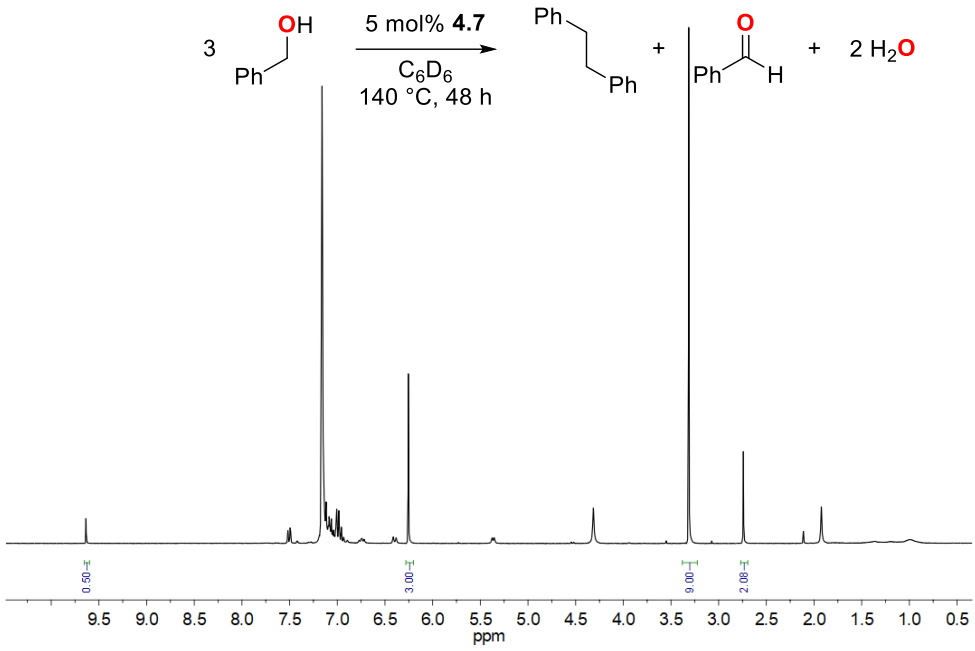

Figure D.36 ^{1}H NMR spectrum of catalysis with benzyl alcohol (C_6D_6, 300 MHz, 298 K)[316]

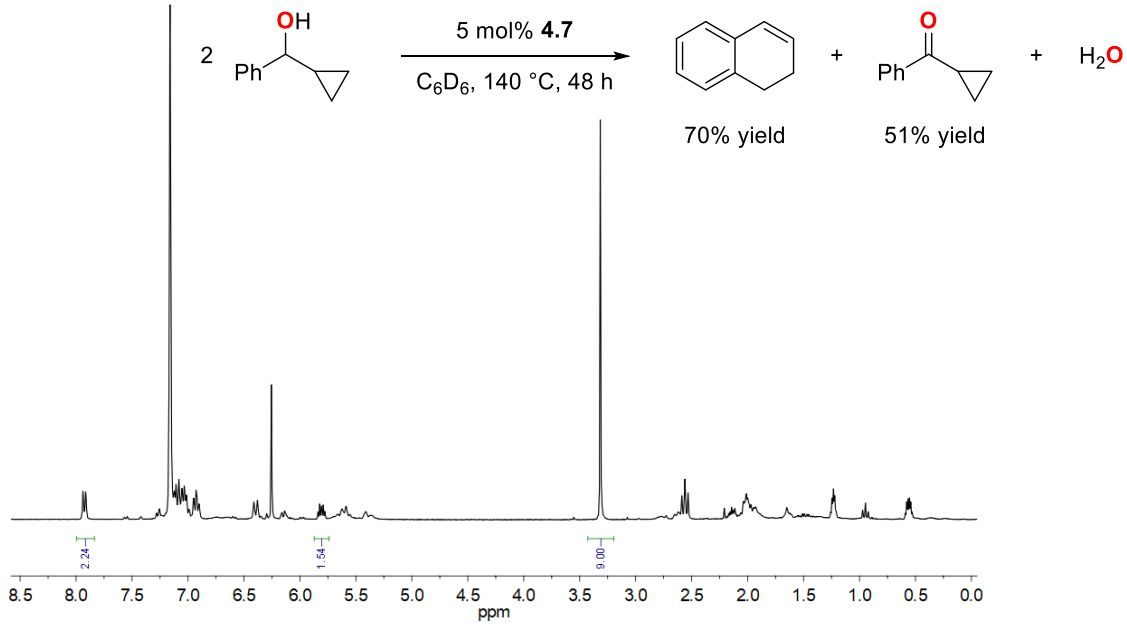

Figure D.37 ^{1}H NMR spectrum of the radical ring-opening experiment (C_6D_6, 300 MHz, 298 K)

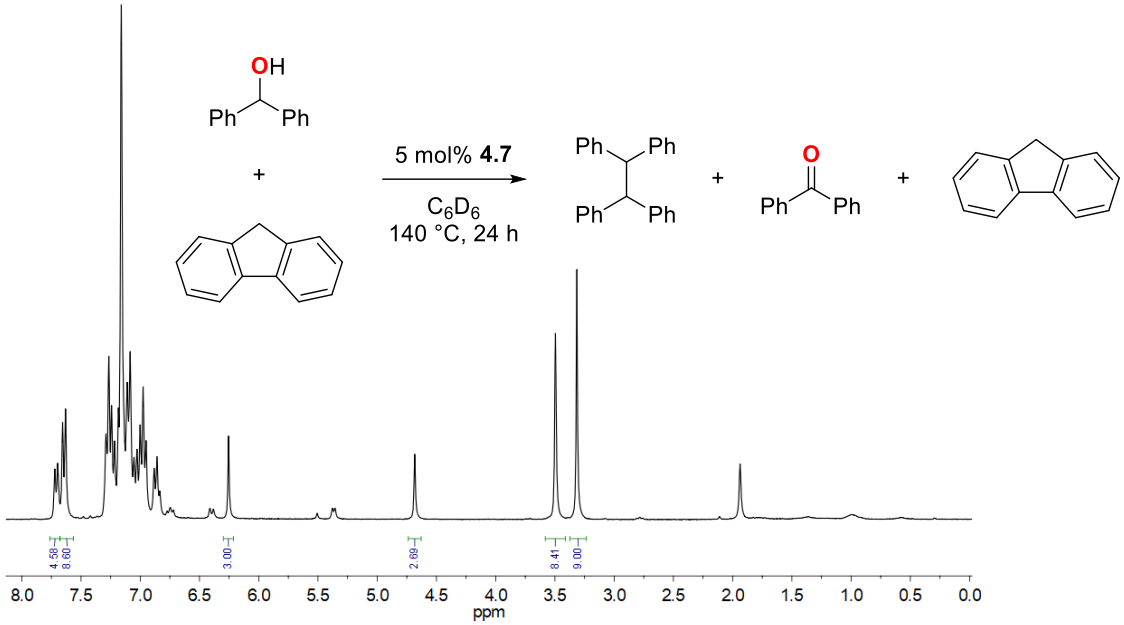

Figure D.38 ^{1}H NMR spectrum of the fluorene trapping experiment (C_6D_6, 300 MHz, 298 K)

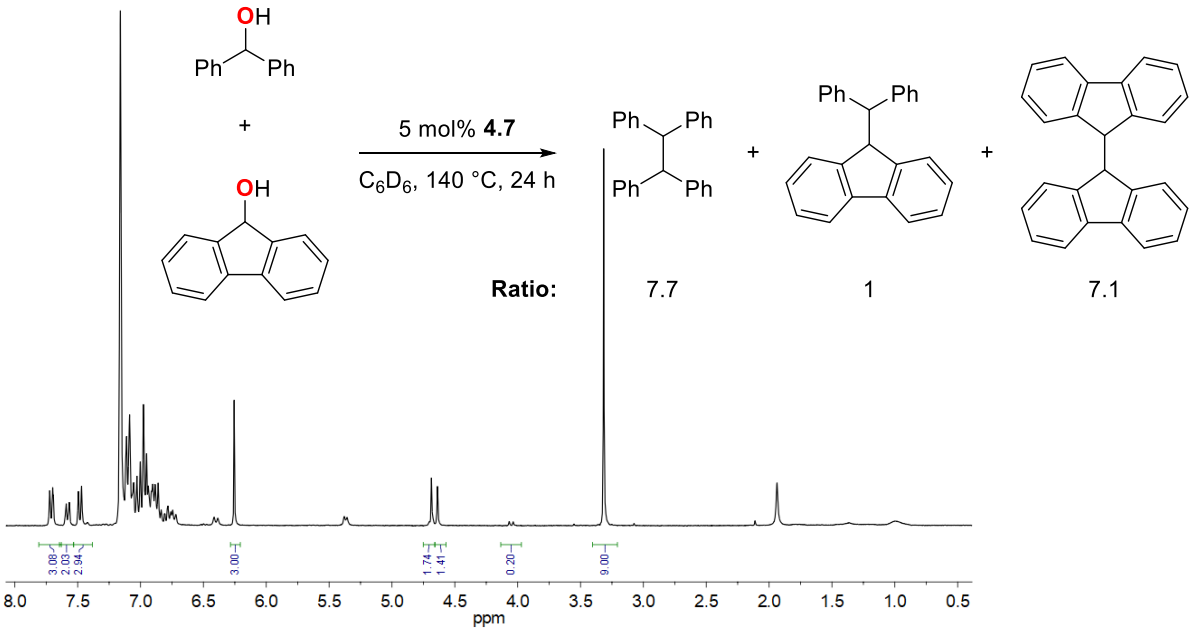

Figure D.39 ^{1}H NMR spectrum of the fluorenol cross-over experiment (C_6D_6, 300 MHz, 298 K)[315]

D.6 Selected NMR Spectra for Chapter 6

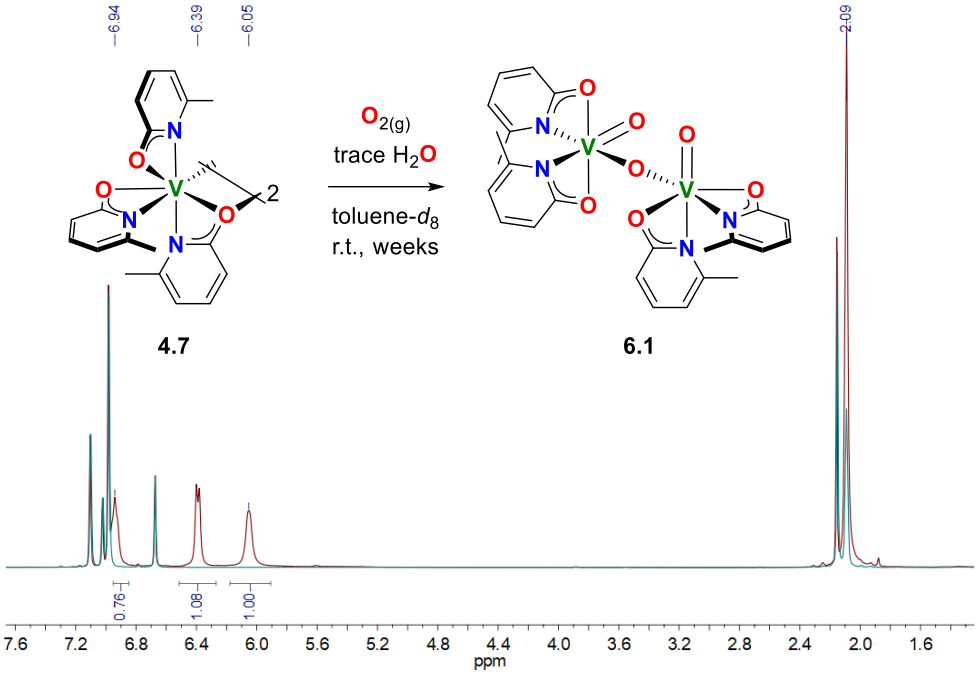

Figure D.40 ^{1}H NMR spectrum of the reaction of **4.7** with O_2, focusing on diamagnetic signals (C_7D_8, 400 MHz, 298 K; blue = before O_2 addition and red = 30 min after O_2 addition)

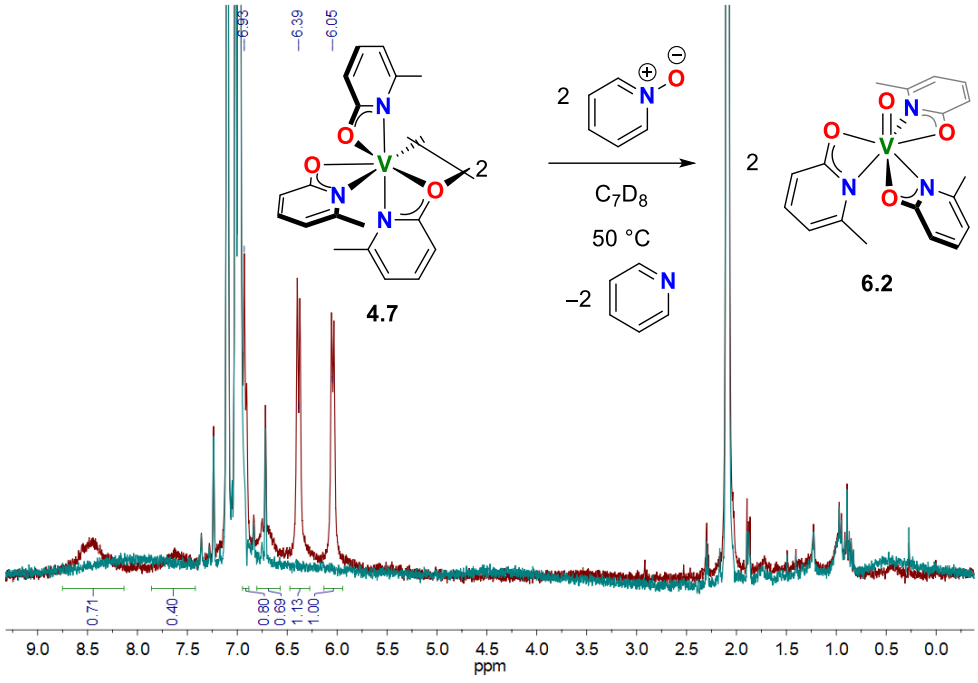

Figure D.41 ^{1}H NMR spectrum of the reaction of **4.7** with pyridine-*N*-oxide (C_7D_8, 400 MHz, 298 K; blue = before heating and red = after 17 h at 50 °C)